

ETDE/CH-mf-- 917150556

PAUL SCHERRER INSTITUT



Paul Scherrer Institut Tel. 056 310 21 11
CH-5232 Villigen PSI Telefax 056 310 21 99
Switzerland Telex 827 417 psi ch
<http://www.psi.ch>

Annual Report 1996

Annex V

PSI General Energy Technology

Newsletter 1996

MASTER

DISTRIBUTION OF THIS DOCUMENT IS UNLIMITED

Department of General Energy Technology

Editing: Ch. Daum, J. Leuenberger

RB



COVER PHOTOGRAPH

Measurement site during the VOTALP field campaign of September 1996 in the Mesolcina Valley. Sensors for ozone and meteorological parameters are mounted on top of the 12-m tower. Components of the optical equipment to measure the ozone concentration and wind speed on a light path across the valley are visible on the ground to the left of the tower.

DISCLAIMER

**Portions of this document may be illegible
in electronic image products. Images are
produced from the best available original
document.**

TABLE OF CONTENTS

| | |
|---|----|
| Introduction | 1 |
| A. Wokaun | |
| Renewable Energies | 3 |
| Gasification of Wood in a Fluidized Bed Reactor | 4 |
| L. C. de Sousa, T. Marti, M. Frankenhaeuser | |
| The Influence of Chlorine on the Gasification of Wood | 6 |
| C. von Scala, R. Struis, S. Stucki | |
| Combined Coal Gasification and Fe₃O₄-Reduction Using High-Temperature Solar Process Heat | 8 |
| Y. Tamaura (Tokyo Institute of Technology, Japan), K. Ehrensberger, A. Steinfeld | |
| Wüstite - A Solar Energy Carrier | 10 |
| A. Weidenkaff, P. Nüesch, A. Wokaun, A. Reller (University of Hamburg, Germany) | |
| Production of Filamentous Carbon and H₂ by Solarthermal Catalytic Cracking of CH₄ | 12 |
| V. Kirillov, G. Kuvshinov (Boreskov Institute of Catalysis, Russia), A. Reller (University of Hamburg, Germany), A. Steinfeld | |
| Photochemistry at High Temperatures - Potential of ZnO as a High Temperature Photocatalyst | 14 |
| M. Schubnell, P. Beaud, I. Kamber | |
| Materials Development and Methods of Characterization for Energy Research | 17 |
| Recycling of Greenhouse Gases via Methanol | 18 |
| A. Bill, B. Eliasson (ABB Corporate Research Center, Baden-Dättwil, Switzerland), U. Kogelschatz (ABB Corporate Research Center, Baden-Dättwil, Switzerland) | |
| Thermal Stability of Nafion Membranes under Mechanical Stress | 20 |
| M. Quintilii, R. Struis | |
| Solid State Diffusion and Reaction in ZnO/SiO₂ in Thin Films | 22 |
| A. Jakob, S. Stucki, B. Schnyder, R. Kötz | |
| Kinetics with Deactivation of Methylcyclohexane Dehydrogenation for Hydrogen Energy Storage | 24 |
| G. Maria, A. Marin, C. Wyss, S. Müller, E. Newson | |
| Time Resolved FTIR Study of the Catalytic CO Oxidation under Periodic Variation of the Reactant Concentration | 27 |
| J. Kritzenberger, A. Wokaun | |
| XPS Analysis of Boron Doped Heterofullerenes | 29 |
| B. Schnyder, H.-J. Muhr (ETH Zürich, Switzerland), R. Nesper (ETH Zürich, Switzerland), R. Kötz | |
| Intermittent Contact Atomic Force Microscopy in Electrochemical Environment | 31 |
| P. Häring, R. Kötz, H. Siegenthaler (University of Bern, Switzerland) | |
| In-Situ Investigation of the Calcination Process of Mixed Oxide Xerogels with Raman Spectroscopy | 33 |
| J.-C. Panitz | |
| Development and Characterization of a Rare Earth Emitter for a Thermophotovoltaic Power Generator | 35 |
| W. Durisch, J.-C. Panitz | |
| Azo Group Containing Compounds: Investigation of the Decay Mechanism | 37 |
| D. Franzke, J. Kritzenberger, Th. Kunz | |

| | |
|--|-----------|
| Microstructuring of Triazene Containing Copolyester Films | 39 |
| Ch. Hahn, Th. Kunz, A. Wokaun | |
| Photochemically Induced Oscillations of Aromatic Pentazadienes | 41 |
| Th. Kunz, Ch. Hahn, A. Wokaun | |
| Electrochemical Energy Storage and Conversion | 43 |
| Bipolar Zinc / Oxygen Battery Development | 44 |
| S. Müller, C. Schlatter (Swiss Federal Institute of Technology, Lausanne, Switzerland) | |
| Progress Towards a 20 Ah/12 V Zinc/Air - Battery | 46 |
| F. Holzer, S. Müller, O. Haas | |
| Porous Graphite Electrodes for Rechargeable Ion-Transfer Batteries | 47 |
| P. Novák, W. Scheifele, O. Haas | |
| Use of Ab Initio Quantum Chemical Methods in Battery Technology | 49 |
| E. Deiss | |
| Glassy Carbon Based Supercapacitor Stacks | 51 |
| M. Bärtsh, A. Braun, R. Kötz, O. Haas | |
| Fuel Cell Membrane Preparation: Effects of Base Polymer | 53 |
| H.P. Brack, G.G. Scherer | |
| Cyclic Voltammetric Investigations of Microstructured and Platinum-Covered Glassy Carbon Electrodes in Contact with a Polymer Electrolyte Membrane | 55 |
| G.G. Scherer, Z. Veziridis, M. Staub, M. Freimuth (Institut für Mikrotechnik Mainz IMM, Mainz, Germany) | |
| Polymer Electrolyte Fuel Cells : Flow Field for Efficient Air Operation | 57 |
| F.N. Büchi, A. Tsukada, O. Haas, G.G. Scherer | |
| Combustion Research | 59 |
| Catalytically Stabilized Combustion of Lean Methane-Air-Mixtures: A Numerical Model | 60 |
| U. Dogwiler, P. Benz, I. Mantzaras | |
| Numerical and Experimental Investigation of NO_x Formation in Lean Premixed Combustion of Methane | 62 |
| K. Bengtsson, P. Benz, T. Marti, R. Schären, A. Schlegel | |
| Formation of Nitric Oxide in an Industrial Burner Measured by 2-D Laser Induced Fluorescence | 64 |
| A. Arnold, R. Bombach, B. Käppeli | |
| Beam Steering Effects in Turbulent High Pressure Flames | 66 |
| B. Hemmerling, B. Käppeli | |
| A Study of Relaxation Mechanisms in the A²Σ⁺ State of Nitric Oxide by Time Resolved Double Resonant Polarization Spectroscopy | 68 |
| A. Stampanoni-Panariello, R. Bombach, B. Hemmerling, W. Hubschmid | |
| Laser-Induced Gratings in the Gas Phase Excited Via Raman-Active Transitions | 70 |
| D.N. Kozlov (General Physics Institute, Russian Academy of Sciences, Moscow, Russia), R. Bombach, B. Hemmerling, W. Hubschmid | |
| Stimulated Emission Pumping of NH in Flames by Using Two-Color Resonant Four-Wave Mixing | 72 |
| P.P. Radi, H.-M. Frey, B. Mischler, A.P. Tzannis, P. Beaud, T. Gerber | |
| Rotational Energy Transfer of the A²Σ⁺(V'=1) State of OH | 74 |
| P. Beaud, P. Radi, H.-M. Frey, B. Mischler, A.P. Tzannis, T. Gerber | |
| Phase-Conjugate Resonant Holographic Interferometry Applied to NH Concentration Measurements in a 2D Diffusion Flame | 75 |
| A.P. Tzannis, P. Beaud, H.-M. Frey, T. Gerber, B. Mischler, P.P. Radi | |

| | |
|--|------------|
| Mass Spectrometric Characterization of a Pyrolytic Radical Source Using Femtosecond Ionization | 76 |
| H.M. Frey, P. Beaud, B. Mischler, P.P. Radi, A.P. Tzannis, T. Gerber | |
| Consequences of Energy Use for Atmosphere and Climate | 77 |
| Vertical Ozone Transport in the Alps (VOTALP): The Valley Experiment 1996 | 78 |
| M. Furger, J. Dommen, W.K. Graber, A. Prévôt, L. Poggio, S. Andreani, J. Keller, W. Portmann, D. Bürki, R. Erne, R. Richter, M. Tinguely | |
| PSI Contribution to the EU Project ECOMONT | 80 |
| W. Portmann, R.T. Siegwolf, M. Saurer, Y. Scheidegger, P. Geissbühler, M. Furger, L. Poggio, R. Erne, R. Richter, D. Bürki, W.K. Graber | |
| CO₂-Recycling by Plants: How Reliable is the Carbon Isotope Estimation ? | 82 |
| R.T.W. Siegwolf, M. Saurer, Ch. Körner (University of Basel, Switzerland) | |
| ¹⁸O/¹⁶O Determination in Organic Matter | 84 |
| M. Saurer, R. Siegwolf | |
| Classification of Windfields: A Diagnostic Tool for Real-Time Determination of Local Air Pollution Dispersion | 85 |
| W.K. Graber, D. Bürki | |
| Decadal Changes of Weather Types in the Alpine Region | 87 |
| G. Stefanicki, P. Talkner, R.O. Weber | |
| Short-Range Dynamics and Prediction of Mesoscale Flow Patterns in the Mistral Field Experiment | 89 |
| R.O. Weber, P. Kaufmann, P. Talkner | |
| Climatology of Local Flow Patterns Around Basel | 91 |
| R.O. Weber | |
| Topological Entropy of Autonomous Flows | 93 |
| R. Badii | |
| Saddle Point Avoidance in Barrier Crossing Problems | 95 |
| P. Talkner, A.N. Drozdov (present address: Universidad de Sevilla, Spain) | |
| The Novel Phenomenon of Noise-Catalyzed Chaos-Order Transitions | 97 |
| F. Gassmann | |
| Swiss Taxation Policies to Curb CO₂ Emissions | 99 |
| O. Bahn, E. Fragnière (HEC-Lausanne, Switzerland), S. Kypreos | |
| Modelling Regional Trade of CO₂ Certificates | 101 |
| B. Büeler (IFOR-ETHZ & PSI), O. Bahn, S. Kypreos, H.-J. Lüthi (IFOR-ETHZ) | |
| Appendix | 103 |

INTRODUCTION

A. Wokaun

Surveying the results of General Energy Research in 1996, three major trends can be identified. First, in areas where research results have reached an advanced stage, decisive steps have been taken to promote a transfer towards industrial realization; examples include biomass gasification, advanced battery concepts, and combustion research. Second, in projects with longer term orientation, several options are being evaluated by exploratory studies, e.g. in solar chemistry and reaction analysis. Third, in line with the strategic planning of our institute, the development and characterization of materials for energy research has received increased attention.

1 RENEWABLE ENERGIES

Besides the major share of hydroelectricity, biomass is providing a significant contribution of renewables to satisfy the Swiss energy demand. For a future sustainable transportation system, we are promoting the utilization of wood residues and scrap wood for methanol production. Important parameters influencing the production of synthesis gas from biomass have been studied, and the influence of inorganic impurities (e.g. salts, heavy metals) on the gasification kinetics has been quantified.

The goal of the High Temperature Solar Technology group is the production of solar fuels by using concentrated solar radiation. On the route towards the production of solar hydrogen, project work has continued on two-step cycles for the solar driven water splitting reaction. As an important intermediate step, we are studying the combined use of solar energy and fossil fuels. The solar cracking of hydrocarbons, to produce hydrogen and amorphous carbon, is an interesting approach towards the decarbonization of fossil fuels, which is internationally being considered as a carbon dioxide mitigation option.

2 MATERIALS DEVELOPMENT AND METHODS OF CHARACTERIZATION FOR ENERGY RESEARCH

Storage of hydrogen in the form of synthetic liquid fuels is a key technology in future hydrogen based energy systems. Methanol production, utilizing either synthesis gas from biomass or recycled CO₂ and H₂ from renewable sources, represents a promising option. We are reporting on both catalytic aspects of the synthesis, and on a novel process engineering approach in which membranes are used to increase the hydrogen yield.

Progress in energy research strongly depends on the availability of novel functional materials, to be used as catalysts, electrodes, and in combustion devices. Advances have been made in the preparation of porous oxides, and of rare earth compounds with tailored light emission properties.

Understanding the occurring solid state chemical reactions turned out to be crucial in designing a process for the evaporative removal of heavy metals from solid residues of municipal waste incinerators.

Materials development is strongly dependent on the advancement of characterization techniques. In 1996, novel results have been obtained on the *in situ* monitoring of electrode materials by atomic force microscopy, and the study of solid state chemical transformations by Raman microscopy.

For the use in microtechnology applications, photopolymers with tailored absorption and decomposition properties have been developed based on studies of the mechanism of photolytic decomposition, and the high resolution structuring of these materials by excimer laser ablation was demonstrated.

3 ELECTROCHEMICAL ENERGY STORAGE AND CONVERSION

Among the advanced electricity storage systems which appear promising for traction applications, lithium ion transfer batteries have been further enhanced in energy density by the development of new electrode materials. With the rechargeable zinc / air battery, we have proceeded from the individual 100 cm² cells to realizing an 8 Ah bipolar stack of seven cells.

Electrochemical double layer capacitors ('supercapacitors') are developed for electrical energy storage on a much shorter time scale, with a view to applications in power electronics. In 1996, we implemented an activation procedure for glassy carbon electrodes that resulted in capacities > 0.1 F cm⁻², and have assembled them into a three cell stack.

Combining renewable fuels with highly efficient, low-polluting converters and advanced vehicles capable of operation at low specific consumption will be the key for sustainable development in transportation. For this aim we are developing low temperature polymer electrolyte fuel cells. Progress is reported both for the preparation of high performance membranes, and for innovative stack design concepts.

4 COMBUSTION RESEARCH

Among the advanced techniques for lowering NO_x emissions in the combustion of gaseous fuels, we are installing a test setup for investigating the catalytic combustion of methane; significant progress has been achieved in modelling the heterogeneous reaction mechanism. Powerful laser diagnostic techniques were combined to provide quantitative information on the generation of NO in an industrial burner. The challenges of setting up optical measurements in the turbulent medium of a high pressure combustor have been addressed.

In a project aimed at supplementing pivotal information on reaction mechanisms in combustion processes, the concentrations of two important reactive intermediates, i.e. the NH and OH species, are visualized by a resonant holographic technique. The operation of a pyrolytic radical source represents a milestone towards elucidating the initial steps of soot generation in Diesel fuel combustion.

5 CONSEQUENCES OF ENERGY USE FOR ATMOSPHERE AND CLIMATE

Air pollution due to energy related emissions does not represent a regional problem, but is strongly influenced by the transboundary transport of pollutants. As it is therefore mandatory to address this problem in international collaboration, we have initiated in 1996 two European projects in this field. A first measurement campaign was successfully conducted in the valley Mesolcina (Graubünden, Switzerland) to study the consequences of Vertical Ozone Transport in the ALPs (project VOTALP). The second EU activity, ECOMONT, addresses the consequences of land use changes on mountain ecosystems. In this context, the method of isotope ratio mass spectrometry has proven invaluable to study the interacting effects of water and

CO₂ supply on plant growth, both for quantifying microclimatic effects, and for reconstructing climatic conditions from the isotope archives stored in tree rings. These archives are highly relevant for the time period over which changes of atmospheric CO₂ concentrations have been induced by anthropogenic activities.

Measurement campaigns are necessarily restricted in time and space, and networks of measurement stations record data at distinct locations. In order to proceed to data that are representative for a country and for the course of an entire year, we are quantifying the yearly occurrence of characteristic wind field and weather classes. The discovery that the frequency of advective weather types has changed significantly over the past 50 years, represents another piece of evidence for significant changes in global climate that can be detected even on a national scale.

Our studies of the consequences of air pollution are contributing towards PSI's program for a comprehensive assessment of energy systems. In addition, we are investigating policy options to deal with climate change, in particular strategies for curbing CO₂ emissions by joint implementation and international agreements.

In summary, the results achieved in 1996 show that several innovative technologies developed at PSI during the past few years have been promoted towards transfer and industrial realization. The exploratory research in long-term oriented projects is expected to achieve further focusing during 1997. In strengthening its expertise in the development and characterization of energy related materials, the department is increasingly contributing to the mission of PSI as a center of structuring, spectroscopy and characterization of advanced materials.

Renewable Energies

GASIFICATION OF WOOD IN A FLUIDIZED BED REACTOR

L. C. de Sousa, T. Marti, M. Frankenhaeuser

A first series of gasification experiments with our fluidized bed gasifier was performed using clean sawdust as fuel. The installation and the analytical systems were tested in a parametric study in which gasification temperature and equivalence ratio were varied. The data acquired will serve to establish the differences between the gasification of clean wood and the gasification of Altholz (scrapwood) and wood/plastics mixtures.

1 INTRODUCTION

Biomass is a precious resource as it is the only renewable carbon source available on earth. Biomass can be gasified to generate energy or to produce chemicals or fuels. As PSI's BIOMETH feasibility study [1] showed, methanol for fuel usage can be produced from wood with existing technology at a competitive price in Switzerland. The costs of the feedstocks gasified strongly influence the cost of the produced methanol. Due to their zero or negative price, carbon containing wastes such as Altholz (scrapwood from building demolition and other sources) or industrial refuse plastics are an attractive addition to the expensive clean wood from the forest. The contaminants present in these wastes [2] are thought to influence the gasification process. At PSI we aim at understanding what differences these contaminants cause in gasification and how to drive the gasification process to obtain a pure gas and disposable residues. To see the differences in gasification products caused by the use of a different fuel than „pure“ forest wood, the base case for comparison must be well understood. As in numerous publications on the influence of experimental parameters on the gasification [3] we test whether our gasifier is working properly, i.e. if our results are comparable and compatible with those obtained by other researchers and if the gasifier is, as planned, simulating larger installations properly. To answer these questions we started a parametric study, in which the values of the most important variables were changed. In fluidized bed gasification of biomass the most important process variables are:

- gasification temperature
- oxidant to fuel or equivalence ratio
- fuel humidity, composition and size
- steam to biomass ratio (when steam is used)
- size and nature of the inert bed material

2 EXPERIMENTAL

The fluidized bed gasification facility at PSI is described elsewhere [2]. In our parametric study we used air at a fixed feeding rate of $7 \text{ m}^3_{\text{N}}/\text{h}$ and set the reactor's temperature at 700, 800 and 900°C. The equivalence ratio was set at 0.2, 0.3 and 0.4 by changing the biomass feed rate. We determined material balances over the reactor and the tar content of the gas at steady-state. Table 1 shows the experimental conditions used. The fuel used in all tests was a dried sawmill residue with 1 to 2% humidity. The mean particle

size was 830 μm . In all experiments we continuously measured the concentrations of N_2 , O_2 , CO_2 , CO , H_2 , CH_4 and Ar in the dry syngas with a mass spectrometer. The gas composition reached steady-state very rapidly, i.e. in less than 10 minutes upon starting gasification.

| Run Name | Equivalence Ratio | Temperature |
|----------|-------------------|-------------|
| 9606131 | 0.19 | 800°C |
| 9606251 | 0.187 | 800°C |
| 9607051 | 0.185 | 800°C |
| 9607161 | 0.34 | 850°C |
| 9607301 | 0.31 | 800°C |
| 9608061 | 0.23 | 715°C |
| 9608081 | 0.21 | 900°C |

Table 1: Experimental conditions reported.

3 RESULTS AND DISCUSSION

In this short overview we are going to discuss briefly the mass balances calculated and the tar analysis performed.

3.1 Material Balances

In steady state the sum of the output massflows must be equal to the sum of the input massflows:

$$\sum_i \dot{m}_{i, \text{INPUT}} = \sum_j \dot{m}_{j, \text{OUTPUT}}$$

$$\dot{m}_{\text{Wood}} + \dot{m}_{\text{Air}} = \dot{m}_{\text{Syngas, dry}} + \dot{m}_{\text{Water}} + \dot{m}_{\text{Ash}}$$

The input massflows of air and biomass are continuously monitored by a massflow controller and by a balance. We calculated the dry syngas massflow based on a nitrogen balance and the measured dry syngas composition. The water massflow was either measured by condensing the water from a product gas side stream or calculated by an elemental balance of either hydrogen or oxygen. We determined the ash massflow by weighing the ashes collected by the cyclone over a known period of time. Table 2 gives an overview of the differences found in the mass balances with different methods used to calculate the water content of the syngas.

With the measured water content the overall mass balances were unsatisfactory. This is probably due to incomplete water condensation together with an inaccurate sampling method. In the last three runs we tried to improve accuracy by using the tar sampling train for water condensation as well. The measured water content of the gas was then higher, but the mass balances did still not close up. Using the hydrogen balance to calculate the water content of the syngas im-

proved the overall mass balances. However, we found that this method over-estimates the oxygen output from the reactor. Using the oxygen balance to calculate the water content of the syngas did not improve the accuracy of our mass balance.

| Run Name | Difference in mass balance as $\frac{\text{Input} - \text{Output}}{\text{Input}}$ | | |
|----------|---|-----------|-----------|
| | Water contents of syngas calculated by: measurement | H-balance | O-balance |
| 9606131 | - | 1.21% | 7.27% |
| 9606251 | 10.23% | 1.48% | 7.36% |
| 9607051 | 11.21% | 1.28% | 6.89% |
| 9607161 | 7.82% | -1.35% | 2.46% |
| 9607301 | 3.40% | -2.48% | 2.16% |
| 9608061 | 14.94% | 1.68% | 6.80% |
| 9608081 | 9.08% | 1.80% | 5.80% |

Table 2: Overall mass balance closure for performed experiments.

The most likely reasons for the error in the overall mass balance are the inaccuracies in the measurement of the biomass feeding rate and in the assumed elemental composition of the fuel. Also, the syngas may contain simple hydrocarbons (e.g. ethylene, ethane, etc.) which were not detected in the gas composition analysis. An improved water sampling method as well as off-line gas analysis for hydrocarbons will be used in the future. The fuel feeding system will be modified to improve the accuracy of the feeding rate measurement.

3.2 Tar Contents

We sampled and quantified tars by a method described in detail elsewhere [4]. The gas sampled passes through a glasswool filter at 300°C where tar components with a high boiling point condense („heavy“ tars). After the filter the gas passes a series of impingers containing CH_2Cl_2 , where all other components are absorbed („light“ tars). The heavy tars are extracted from the filter and their amount is determined gravimetrically.

| Number | Compound | Contents in train sampling bottle (mg) | | | Components total mass (mg) |
|--------|--------------------|--|--------|-------|----------------------------|
| | | nr. 1+2 | nr. 3 | nr. 4 | |
| 1 | Benzene | 0.00 | 508.96 | 22.36 | 531.32 |
| 2 | Toluene | 0.00 | 143.39 | 0.00 | 143.39 |
| 3 | Xylene | 0.00 | 10.38 | 0.00 | 10.38 |
| 4 | Styrene | 0.00 | 65.20 | 0.00 | 65.20 |
| 5 | Phenol | 45.10 | 14.66 | 0.00 | 59.76 |
| 6 | Naphtalene | 80.79 | 110.41 | 0.00 | 191.20 |
| 7 | Indene | 0.00 | 0.00 | 0.00 | 0.00 |
| 8 | 2-Methylnaphtalene | 8.11 | 8.97 | 0.00 | 17.07 |
| 9 | 1-Methylnaphtalene | 10.33 | 11.53 | 0.00 | 21.86 |
| 10 | Biphenylene | 0.00 | 5.41 | 0.00 | 5.41 |
| 11 | Acenaphtene | 0.00 | 0.00 | 0.00 | 0.00 |
| 12 | Fluorene | 12.03 | 13.35 | 0.00 | 25.38 |
| 13 | Pheneantrene | 15.13 | 19.55 | 0.00 | 34.69 |
| 14 | Antracene | 8.67 | 11.06 | 0.00 | 19.73 |

Light Tars concentration in Syngas: (mg/m³) 10'353.30

Table 3: Tar compounds identified for run 9607301.

The light tars are analysed qualitatively and quantitatively using gas chromatography (GC). Table 3 gives an example of the GC analysis giving approximate quantities of individual tar compounds. Figure 1 shows the corresponding chromatogram. As expected the

total tar concentration was around 10 g/m³. The main components observed were benzene and naphthalene. From the analysis of two experiments the trend towards the formation of less „light“ compounds and a larger percentage of PAH's when increasing gasification temperature [5] was observed. The tar analysis method will have to be improved both qualitatively and quantitatively as this information is expected to be most sensitive to varying input parameters (type of fuel, contaminants, etc.).

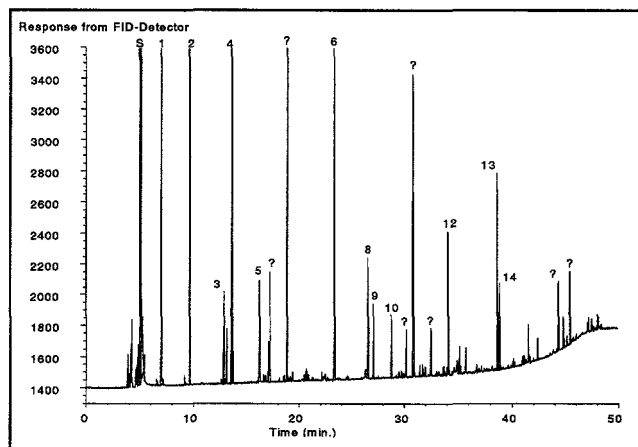


Fig. 1: Chromatogram for tar analysis of run 9607301. Sampling bottle nr. 3. Peak numbers see table 3. S: Solvent (CH_2Cl_2). „?“ denotes peaks from substances not yet identified.

4 CONCLUSIONS

The test runs carried out in the summer of 1996 show that our fluidised bed gasification reactor is running satisfactorily. To achieve better mass balances some improvements still have to be made on the reactor's feeding system as well as on the analytical systems used. A standard reference sawdust of known and constant composition will be used in the future to generate reference data for uncontaminated wood.

5 REFERENCES

- [1] „BIOMETH Methanolproduktion aus Biomasse-Abfällen in der Schweiz, Phase 1: Machbarkeitsstudie“, Schlussbericht der Projektleitung, Bundesamt für Energiewirtschaft, Bern, (1996).
- [2] de Sousa L.C.; Hütter P.; Mayor J.C.; Quintillii M.; „Fluidized bed reactor for the gasification of biomass“, PSI - Annex V, (1994).
- [3] Narvárez I.; Orío A.; Aznar M.P.; Corella J.; „Biomass gasification with air in an atmospheric bubbling fluidized bed. Effect of six operational variables on the quality of the produced raw gas.“ Ind. Eng. Chem. Res., **35**, 2110-2120, (1996).
- [4] de Sousa L.C.; „Description of PSI's tar sampling method“. PSI-Internal report, to be published.
- [5] Simell P.; Kurkela E.; Ståhlberg P.; „Formation and catalytic decomposition of tars from fluidized-bed gasification.“, Advances in Thermochemical Biomass Conversion 265-279, (1992).

THE INFLUENCE OF CHLORINE ON THE GASIFICATION OF WOOD

C. von Scala, R. Struis, S. Stucki

Chlorides of the heavy metals copper, lead and zinc inhibit the CO₂-gasification reaction of charcoal. This is observed either by impregnating the wood with the salts before pyrolysis or by mechanically mixing the salts with the charcoal before gasification. Charcoal impregnated or mixed with ammonium chloride reacts more slowly than untreated charcoal. Treating the charcoal with HCl also influences negatively the gasification reactivity, indicating that chlorine plays an important role in the gasification.

1 INTRODUCTION

The aim of the BIOMETH project [1] is to produce methanol through gasification of waste wood, e.g. demolition wood or residues of wood processing industries. This waste wood is, however, contaminated with substances that are not normally found in untreated forest wood, such as heavy metals and chlorine. The aim of this study is to determine how these contaminants influence the gasification process.

It has been known that the impregnation of coal with alkali carbonates increases their reactivity [3]. Little work has been done with heavy metals. However, as documented in [4], they are present as contaminants in waste wood, especially zinc, lead and copper.

To accomplish gasification, it is inevitable to pass through a pyrolysis step. We perform the pyrolysis in a tubular oven, and the resulting charcoal is used for the gasification experiments. In this paper we just show results from the gasification step. Since it is the slowest step, it is an important parameter for the design of a gasifier.

Our chosen gasification agent is CO₂, and if we assume that charcoal is mostly composed of C, the main reaction we are looking for is:



2 EXPERIMENTAL

The reactivity of charcoal was determined in a thermogravimetric analyzer (TGA). About 10 mg of ground charcoal was gasified with CO₂. A typical run can be seen in Figure 1. As a pre-treatment step, a temperature ramp until 900°C in an inert atmosphere was introduced to complete the pyrolysis. After stabilization of the temperature at 800°C, the gasification agent (CO₂, 40 ml_n/min) was introduced. The gasification time τ (see Figure 1) was chosen for the quantification of the weight loss curves. It is defined as the time that the char takes to react completely, and only the ash is left (1-6 wt.-%).

Our first approach to study the influence of contaminants was to impregnate pieces of wood with salts of sodium, potassium, calcium, magnesium, copper, zinc and lead. The impregnation procedure is described in [2]. The impregnated wood pieces were pre-pyrolysed in the tubular oven at 600°C in an inert atmosphere and the resulting charcoal was ground.

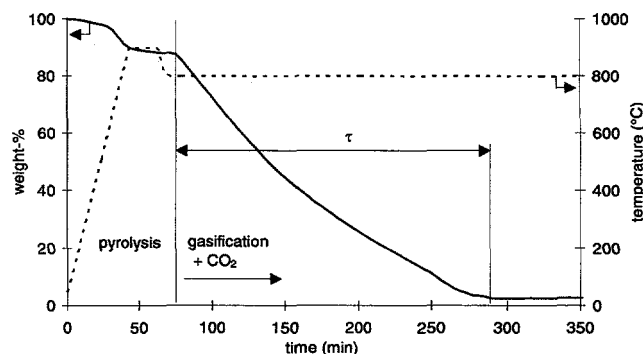


Fig. 1: TGA-experiment.

3 RESULTS

Some gasification results of the impregnated samples have been presented in [2], and they can be summarised as follows:

Charcoal from wood impregnated with alkali metals (K, Na) reacts faster than the untreated one. The alkali metals decrease the gasification time of the charcoal, as expected, by a factor of about 5. For the samples impregnated with Ca and Mg, there is not much change compared to the untreated samples. On the other hand, the reactivity of the samples impregnated with heavy metals, especially the ones impregnated as chlorides, decreases. The gasification of chars from wood impregnated with lead and zinc chloride is about 2.5 times slower than the char from untreated wood. In all cases the samples impregnated with chloride salts show a significant increase in the reaction time compared to the other anions. The chloride anion seems therefore to influence the gasification negatively.

One possible explanation for the decrease in reactivity is that during the impregnation, an exchange occurred between the naturally present alkali metal ions in wood and the heavy metals, followed by an evaporation of the chloride salts during the post-pyrolysis (zinc and lead chlorides have a lower boiling point than the other salts), leaving a charcoal that is poorer in metals than the natural one. However ICP-AES (Inductive Coupled Plasma Atom Emission Spectroscopy) measurements of the charcoal showed no decrease in the concentration of the naturally present metals after impregnation. The remaining impregnation solutions were also ana-

lysed by ICP-AES, and also there it was not possible to detect significant quantities of the naturally present metals. Therefore this hypothesis of the leaching out of the alkali compounds does not explain our results.

To investigate possible effects of the impregnation itself on the reactivity of charcoal, a blank experiment was carried out by using just water. The ICP-AES measurements for the resulting charcoal and for the remaining solution showed no leaching of the naturally present metals. This charcoal made of "boiled" wood reacts as fast as the untreated, standard charcoal, proving that the impregnation process itself does not influence the reactivity.

To determine if the salts change the charcoal structure during pyrolysis, experiments were made by mechanically mixing some of the salts used for impregnation with the standard untreated charcoal sample and gasifying the mixture in the TGA. The mixing ratio was about 5 mg of salt with 10 mg of charcoal. The results can be seen in Figure 2.

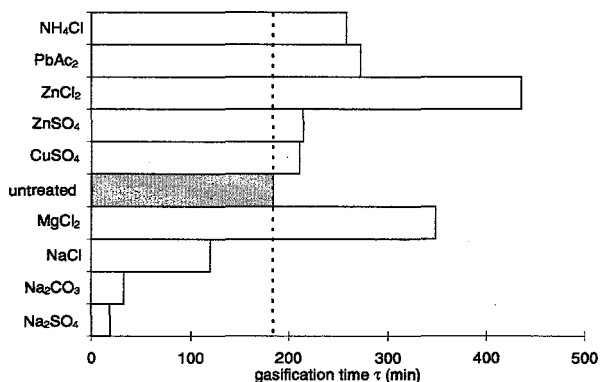


Fig. 2: Gasification of charcoal mixed with salts.

As can be seen in Figure 2, the samples of charcoal mixed with salts show similar trends as the impregnated samples. Sodium increases, heavy metals inhibit the gasification of the charcoal. The negative effect of chlorides is even more prominent. The sample mixed with NaCl reacts significantly more slowly than the ones mixed with other sodium salts. The sample mixed with ZnCl₂ also reacts more slowly than the ones mixed with other heavy metals. The sample mixed with MgCl₂, which did not show any effect as impregnation solution, reacts slower than the pure sample. NH₄Cl, which decomposes at 340°C to NH₃ and HCl, was also used and again slower reaction can be observed. A wood sample was impregnated with NH₄Cl, and the resulting charcoal showed also a reduction in gasification activity.

To investigate the effect of chlorine we stirred a sample of the standard untreated charcoal in a solution of

18 wt-% HCl at room temperature for 48 hours, filtered and dried it. This sample, gasified in the TGA, reacts 3 times slower than the original sample. We treated another sample of standard charcoal with HCl (dry) at 800°C, and this sample reacts more than 5 times slower than the untreated one.

From the results of the experiments described above we presume that there is a poisoning of the catalytically active centres by the chloride ions. Our standard untreated charcoal has a potassium concentration of 1.8 mg/g. This natural alkali metal content could be deactivated during the gasification itself by volatilisation of the heavy metal chlorides, mobilizing the chlorine, leading to an inhibition of the gasification reaction.

4 CONCLUSIONS

Chlorides inhibit the catalytic activity of the active centres in charcoal. This inhibition process occurs through the volatilisation of the chloride salts, explaining the inhibiting effect by just mixing the salts or by the HCl treatment at 800°C. The chloride salts show a relatively low boiling point, and under our conditions they are completely in the gas phase. A possible mechanism is that the active centres in charcoal are alkali carbonates, especially K₂CO₃, that is neutralised to KCl, which is no active form for the gasification catalysis. This, however, does not explain the moderate accelerating effect of NaCl. Further work has to be done to understand and explain this inhibiting effect of chlorine.

5 ACKNOWLEDGEMENTS

The authors would like to thank Prof. R. Prins (ETHZ) for the useful discussions.

6 REFERENCES

- [1] S. Stucki, "BIOMETH - Methanolproduktion aus Biomasseabfällen in der Schweiz. Phase 1: Machbarkeitsstudie", Schlussbericht der Projektleitung, (1996).
- [2] C. von Scala, R. Struis, S. Stucki, "The Influence of Heavy Metals on the Gasification of Wood", PSI - Annual Report / Annex V: General Energy Research, (1995).
- [3] K. Hidden, A. Wilhelm, "Catalytic Effects of Inorganic Substances on Reactivity and Ignition Temperature of Solid Fuels", Ger. Chem. Eng., 3, pp. 142-147, (1980).
- [4] P. Hasler, T. Nussbaumer, R. Bühler, "Vergasung von Biomasse für die Methanol-Synthese", Schlussbericht im Sektor Technik Projekt BIOMETH, (1994).

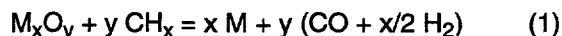
COMBINED COAL GASIFICATION AND Fe_3O_4 - REDUCTION USING HIGH-TEMPERATURE SOLAR PROCESS HEAT

Y. Tamaura (Tokyo Institute of Technology, Japan), K. Ehrensberger, A. Steinfeld

The coal/ Fe_3O_4 system was experimentally studied at PSI solar furnace. The reactants were directly exposed to a solar flux irradiation of 3,000 suns (1 sun = 1 kW/m²). The combined gasification of coal and reduction of Fe_3O_4 proceeded rapidly after only one second exposure, suggesting an efficient heat transfer and chemical conversion by direct solar energy absorption at the reaction site. The proposed solar thermochemical process offers the possibility of converting coal to a cleaner fluid fuel with a solar-upgraded calorific value.

1 INTRODUCTION

Coal can be converted to a cleaner fuel when combined with solar energy. This mixture could be efficiently accomplished via high-temperature thermochemical processes using metal oxides and solar process heat [1,2]. While the metal oxide is reduced using coal as the reductant, coal is gasified to syngas using the metal oxide as the oxidant. The overall reaction can be represented by:



where M_xO_y denotes the metal oxide, CH_x denotes the coal, and x depends on the hydrogen content of the coal. The products are syngas and the metal. With this strong endothermic transformation, solar energy is converted to chemical energy that can be stored and transported over long distances.

In a second, exothermic step, the metal (or lower-valence metal oxide) can either be reacted with water to form hydrogen or can be used in a fuel cell or battery to directly generate electricity. In either case, the chemical product is the metal oxide which is recycled to the solar process. The hydrogen can be used for enriching or adjusting the quality of the syngas produced in the solar process, or it can be further processed for heat and power generation. Such scheme is represented in Figure 1.

A recent review paper discusses various thermochemical schemes, involving metal oxides redox systems, for the conversion of solar energy into fluid fuels [3]. The potential for CO_2 mitigation by these solar processes has been analyzed [4,5]. The amount of fuel needed to reduce metal oxides could be substantially reduced if it were used exclusively as a reducing agent and process heat were supplied by solar energy, thus minimizing the build-up of greenhouse-effect gases and pollutants derived from the combustion of fossil fuels for heat generation. The solar carbothermic reduction of metal oxides (e.g. Fe_2O_3 , ZnO , MgO , TiO_2 , Al_2O_3 , SiO_2), using C or CH_4 as reducing agents, has been experimentally demonstrated in solar furnaces [6-8]. The chemical equilibrium composition of the system Fe_3O_4 and C(gr) was computed for various temperatures and stoichiometries [1,6].

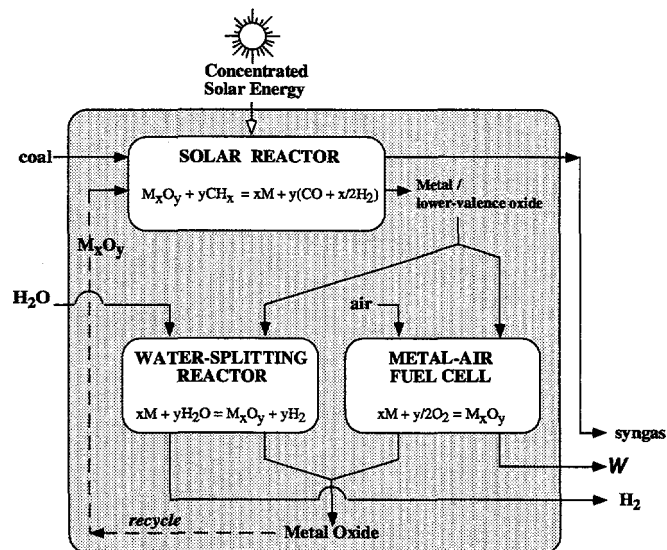


Fig. 1: Scheme of a 2-step thermochemical process for solar-upgrading coal and for the production of syngas, hydrogen, and electricity, using coal and water as feedstock and concentrated solar energy as the source of process heat.

2 SOLAR EXPERIMENTATION

The reaction of coal and Fe_3O_4 was studied at TIT laboratory using an infrared electric furnace, and at PSI solar furnace using a solar reactor that controls the time duration of exposure to the solar irradiation; the results are reported in [1]. Results from the solar furnace experiments in which Fe_3O_4 /coal pellets where directly irradiated are given in Figure 2 (pelleted samples: equimolar ratio of Fe_3O_4 and C in coal; anthracite coal stoichiometry: $\text{CH}_{0.2}$). The variation of the carbon content remaining in the sample product (curve A) and of the x-ray diffraction's peak ratio of $I(311)_{\text{Fe}_3\text{O}_4}$ to $I(200)_{\text{FeO}}$ for the sample product (Curve B) are plotted as a function of the time duration of exposure to the solar irradiation. Solar irradiation flux intensity, measured optically, was 303 W/cm². The carbon content decreased rapidly between 0.8 and 1.0 sec, and was accompanied by a rapid decrease in the x-ray diffraction's peaks ratio. The solid phase change from Fe_3O_4 to FeO was relatively fast at about 1473 K because both crystals have the same

packed cubic structure of oxygen and their cation movement is assisted by electron hopping between Fe^{2+} and Fe^{3+} in the B sites of the spinel structure. Thus, lattice oxygen was continuously released from Fe_3O_4 and helped maintain a high rate of coal gasification. The solid products consisted of a mixture of FeO and remaining coal ash. Hydrolysis of solid products at temperatures below about 900 K yielded H_2 and a solid mixture of Fe_3O_4 and ash. By magnetic separation it is possible to recover Fe_3O_4 from the ash and recycle it to the solar reactor, but further studies are required to assure the cycling capability of this chemical system.

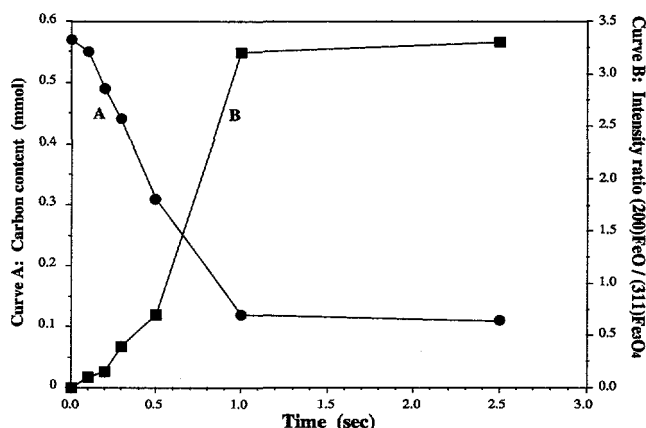


Fig. 2: Change in the carbon content (curve A) and change in the x-ray diffraction peak intensity ratio of $I(311)\text{Fe}_3\text{O}_4$ to $I(200)\text{FeO}$ (curve B), for the Fe_3O_4 /coal sample as a function of the time interval of exposure to the solar irradiation. Solar irradiation flux intensity = 303 W/cm^2 . Pelleted sample: equimolar ratio of Fe_3O_4 and C in coal; anthracite coal stoichiometry: $\text{CH}_{0.2}$.

3 SUMMARY

Exploratory experiments were performed in the solar furnace with the coal/ Fe_3O_4 system. They demonstrated that efficient heat transfer and chemical conversion can be achieved by direct absorption of concentrated solar energy at the reaction site, by-passing the limitations imposed by indirect energy transport via heat exchangers.

When compared with the conventional steam gasification of coal, the gasification rate is, under proper conditions, higher using a metal oxide as the oxidant [1,2].

From the thermodynamic standpoint, the reaction with metal oxides is more endothermic:



Thus, more solar energy can in principle be stored per unit mass of coal. An additional advantage is the simultaneous reduction of the metal oxide, yielding a metal (or lower-valence oxide) that can be further processed to pure, uncontaminated H_2 . A drawback of using metal oxides as the oxidant (instead of steam) is that the composition of the syngas is deficient in hydrogen. To some extent, the quality of the syngas can be controlled by means of the water-gas shift reaction. Studies are underway to investigate the gasification of coal using a mixture of steam and Fe_3O_4 for yielding high-quality syngas suitable for methanol synthesis.

4 ACKNOWLEDGEMENTS

This work was supported in part by the BEW-Swiss Federal Office of Energy and by the Japanese Ministry of Education and Science.

5 REFERENCES

- [1] Y. Tamaura, Y. Wada, T. Yoshida, M. Tsuji, K. Ehrensberger, A. Steinfeld, *Energy - The International Journal* **22**, pp. 337-342, (1997).
- [2] M. Tsuji, Y. Wada, Y. Tamaura, A. Steinfeld, P. Kuhn, *Energy & Fuels* **10**, pp. 225-228, (1996).
- [3] A. Steinfeld, P. Kuhn, A. Reller, R. Palumbo, J. Murray, Y. Tamaura, *Hydrogen Energy Progress XI*, pp. 601-609, (1996).
- [4] A. Steinfeld, P. Kuhn, Y. Tamaura, *Energy Conversion & Management* **37**, pp. 1327-1332, (1996).
- [5] A. Steinfeld, G. Thompson, *Energy - The International Journal* **19**, pp. 1077-1081, (1994).
- [6] A. Steinfeld, E.A. Fletcher, *Energy - The International Journal* **16**, pp. 1011-1019, (1991).
- [7] J.P. Murray, A. Steinfeld, E.A. Fletcher, *Energy - The International Journal* **20**, pp. 695-704, (1995).
- [8] A. Steinfeld, A. Frei, P. Kuhn, D. Willemin, *Int. J. Hydrogen Energy* **20**, pp. 793-804, (1995).

WÜSTITE - A SOLAR ENERGY CARRIER

A. Weidenkaff, P. Nüesch, A. Wokaun, A. Reller (University of Hamburg, Germany)

Hydrogen is produced when wüstite ($Fe_{1-y}O$) is oxidised by water. This reaction is part of a two-step thermochemical metal oxide cycle for the storage of solar energy in the form of chemical energy carriers, characterised by a high chemical potential. The reaction was studied in a tubular furnace with on-line gas analysis and further characterised in detail by DTA and high-temperature X-ray powder diffraction. The influence of non-stoichiometry, morphology and temperature on the mechanism and kinetics of the water-splitting reaction was determined.

1 INTRODUCTION

High temperature chemistry driven by concentrated solar flux is investigated as an option for the substitution of non-renewable energy systems such as coal, mineral oil and uranium. The amount of energy stored by solar thermal reduction of metal oxides (highly endothermic process) can be used to split water for producing hydrogen which is a „non-polluting“ fuel when, for example, used in a fuel cell to produce electricity.

The two-step iron oxide water-splitting cycle for the solar-driven production of hydrogen consists of the solar-thermal reduction of magnetite to wüstite, and the subsequent reoxidation with water leading back to magnetite [1]. In this process the reduced iron-oxide phase has to be quenched to avoid reoxidation.

Wüstite is not stable at temperatures below 840 K. However, by suitable quenching procedures the metastable phase may be stabilised at room temperature and becomes storable for years.

The water-splitting reaction serves to transfer the energy stored in the wüstite phase onto hydrogen as a secondary energy carrier. To optimise this reaction we studied the reactivity of the parent iron oxide phase and the mechanism and kinetics of this process at different temperatures.

2 EXPERIMENTAL

For the preparation of the wüstite phases of different non-stoichiometries we have chosen two methods:

a Synproportionation of iron and magnetite or
b Thermal dissociation of iron-oxalate precursors in an electric furnace. By variation of the oxygen partial pressure with a defined gas mixture of hydrogen and water in argon and the temperature we can synthesise $Fe_{1-y}O$ samples of non-stoichiometries of $0,05 < y < 0,12$. The samples were quenched to room temperature in less than 10 seconds.

The *in-situ* reaction kinetic studies were performed in a high-temperature X-ray powder diffraction camera and an experimental set-up where the product gases are identified and determined *on-line* in the mass spectrometer and quantified in a gas chromatograph.

3 RESULTS

The exothermic reaction of wüstite with water yielding hydrogen and magnetite is influenced by non-stoichiometry and morphology of the parent wüstite phases and the reaction temperature.

In wüstite phases with a low non-stoichiometry ($y \rightarrow 0$) more Fe(II) ions are available and more hydrogen can be produced. However, the comparison of the hydrogen signals of samples of wüstite with different non-stoichiometries shows that the reaction runs faster with wüstite phases of high non-stoichiometry (Figure 1).

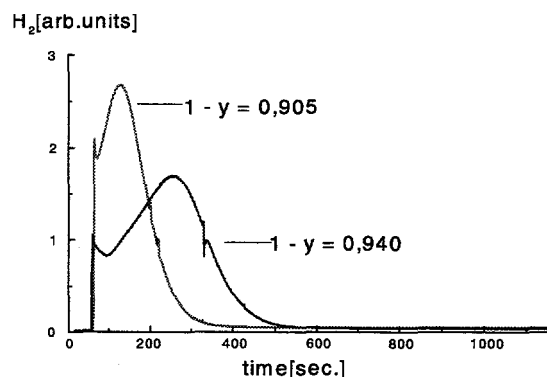


Fig. 1: On-line MS signal of the water splitting reaction with $Fe_{0,905}O$ and $Fe_{0,940}O$.

The reason might be, that the octahedral vacancies and tetrahedral iron sites (normally not occupied in the rock salt structure) lead to the formation of defect clusters which can be described as nuclei for the formation of a spinel structure in the rock salt structure of wüstite (Figure 2).

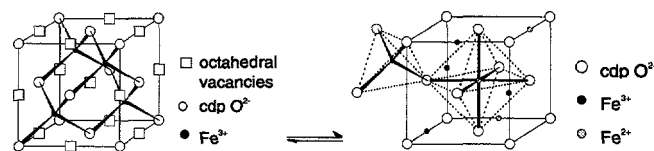


Fig. 2: Part of the defect structure of wüstite (left) and the inverse spinel structure of magnetite (right).

With Differential thermal analysis and high temperature X-ray diffraction camera we observed that heating

quenched wüstite phases in inert atmosphere leads to a two step disproportionation into iron and magnetite. By scanning the differential temperature to an inert reference we can see the exothermal first transition step of disproportionation taking place at about 300°C. As products an iron-rich 'nearly stoichiometric' phase and an iron depleted phase with spinel structure are formed [2,3]. The exothermal second step to iron and magnetite occurs about 330°C and the endothermic synproportionation back to wüstite is observed at 580°C. The heat of transition increases with increasing iron content (Figure 3).

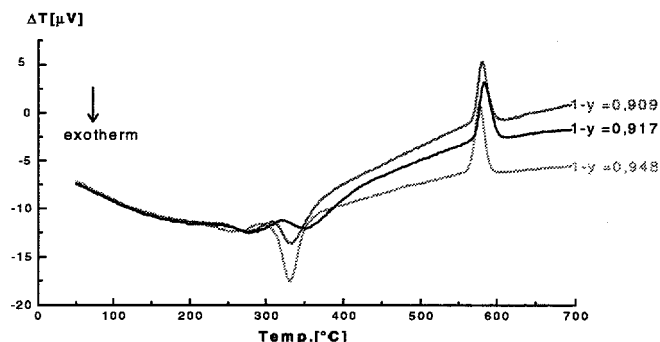


Fig. 3: Differential thermal analysis of the two-step disproportionation of wüstite.

Below the range of stability of wüstite, disproportionation and water splitting reaction are overlapping. To determine the active species for the water splitting reaction, both reactions were carried out in the high temperature X-ray camera under the same conditions at various temperatures (573 K, 673 K and 773 K).

At 573 K and 673 K a 'nearly stoichiometric' wüstite phase and magnetite are formed very fast. In a subsequent slower step this phase disproportionates into iron and magnetite.

At 773 K the 'nearly stoichiometric' wüstite phase is not formed. In this case the transition is very slow, within 90 minutes only 30% of the wüstite phase has been disproportionated.

At 773 K the water splitting reaction is much faster than the disproportionation. In this case the active species must be the non-stoichiometric Fe_{1-y}O . At lower temperature, where the 'nearly stoichiometric' wüstite phase is formed, the water splitting reaction is much slower. For the 'nearly stoichiometric' wüstite phase the reaction velocity of the disproportionation and the water splitting is similar. The iron which is formed due to the disproportionation is oxidised at about the same rate.

In temperature ranges of stability of wüstite a very strong evolution of hydrogen is registered during the first two minutes of the reaction.

The water splitting reaction with small particles of iron is very fast in the beginning and stops after a few

seconds. After one hour reaction time just 20 % of the theoretical amount of hydrogen that can be reached by reaction of water with pure iron is formed. The reasons for this behaviour can be assumed to be the formation of an inert oxide layer and an overheating of the surface.

4 DISCUSSION AND OUTLOOK

The reason why non-stoichiometric metastable wüstite phases are very suitable energy carriers resides predominantly in their structure. In the iron oxide-system redox reactions are fast and reversible. Compared to stoichiometric metal oxides, a smaller amount of activation energy is sufficient to change the crystal structure. Iron oxides can be treated like iron dissolved in an oxygen solution. Reduction would correspond to a concentration of iron, oxidation a dissolution.

The kinetics and mechanism of the water splitting reaction with wüstite phases depends upon whether the nearly stoichiometric wüstite phase is formed or not, i.e. on the temperature range. Oxidation of non stoichiometric wüstite is much easier, probably because of the large amount of defect clusters, which can serve as nuclei for a magnetite formation as mentioned before. Water splitting starting from the 'nearly stoichiometric' wüstite phase or from iron, which is formed during the disproportionation, do both occur in the lower temperature range, but the reaction is much slower.

The enhanced evolution of hydrogen at the beginning of the reaction, which increases with temperature, is due to the rapid oxidation of the surface area. We assume that it depends on the mobility of iron ions in the surface regions. Later on magnetite is formed in the surface layers which leads to a blocking of diffusion channels for the gaseous products and to formation of a diffusion barrier in the solid, i.e. the mobility of iron in magnetite is restricted.

The following increase in the hydrogen evolution can be explained by the recrystallisation of the product layer in the atmosphere containing water and the subsequent formation of new diffusion channels.

5 ACKNOWLEDGEMENT

Financial support by the Bundesamt für Energiewirtschaft (BEW) is gratefully acknowledged.

6 REFERENCES

- [1] Nakamura, T. *Solar Energy* 19, 467-475 (1977).
- [2] Hentschel, B. *Zeitschrift für Naturforschung* 25, 1996-1997 (1970).
- [3] Stølen, S., Glöckner, R. & Grønvold, F. *Thermochemica Acta* 256, 91-106 (1996).

PRODUCTION OF FILAMENTOUS CARBON AND H₂ BY SOLARTHERMAL CATALYTIC CRACKING OF CH₄

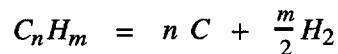
V. Kirillov, G. Kuvshinov (Boreskov Institute of Catalysis, Russia), A. Reller (University of Hamburg, Germany), A. Steinfeld

The catalytic thermal decomposition of methane has been experimentally studied using high-temperature solar process heat. Nickel catalyst particles, fluidized in methane, were directly irradiated at the PSI solar furnace. Carbon deposition consisted of randomly interlaced filaments that grew as fibers and hollow nanotubes (of approx. 30 nm diameter) originating at each catalytic particle.

1 INTRODUCTION

Gaseous hydrocarbons are found in natural gas and are also derived from the oil refining and coal processing industries. A large amount of these natural and oil tail gases, being economically unattractive, are usually flared and discharged to the environment. Alternatively, the decomposition of hydrocarbons offers the possibility of producing two valuable chemical commodities: carbon and hydrogen-rich gas mixtures. Clean carbon finds application in adsorption/desorption processes, and as a reducing agent in the metallurgical industry. Filamentous carbon, a much more valuable carbon material than conventional soot, is employed in composite materials where high-temperature stability and high-strength is required. Hydrogen-rich gas mixtures are widely used in the chemical industry for the direct production of ammonia, methanol, and other synthetic fuels and chemicals. Hydrogen-containing mixtures, when not contaminated with carbon oxides, may be used for fuelling fuel cells without inhibiting platinum-made electrodes.

The decomposition of hydrocarbons are high-temperature endothermic processes. Concentrated solar energy can be used as the clean source of high-temperature process heat, avoiding the emission of pollutants while upgrading the calorific value of the products. The general stoichiometric reaction can be represented by:



These reactions proceed at temperatures in the 800-1000 K range when conducted at atmospheric pressure. Recent reviews on the production of carbon fibers by cracking of hydrocarbons have been published [1,2]. The carbon deposition process can be catalysed by many metals; Ni, Ni/Cu, and Ni/Cu/Zn alloys have shown the highest activities [3,4]. The filament growth mechanism consists of hydrocarbon adsorption at the catalyst surface followed by carbon diffusion through the catalyst particle [1,2,5]. The kinetics of carbon formation from CH₄-H₂ on silica-supported Ni and Ni-Cu catalysts were measured in the range 723-863 K [6]. The rate limiting-step is usually attributed to the diffusion of carbon through the Ni particle [1 and literature cited therein].

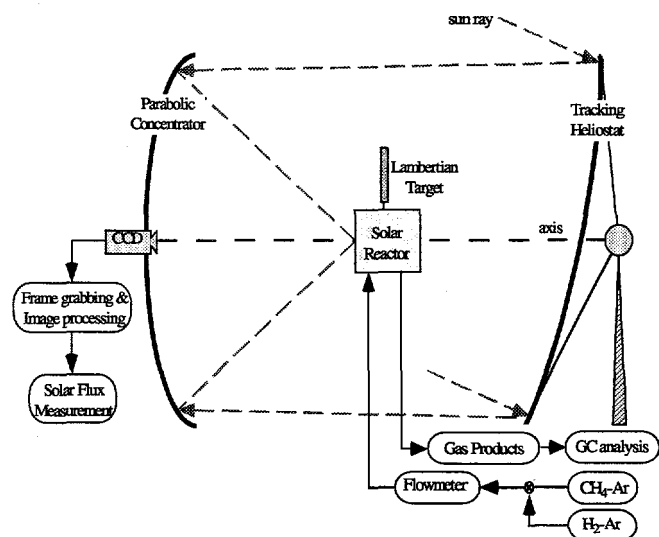


Fig. 1: Experimental set-up at the PSI solar furnace (dimensions are not to scale).

2 EXPERIMENTAL

Experimentation was conducted at the PSI solar furnace [7]. The experimental set-up is shown in Figure 1. The solar receiver-reactor system, depicted in Figure 2, consisted of a 2 cm-diameter quartz tube containing a fluidized bed of Ni catalyst and Al₂O₃ grains. A secondary reflector, composed of a 2D-CPC (compound parabolic concentrator) coupled to an involute, provided uniform irradiation on the tubular reactor. With this arrangement, the catalytic particles were directly exposed to the incoming high-flux solar beam. The catalytic precursors contained 90 wt% Ni and 10 wt% alumina and were prepared by coprecipitation as metal hydroxides [3]. The fluidized bed was solar-heated to the desired temperature under a flow of argon and isothermally subjected to a reacting gas flow of 1.16 l_n/min 10%CH₄-Ar and 0.52 l_n/min 2%H₂-Ar. Pressure was maintained slightly above atmospheric. Hydrogen was added to the feedstock gas and the temperature was kept below 850 K to prevent rapid deactivation of the catalyst. Figure 3 shows the fluidized-bed temperature (measured by a thermocouple type-K submerged into the bed) and the hydrogen content in the outlet gas

(measured by GC) during a representative solar experiment. The outlet gas composition showed 40% chemical conversion of CH_4 to H_2 in a single pass of 0.6 seconds through the 5 cm bed-height. Conversion decreased with time as carbon grew over the catalyst. Carbon deposited on the catalyst at a rate of approximately 8 gr per hour and per gram catalyst. Temperatures above about 850 K resulted in a momentary increase of the carbon deposition rate but lead subsequently to a rapid deactivation of the catalyst. Laboratory experiments, optimized for maximizing the carbon yield per unit mass of catalyst until its complete deactivation, have yielded a total of up to 200 gr carbon per gr catalyst [3,4]. The carbon obtained consisted of 1 to 2 mm granules being built by randomly interlaced filaments, including fibers and hollow nanotubes of approx. 30 nm diameter, having the following properties: BET specific surface area of $92 \text{ m}^2/\text{g}$, pore volume of $0.414 \text{ cm}^3/\text{g}$, and average pore diameter of 18 nm. Transmission electron micrographs, shown in Figure 4, revealed that each catalyst particle gave rise to a single filament of the same diameter as that of the particle at its head. The carbon texture is influenced by the filament growth mechanism which, in turn, is dependent on the catalyst, gas composition, and process operation conditions.

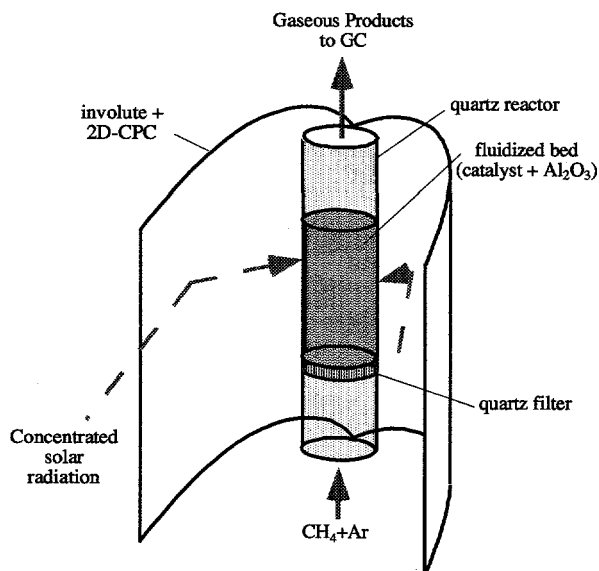


Fig. 2: Scheme of the solar reactor configuration.

3 SUMMARY

The technical feasibility of the solar decomposition of methane has been demonstrated using a small scale fluidized-bed solar reactor. The direct irradiation of the catalyst provided effective heat transfer to the reaction site. Potential applications of such process are the clean conversion of natural and oil tail gases into valuable chemical commodities.

4 ACKNOWLEDGEMENTS

This work has been funded in part by the BEW-Swiss Federal Office of Energy.

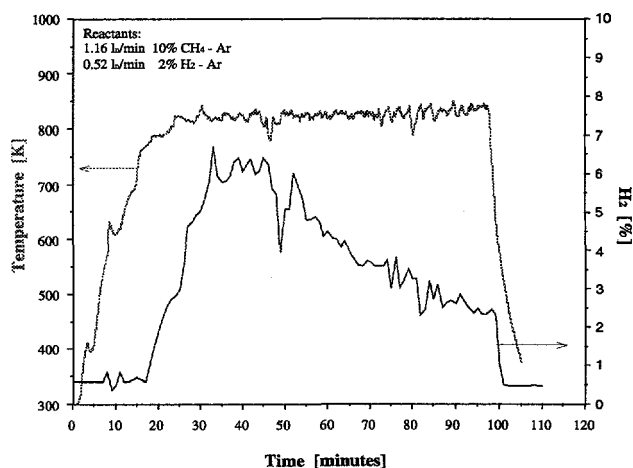


Fig. 3: Fluidized-bed temperature and H_2 content of product gas during a solar experiment.

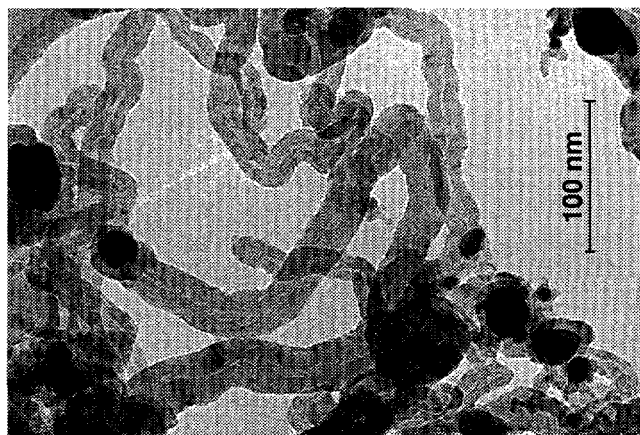


Fig. 4: Transmission electron micrograph of carbon formed by solarthermal catalytic cracking of methane.

5 REFERENCES

- [1] R.T.K. Baker, *Carbon* **27**, pp. 315-323, (1989).
- [2] G.G. Tibbetts, M. Endo, C.P. Beetz, *SAMPE Journal* **22**, pp. 30-35, (1986).
- [3] V.A. Likholobov et al., *React. Kinet. Catal. Lett.* **54**, pp. 381-411, (1995).
- [4] V.N. Parmon, G.G. Kuvshinov, V.A. Sobyanim, *Hydrogen Energy Progress XI*, pp. 2439-2448, (1996).
- [5] G.G. Tibbetts, M.G. Devour, E.J. Rodda, *Carbon* **25**, pp. 367-375, (1987).
- [6] I. Alstrup, M.T. Tavares, *J. of Catalysis* **139**, pp. 513-524, (1993).
- [7] Information on the solar furnace at PSI can be obtained via Internet at:
http://www1.psi.ch/www_f5_hn/Solar/solar_home.html

PHOTOCHEMISTRY AT HIGH TEMPERATURES - POTENTIAL OF ZNO AS A HIGH TEMPERATURE PHOTOCATALYST

M. Schubnell, P. Beaud, I. Kamber

Direct conversion of solar radiation into useful, storable and transportable chemical products is the primary goal of solar chemistry. In this paper we discuss some fundamental aspects of photochemistry at elevated temperatures. We show that luminescence can serve as an indicator of the potential use of a system as a photoconverter. As an example we present experimental data on the chemical potential and on the lifetime of the excited states of ZnO. The low luminescence quantum yield together with a lifetime of about 200 ps indicate that an efficient photochemical conversion on ZnO is highly improbable. We believe this to be a general feature of chemical systems based on a semiconductor photocatalyst, in particular of photoreactions at a solid/gas interface.

1 INTRODUCTION

In solar energy research the attempt to directly convert concentrated solar radiation into chemically stored energy has attracted much attention in recent years. One can think of two principally different ways to achieve this, thermochemistry or photochemistry. Several authors have also discussed a possible „synergism“ between the two ways (see [1] and references therein). In this paper we address thermodynamic and kinetic constraints imposed onto a photochemical system that is able to store work at high temperatures. We hereby only consider systems with a semiconductor as photocatalyst. In such a system the absorption of a photon with energy higher than the bandgap of the semiconductor results in electron-hole pairs. Ideally, the electrons are subsequently used for reduction and the holes for oxidation of the educts. This leads to high probabilities for the backreactions, i.e. the photooxidation and the photoreduction of the products. A second fundamental limitation is due to the fact that photochemistry is only possible as long as the bandgap of the semiconductor is much larger than the typical phonon energy. Therefore, for solar driven high temperature photocatalytic reactions only wide bandgap semiconductors can be used.

ZnO has a band gap of about 3.4 eV at 5 K shifting to about 3.1 eV at 300 K. The holes, created as minority carriers under illumination in the valence band have a strong oxidizing potential. Therefore, most photoreactions will be oxidation or decomposition reactions. Zinc oxide is known as a phosphor and its luminescence properties are well investigated at low temperatures. Furthermore, several authors have investigated photocatalysis, photosorption and photoconductivity on ZnO (see e.g. [2] and references therein).

It has been pointed out by thermodynamic arguments that the excited states in any photosystem converting light into useful energy must exhibit a positive chemical potential under illumination. This necessarily means that such a system has to show some luminescence [3]. This is equally true for a photochemical and for a photovoltaic system. However, the luminescence quantum yield may be very low (i.e. not detectable) for large band gap systems that still exhibit a

considerable chemical potential. According to [4] the chemical potential of the excited state μ can be calculated explicitly for an ideal two level system:

$$\mu = kT \ln \frac{\int_0^{\infty} I_s(e) \alpha(e) de}{\int_0^{\infty} I_{BB}(e) \alpha(e) de} + kT \ln \Phi \quad (1)$$

Here e is the photon energy, $\alpha(e)$ the absorptivity of the system, $I_s(e)$ the intensity of the radiation impinging on the system, I_{BB} the blackbody irradiation due to the surrounding, and Φ the luminescence quantum yield defined as the radiative recombination rate divided by the total recombination rate.

Eqn. (1) can be used to estimate the chemical potential of a photoactive system in a rather simple way. The only quantities one needs to know are the irradiation I_s , the luminescence quantum yield Φ , and the absorptivity $\alpha(e)$ of the sample. Thus knowledge of in principle readily measurable macroscopic quantities delivers information on a microscopic, experimentally not directly accessible quantity.

According to eqn. (1) luminescence is crucial for a positive chemical potential of the excited states. If luminescence is detected, the potential energy storage capability of the system is demonstrated. Contrarily, no photoluminescence usually indicates high loss rates and therefore a low potential for a direct photochemical conversion process. However, an (undetectable) low luminescence can also be due to a low absorptivity of the photocatalyst.

Apart from the above discussed thermodynamic limits, kinetic restrictions due to the finite lifetime of the excited state have to be considered as well. The lifetime of the excited state determines a time interval within which the primary step of the photoreaction has to take place. In case of a photovoltaic cell this primary step corresponds to the charge separation within the p-n-junction. In a photochemical system this primary step can be identified as the reaction of the photo-generated electrons and holes with adsorbed educts. Due to increased thermal quenching the radiative life

time of the excited state will decrease with increasing temperature thus decreasing the reaction probability. However, since the collision frequency of the educts with the surface of the photocatalyst increases at higher temperatures, this effect might at least partly be compensated in at moderate temperatures. The extent of this compensation depends on the details of the reaction mechanism.

Besides the thermodynamic and temporal limitations already discussed a "thermal" limitation of a photochemical surface reaction has to be considered as well: assuming that only adsorbed species can react with the photoactive system, the adsorption energy sets an upper temperature range above which the probability of a photoreaction decreases exponentially due to thermally activated desorption of surface species.

2 EXPERIMENTAL

The experimental setup basically consists of a sample holder placed in a vacuum system. The sample holder is a cylindrical block of nickel (dia. 25 mm, height 30 mm) which can be heated electrically up to 1100 K. The samples are placed in a dent within the Ni-block. The temperature of the sample is measured with a thermocouple welded close to the surface of the dent within the block. The vacuum system has been designed such as to allow dynamical control of the atmosphere within the system.

Temporally integrated luminescence spectra were recorded with a 13 bit 1024 diode array system mounted onto a 25 cm spectrograph allowing a spectral resolution of 1 nm. The samples were excited with the third harmonic of a Nd:YAG laser (355 nm, $5 \cdot 10^7$ W/cm²) operated at 10 Hz. For the time resolved measurements, ultrashort pulses at a wavelength of 282 nm, corresponding to the third harmonic output of a Ti:Sapphire chirped pulse amplification system (CPA 1000, Clark MXR) were used for excitation. The pulse duration was around 1 ps and the intensity was kept below $5 \cdot 10^7$ W/cm² to avoid stimulated emission which was clearly observed at higher intensities. The dispersed luminescence spectra were imaged on a streak camera equipped with a 16 bit CCD-camera. The time resolution when integrating over multiple pulses was 25 ps and the spectral resolution was again 1 nm.

The luminescence was collected with an ellipsoidal reflector and focused onto a fused silica fiber placed in the second focal point of the ellipsoid. The radiation absorbed by the sample was calculated as the difference of laser light reflected from the sample relative to a calibrated reference reflectance standard. A photodiode placed in a small integrating sphere intercepts a weak reflection of the laser pulse to monitor the (relative) laser pulse energy during the experiment.

Dense layers of ZnO were prepared on 10 mm diameter sapphire discs by settling using an aqueous dispersion of ZnO. SEM images of platinized samples show that the ZnO crystallites form a homogeneous and compact layer on the sapphire substrate. From the SEM pictures a layer thickness of about 2.5 μ m is obtained. From this number and the known amount of ZnO on the substrate we conclude that the layers consists of about 80 % void volume.

Prior to a measurement the samples were carefully dehydrated *in situ* according to the following procedure. The samples were mounted in the sample holder. The vacuum chamber was then evacuated and the sample quickly heated to 373 K. After 1 h at 373 K the temperature was ramped to 773 K at 100 K/h under dynamical vacuum. The samples were kept at 773 K for 2 h and then left to cool down to 300 K. After this procedure the samples are free of physisorbed and chemisorbed water and are oxygen deficient.

3 RESULTS

In Figure 1 we show corrected luminescence spectra of dry, oxygen deficient ZnO at 10^{-7} mbar at temperatures between 300 K and 630 K. From the position and the intensity of the signal the emission was attributed to direct bandgap recombination. As expected the luminescence intensity decreases with increasing temperature. Since the vibrational levels become more and more occupied, the spectra are red shifted at higher temperatures. Furthermore the luminescence spectra broaden with increasing temperature which is again due to increased phonon populations.

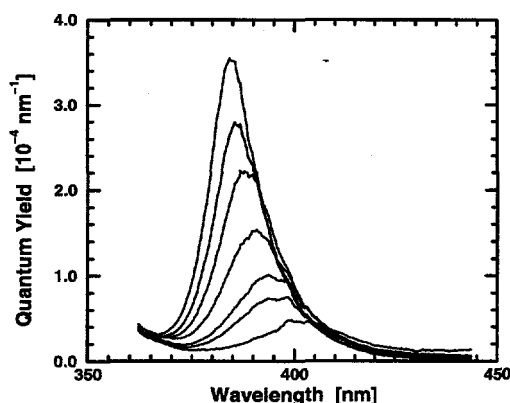


Fig. 1: Luminescence spectra of oxygen deficient ZnO at 310, 350, 390, 450, 510, 570 and 630 K.

When compared with spectra taken from ZnO samples that were only briefly evacuated at room temperature, i.e. "dry" samples that are only freed of physisorbed water, the shape of the spectra are identical; however, the total intensity at 300 K is about 6 times larger in the latter case. This indicates that in the oxygen deficient samples defects act as additional traps that increase the non-radiative rates thus quenching the luminescence. When the „dried-only“ samples are heated under dynamical vacuum the same signals as

for the oxygen deficient samples are finally obtained at 630 K. For non-oxygen deficient samples the dependence of quenching on temperature is a superposition of two effects. First, heating of ZnO under dynamical vacuum generates oxygen defects acting as traps for the excited states. Second, quenching due to phonon collisions as mentioned before decreases the luminescence quantum yield. In case of the oxygen deficient samples only the latter mechanism is observed.

Applying Eqn. (1) to the integrated data shown in Figure 1 and assuming a diluted 5672 K Planck spectrum as irradiance the chemical potential of the excited states of ZnO can be estimated. For simplicity the absorption spectrum of ZnO was approximated by a step function. Values for E_g were taken from [5]. Results are given in Figure 2 for various concentration factors. It can be seen that even at 600 K a considerable chemical potential is available. However, it decreases with increasing temperature much faster than the corresponding bandgap energy. Clearly visible is the benefit of working with concentrated radiation for which μ is larger and for which its decrease is less dramatic than for unconcentrated radiation.

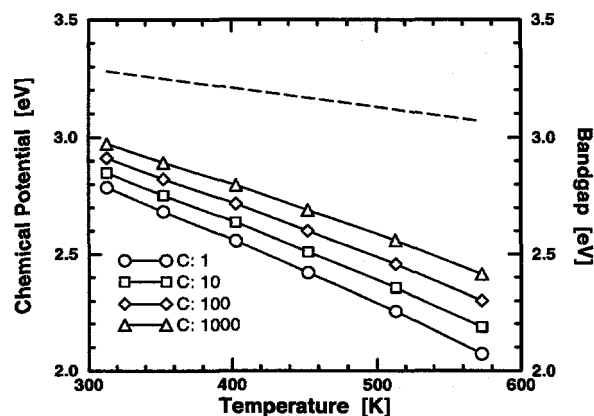


Fig. 2: Temperature dependence of the band gap energy E_g (dashed) and the chemical potential of the excited state of ZnO (solid) for various concentration factors C .

So far we have only discussed thermodynamic constraints imposed on a photochemical system due to a finite value of μ . However, if a photochemical reaction should be driven by the excited state, its lifetime sets a fundamental limitation on the time scale within which the reaction has to occur. We therefore also determined the lifetime of the excited states in ZnO by time resolved luminescence spectroscopy. The time resolved luminescence (c.f. Figure 3) does not show any spectral changes during the decay and therefore exhibits a wavelength independent temporal behavior. We generally find that the decay of the total intensity can be phenomenologically described by a superposition of two exponentials. We further conclude that a photochemical reaction does have to take place within about 300 ps at room temperature. This time decreases to about 260 ps at 873 K. These times corre-

spond to the time interval within which the luminescence decreases from its maximum value by 90 %.

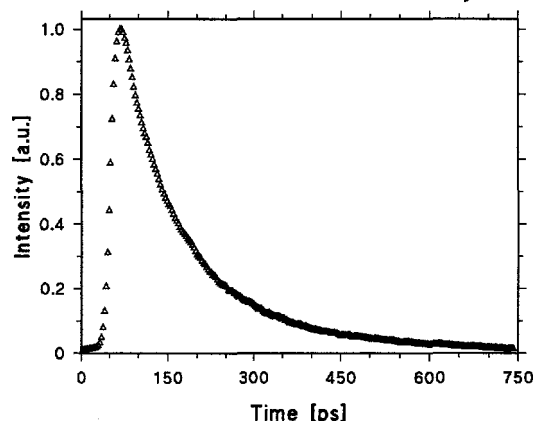


Fig. 3: Temporal evolution of the luminescence of oxygen deficient ZnO at 573 K

4 CONCLUSIONS

We have shown that the excited state of ZnO still exhibits a considerable chemical potential at temperatures as high as 600 K. Time resolved luminescence measurements indicate that a reaction that utilizes this potential has to occur within typically 200 - 300 ps. Otherwise the excited state will be lost due to luminescence or due to non radiative decay. This short time constant makes an efficient photochemical conversion of radiation on ZnO into useful products highly improbable. We believe this to be a general feature of photoreactions at solid/gas interfaces. Therefore photochemistry can only modestly contribute to high temperature conversion of solar energy into useful chemicals. This general conclusion is further supported by experimental work done on the photosynthesis of methane on TiO_2 [6].

5 ACKNOWLEDGEMENTS

We thank Dr. V. Shklover, Laboratorium für Kristallographie, ETHZ, for the SEM analysis. This work has been supported by the Swiss Federal Office of Energy.

6 REFERENCES

- [1] H. Ries, „What can we expect from photo- plus thermochemistry?“, Solar Thermal Technology, 597-603, (1988).
- [2] W. Hirschwald et al., „Zinc Oxide“, Vol. 148 of *Topics in Current Chemistry*, Springer, (1988).
- [3] M.D. Archer, J.R. Bolton, J. Phys. Chem. 94, 8028 - 8038, (1990).
- [4] R.T. Ross, M. Calvin, Biophys. J. 7, 595, (1967).
- [5] G.H. Jensen, T. Skettrup, Phys. Stat. Sol. B 60, 169-173, (1973).
- [6] F. Saladin, L. Forss, I. Kamber, J. Chem. Soc., Chem. Commun., 533-534, (1995).

**Materials Development and Methods of Characterization for
Energy Research**

RECYCLING OF GREENHOUSE GASES VIA METHANOL

A. Bill, B. Eliasson (ABB Corporate Research Center, Baden-Dättwil, Switzerland),
U. Kogelschatz (ABB Corporate Research Center, Baden-Dättwil, Switzerland)

Greenhouse gas emissions to the atmosphere can be mitigated by using direct control technologies (capture, disposal or chemical recycling). We report on carbon dioxide and methane recycling with other chemicals, especially with hydrogen and oxygen, to methanol. Methanol synthesis from CO₂ is investigated on various catalysts at moderate pressures (≤ 30 bar) and temperatures (≤ 300 °C). The catalysts show good methanol activities and selectivities. The conversion of CO₂ and CH₄ to methanol is also studied in a silent electrical discharge at pressures of 1 to 4 bar and temperatures close to room temperature. Methanol yields are given for mixtures of CO₂/H₂, CH₄/O₂ and also for CH₄ and air mixtures.

1 INTRODUCTION

One possible approach to mitigate the emissions of carbon dioxide and methane to the atmosphere would be to recycle the carbon in a chemical process to form useful products like methanol or dimethyl-ether for example. Methanol has the advantage that it is liquid under normal conditions. It can be as easily stored and transported as gasoline and it can be used in conventional combustion engines without requiring any major adjustments. Methanol has twice the energy density of liquid hydrogen. Methanol synthesis can also be looked upon as a storage mechanism for gaseous hydrogen.

If pure hydrogen is available the easiest method for converting it with CO₂ to methanol is to use a catalyst and combine both gases in a thermal reactor at about 220 °C and under moderate pressure (20 - 50 bar). This conversion requires no extra energy as the reaction is exothermic and the heat and energy needed originate from the hydrogen and the reaction itself. The function of carbon dioxide as a storage medium for hydrogen is evident in this case.

If no hydrogen is available, also hydrogen donor molecules and greenhouse gases can be treated in a silent discharge reactor, i.e. a non equilibrium high pressure discharge reactor [1]. It generates high energy electrons, which in turn dissociate the carbon dioxide or the methane molecules and allow them to form new molecules. In this case we have to supply external energy, namely the electrical energy to run the discharge. But we have two decisive advantages compared to the thermal reactor. In principle, we can use any kind of hydrogen donor, which can be dissociated, for instance water vapor or hydrogen sulfide. Maybe more important, we do not have to use a catalyst. Therefore we can run the reaction at moderate or low temperatures in the discharge, which is preferably for exothermic reactions.

2 EXPERIMENTAL

The experimental configurations for the packed bed reactor, as well for the silent discharge reactor, are described elsewhere [2,3].

To evaluate the hydrogenation catalysts, a stainless steel conventional plug-flow packed-bed reactor is used. It is located inside an oven. Experiments are performed with 4 - 6 g of catalyst under isothermal conditions ($T_{\max} = 350$ °C) and at pressures below 30 bar. Reactants are supplied from pre-calibrated mass flow controllers and the pressure is controlled by an electronic back-pressure regulator. The product stream from the reactor is analyzed by gas chromatography.

The silent discharge reactor is mounted in a high pressure vessel of cylindrical shape, which can be run at pressures up to 10 bar and controllable temperatures up to 400 °C. A silent discharge [3] is maintained in an annular gap of 1 mm width formed by an outer steel cylinder and an inserted cylindrical quartz tube. The steel cylinder serves as the ground electrode and an alternating high voltage of 18 kHz frequency is applied to a gold coating on the inside of the quartz tube. The power is accurately measured and can be regulated between 50 W and 900 W by adjusting the amplitude of the applied voltage. Different feed gases can be mixed before entering the discharge reactor. The individual flow rates are controlled by mass flow controllers. A regulating valve at the exit of the reactor controls the pressure in the discharge. Most of the products are analyzed by gas chromatography. Oxygen concentration can be measured by a special oxygen monitor based on paramagnetism.

3 RESULTS AND DISCUSSION

3.1 Experiments performed in the packed-bed reactor

We focus on the methanol synthesis from H₂ and CO₂, carbon dioxide being used as the sole C-source. Academic, as well as industrial catalysts have been tested at 20 bar, at a space velocity of 4500 h⁻¹ (residence time 0.8 s) and with a feed ratio H₂/CO₂ = 3. CO₂ hydrogenation in a thermal reactor not only leads to production of methanol but also to the formation of CO, H₂O and some CH₄ (at temperatures higher than 280 °C). The methanol amount increases with temperature up to about 220 °C. How

ever it starts to decrease above 220 °C (as expected for an exothermic reaction), in spite of a continuous increase in the conversion of CO₂. The selectivity rapidly shifts in favor of carbon monoxide, which is produced by the reverse water gas shift reaction.

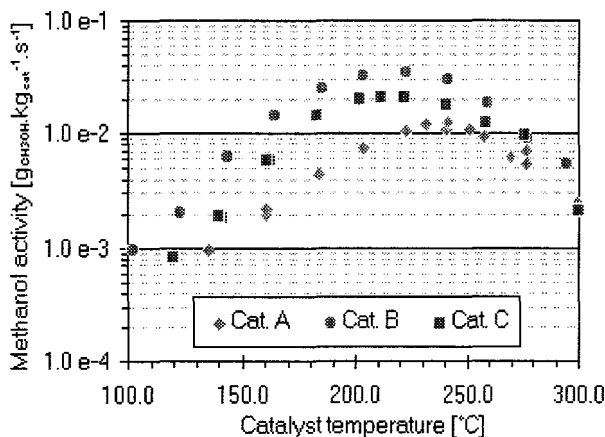


Fig. 1: Activity as a function of the temperature ($H_2/CO_2=3$, $P_{tot}=20$ bar, space velocity(S_v)= $4500h^{-1}$).

According to all investigated catalysts, the optimum for the methanol yield is obtained in the temperature range between 220 and 240 °C (Figure 1). Best activity is obtained with catalyst B. It gives, for the selected experimental conditions, a methanol yield of $124.8 g_{CH_3OH} \cdot g_{cat}^{-1} \cdot h^{-1}$.

3.2 Experiments performed with the silent discharge reactor

Various experiments were performed with different feed gases, namely pure CO₂, pure CH₄, H₂+CO₂ mixtures, CH₄+O₂ and CH₄ plus air.

In this section we focus on the experiment with the H₂/CO₂ (3:1) mixture. A typical product distribution is given in Figure 2.

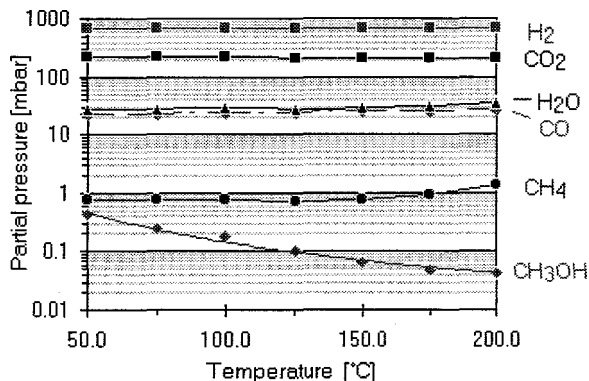


Fig. 2: Partial pressures as a function of the temperature (electrical power= 400 W, $H_2/CO_2=3$, $P_{tot}=1$ bar, $Q_{tot}=1$ NI.min⁻¹).

Carbon monoxide and water are the major products. They are produced in the same amount which slightly increases with temperature. Methanol and methane are also produced in smaller amounts that depend on temperature. Methanol formation decreases with rising temperature, as expected for an exothermic reaction ($(\Delta H^0)_{298} = -49.5$ kJ.mol⁻¹) [4]. A maximum methanol yield of 0.2 % is obtained at the lowest investigated temperature (50 °C).

All the other results, especially the methanol synthesis from methane and air mixtures, are reported elsewhere [3].

4 CONCLUSIONS

For a packed-bed reactor, it has been shown that under moderate pressure and temperature conditions, fair methanol activity can be obtained and that equilibrium values are already reached at 250 °C [5].

In a silent discharge reactor, it has also been demonstrated that methanol can be synthesized from mixtures of methane with CO₂, oxygen or air and mixtures of CO₂ with H₂. The excited species generated by the dissociation of the feed gases are energetic enough to initiate reactions at room temperature and atmospheric pressure that would normally require the use catalysts and elevated temperatures and pressures.

5 REFERENCES

- [1] B. Eliasson, U. Kogelschatz, "Modeling and Applications of Silent Discharge Plasmas", *IEEE Transactions on Plasma Science*, **19**, (2), (1991).
- [2] J.G. Highfield, A. Bill, B. Eliasson, F. Geiger, E. Uenala, "The role of simple alcohols in renewable hydrogen energy", Proc. 11th Int. Symp. Alcohol Fuels (ISAF XI), Sun City, South Africa, (1996).
- [3] A. Bill, B. Eliasson, E. Killer, U. Kogelschatz, "Hydrogenation of carbon dioxide and oxidation of methane in an electrical discharge", Proc. 11th World Hydrogen Energy Conf. (HYDROGEN '96), Stuttgart, Germany, Proc. Vol. III, pp. 2449-2459, (1996).
- [4] M.W. Chase, C.A. Davies, J.R. Downey, D. J. Frurip, R. A. Mc Donald, A. N. Syverud, *J. Phys. Chem. Ref. Data*, **14**, Suppl. 1. (JANAF TABLES), (1985).
- [5] A. Bill, B. Eliasson, J.G. Highfield, E. Killer, "Synthesis and steam-reforming of simple alcohols: an option for a CO₂ neutral energy cycle", Book of abstracts, 3rd Int. Conf. on Carbon Dioxide Utilization (ICCDU III), Norman (OK), USA, (1995).

THERMAL STABILITY OF NAFION MEMBRANES UNDER MECHANICAL STRESS

M. Quintilii, R. Struis

The feasibility of adequately modified fluoro-ionomer membranes (NAFION®) is demonstrated for the selective separation of methanol synthesis products from the raw reactor gas at temperatures around 200 °C. For an economically relevant application of this concept on a technical scale the Nafion membranes should be thin ($\approx 10 \mu\text{m}$) and thermally stable over a long period of time (1-2 years). In cooperation with industry (Methanol Casale SA, Lugano, CH), we test the thermal stability of Nafion hollow fibers and supported Nafion thin sheet membranes at temperatures between 160 and 200 °C under mechanical stress by applying a gas pressure difference over the membrane surface ($\Delta P \leq 40 \text{ bar}$). Tests with the hollow fibers revealed that Nafion has visco-elastic properties. Tests with 50 μm thin Nafion sheets supported by a porous metal carrier at 200 °C and $\Delta P=39 \text{ bar}$ showed no mechanical defects over a period of 92 days.

1 INTRODUCTION

Methanol synthesis technology overcomes the equilibrium restrictions on product yield by applying high operating pressure and by recycling the unconverted synthesis gas after product separation by condensation [1]. At PSI we demonstrated the feasibility of adequately modified fluoro-ionomer membranes (i.e., lithium exchanged NAFION) for the selective separation of the methanol synthesis products, methanol and water, from the raw reactor gas at temperatures around 200 °C [2] (Patent pending). A membrane separator of technical relevance will have to be mounted with thin membranes ($\sim 10 \mu\text{m}$) and operated with a certain pressure difference across the membrane (driving force). In corporation with one of the leading engineering companies in the field of methanol plants (Methanol Casale SA, Lugano, CH), hollow fibers and supported films made of NAFION are evaluated in our laboratory as potential forms for technical applications. In this work we report on the thermal stability of these materials at temperatures between 160 and 200 °C under mechanical stress given by the gas pressure difference ($\leq 40 \text{ bar}$) across the membrane.

2 RESULTS WITH NAFION HOLLOW FIBERS

The hollow fibers obtained from Perma Pure Ltd., USA, have a wall thickness and inner radius equal to 63.5 μm . Prior to the stability tests the protons counteracting the sulphonate groups (Equivalent Weight = 1100 g/mol) are exchanged with lithium ions. [2,3] The experimental set-up is sketched in Figure 1. A single fiber is installed in a bended stainless steel tube ($\varnothing_{\text{inner}} = 4 \text{ mm}$). The ends of the fiber are sealed with septa. Nitrogen gas is fed to the inner part of the fiber with $P(\text{N}_2)$ slightly above 1 bar. The lower part of the test module is heated in an oil bath. After reaching the temperature of interest, mechanical stress is exerted on the fiber's outside wall by introducing an air pressure (P) in the metal tube. The flow rate of nitro-

gen through the fiber is then derived from the gas amount captured as a function of time in a measuring beaker filled with water.

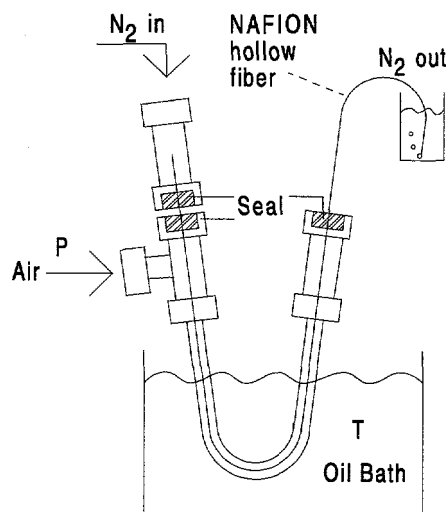


Fig. 1: Experimental set-up.

A typical experimental run is shown in Figure 2.

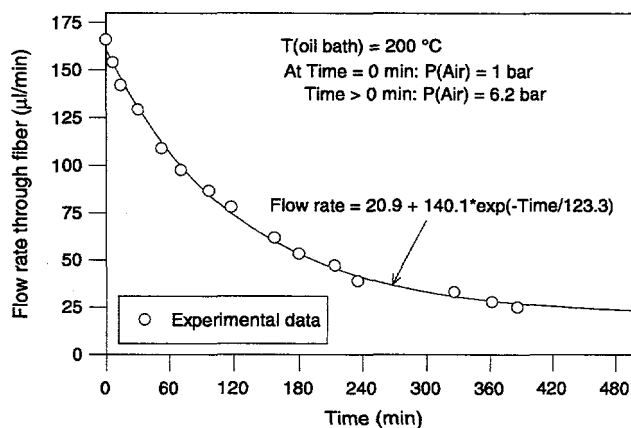


Fig. 2: Typical experimental run.

The experiment is stopped after reaching a steady nitrogen flow rate. Figure 3 shows the *steady* flow rates as a function of temperature and air pressure exerted on the fiber's outside wall. At 200 °C the nitrogen flow is found to drop drastically with increasing stress created by the pressure difference across the membrane. For the lower temperatures, the drop becomes increasingly smaller, and for $T=160\text{ °C}$ with $P \approx 20$ bar, the drop is less than 15 % of the value obtained with $P=1$ bar. Using Poiseuille's formula, which describes the flow rate of a gas through a tube of radius r and length L [4], the observed decrease in flow can be correlated with a reduced average inner diameter of the hollow fiber. After the last test run, the stressed fiber was quenched in ice water and the reduction in the fiber radius was optically verified using a microscope.

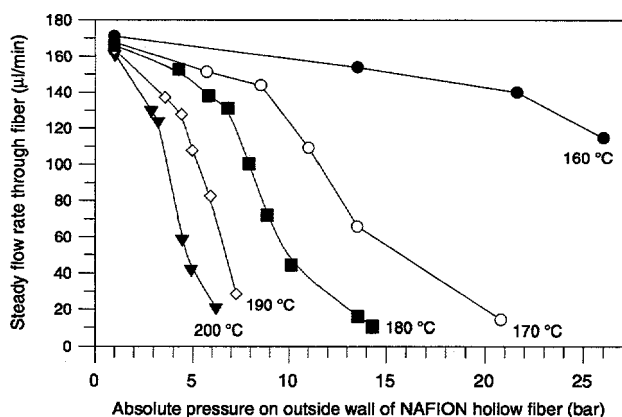


Fig. 3: Steady flow rates of nitrogen through a Nafion hollow fiber as a function of temperature and pressure exerted on the fiber's outside wall.

Note that all results have been obtained with *one and the same fiber*. This was possible because the elastic properties of the fiber allowed the continuous regeneration of the fiber dimensions (and hence the nitrogen flow through the fiber) to their initial values under starting conditions (viz., $P=1$ bar; $T=200\text{ °C}$).

3 RESULTS WITH NAFION SHEET MEMBRANES

The layout of the test cell for the flat sheet membranes is shown in Figure 4. A 50 μm thin NAFION sheet membrane in the lithium form (Equivalent Weight = 1100 g/mol) is fitted in a two chamber stainless steel cell where the sheet is supported by a porous metal ($\varnothing_{\text{pores}} \approx 50\text{ μm}$). The cell is kept at 200 °C while maintaining a constant air pressure of 40 bar in the first and atmospheric pressure in the second chamber. The permeative flow through the membrane is measured by a mass flow meter and is digitally recorded as a function of time.

Figure 5 shows that the porous metal is well suited to stabilize the membrane sheet over a long period of

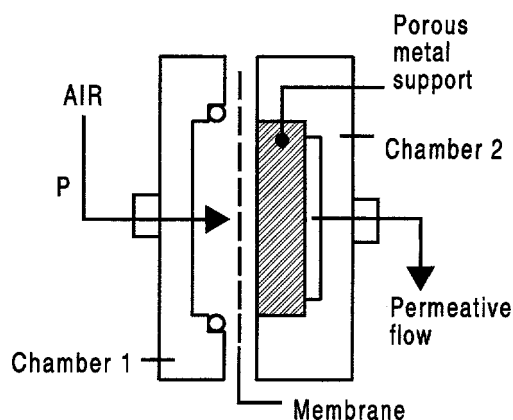


Fig. 4: Layout of test cell used for membrane sheets.

time under conditions which, otherwise, would certainly have led to membrane failure.

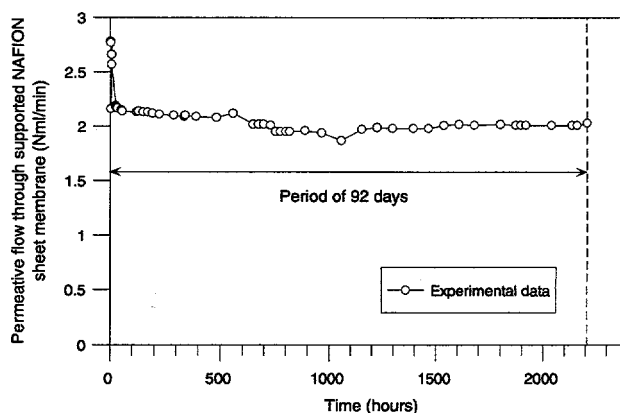


Fig. 5: Long term performance test for a supported sheet membrane at 200 °C and $\Delta P=39$ bar.

4 ACKNOWLEDGEMENTS

We thank Perma Pure Ltd, USA, for supplying us with the Nafion hollow fibers, Dr. G. Scherer (PSI) for the Nafion flat sheet membranes, P. Binkert (PSI) for the skilled manufacture of the test cells and the Kommission für Technologie und Innovation for their financial support (KTI-Projekt 3101.1).

5 REFERENCES

- [1] G.C. Chinchén et al., "Synthesis of methanol; Part 1. Catalysts and kinetics", *Appl. Catal.*, **36**, 1-65, (1988).
- [2] R.P.W.J. Struis, S. Stucki, M. Wiedorn, "A membrane reactor for methanol synthesis", *J. of Membrane Sci.*, **113**, 93-100, (1996).
- [3] R.S. Yeo and A. Eisenberg, "Physical properties and supermolecular structure of perfluorinated ion-containing (Nafion) polymers", *J. Appl. Polym. Sci.*, **21**, 875, (1977).
- [4] Physical Chemistry, P.W. Atkins (Ed), Oxford University press, Oxford, 4th Edition 741, (1990).

SOLID STATE DIFFUSION AND REACTION IN ZNO / SiO₂ IN THIN FILMS

A. Jakob, S. Stucki, B. Schnyder, R. Kötz

Detoxification of fly ash from waste incineration by evaporating harmful heavy metals is limited by the formation of stable heavy metal-matrix compounds. To study the rate of these heavy metal-matrix reactions, experiments were performed with the diffusion couple ZnO (heavy metal)-SiO₂ (matrix). The atomic concentration profiles after different annealing treatments were analysed by X-ray photoelectron spectroscopy (XPS).

1 INTRODUCTION

The residues from municipal solid waste (MSW) incineration, mainly bottom ash and fly ash, contain considerable amounts of harmful heavy metals such as Cd, Cu, Pb, and Zn. Recycling of the incineration residues is, at least in Switzerland, only possible if the toxic heavy metals are completely separated from the non-toxic solids. Techniques based on thermal treatment are most promising to detoxify the MSW residues.

In the present work, the formation of a stable heavy metal silicate which competes with the heavy metal evaporation was studied. As a simplified model for the complex heavy metal - glass matrix couples in MSW fly ash, diffusion and reaction of ZnO-SiO₂ couples were studied by XPS.

2 METHODS

Figure 1 shows schematically the test sample and the experimental procedure. The test sample was prepared by oxidizing a silicon wafer and subsequent coating of the SiO₂ surface with ZnO by reactive sputtering. The thermal treatment to allow diffusion and chemical reaction between the SiO₂ and ZnO was performed in argon atmosphere at 900 °C for periods between 5 min and 2 h. The concentration depth profiles of the annealed samples were measured by alternating XPS measurements and argon sputtering in a ESCALAB 220i XL from VG-Scientific. Details concerning the sputter condition as well as the XPS measurement and quantification are given in [1].

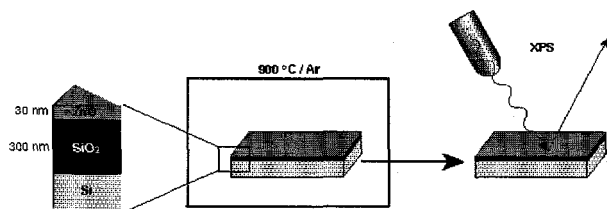


Fig. 1: Test sample and experimental procedure

The annealed samples were additionally studied by glancing incidence X-ray diffraction (XRD) on a Philips X'Pert instrument. The fixed incidence angle of the X-ray beam was 2°.

3 RESULTS

Figure 2 shows the XPS depth profile analysis of the reference sample. The atomic composition across the ZnO and SiO₂ layers is plotted as a function of the argon sputter time. The ZnO layer is separated from the SiO₂ layer by a sharp concentration gradient at a depth corresponding to ≈ 180 s sputter time.

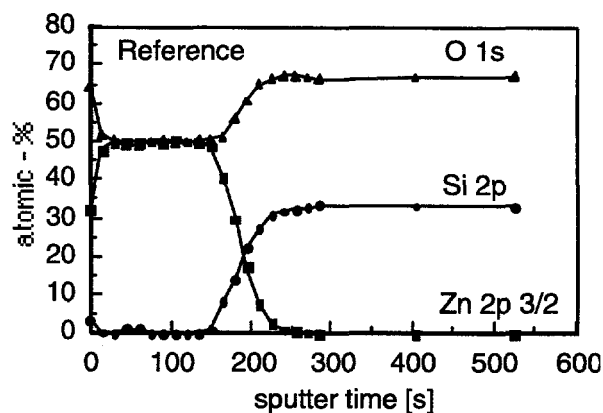


Fig. 2: Atomic concentration profiles of the untreated test sample measured by XPS.

The concentration profiles of the heat treated samples are shown in Figure 3. Already after 5 min at 900 °C (Figure 3a) about 5% silicon is detected by XPS measurement at the surface of the sample. Zinc diffused to some extent into the SiO₂ layer. In contrast to the reference specimen (Figure 2), the Zn and Si concentration profiles between the SiO₂ and the former ZnO are no longer simple gradients but have a "double-S" shape. The intermediate inflection point, i.e. the inflection point between the two "S" shaped curves, is located at about 200 s. Samples annealed at 900 °C for periods of 10, 15, 20 25 and 30 min. [1], all showed the same concentration profiles, with random shifts in the inflection point by ± 15 sec. The pronounced "double-S" shape of the concentration curves disappears only after extended annealing times (Figure 3b). The concentration gradients tend to disappear gradually in a slow diffusion process.

The diffractograms of the samples heat treated in argon at 900 °C for 5 min and 2 h, respectively, are nearly identical and can best be explained with the compound Zn₂SiO₄ (Willemite) [1].

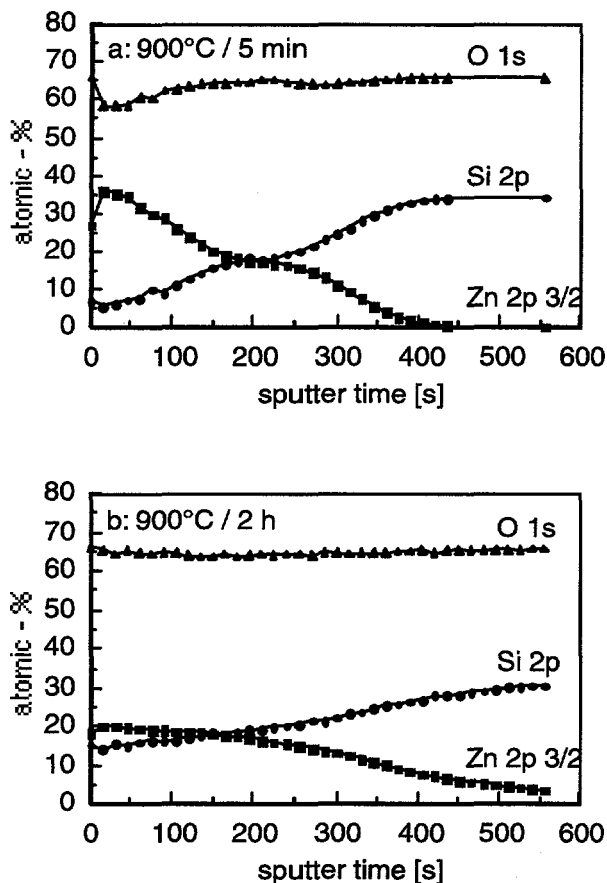


Fig. 3: Atomic concentration profiles measured by XPS of samples diffusion annealed in argon at 900 °C during a: 5 min; b: 2 h.

4 DISCUSSION AND CONCLUSION

Diffusion experiments with ZnO-SiO₂ couples have already been carried out by Schmalzried and Duckwitz [2]. Those experiments, however, are comparable to our study only to some extent: they deal with macroscopic samples, diffusion annealed at distinctly higher temperatures around 1250-1450 °C. Under these conditions a reaction layer of Zn₂SiO₄ was found to form which separates ZnO from SiO₂. After a first stage, the main diffusion is controlled by the transport of the diffusing species through the Zn₂SiO₄ barrier, resulting in a parabolic ($d \sim \sqrt{t}$) rate law for the growth of the Zn₂SiO₄ reaction layer thickness. In the first stage of diffusion, where the mass transport through the ZnO-SiO₂ phase boundary seems to be rate controlling, a linear rate law was found for the growth of the Zn₂SiO₄.

The concentration profiles illustrated in Figure 3 show that in our experiments no distinct reaction layer can be observed. Comparing the reference material in Figure 2 with the sample annealed for 5 min (Figure 3a) reveals that Si is detected at the surface of the annealed sample and that "double S" shaped concen-

tration profiles of Zn and Si are established by a fast initial process which is then decelerated (cf. [1]). The presence of Si already at the surface of the shortly annealed sample could be explained by microcracking of the ZnO layer or by a rearrangement/recrystallization of the ZnO layer during the heat treatment which could uncover the SiO₂ layer. However, the fast initial formation of the "double S" concentration profiles which essentially do not change until long heat treatment periods can best be explained by the formation of a diffusion barrier which decelerates the fast initial diffusion within the first five minutes of heat treatment.

The concentration profiles indicate that the diffusion barrier, located at the intermediate inflection point, is made up of 19% Zn, 19% Si, and 62% O, which approximately corresponds to a ZnO to SiO₂ ratio of 1. This ratio equals the non equilibrium zinc metasilicate ZnSiO₃ which, however, forms only at temperatures/pressures above 850 °C/30 kbar [3]. As the ZnO-SiO₂ equilibrium phase diagram [4] excludes solid solutions between SiO₂ and ZnO as well as any compound other than Zn₂SiO₄ the above composition may, in the equilibrium state, only be a mixture of ZnO grains and SiO₂ grains or, a mixture of 75% Zn₂SiO₄ + 25% SiO₂. The XRD measurement gives evidence of the presence of zinc silicate Zn₂SiO₄ (willemite). Both equilibrium mixtures, however, the ZnO/SiO₂ as well as the Zn₂SiO₄/SiO₂ mixture, would not act as a diffusion barrier.

Further investigations are necessary to confirm and identify the proposed formation of a diffusion barrier.

5 ACKNOWLEDGEMENTS

This work was performed within the Priority Programme Environment of the Swiss National Science Foundation. Its financial assistance is gratefully acknowledged. Thanks go to Mrs. T. Mezzacasa, Applied Solid State Physics, Paul Scherrer Institut for preparing the oxidized silicon wafer and to Mr. Y. Ruedin from ASULAB S.A., Switzerland for the ZnO coating.

6 REFERENCES

- [1] A. Jakob, S. Stucki, B. Schnyder and R. Kötzi, submitted to Solid State Ionics.
- [2] C.A. Duckwitz and H. Schmalzried, Z. physik. Chem. Neue Folge 76, 173, (1971).
- [3] Y. Syono, S.I. Akimoto and Y. Matsui, J. Sol. State Chem. 3, p. 369, (1971).
- [4] E.N. Bunting, Bur. Standards J. Research 4 (1930) 134; in: E.M. Levin, C.R. Robbins and H.F. McMurdie, Phase Diagrams for Ceramists Ed.: M.K. Reser, The American Ceramic Soc., Columbus, Ohio (1964).

KINETICS WITH DEACTIVATION OF METHYLCYCLOHEXANE DEHYDROGENATION FOR HYDROGEN ENERGY STORAGE

G. Maria, A. Marin, C. Wyss, S. Müller, E. Newson

The methylcyclohexane (*mch*) dehydrogenation step to recycle toluene and release hydrogen (*hyd*) is being studied as part of a hydrogen energy storage project. The reaction is performed catalytically in a fixed bed reactor, and the efficiency of this step significantly determines overall system economics. The fresh catalyst kinetics and the deactivation of the catalyst by coke play an important role in the process analysis. The main reaction kinetics were determined from isothermal experiments using a parameter sensitivity analysis for model discrimination [1]. An activation energy for the main reaction of 220 ± 11 kJ/mol was obtained from a two-parameter model. From non-isothermal deactivation in PC-controlled integral reactors, an activation energy for deactivation of 160 kJ/mol was estimated. A model for catalyst coke content of 3-17 weight% was compared with experimental data.

1 INTRODUCTION AND SCOPE OF THE WORK

In a project now at the pilot-plant stage, the concept of a hydrogenation - dehydrogenation cycle coupled to water electrolysis using surplus (summer) electricity is being studied as a method of seasonal storage of electricity from summer to winter. The endothermic dehydrogenation reaction of methylcyclohexane to toluene (*tol*) over fixed bed commercial reforming catalysts has been developed to provide such high yields of toluene that preliminary economic comparisons with new hydropower projects show comparable costs for "regenerated" electricity. Pure *mch*, or mixed with hydrogen (*hyd*) in the feed, is converted in an equilibrium limited reaction:



The purpose of this paper is to develop both fresh catalyst and deactivation kinetics for a commercial, sulfided, platinum on alumina reforming catalyst, at various reaction severities using a three stage laboratory scale experimental program.

The initial, quasi-isothermal experiment in a differential microreactor at different temperature levels was scaled up to a series of non-isothermal integral reactors followed by high severity deactivation in constant conversion operation. Finally, increasing temperature experiments with integral reactors are used to complete the kinetic model with deactivation terms checked under a wide range of severe operating conditions: 200 - 400 hours continuous operation, high liquid hourly space velocities (*LHSV*) of 3 - 20 1/h, 0 - 10 *hyd/mch* feed ratio, 6 - 16 atm pressure, 250°C - 550°C temperature in the reactors.

2 MICROREACTOR EXPERIMENTS AND MAIN REACTION KINETICS

The first stage experiments were carried out in a differential continuous microreactor (Figure 1), containing approximately 0.05 cm³ of commercial, sulfided, monometallic noble metal catalyst of small particles, diluted 1:5 with an inert material [3].

A set of quasi-isothermal experiments at 7 atm and four low temperature levels (282°C, 290°C, 298°C, 309°C), high dilution of the feed with *hyd* (1.6-10 molar *hyd/mch* feed ratio), and helium (0-3.3 molar *He/mch*) and high weight hourly space velocity (*WHSV* = 15-58 1/h) feed rates, allowed identification of the fresh-catalyst kinetics and derivation of the corresponding Arrhenius parameters:

$$r_{\textit{mch}} = d(x_{\textit{mch}})/d(W/F_{\textit{mch}}) =$$

$$k_{\textit{pmch}} [1 - p_{\textit{tol}} p_{\textit{hyd}}^3 / (K_{\textit{eq}} p_{\textit{mch}})] / (1 + \sum_j K_j p_j), \quad (2)$$

[*i* = *mch*, *tol*, *hyd* species; $x_{\textit{mch}}$ = *mch* conversion; p_i = partial pressure of component *i*, (atm); *r* = reaction rate, (mol/(g.h)); *W* = catalyst mass, (g); $F_{\textit{mch}}$ = *mch* feed flow rate, (mol/h); $K_{\textit{eq}}$ = equilibrium constant, (atm³) experimentally derived by Rimensberger [4]].

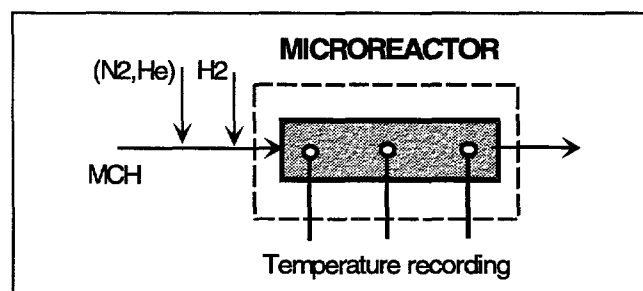


Fig. 1: Experiments in the continuous microreactor system.

By using a short-cut estimation technique for isothermal data [1], a rapid model discrimination followed by a weighted least squares nonlinear estimation gave the following model parameters: $k = 20.46 \exp[-26540(1/T - 1/650)]$, mol/(g.h.atm). The estimated activation energy ($E/R = 26540$ K, *R* = universal gas constant) is comparable with those reported in the literature for similar catalysts ($E/R = 14683$ -21770 K, [5]).

3 NON-ISOTHERMAL INTEGRAL REACTOR EXPERIMENTS FOR FRESH CATALYST AND MILD REACTION CONDITIONS

In order to check the main reaction kinetics derived from the microreactor data sets, two fixed-bed integral reactors in series were used (Figure 2a). Each reactor

was filled with approx. 21 cm³ of the same catalyst diluted with inert material in a ratio of 1:10 in order to diminish the cold spot temperatures in the reactors. The dual reactor system was completely PC-controlled, allowing several hundred hours of continuous operation. The feed gas and liquid were automatically monitored and on-line GC-FID-MS product analyses were continuously recorded. The axial temperature profile was measured using eleven thermocouple location points in each reactor. To check the kinetic model, the differential heat balance equation for a pseudohomogeneous plug-flow reactor model was solved to predict the product distribution and axial temperature profile under non-isothermal operating conditions:

$$F c_g \frac{dT}{dV_r} = (-\Delta H_r) r_{mch} \rho_{cat} y_{cat} + 4 / d_t u (T - T_{bed}), \quad (3)$$

[where F = overall mass feed flow rate, (kg/h); c_g = mean gas heat capacity, (kJ/kg.deg); T = axial reactor temperature, (K); V_r = reactor volume, (m³); $(-\Delta H_r)$ = heat of reaction, (kJ/kmol); ρ_{cat} = catalyst density, (kg/m³); y_{cat} = volumetric fraction of the catalyst in the reactor bed, (m³/m³); u = overall radial heat transfer coefficient, (W/m².K); d_t = inlet reactor diameter, (m)].

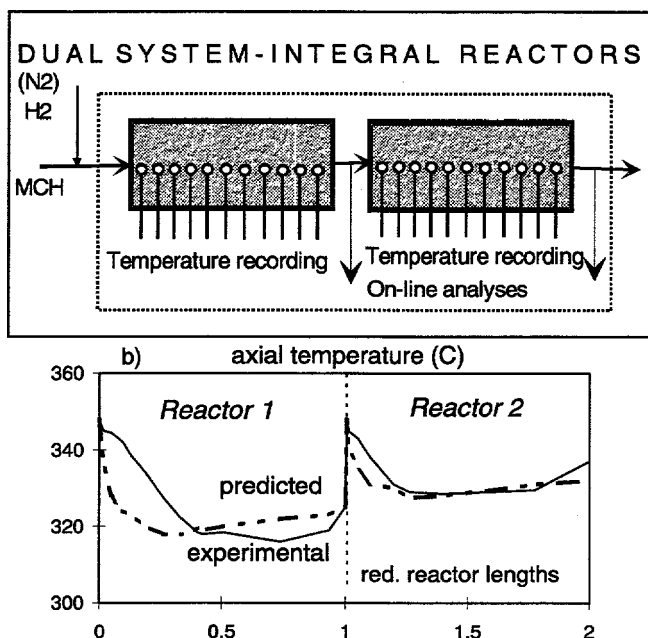


Fig. 2: (a) The dual system of integral reactors used to check the fresh catalyst kinetics. (b) Axial temperature profiles at 50 hours-on-stream and 6 atm overall pressure.

The evaluated radial heat transfer coefficient is in the range of 60-120 W/m²K, depending on the operating conditions. The one-dimensional model predictions (toluene yields and temperature profile in the reactors, Figure 2b) for steady-state operating conditions are in good agreement with the experimental data for various times-on-stream and high catalyst activity, excepting the first third of the cold spot in the first reactor. A further model refinement including the inlet axial temperature gradient will lead to increased temperature prediction capabilities.

4 NON-ISOTHERMAL INTEGRAL REACTOR EXPERIMENT FOR SEVERE OPERATING CONDITIONS: CATALYST DEACTIVATION

The same dual reactor system is used to study the catalyst deactivation in various conditions, following an increasing reaction temperature strategy at various overall pressures. The same pseudo-homogeneous integral reactor model is used for simulation, assuming intrinsic kinetics up to 420°-450°C. For higher temperatures, correction of the main kinetic constant has to take into account the particle mean effectiveness (η), and the subsequent decrease of the preexponential factor. In order to include also a kinetic term for the catalyst deactivation process, a discrimination among zero, 1st and 2nd order deactivation models was performed. For each of the deactivation models tried, various coke precursors were proposed: *mch*, *tol*, or the sum of hydrocarbons present in system (*mch+tol+secondary products*). A zero-order deactivation model was found to be more suitable (Van Trimpont *et al.*, 1988 [6]) and in satisfactory agreement with the experimental catalyst activity decay, mainly influenced by only the temperature level. Such a model assumes that the coke deposit originates from the hydrocarbons (feed *mch* and intermediate components in equilibrium with the feed), which present an approximate constant sum of concentrations. The coke formation increases with increasing temperatures and decreasing hydrogen partial pressures, then the catalyst relative activity a/a_0 declines with time-on-stream according to the relationship:

$$k = \eta k(\text{fresh catalyst}) a/a_0 = \eta k(\text{fresh catalyst}) \exp\left[-\int_0^t k_d / (1 + K_H p_{hyd}^2) dt\right], \quad (4)$$

[t = time-on-stream, (h); k_d = deactivation constant, (1/h); K_H = adsorption-desorption constant, (1/atm²); η = particle mean effectiveness].

The catalyst effectiveness factor is dependent on the temperature and location in the reactor, being correlated with an approximate formula derived from the Thiele modulus [2].

In order to estimate the deactivation model parameters, three sets of experimental data were considered, covering a wide range of operating conditions: i) 6 atm data set, $LHSV = 3-10$, 1-4 *hyd/mch* in the feed, temperatures in the range of 350-550°C; ii) 10 atm overall pressure data set, $LHSV = 5-10$, 0-0.8 *hyd/mch* in the feed, temperatures in the range of 300-450°C; iii) 16 atm overall pressure data set, $LHSV = 10$, no *hyd* in feed, temperatures between 350-450°C. The prediction of the catalyst activity in the reactors implies repeated simulation of the one-dimensional dynamic model over reactor lengths and times-on-stream. The simulation uses the experimental axial dynamic temperature profile in each of the reactors (on-line recorded by the PC-controlled reactor system), and assumes the quasi-stationarity of the temperature and activity profiles between two time-integration steps

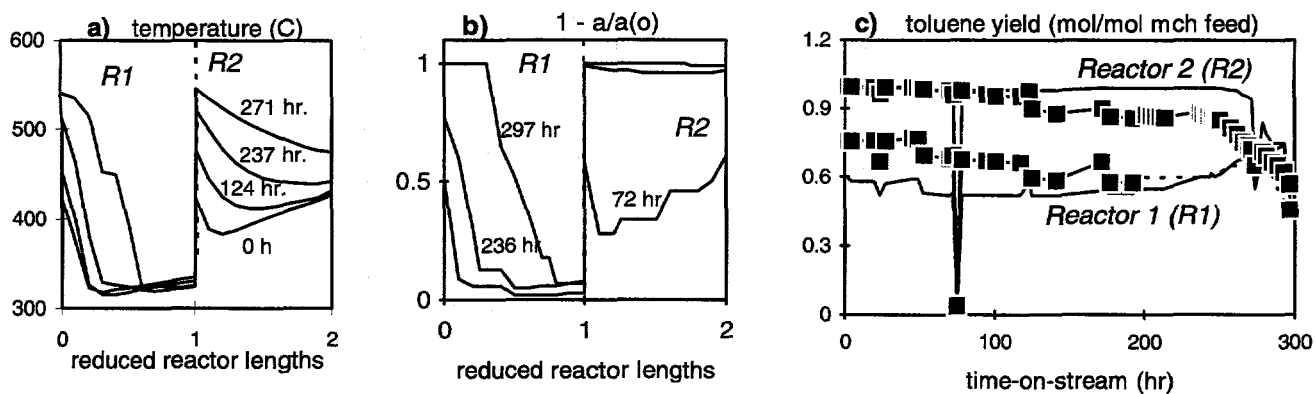


Fig. 3: (a) Time evolution of the axial temperature experimental profiles; (b) [1 - catalyst activity]; (c) toluene yield (—●— - experimental values; ——— predicted values) in the reactor system for 6 atm data set.

(approximately hourly based). The estimated model parameters (k , k_d , K_H), considered to follow an Arrhenius-type dependence with the temperature, present the following values:

$$k = a/a_0 \eta 20.46 \exp[-26540(1/T - 1/650)], \text{mol}/(\text{g.h.atm});$$

$$k_d = 0.08 \exp[-19500(1/T - 1/650)], 1/(\text{h.atm});$$

$$K_H = 0.8 (1/\text{atm}^2) \text{ constant.} \quad (5)$$

In Figure 3 the experimental temperature profiles, experimental and predicted toluene yields and the catalyst activity profiles for 6 atm are shown.

5 SUMMARY

The dehydrogenation of methylcyclohexane to toluene was studied in a wide range of operating conditions, including low and high pressures (6-16 atm), and low-mean-high severity reaction conditions. Two different experimental scales were used, i.e. an isothermal microreactor and a PC-controlled dual reactor system which allowed several hundred hours of continuous deactivation and data recording. Thus, particular data sets were generated and a proposed kinetic model was built-up and checked step-by-step. Short-cut estimation techniques for isothermal data, coupled with a complex estimation for the complete model under a wide range of operating conditions and severity of deactivation, revealed the importance of different parts of the model and allowed the correlation of catalyst and reactor performance. Activation energies were determined for fresh and deactivated catalysts.

6 ACKNOWLEDGEMENTS

The financial support of the Swiss Federal Institute of Technology (ETH-Zürich), and the Swiss Federal En-

ergy Research Fund is acknowledged. UOP Ltd. (UK) supplied the commercial catalyst.

7 REFERENCES

- [1] Maria, G. and Rippin, D.W.T., 1996, Recursive Robust Kinetics Estimation by Using a Mechanistic Short-Cut Technique and a Pattern-Recognition Procedure, *ESCAPE6 - 6th European Symposium on Computer Aided Process Engineering*, May 26-28, Rhodes (Greece); also in *Comp. Chem. Engng. S20*, 587-592, (1996).
- [2] Maria, G., Marin, A., Wyss, C., Mueller, S. and Newson, E., Modelling and Scaleup of the Kinetics with Deactivation of Methylcyclohexane Dehydrogenation for Hydrogen Energy Storage, *Chem. Eng. Sci.* 51, 2891-2896, (1996).
- [3] Müller, S., Heterogenised Platinum Clusters as Dehydrogenation Catalysts, *Ph. D. Dissertation*, ETH No. 11160, Paul Scherrer Inst., Villigen (Switzerland), (1995).
- [4] Rimensberger, K., Kinetische Untersuchungen der Dehydrierung von Methylcyclohexan zu Toluol im Mikropulsreaktor, im kontinuierlichen Mikropulsreaktor und im Laborfestbettreaktor, *Ph. D. Dissertation*, ETH No. 8278, Zürich, (1987).
- [5] Van Trimpont, P.A., Marin, G.B. and Froment, G.F., Kinetics of Methylcyclohexane Dehydrogenation on Sulfided Commercial Platinum / Alumina and Platinum - Rhenium / Alumina Catalysts, *Ind. Eng. Chem. Fundam.* 25, 544-553, (1986).
- [6] Van Trimpont, P.A., Marin, G.B. and Froment, G.F., Reforming of C₇ Hydrocarbons on a Sulfided Commercial Pt/Al₂O₃ Catalyst, *Ind. Eng. Chem. Res.* 27, 51-57, (1988).

TIME RESOLVED FTIR STUDY OF THE CATALYTIC CO OXIDATION UNDER PERIODIC VARIATION OF THE REACTANT CONCENTRATION

J. Kritzenberger, A. Wokaun

Oxidation of CO over a palladium/zirconia catalyst obtained from an amorphous $Pd_{25}Zr_{75}$ precursor was investigated by time resolved FTIR spectroscopy [1]. Sine wave shaped modulation of the reactant concentration, i.e. variation of CO or O_2 partial pressure, was used to induce dynamic variations of the IR signals of product (CO_2) and unconverted reactant (CO), which were detected in a multi-pass absorption cell. The phase shift ϕ between external perturbation and variation of the CO_2 signal was examined in dependence on temperature ($100^\circ C \leq T \leq 350^\circ C$) and modulation frequency ($1.39 \times 10^{-4} Hz \leq \omega \leq 6.67 \times 10^{-2} Hz$). From the phase shift values, a simple Eley - Rideal mechanism is excluded, and the rate limiting step of the Langmuir - Hinshelwood mechanism for the CO oxidation may be identified. Adsorption and possible surface movement of CO to the actual reaction site determine the rate of the CO oxidation on the palladium/zirconia catalyst used in our study. The introduction of an external perturbation is a first step towards the application of two-dimensional infrared spectroscopy [2-4] to heterogeneous catalyzed reactions.

1 EXPERIMENTAL

After recording the background spectrum a modulation experiment was started by varying the inlet mass flow of one reaction gas sinusoidally using the desired modulation frequency. Each change in the mass flow of the reaction gas was compensated by the inverse change in the N_2 mass flow. A set of 60 spectra was recorded during approximately 2 modulation periods. The phase shift ϕ between the CO signal and the CO_2 signal is deduced by determining the arithmetic average of one phase shift of peak maxima and one phase shift of peak minima. Examination of a contour plot of the spectra is a convenient way to determine ϕ .

2 RESULTS

Modulation experiments were performed in dependence on temperature using two different modulation frequencies, i.e. $1.66 \times 10^{-2} Hz$ and $4 \times 10^{-2} Hz$ corresponding to periods of 60 s and 25 s, respectively. Figure 1 shows the phase shift of the CO_2 signal relative to the phase of the external perturbation of the system, performed as cyclic variation of the CO inlet concentration compensated by a 180° phase shifted nitrogen variation as described in the experimental section.

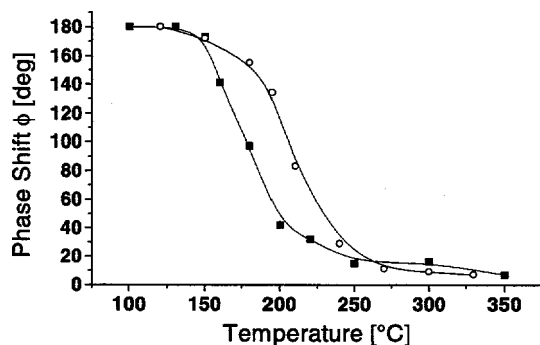


Fig. 1: Phase shift ϕ between the CO_2 signal and the CO signal versus T for modulation frequencies $\omega_{CO} = 1.67 \times 10^{-2} Hz$ (-■-) and $\omega_{CO} = 4 \times 10^{-2} Hz$ (-○-).

In Figure 1 three different regions of ϕ values can be separated. For $T \leq 150^\circ C$ the system responds with a phase shift $\phi \approx 180^\circ$ of the CO_2 signal. Obviously a 180° phase shift of CO_2 relative to CO characterizes an inverse reaction zone (reaction order -1), in which a higher CO inlet concentration yields a lower CO_2 production and reverse. Note that the 180° phase shift holds for both modulation frequencies. For $T \geq 240^\circ C$ a phase shift $\phi < 30^\circ$ is detected which becomes slowly smaller with increasing temperature. A phase shift of $\phi < 30^\circ$ reflects the area of reaction order +1 in CO, i.e. the more CO is available the more CO_2 is produced. Note the similar phase shifts for both modulation frequencies. For intermediate temperatures a strong dependence of ϕ on T is detected. The phase shift decreases starting at $\phi = 180^\circ$ ($T = 130^\circ C$) to $\phi \approx 30^\circ$ ($T = 240^\circ C$). In this region ϕ depends on the modulation frequency, i.e. at the same temperature a modulation period of 25 s yields a higher value of ϕ compared to a modulation period of 60 s.

Interpretation of the $\phi(\omega)$ data as a function of temperature calls for a model for the dependence of the phase shift ϕ on the modulation frequency ω . The corresponding experiments for a modulation of $p_{CO}/p_{O_2} = 4 \times 10^{-3} \pm 2 \times 10^{-3}$ performed by varying the modulation frequency at $T = 180^\circ C$ are shown in Figure 2.

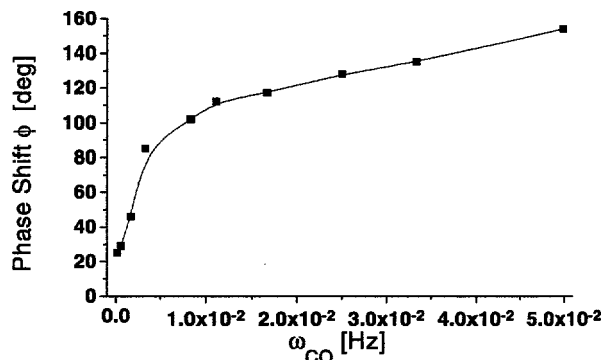


Fig. 2: Phase shift ϕ between the CO_2 signal and the CO signal for different modulation frequencies ω_{CO} ($T = 180^\circ C$).

In classical physics, similar curves for the dependence of phase shift on the modulation frequency are encountered for forced vibrations of a damped harmonic oscillator. Solution of the differential equation

$$m \frac{d^2 x}{dt^2} + r \frac{dx}{dt} + kx = K_0 e^{i\omega t} \quad (1)$$

yield

$$\tan(\phi) = \frac{r}{m} \frac{\omega}{\omega_0^2 - \omega^2} \quad (2)$$

with phase shift ϕ , modulation frequency ω , eigenfrequency of the oscillator ω_0 , oscillator parameters m , r , k , and modulation amplitude K_0 . The quantity $\frac{r}{m}$ determines the lifetime τ according to

$$\tau = 2 \frac{m}{r} \quad (3)$$

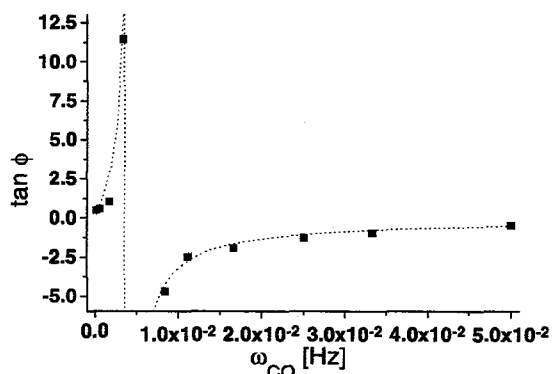


Fig. 3: Simulation of the modulation experiment using $p_{CO}/p_{O_2} = 4 \times 10^{-3} \pm 2 \times 10^{-3}$. Fit of $\tan(\phi)$ versus ω_{CO} using equation (2) yields $\omega_0 = (4.3 \pm 0.2) \times 10^{-3}$ Hz and $\tau = 77$ s.

Figure 3 shows a plot of $\tan(\phi)$ versus ω_{CO} for a modulation experiment using $p_{CO}/p_{O_2} = 4 \times 10^{-3} \pm 2 \times 10^{-3}$ ($T = 180^\circ\text{C}$). A fit of these values using equation (2) yields an eigenfrequency $\omega_0 = (4.3 \pm 0.2) \times 10^{-3}$ Hz and a lifetime $\tau = 77$ s. The eigenfrequency ω_0 may be associated with an overall rate constant, and will be used as a characteristic value to compare the reaction rate of the CO oxidation under different p_{CO}/p_{O_2} partial pressure ratios.

For a modulation experiment performed at $p_{CO}/p_{O_2} = 3.33 \times 10^{-4} \pm 1.66 \times 10^{-4}$ ($T = 180^\circ\text{C}$) a fit of $\tan(\phi)$ versus ω_{CO} using equation (2), yields an eigenfrequency of $(2.20 \pm 0.03) \times 10^{-2}$ Hz and a lifetime $\tau = 27$ s. Thus, with decreasing partial pressure ratio p_{CO}/p_{O_2} the system is shifted towards the linear reaction regime, and therefore one expects an increasing reaction rate.

3 DISCUSSION

Supposing the validity of the Eley - Rideal mechanism an increasing CO partial pressure should yield an increasing or at least a constant CO_2 production even at high p_{CO} values. In contrast, we find a phase shift of 180° independent of ω_{CO} for $p_{CO}/p_{O_2} \geq 3.2 \times 10^{-2}$, which is in contradiction to the Eley - Rideal mechanism [1]. Taking into account the additional observation that the modulation amplitude of CO_2 production increases with CO partial pressure, the only possible explanation for the existence of a negative power dependence is a competition of CO and O_2 for adsorption sites. At high p_{CO} values the surface is covered by adsorbed CO, and the oxidation rate is limited by the number of adsorption sites available for O_2 . Lowering the CO concentration increases the number of accessible O_2 adsorption sites and leads to an increase in CO_2 production. Therefore we conclude that the CO oxidation over a palladium/zirconia catalyst obtained from an amorphous $\text{Pd}_{25}\text{Zr}_{75}$ precursor is dominated by the Langmuir - Hinshelwood mechanism. In contrast to the observation that ϕ never reaches zero in experiments employing a modulation of the CO inlet concentration, we consistently detect $\phi = 0$ when varying the O_2 partial pressure for all experimental conditions. Obviously the CO_2 production follows immediately (within experimental limits) any change in the O_2 concentration. As the oxidation step is apparently fast, we conclude that the process of adsorption followed by surface movement of CO to the actual reaction site determines the rate of the CO oxidation.

Application of modulation spectroscopy in terms of varying the inlet mass flow of the reactant gases to the study of heterogeneous catalyzed reactions is a straightforward method to examine mechanistic and kinetic aspects of possible reaction paths. Based on this investigation we will expand the technique to the study of catalyst surfaces by diffuse reflectance spectroscopy. Detection of signal variations of surface bound species when introducing an external perturbation to the system and application of the formalism of two-dimensional IR-spectroscopy will give further insight to reaction paths and kinetics of intermediates.

4 REFERENCES

- [1] J. Kritzenberger and A. Wokaun, *J. Mol. Catal.*, in press (1997).
- [2] I. Noda, *J. Am. Chem. Soc.*, **111**, 8116 (1989).
- [3] I. Noda, *Appl. Spectrosc.*, **44**, 550 (1990).
- [4] I. Noda, A.E. Dowrey, and C. Marcott, *Appl. Spectrosc.* **47**, 1317 (1993).

XPS ANALYSIS OF BORON DOPED HETEROFULLERENES

B. Schnyder, H.-J. Muhr (ETH Zürich, Switzerland), R. Nesper (ETH Zürich, Switzerland), R. Kötz

Boron heterofullerenes were generated through arc-evaporation of doped graphite rods in a helium atmosphere. According to mass spectrometric analysis only mono-substituted fullerenes like $C_{59}B$, $C_{69}B$ and higher homologues together with a large fraction of higher undoped fullerenes were extracted and enriched when pyridine was used as the solvent. XPS analysis of the extracts indicated the presence of two boron species with significantly different binding energies. One peak was assigned to boric acid. The second one corresponds to boron in the fullerene cage, which is mainly $C_{59}B$, according to the mass spectrum. This boron is in a somewhat higher oxidation state than that of ordinary boron-carbon compounds. The reported synthesis and extraction procedure opens a viable route for production of macroscopic amounts of these compounds.

1 INTRODUCTION

Doping fullerenes has a strong influence on their molecular as well as bulk properties. Figure 1 illustrates the three possible means of doping fullerenes. In exohedral doping atoms are bonded externally to the fullerene cage, as in K_3C_{60} . Endohedral bonding means that one or more atoms are enclosed by the fullerene cage ($La@C_{82}$). (The symbol @ means that the lanthanide is inside a C_{82} cage). Boron is an integral part of the cage in the $C_{59}B$ described in this work.

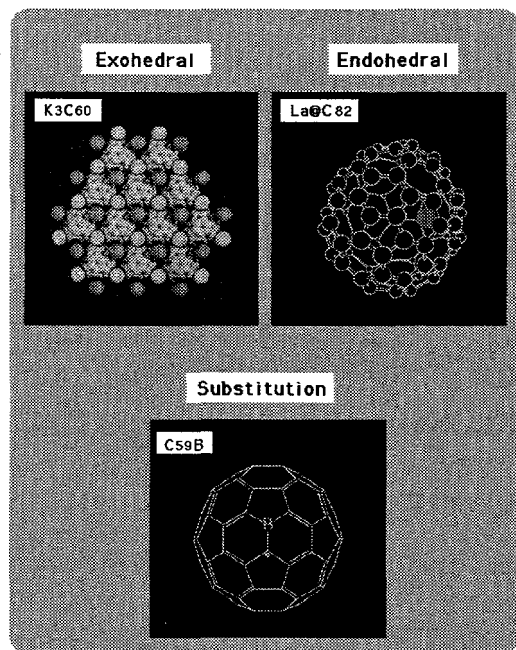


Fig. 1: The three modes of doping fullerenes.

Exo- or endohedral doping has been well examined [1] whereas less is known about the third possibility, doping through substitution with a neighboring element of carbon - such as boron or nitrogen.

The first experiment results were reported by Smalley et al. [2,3] who generated boron heterofullerenes $C_{60-x}B_x$ ($x = 1-6$) in the gas phase.

No bulk production of these materials has been reported to date. We present here a useful procedure for the production of macroscopic amounts of boron

heterofullerenes using a modified Krätschmer-Huffman process [4].

2 EXPERIMENTAL

Soot was produced in a modified fullerene reactor through arc-evaporation of doped graphite rods in a helium atmosphere. The best results are obtained if the doping content lies between 10-15 wt.%. Boron nitride, boron carbide and boron are suitable doping materials.

Samples were extracted in a soxhlet with dry pyridine under a reduced atmosphere of 30 mbar argon at 60°C. In contrast to the more commonly used carbon disulfide or toluene, the polar solvent pyridine extracts the more polar heterofullerenes through the formation of solvent adducts due to their enhanced Lewis acidity [3]. The extracts were handled and stored in a dry and oxygen-free atmosphere. After soxhlet extraction with pyridine the dark brown solution is filtered, the solvent removed and the residue dried at room temperature under high vacuum. Finally, the residue is thoroughly washed with dry carbon disulfide to achieve a pre-separation into undoped and doped fullerenes.

The extracts were characterized with a reflector time-of-flight mass spectrometer and X-ray photoelectron spectroscopy (XPS). XPS measurements were carried out on samples in the form of pellets, 6 mm in diameter, pressed under argon. Depth profiling were obtained by sputtering the surface of the sample with Ar^+ ions (3 keV, 1 μA , corresponding to 20 $\text{\AA}/\text{min}$ ref. to Al_2O_3).

3 RESULTS AND DISCUSSION

The treatment of the original pyridine extract with carbon disulfide leads to a separation of $C_{59}B$ and $C_{69}B$ from C_{60} and C_{70} but not from the higher undoped fullerenes (mainly C_{74} and C_{84}) which also show an enhanced solubility in pyridine.

C_{74} and C_{80} are present at relatively high concentration. These fullerenes are normally detected only at trace levels in the toluene extract of the soot of resistively heated graphite [5].

Somewhat surprising is the observation that only mono-substituted heterofullerenes can be extracted from the soot. There was no sign of multiply substituted species in the mass spectra of the residue after extraction. This may be due to a decomposition reaction of the latter which does not affect the more stable mono-substituted fullerene species. In fact, a possible end product of a decomposition of boron heterofullerenes is always present in the final extract: boric acid or boron oxide, both of which are also readily soluble in pyridine. This undesired side reaction might result from the contamination of the soot with moisture during the soot collection which is carried out in air, or contamination through leaks in the reactor. The boric acid can be selectively removed to a great extent by washing the extract with diethyl ether or acetone.

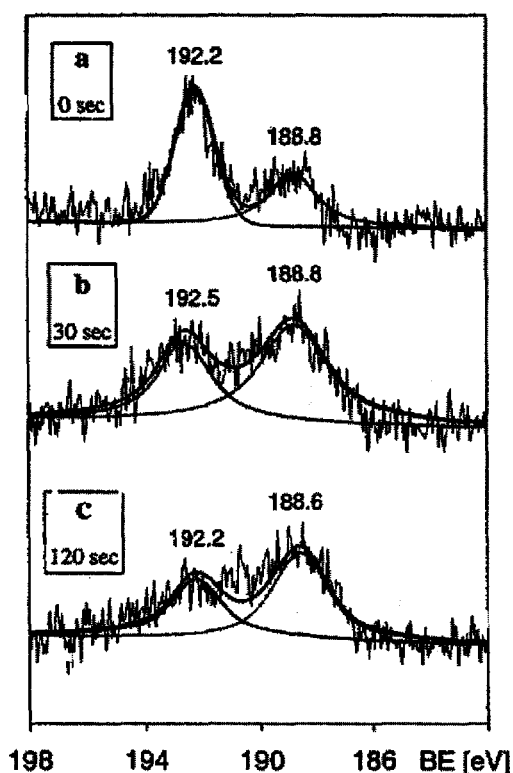


Fig. 2: X-ray photoelectron spectra of the B 1s core level region: a) as received sample, b) sample sputtered for 30 s, c) sample sputtered for 120 s.

The XPS spectra of the B 1s core level region of the washed extract are shown in Figure 2a - 2c. The surface of the unsputtered sample contains two boron species with significantly different binding energies. The peak at 192.3 eV is due to boric acid or boron oxide (see Table 1). The second one at 188.8 eV is assigned to boron in the heterofullerenes, mainly $C_{59}B$ and $C_{69}C$, according to the mass spectra. A comparison of the B 1s core level binding energies of a selection of boron compounds in Table 1 provides evidence that boron is in a somewhat higher oxidation state in the heterofullerenes than in ordinary boron-carbon compounds e.g. $B_{13}C_2$ or $NaBPh_4$.

Argon sputtering for thirty seconds decreases the intensity of the peak at 192.3 eV, and the peak at 188.8 eV becomes dominant in the spectrum. Further sputtering (Figure 2c) does not change the spectrum significantly, only the heterofullerene to boron oxide ratio increases and finally reaches a value of 1.7. The decrease in intensity of the peak at higher binding energies is a result of the higher concentration of boron oxide at the surface. Because the pellet is made from powder containing boron oxide on the particle surface, it is not possible to remove the boron oxide completely through sputtering.

| Substance | B 1s [eV] |
|----------------|---------------------|
| $B_{13}C_2$ | 186.7, 186.5 |
| B | 187.2, 187.3 |
| $B_{10}H_{14}$ | 187.8 |
| $NaBPh_4$ | 187.2, 187.5 |
| $C_{2n-1}B$ | 188.8 |
| BN | 190.3, 190.5 |
| B_2O_3 | 192.4, 192.0, 193.1 |
| $B(OH)_3$ | 192.8, 193.0 |
| $NaBF_4$ | 195.1 |

Tab.1: Comparison of the B 1s core level binding energies of known boron compounds with boron heterofullerenes (see references in [6]).

More details concerning the production and experimental conditions and additional results have been reported elsewhere [6,7].

4 ACKNOWLEDGMENT

The financial support of the Swiss National Science Foundation is gratefully acknowledged.

5 REFERENCES

- [1] A. Hirsch, The chemistry of the fullerenes, Thieme Verlag, Stuttgart, (1994).
- [2] Y. Chai, T. Guo, C. Jin, R.E. Haufler, L.P.F. Chibante, J. Fure, L. Wang, J.M. Alford and R.E. Smalley, J. Phys. Chem. 95, 7564, (1991).
- [3] T. Guo, C. Jin and R.E. Smalley, J. Phys. Chem. 95, 4984, (1991).
- [4] W. Krätschmer, L.D. Lamb, K. Fostiropoulos and D. Huffman, Nature 347, 354, (1990).
- [5] C. Thilgen, F. Diederich and R.L. Whetten, in: Buckminsterfullerenes, ed. W.E. Billups and M.A. Ciufolini, VCH Publishers, Weinheim, p. 59, (1993).
- [6] H.-J. Muhr, PhD Thesis Nr. 11806, Swiss Federal Institute of Technology, Zürich, (1996).
- [7] H.-J. Muhr, R. Nesper, B. Schnyder and R. Kötzer, Chem. Phys. Letters 249, 399, (1996).

INTERMITTENT CONTACT ATOMIC FORCE MICROSCOPY IN ELECTROCHEMICAL ENVIRONMENT

P. Häring, R. Kötz, H. Siegenthaler (University of Bern, Switzerland)

In situ measurements with Atomic Force Microscopy (AFM) may cause surface modifications due to the tip-surface interactions. As an alternative and less destructive method, Intermittent Contact Atomic Force Microscopy (ICAFM) has been tested in an electrolytic environment. In the ICAFM mode the tip is not constantly in contact with the surface under investigation but is tapping onto the surface with a certain frequency. A commercial Park Scientific Instruments Microscope has been modified to enable *in situ* experiments with ICAFM. It was possible to image iridium oxide films with ICAFM in the electrolytic environment without any noticeable surface modifications.

1 INTRODUCTION

Electroactive materials exhibit pronounced changes of their chemical and physical properties during electrochemical oxidation/reduction. Such materials for instance conducting polymers or metal oxides are used in charge storage devices, electrochromic displays or in sensors and actuators.

With Scanning Probe Microscopy (SPM) it is possible to characterize the surface morphology and its changes *in situ* [1-4]. Further, *in situ* measurements of dimensional changes are possible in all three space directions. One thus can study material changes (crack formation, swelling, shrinking) during the electrochemical reaction *in situ* and in real time.

Dimensional and morphological changes of electroactive films may cause mechanical stress and pressure within the devices and will affect adhesion behavior of electroactive films on their substrates as well as long-term stability during repetitive electrochemical cycling.

SPM investigations are successful as long as the tip-surface interactions will not influence the measurements. Depending on the mechanical and electronic properties of the sample under investigation, it may be important to choose the least destructive imaging method.

We report about *in situ* imaging of iridium oxide films using AFM and ICAFM.

2 EXPERIMENTAL

AFM investigations were performed with a *Park Scientific Instruments* model AP-100 Autoprobe CP scanning probe microscope equipped with home built electrochemical cell and an *EG&G Versastat 253 Potentiostat/Galvanostat*.

The electrolyte in the AFM electrochemical cell was 1M sulfuric acid. A Pt wire served as the counterelectrode. An Ag/AgCl electrode separated from the main compartment by a ceramic diaphragm was used as a reference electrode.

Anodic Iridium oxide films (AIROF) were produced on an iridium metal film on glass as a working electrode in 1 M sulfuric acid. The films were grown by potential

cycling between -190mV and 1350mV vs. a saturated calomel reference electrode (*Metrohm*) with scan rates of 200 to 1000 mV/s. The reversible charge exchange was between 3 and 10 mC/cm².

Samples were prepared in a separate, external electrochemical cell (*Metrohm*).

After preparation the electrodes were immediately transferred to the electrochemical cell of the scanning probe microscope.

3 RESULTS

In situ AFM experiments on AIROF's showed strong surface modifications during scanning. An influence of force load and scan speed could be observed.

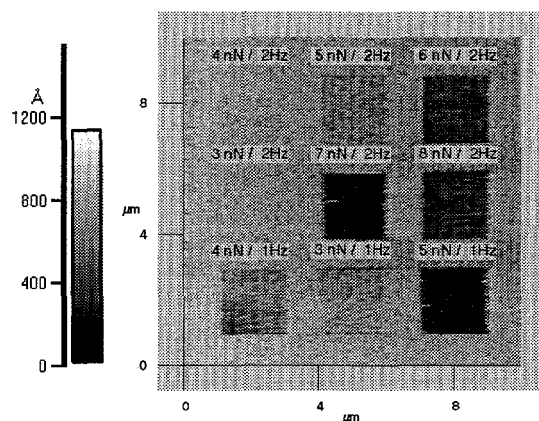


Fig. 1: AFM topographic image of an iridium oxide film in sulfuric acid in the reduced state after scanning nine 2x2µm images with different scan parameters. An influence of force load (indexed in nN), scan speed (indexed in Hz) and lateral scan range can be observed.

Surface changes due to the scanning tip during the experiment leads to an error of the recorded data. Figure 1 shows an AFM topographical image of an iridium oxide film in sulfuric acid in the reduced state after scanning nine 2x2µm images with different scan parameters. The surface modifications exhibited are due to wear by the AFM tip. Accurate measurements of height changes or roughness are no longer possible then.

We conclude that for soft and mechanically less stable materials, AFM is not suitable as method for in situ height measurements.

As an alternative and less destructive method, in situ ICAFM has been tested. The commercial *Park Scientific Instruments* microscope had to be modified to develop this technique for in situ applications. The ICAFM method requires a modulation of the tip-sample distance by a certain frequency. In order to prevent technical problems like corrosion of the tip and the piezo contacts or shunt currents due to insulation problems within the electrochemical cell, an indirect way of z-modulation was chosen via the scanner piezo. With this setup it will be possible to use the in situ cell in a closed configuration under inert atmosphere too.

Figure 2 shows a schematic of the in situ ICAFM experimental setup.

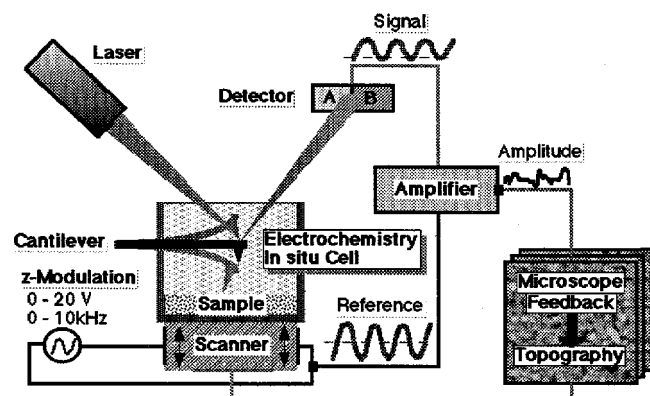


Fig. 2: Experimental setup for in situ ICAFM applications. The frequency modulation (frequency synthesizer output) is connected to the z-piezo electrodes of the scanner (indirect modulation).

While in the AFM mode the tip is constantly in contact with the sample surface and a certain force load is applied, in the ICAFM mode the tip is tapping onto the surface with a certain frequency. The frequency has to be higher than the time constant of the microscope feedback in order to prevent mixing of surface topographical information with modulation effects. The typical modulation frequency was between 7 and 9kHz. It was possible to obtain images of the topography of AIROF's in the electrolytic environment without any surface modification in the ICAFM mode.

The lateral resolution (x- and y-direction) was of the order of about 50nm and the resolution in height (z-direction) was of the order of about 5nm.

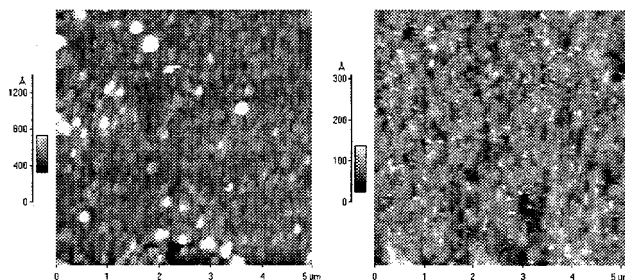


Fig. 3: In situ ICAFM (left hand side) and AFM (right hand side) topographical image of an iridium oxide surface in the electrolytic environment in the reduced state.

While the rms-roughness of the images obtained in the ICAFM mode was higher by about a factor of 3, the lateral resolution is lower than that obtained in the AFM mode (Figure 3). The reason of the lower roughness exhibited in the AFM scans is probably due to wear produced by the AFM tip.

4 CONCLUSIONS

Intermittent Contact Atomic Force Microscopy is a good alternative method to classical AFM for in situ surface characterizations on soft and less rigid materials. It is possible to image surfaces of electroactive materials in different electrochemical states within the electrolytic environment.

5 ACKNOWLEDGMENT

This work was supported by the Swiss National Science Foundation, Grant #21-39325.93.

6 REFERENCES

- [1] R. Nyffenegger, Ph.D. thesis, University of Bern, (1994).
- [2] P. Häring, R. Kötz, *Journal of Electroanalytical Chemistry* 385, pp. 273-277, (1995).
- [3] R. Nyffenegger, E. Ammann, H. Siegenthaler, R. Kötz, and O. Haas, *Electrochimica Acta* 40, pp. 1411-1415, (1995).
- [4] R. Chen, Y. Mo, and D.A. Scherson, *Langmuir* 10, pp. 3933-3936, (1994).

IN-SITU INVESTIGATION OF THE CALCINATION PROCESS OF MIXED OXIDE XEROGELS WITH RAMAN SPECTROSCOPY

J.-C. Panitz

The controlled calcination of materials derived by sol-gel reactions is important for the evolution of the final structure. Raman spectroscopy is an ideal tool for the identification of surface species under in-situ conditions, as demonstrated in the following for the example of a molybdenum oxide-silica mixed xerogel. Raman spectra of this particular sample were recorded at temperatures as high as 1173 K, and compared with those of a reference material.

1 INTRODUCTION

Raman spectroscopy has become one of the most versatile methods for characterization of chemical composition of a sample. This is partly due to the improvement in experimental techniques achieved during the last decade, which compensates for the inherent weakness of the Raman effect itself [1]. Recent advances include the 3D-imaging of turbid samples [2] and the use of a Near-Field Scanning Optical Microscope for increased spatial resolution [3].

The advantage of Raman techniques is that they can be applied to almost every sample, be it a gas, a liquid or a solid. In this contribution, the usefulness of Raman spectroscopy for materials characterization is demonstrated by monitoring a calcination process at elevated temperatures under controlled atmosphere [4]. The calcination step is an important part in the preparation of materials via the sol-gel process with influence on the final structure of the material.

2 EXPERIMENTAL

A molybdenum oxide-silica mixed xerogel was prepared by a non-aqueous sol-gel reaction using a mixture of molybdenum(VI)oxytetrachloride and tetraethoxysilane. Formic acid was used as agent for the acidolysis reaction. After drying of the wet gel at 413 K, the gel was crushed in a rotating blade grinder. A small piece of the xerogel was placed in a heatable microscope stage under a controlled flow of air. In addition, the microscope stage contained also a piece of a reference silica material prepared under identical conditions, but without the molybdenum oxide precursor. Raman spectra were recorded with a Raman microscope (DILOR LabRam). A Helium-Neon Laser was used for excitation, and a CCD was used for detection of Raman scattered photons.

3 RESULTS AND DISCUSSION

Raman spectra recorded at temperatures between 873 and 1173 K are displayed in Figure 1, showing typical features of dispersed molybdate species and the silica carrier. Whereas it is possible to acquire good-quality spectra up to 1073 K, the thermal emission of the sample recorded at 1173 K buries most of the Raman bands. Nevertheless, as proved by the

inset in the lower right spectrum of Figure 1, Raman bands are still discernible at this temperature.

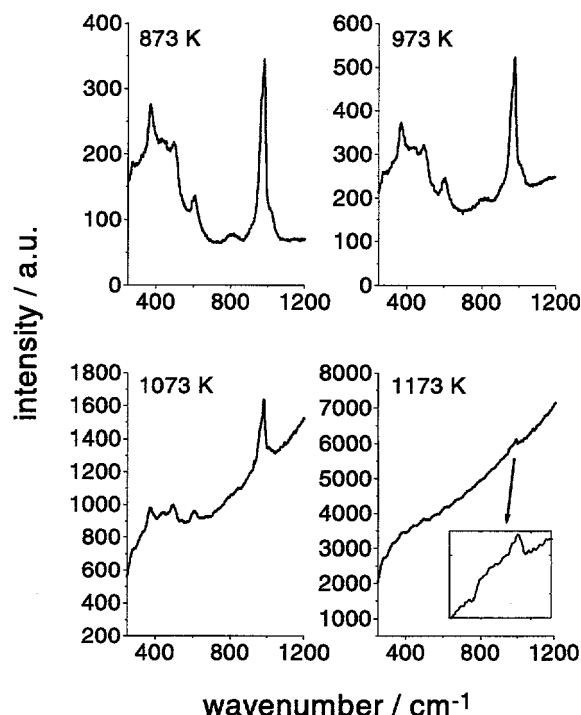


Fig. 1: Raman spectra of a molybdenum oxide - silica mixed xerogel recorded during the course of the calcination.

Figure 2 shows the Raman spectrum of the xerogel containing molybdenum oxide (Figure 2a) against the Raman spectrum of the silica reference material (Figure 2b), recorded under identical conditions. Using these two spectra, trace c was calculated by subtracting the weighted spectrum of the silica reference from the Raman spectrum of the molybdenum oxide-silica material. Interestingly, Figure 2c reveals that the band at 800 cm^{-1} is apparently due to the silica carrier only, and not to vibrations within Mo-O-Mo linkages. This is an indication that at the given temperature, the molybdenum oxide species are dispersed very effectively on the surface. In the course of the calcination, the intense Raman signals of crystalline MoO_3 are never observed, which also points to a very effective dispersion of the molybdenum oxide species on the surface.

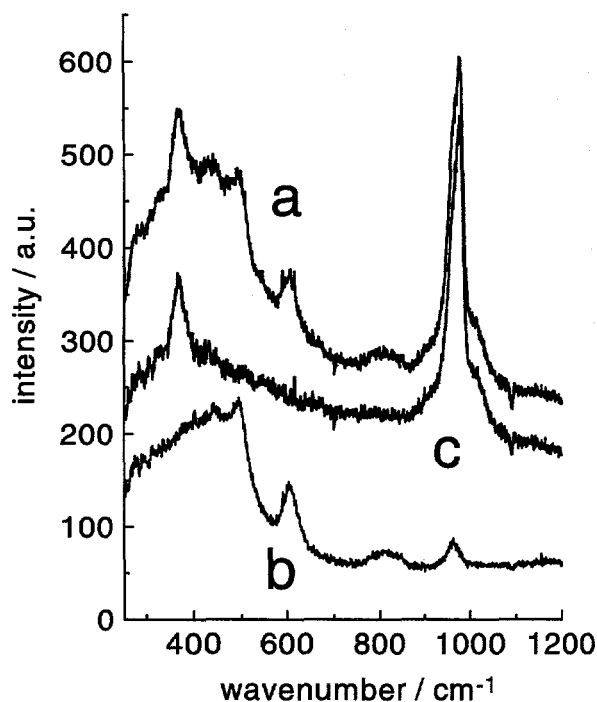


Fig. 2: Raman spectra recorded at 873 K. Trace a: molybdenum oxide - silica mixed xerogel, b: silica reference, c: calculated difference spectrum.

The course of the non-Raman emission intensity recorded during the calcination deserves attention, too. The intensity at an off-band position (1190 cm^{-1}) is shown in Figure 3 against temperature. The recorded

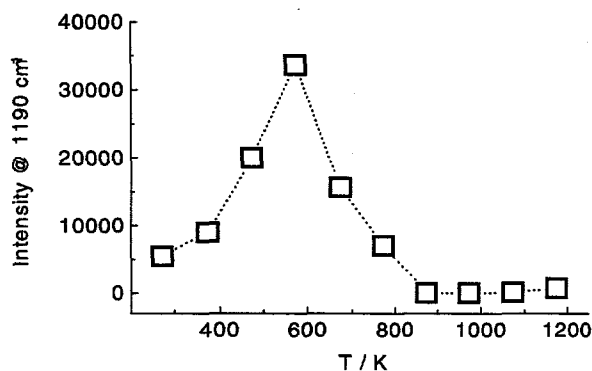


Fig. 3: Off-band (non-Raman) emission intensity recorded during the calcination, indicating that burn-off of organic residues from the sol-gel reaction is complete at 873 K.

intensity is probably due to fluorescence emitted by organic residues trapped in the gel pores after drying at 413 K. After a strong rise in the beginning of the calcination experiment, the intensity decreases at temperatures greater than 573 K. Under the conditions of the experiment, the burn-off process is completed at 873 K. The information contained in Figure 3 may be used to select the most appropriate calcination temperature. In the present case, a temperature of about 623 K would be a good choice for a calcination process with minimum disruption of the gel network.

4 OUTLOOK

With the described setup it is possible to optimize the calcination process needed for structural evolution and densification of sol-gel materials. The case presented is just an example out of the gamut of experiments possible with Raman spectroscopy.

Future applications include the characterization of heterogenous catalysts under working conditions; and the investigation of the high-temperature structural properties of refractory composite ceramics by Raman imaging. With an spectroelectrochemical cell specially designed for a microscope, that is currently under construction, the characterization of electrodes using Raman imaging techniques will be started within 1997.

5 REFERENCES

- [1] J.J. Laserna (ed.), „*Modern techniques in Raman spectroscopy*“, Wiley, Chichester, (1996).
- [2] C.J.H. Brenan, I.W. Hunter, „*Volumetric Raman Microscopy Through a Turbid Medium*“, *J. Raman Spectrosc.*, 27, 561-570, (1996).
- [3] C.L. Jahnke, H.D. Hallen, M.A. Paesler, „*Nano-Raman Spectroscopy and Imaging with a Near-Field Scanning Optical Microscope*“, *J. Raman Spectrosc.*, 27, 579-586, (1996).
- [4] J.-C. Panitz, *Applied Spectroscopy*, accepted for publication.

DEVELOPMENT AND CHARACTERIZATION OF A RARE EARTH EMITTER FOR A THERMOPHOTOVOLTAIC POWER GENERATOR

W. Durisch, J.-C. Panitz

Energy conversion based on thermophotovoltaic (TPV) methods has recently attracted renewed interest. Efforts at PSI are directed towards the development of a modular TPV system based on existing technology to demonstrate the feasibility of this method. Here, we report first results obtained with a prototype TPV generator based upon a modified rare earth emitter, a heat reflecting filter and commercial silicon solar cells. The preparation of the modified emitter is described, and first results of spectroscopic and electrical characterization of the TPV system are presented. The introduction of the modified emitter leads to a efficiency gain of 30-40 %.

1 INTRODUCTION

Thermophotovoltaic (TPV) power generation is based on the conversion to electricity of the radiation emitted by a heat source by means of a suitable photocell. The principle of TPV was first demonstrated in 1963 using photocells made of germanium [1]. In recent years, there has been renewed interest in TPV based energy conversion, especially for application in power generators for deep space missions. Several research groups, including one at PSI, consider TPV also as useful means for the co-generation of heat and electricity [2, 3].

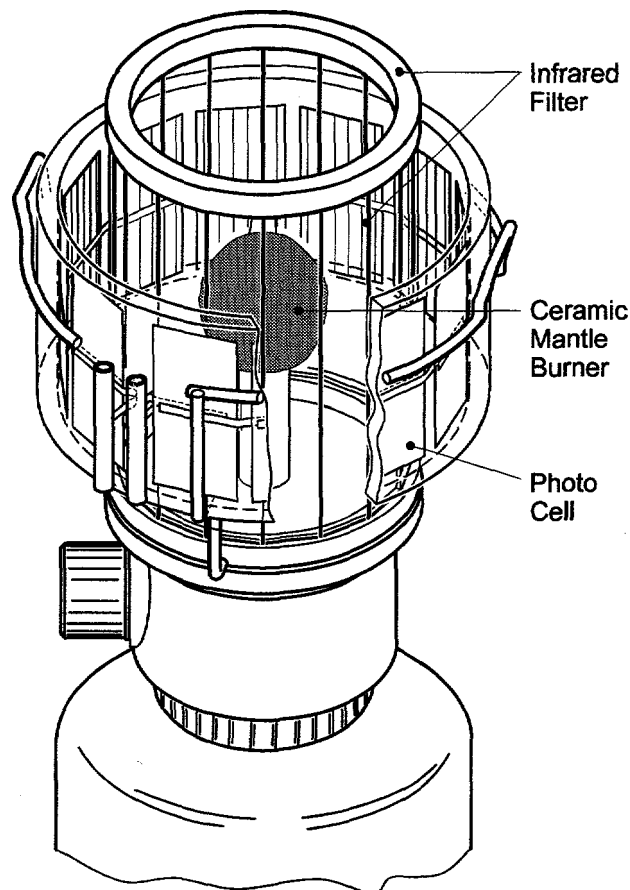
Efforts at PSI are directed towards two ends. In a more application-oriented project co-sponsored by the Swiss natural gas industry (FOGA), a TPV generator based on existing technology will be developed, exploring aspects of system optimization and integration into household natural gas burners on power scales up to 10 kW (thermal) and some 100 W (electrical). In a second project, which is in preparation, more basic questions will be addressed, especially the development of novel selective emitters and photocells with bandgap adjusted to the emission characteristics of the emitter.

The TPV prototype converter used by us essentially consists of hardware sold by camping gaz[®], namely a ceramic mantle mounted on a burner fuelled with a butane/air mixture. The mantle burner is surrounded by ITO glass for rejection of infrared radiation, and by an outer array of silicon solar cells mounted in cylindrical configuration. Figure 1 shows the demonstration model. In the following, we will describe the results of introductory experiments.

2 PREPARATION OF MODIFIED RARE EARTH EMITTER

Commercially available mantles are based on cerium and praseodymium oxides deposited within an yttria matrix. Therefore, the emission of the mantle burner was modified by depositing ytterbia onto the mantle in order to improve the matching between the spectral sensitivity of the silicon photocells and the emission characteristics of the emitter. To this end, a solution of

$\text{Yb}(\text{NO}_3)_3 \cdot 5 \text{H}_2\text{O}$ was prepared in a mixture of ethanol and water.



DW50-41-H82

Fig. 1: TPV power generator based on a commercial mantle gas burner. The mantle is surrounded by heat-reflecting glass and silicon photocells.

In a first run, this solution was sprayed directly onto the mantle under operating conditions. Though the results of an electrical characterization were quite favorable, this deposition method leads to mechanical damage of the rather fragile mantle material. Therefore, a dip-coating technique was used, where the mantle was dismantled and impregnated by immersing the mantle into the solution. Thereby, mechanical damage due to thermal stress is effectively avoided.

3 CHARACTERIZATION OF MODIFIED MANTLE

The characterization of mantle emission was performed using a fiber optics probe connected to the external port of a Raman microscope (Labram, Dilor). The results of the spectroscopic characterization of the emission properties of the mantles prepared are shown in Figure 2. Trace 2 a) represents the emission spectrum from the mantle as received, and 2 b) depicts the emission spectrum of the ytterbia-coated mantle modified by the dip-coating process. Clearly, a comparison of both spectra gives the result that the total emission yield from the burner at constant fuel consumption has been improved. Furthermore, the ytterbia deposited does not deteriorate the emission from the original mantle, but produces additional emission in a spectral region close to the bandgap of the silicon solar cell.

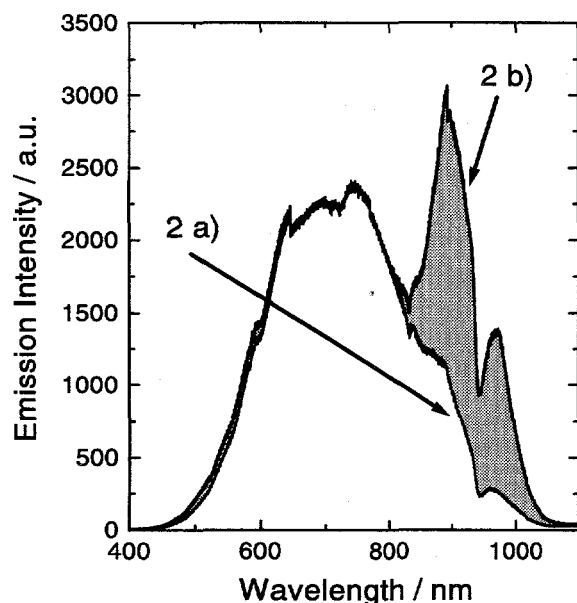


Fig. 2: Spectral characterization of mantle emission. The shaded area represents the increase in emission due to ytterbia deposited.

4 ELECTRICAL CHARACTERIZATION OF PROTOTYPE TPV POWER GENERATOR

The electrical characterisation of the TPV power generator was performed at PSI's test facility for solar photovoltaic components [4]. About 120 current/voltage data points are recorded within ~7 seconds. These are shown in Figure 3, left axis. From the current/voltage pairs, the power/voltage curve is calculated (s. Figure 3, right axis). For both mantles investigated, maximum power occurs at a voltage of ~1.6 V. Again, the ytterbia-coated mantle is of superior performance, giving an efficiency gain of 35 % in electrical power. Taking into account the extremely simple design of our

prototype, the measured output power of 2.2 W is indeed an encouraging result.

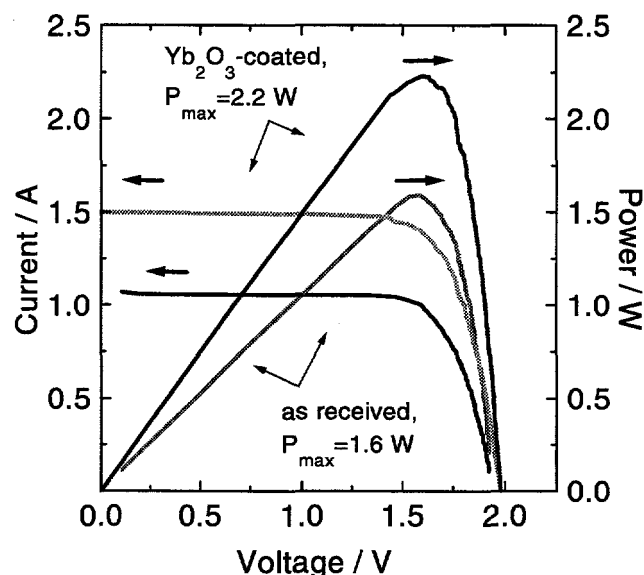


Fig. 3: Current and power output against voltage of the prototype TPV generator. Note the gain achieved by using the ytterbia coated mantle.

5 OUTLOOK

The techno-economical attractiveness of TPV energy conversion will be decided by the availability of a cheap and efficient combination of emitter, filter and photovoltaic devices with optimal performance. In addition, novel concepts in burner design will be needed to raise the efficiency of TPV converters. The results presented may be regarded only as a first step into this direction.

6 ACKNOWLEDGEMENTS

We thank Irena Kusar for preparing Figure 1.

7 REFERENCES

- [1] J. Werth, „*Thermophotovoltaic energy conversion*“, in: Proc. 17th Power Sources Conference, p. 23, (1963).
- [2] L. Broman, „*Thermophotovoltaics Bibliography*“, Progr. Photovoltaics, 3, 65, (1995).
- [3] J.P. Benner, T.J. Coutts, D.S. Ginley (eds.), „*Proceedings 2nd NREL Conference on Thermophotovoltaics*“, AIP Conference Proceedings Vol. 358, American Physics Institute, Woodbury (1996).
- [4] W. Durisch, J. Urban, G. Smestad, „*Characterisation of Solar Cells and Modules under Actual Operating Conditions*“, in: Proceedings of World Renewable Energy Congress, June 1996, Denver, Vol. 1, p. 359, Pergamon, Oxford, (1996).

AZO GROUP CONTAINING COMPOUNDS: INVESTIGATION OF THE DECAY MECHANISM

D. Franzke, J. Kritzenberger, Th. Kunz

We investigated compounds containing the $N=N-X$ ($X=S, P, N_3$) group which are potential candidates for microstructuring by photoresist technology or by photoablation. To elucidate the mechanism of thermal decomposition and photolysis we used infrared and UV spectroscopy, respectively, in solution as well as in the solid state. In this article we describe photolytic and thermolytic properties of one representative molecule for each of three substance classes: diazosulfides, azophosphonates and pentazadienes.

1 INTRODUCTION

During the last years many compounds were synthesized in order to develop new materials which can be used for microstructuring by photoablation or by photoresist technology [1-3]. All these materials contain a functional group which causes absorption in the wavelength range that is used to form the microstructures, and which causes also fracturing of the molecules by photochemical or photothermal cleavage. A possible strategy to develop new materials is synthesizing model compounds which contain the functional group in order to screen the photochemical properties and the influence of additional substituents on these properties. In a next step macromolecules are synthesized containing the functional group in the chain, or standard polymers are doped using the model compounds mentioned above. The design of tailored molecules depends on the understanding of the basic steps of the decomposition mechanism, the occurrence and the nature of intermediate decay products, etc.. Recently, we investigated compounds containing the $N=N-X$ group ($X=S, N_3, P$) with respect to their behaviour in solution as well as in the solid state. These compounds are of interest due to the fact that they can be effectively decomposed at high irradiation intensities. Under daylight and atmospheric conditions, however, they can be handled without further care.

2 EXPERIMENTAL

Irradiation experiments were performed using XeCl excimer lasers from Lambda Physik (LPX 300, Compex 205) with 308 nm wavelength. The pulse energy was chosen in the range between 40 to 500 mJ and the pulse length was about 15 ns. The UV spectra were detected in standard quartz cuvettes with a diode array spectrometer (Polytec XDAP). For monitoring the thermolysis by infrared spectroscopy we used a Bruker IFS 55 FTIR spectrometer equipped with a diffuse reflectance unit (DRIFT). Temperature control and regulation were performed with an environmental chamber (Spectra Tech). The experiments were controlled by LABVIEW programs via a PC. We used a Bomem DA8 FTIR spectrometer equipped with a quartz window to irradiate KBR pellets with UV light. The experimental setup is shown in Figure 1.

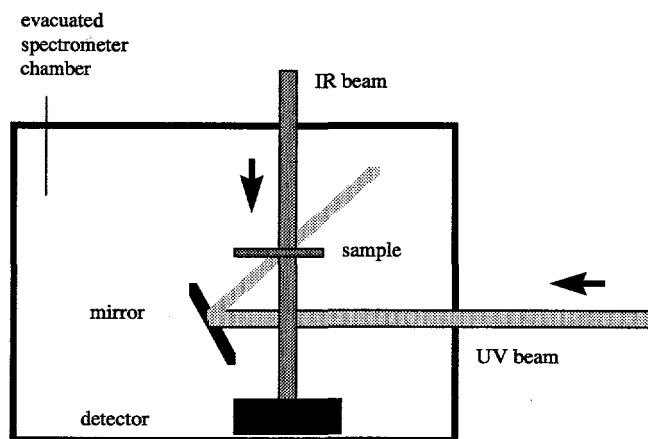
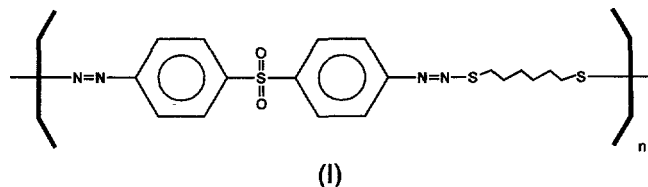


Fig. 1: Setup for irradiation in the IR spectrometer.

3 RESULTS AND DISCUSSION

3.1 Poly(alkylaryldiazosulfide)

As a first example we show the photolysis of a poly(azosulfide) (I) in solution. The repeating unit of this macromolecule contains two $N=N$ units which are part of a conjugated π system separated from the next one by an aliphatic chain. Therefore, three different isomers are detectable in the UV spectra: the Z/Z (maximum of absorption at 275 nm), the E/Z (300 nm) and the E/E -isomer (340 nm). The polymer (I) was synthesized to yield preferably the Z/Z isomer.



The laser photolysis of this compound is shown in Figure 2. It is observed that the main absorption of the compound shifts successively from 340 nm to 300 nm and then to about 275 nm before it diminishes. Two isomerization steps and a subsequent decomposition of the molecule under nitrogen release are a possible explanation for the described behaviour. In contrast, neither photolysis nor thermolysis of (I) in solid state (KBr matrix) exhibits intermediate products.

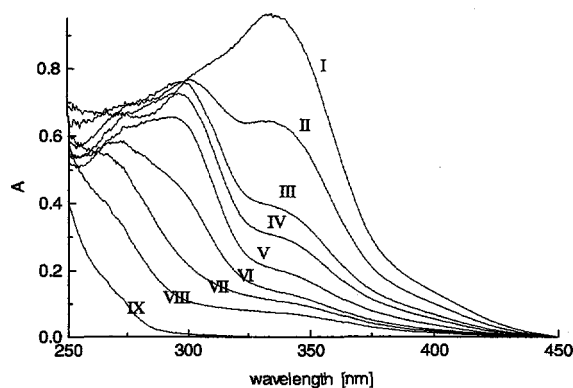


Fig. 2: Photolysis of (I). Trace I shows the UV absorption spectrum of the polymer dissolved in CHCl_3 before irradiation. Subsequent traces were recorded after delivering 1,2,3,5,10,20,50 and 100 pulses of UV light (150 mJ at 308 nm) to the sample.

3.2 Azophosphonates

Azophosphonates are known since 1958 and were recently tested as photoablation materials [2]. We investigated photochemical and thermal degradation of some model compounds. A representative molecule (II) of this class shows no intermediate products when irradiated in solution. This behaviour is in contrast to the results obtained using (I).

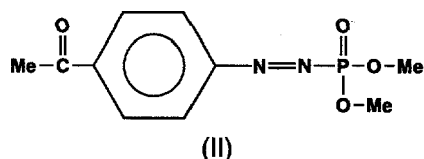


Figure 3 shows the comparison of thermolysis and photolysis of (II) embedded in a KBr pellet monitored by IR spectroscopy. The peak assigned to the carbonyl vibration (1671 cm^{-1}) disappears only upon irradiation of the compound but remains detectable during the thermolysis at $120\text{ }^\circ\text{C}$. This clearly indicates that different reaction conditions lead to different products.

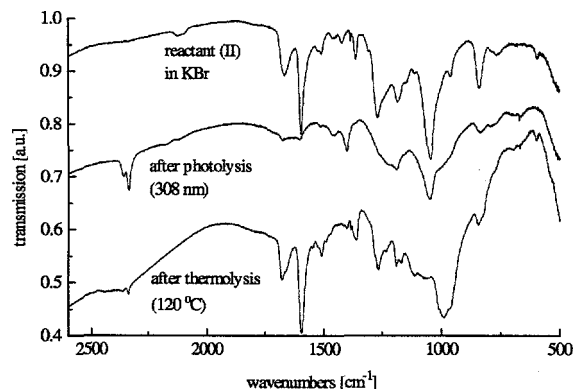


Fig. 3: Thermolysis and photolysis of (II) in KBr.

3.2 Pentazadienes

Aromatic substituted pentazadienes are highly photolabile compounds. In contrast, the compounds are thermally stable up to temperatures of $200\text{ }^\circ\text{C}$, depending on the substituent attached to the aromatic ring. The photochemistry of these compounds in solution has already been subject to numerous investiga-

tions. As an example we tested a compound with unsubstituted phenyl rings at both ends of the nitrogen chain. In contrast to the investigations in solution [4] which show oscillations in the UV-absorption spectra after irradiation with UV laser pulses we could not observe such behaviour in the IR spectra when compound (III) was irradiated in KBr pellets. During the thermolysis we did not observe intermediate products as well. In both cases the compound seems to release nitrogen and to form volatile products which are not retained in the KBr pellet. The spectra presented in Figure 4 show the results of the thermolysis experiment. The peaks vanish with approximately the same rate without showing significant shifts in position.

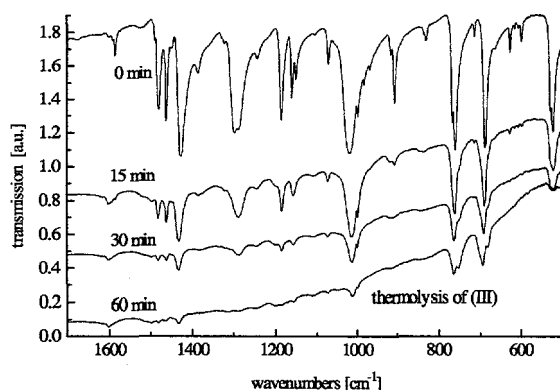
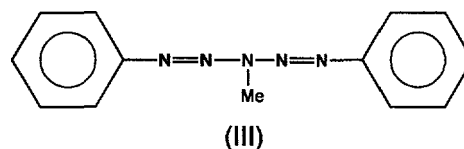


Fig. 4: Thermolysis of (III) in a KBr matrix.

4 CONCLUSIONS AND OUTLOOK

Combination of UV and IR spectroscopy is a useful tool for the investigation of the thermal and photochemical decay of azo group containing compounds. It is shown that the reaction pathway is influenced by the fact whether the compounds are present in the solid state or in solution. Azophosphonate (II) exhibits different reactions paths for thermolysis and photolysis. Our investigations will be continued by a more detailed analysis of the reaction products and a study of the initial reaction steps by time resolved laser spectroscopy.

5 ACKNOWLEDGEMENTS

We thank Prof. O. Nuyken (TU Munich) for a fruitful collaboration, and A. Lang, C. Scherer and A. Baidl for synthesis of the compounds and helpful discussions.

6 REFERENCES

- [1] J. Kritzenberger, D. Franzke, T. Kunz, A. Lang, O. Nuyken, A. Wokaun, to be published.
- [2] C. Scherer, Ph. D. thesis, TU-Munich (1996).
- [3] A. Baidl, Ph. D. thesis, TU-Munich (1996).
- [4] Th. Kunz, Ch. Hahn, A. Wokaun, this vol. p. 41.

MICROSTRUCTURING OF TRIAZENE CONTAINING COPOLYESTER FILMS

Ch. Hahn, Th. Kunz, A. Wokaun

The growing field of microtechnology has an increasing demand for affordable functional materials. Several strategies exist for improving the ablation behaviour of standard polymers. One is the copolymerization of a standard commercial polymer with a specialty polymer, in our case of a polyester and triazene group containing polyester. For comparison of the copolymers with different fractions of triazene groups we have determined the threshold fluences and the effective absorption coefficients. With respect to these ablation parameters, only small differences were found within the set of copolymers investigated. Only with AFM and SEM it was possible to detect that a minimum content of triazene groups is necessary for defined microstructures with sharp edges, whereby a resolution in the sub μm scale has been achieved.

1 INTRODUCTION

Laser ablation is a promising structuring tool in the growing field of microtechnology [1]. Here, the substrate is etched by a simple photochemical mechanism in a single step process, where structuring and development proceed at the same time. This offers the advantage that no subsequent chemical developing steps, such as those in the common resist techniques, are necessary.

From an economical point of view the XeCl* excimer laser is of interest as a irradiation source for ablation experiments. Its use requires polymers with a reasonable absorption at 308 nm, apart from other desirable properties. Polyimide for example is well suited for this application, but other commercial polymers such as PMMA or polycarbonate have no distinctive absorption at 308 nm.

One way to enhance absorption is to dope the material with chromophoric monomers [2]. Another possibility is to design specialty polymers, where a photo-decomposable group is introduced directly into the chain [3]. The advantage is that after irradiation bond breaking will occur and the polymer is fragmented into small parts with no residuals. Regarding economic aspects a blend of the specialty polymer with a commercial polymer is preferable. Then, the obvious question how much of the specialty polymer is necessary for the required microstructuring properties, has to be answered.

In this study we investigated the ablation properties of a copolyester in relation to its triazene content with respect to its application in microstructuring.

2 EXPERIMENTAL

2.1 Setup

The setup for ablation experiments has been described in detail elsewhere [4]. A XeCl* excimer laser (Lambda Physik Compex 205) was used as irradiation source. For determining the etch rate a pinhole mask is demagnified by about 1:10 onto the substrate with a lens system. A matrix of craters is ablated by varying the fluence in one direction and the number of pulses in the other. The ablated depth is determined with a surface profiler (DekTak 8000). For the microstructur-

ing experiments a copper mask is imaged by a reflection objective (Ealing, 1:15) onto the sample surface to avoid lens aberrations. The quality of the obtained structures is investigated by SEM and AFM.

2.2 Material

Polyesters are synthesized by polycondensation of diacyl chlorides and diols. Here the copolyester (Figure 1) was obtained by using a triazene-containing and a common diol. The content of triazene (in percent) is used for identification, e.g. CP50 implies 50 % triazene containing diol is included in the copolyester.

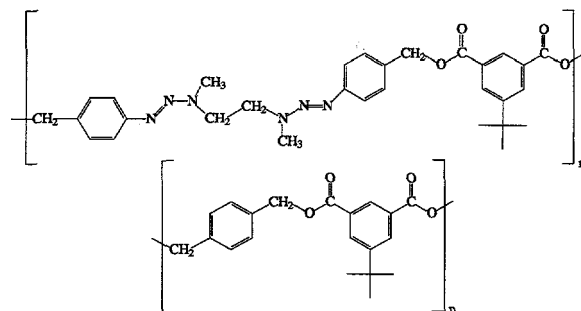


Fig. 1: Chemical structure of the triazene-containing copolyester.

3 RESULTS AND DISCUSSION

The following relationship between etch rate z and fluence F was found experimentally [5]:

$$z = \frac{1}{\alpha_{\text{eff}}} \times \ln\left(\frac{F}{F_0}\right),$$

where F_0 represents the threshold fluence and α_{eff} the effective absorption coefficient. For comparison we determined these characteristic parameters for all copolyester compounds (examples are shown in Table 1).

| | CP0 | CP5 | CP35 | CP90 | CP100 |
|-----------------------|------|------|------|------|-------|
| α_{eff} | 1.16 | 0.95 | 1.48 | 1.52 | 1.50 |
| F_0/Jcm^{-2} | 0.61 | 0.70 | 0.26 | 0.31 | 0.36 |

Table 1

The parameters vary only to a small extent. Even the unmodified polyester CP0 exhibits a reasonable etch rate despite its relatively small absorption coefficient.

Significant differences can only be detected with SEM. The ablated pattern consisted of channels separated by narrow (ca. $2.5\ \mu\text{m}$) and broader (ca. $6.5\ \mu\text{m}$) ridges. In the pure polyester, only the broad ridges are resolved, but even there spilled material and thermal damage prevents sharp contours (Figure 2). Single-pulse experiments resulted in a completely unstructured surface since, due to incubation effects, only foamy structures developed without ablation.

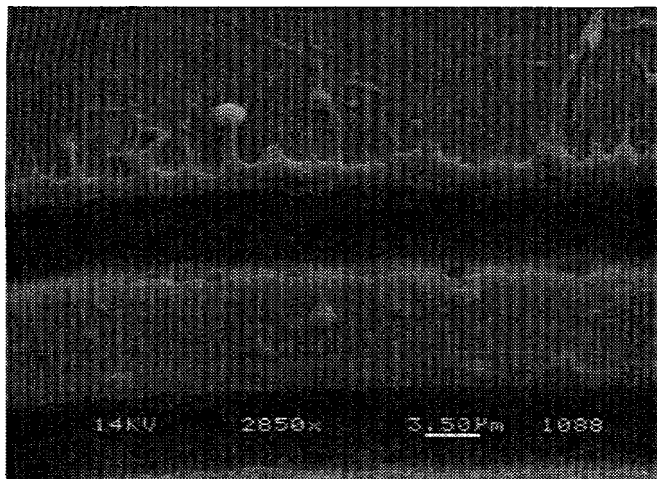


Fig. 2: SEM micrograph of structured CP0.

From a minimum content of $> 35\%$ of triazene-containing diol, sharp microstructures can be obtained. No residual material is left and no thermal damage occurs. The cleanliness of the contours may be judged from Figure 3. In the lower left corner the narrow ridges can be discerned.

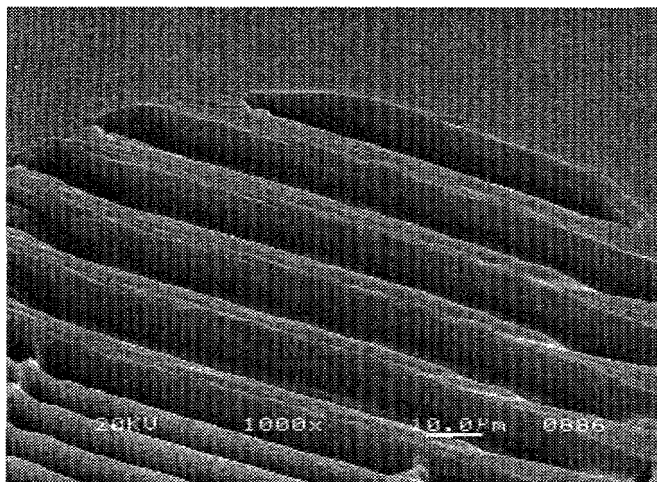


Fig. 3: SEM micrograph of structured CP75.

The quality of the structures was also analyzed by AFM. The micrographs of single-pulse experiments show steep walls and sharp edges (Figure 4). A resolution of better than one μm appears to be possible with this material.

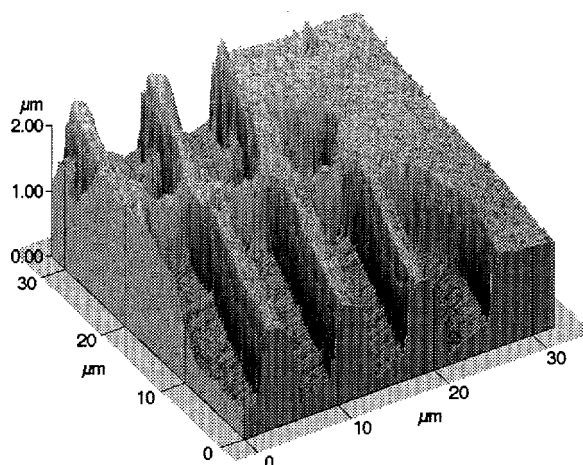


Fig. 4: AFM micrograph of structured CP50.

From a triazene content of $\geq 90\%$ the SEM micrographs exhibited a reduced quality of the structures as a consequence of the development of bubbles which are probably due to the high amount of released nitrogen.

4 CONCLUSIONS

In summary, this study has determined the optimum composition of a copolyester, containing a triazeno group, with respect to applications in microstructuring.

We have found that a minimum content of $\approx 35\%$ triazene-containing diol is necessary for patterning with high resolution of better than one μm , although the etch rates itself are not affected very much by the composition. At a very high triazene content of $\geq 90\%$, bubbles impair the quality of the obtained structures.

5 ACKNOWLEDGEMENTS

Sincere thanks are due to U. Dahn and Prof. O. Nuyken, TU Munich, for stimulating discussions and for providing the polymer samples.

6 REFERENCES

- [1] J. Miller (Ed.), "Laser Ablation", Springer Series in Materials Science 28, Springer Verlag, Berlin (1994).
- [2] Th. Lippert, A. Wokaun, J. Stebani, O. Nuyken, J. Ihlemann, *Angew. Makromol. Chem.* 213, pp. 127-155, (1993).
- [3] Th. Lippert, A. Wokaun, J. Stebani, O. Nuyken, J. Ihlemann, *Angew. Makromol. Chem.* 206, pp. 97-110, (1993).
- [4] Th. Kunz, D. Franzke, A. Wokaun, *PSI Annual Report / Annex V*, pp. 43-45 (1995).
- [5] R. Srinivasan, B. Braren, *Chem. Rev.* 89, pp. 1303-1316, (1989).

PHOTOCHEMICALLY INDUCED OSCILLATIONS OF AROMATIC PENTAZADIENES

Th. Kunz, Ch. Hahn, A. Wokaun

Aromatic pentazadienes are used to enhance the laser induced ablation behaviour of standard polymers with low absorption in the UV. Therefore the photochemistry of substituted 1,5-diaryl-3-alkyl-1,4-pentazadiene monomers was studied with a pulsed excimer laser as irradiation source. The net photochemical reaction proceeds in an overall one-step pathway $A \rightarrow B$. Quantum yields for the laser decomposition were determined to be up to 10%. An oscillating behaviour of the absorption was found during the dark period following the irradiation. The temperature dependence of this dark reaction has been studied. An attempt to model this behaviour in terms of a non-linear coupling between heat released, heat transfer, and reaction kinetics will be described.

1 INTRODUCTION

Due to their photosensitive properties and their thermal stability azo compounds have a wide spread field of interests in research and technology. Compounds containing azo groups are used as photosensitive material in photolithography and laser ablation. These compounds can be used, e.g., in non-silver photographic processes.

Pentazadienes contain, in particular, five nitrogen atoms in a row. Due to the concomitant lability of the molecule, this class of compounds appears to be predestined for applications in photochemical experiments. The first representative of aromatic 1,4-pentazadienes was synthesized 1866 by P.Griess in the reaction of diazotized aniline with ammonia. Since then a wide variety of aromatic 1,4-pentazadienes model compounds as well as polymers have been synthesized to investigate the influence of the substituents on the photolability [1].

Since some hints on a dark reaction were found in the cw-photolysis, but could not be elucidated with the cw-setup, it was decided to use a pulsed laser for excitation. The pulse energy of the XeCl* excimer laser operating at 308 nm with a length of only about 30 ns provides sufficient photochemical turnover for a comprehensive investigation of the time-dependent dark reaction.

2 EXPERIMENTAL

The pentazadiene monomers have been synthesized by the reaction of aromatic diazonium salts and primary amines. The procedure has been described in detail elsewhere [2]. The structural formula is shown in Figure 1.

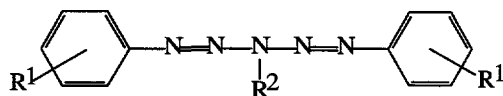


Fig. 1: Structural formula of pentazadienes.

Solutions of the pentazadienes ($R^1 = \text{OMe, CN, Me, Cl, COOEt, H, R}^2 = \text{Me}$) in THF were irradiated in quartz cuvettes. The concentrations were adjusted in the 10^{-5} M range such that UV-Vis spectra could be recorded with an optical density of 1 - 1.5. The photoly-

sis experiments were carried out with a XeCl* excimer laser (Lambda Physik, model Compex 205) as radiation source. The pulse energy delivered to the sample was adjusted to 180 mJ. The UV-Vis spectra were recorded with a diode-array spectrometer (Polytec, model XDAP) a) immediately, b) 25 sec and c) 50 sec after the laser pulse. Temperature controlled cuvettes were used for the kinetic experiments. To prevent condensation on the cuvettes at low temperatures the windows were flushed with N_2 gas during the experiments.

3 RESULTS

3.1 Photoreaction

Samples of the monomer compounds in different solvents were irradiated with the UV-pulses and the course of the decomposition was monitored by UV-Vis spectroscopy. According to Lambert-Beer's law the degree of decomposition was correlated with the absorption of the maximum of the $\pi \rightarrow \pi^*$ transition. The influence of the substituents R^1 on the photochemistry of the chromophores was studied. A typical course of such a photolysis is shown in Figure 2. The almost complete decay of absorption for the strong $\pi \rightarrow \pi^*$ transition at 387 nm within 7 pulses at a pulse energy of 187 mJ indicates the photochemical decomposition of the chromophore.

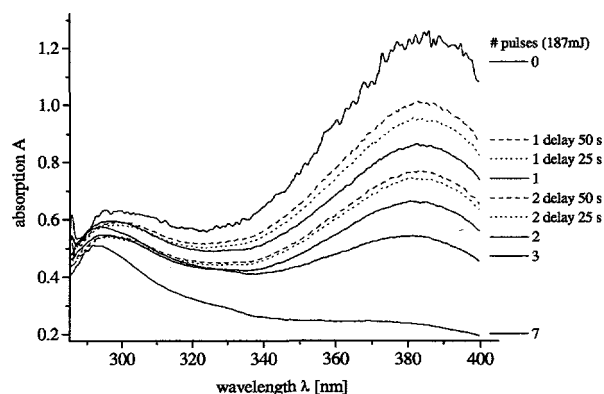


Fig. 2: Course of the photolysis monitored by UV spectroscopy ($R^1 = \text{OMe, R}^2 = \text{Me}$).

The quantum yield for these compounds were determined to range within 6% to 10% depending on the substituent R^1 .

According to the method developed by Mauser et al. [3] absorption-difference diagrams were used for the characterization of the kinetics. The decrease of the absorption at several wavelength $\Delta A(n)$ was plotted against the decrease of the absorption maximum $\Delta A_{\max}(n)$, where n is the number of pulses delivered. A linear dependence with a zero intercept was found, which indicates an uniform first-order reaction $A \rightarrow B$ for all compounds.

3.2 Dark reaction

The chemical reactions associated with the decomposition continue over time much longer than the pulse length. Therefore the spectrometer was set to record the absorption at several wavelengths over a time of 1000 seconds. Ten seconds after starting the measurement the first laser pulse was delivered to the solution (defining $t=t_0$), with the next two pulses delivered with a delay of 400 seconds each. Directly after the pulse the absorption decreases within one data point ($t < 1$ sec.) and increases again to a level lower than the original value. The time for this regeneration is very short compared to the time of the whole dark reaction (≈ 300 s). Afterwards a pronounced but damped oscillation of the absorption band was observed for all investigated compounds. Finally the absorption settles to a constant value. Up to three periods could be observed during a time of five minutes. In Figure 3 the time dependent behaviour of the absorption at λ_{\max} of a model compound ($R^1 = \text{OMe}$) in THF as solvent is shown.

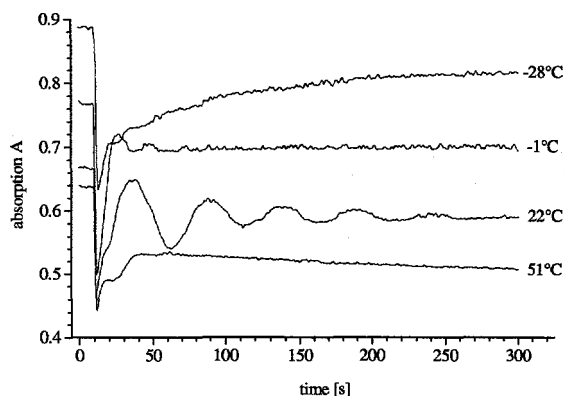


Fig. 3: Oscillatory absorption of the model compound after irradiation with one pulse.

These experiments were carried out at different temperatures. In a temperature region from 8°C to 45°C distinctive oscillations are found. After the decay of the oscillation, a further pulse was delivered to the solution. The experimental data (Figure 4) recorded at three different temperatures (8°C, 24°C, 45°C) could be well represented by the model of a damped harmonic oscillator:

$$A(t) = \Delta A^* \sin(\omega^*(t - t_0) + \varphi) \exp(-k^*(t - t_0)) + A_0$$

With the results of the fits it was found that the amplitude ΔA of the absorption decreases with the temperature and with the degree of decomposition. The oscillation frequency ω increases with the temperature and is independent of the degree of decomposition.

The damping constant k exhibits a minimum around 24°C. This is also evident in Figure 3, since the oscillation phenomenon disappears above and below the optimum temperature (22°).

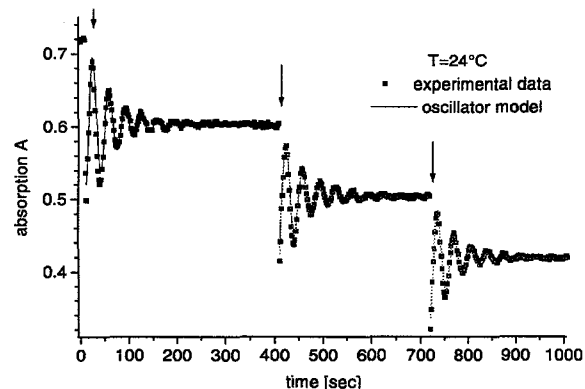
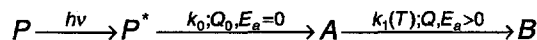


Fig. 4: Fit of the experimental data to the model of a damped harmonic oscillator.

These oscillations may be explained within a thermodynamical model [4] of coupled first-order chemical reactions. The photoproduct P^* is converted into a final product B through an intermediate A . While the first rate constant k_0 is assumed temperature independent, the second rate constant k_1 depends very strongly on the temperature. Therefore this reaction is accelerated by the developed heat of reaction.



In a simulation we were able to demonstrate the influence of the temperature on this system, but failed to correlate the fit parameters with experimental quantities characterising the thermal system (solution, thermostat) under investigation.

4 CONCLUSIONS

The data presented provide insight into the photochemistry of pentazadienes. The overall photoreaction follows a first-order kinetics, while the dark reaction is determined by a non-linear coupling between heat released, heat transfer, and reaction kinetics. The system is very temperature sensitive. Further simulations of these chemical instabilities are in progress.

5 ACKNOWLEDGEMENTS

Sincere thanks are due to A. Baidl and O. Nuyken, TU Munich, for stimulating discussions and for providing the samples.

6 REFERENCES

- [1] Th. Kunz, Ch. Hahn, A. Wokaun, to be published.
- [2] A. Baidl, A. Lang, O. Nuyken, *Macromol. Chem. Phys.*, in press.
- [3] H. Mauser, *Experimentelle Methoden der Physik und Chemie, Band I: Formale Kinetik* 310 (1974).
- [4] P. Gray, S.K. Scott, *Chemical Oscillations and Instabilities*, Clarendon Press, Oxford (1990).

Electrochemical Energy Storage and Conversion

BIPOLAR ZINC/OXYGEN BATTERY DEVELOPMENT

S. Müller, C. Schlatter (Swiss Federal Institute of Technology, Lausanne, Switzerland)

A bipolar electrically rechargeable Zn/O₂ battery has been developed. Reticulated copper foam served as substrate for the zinc deposit on the anodic side, and La_{0.6}Ca_{0.4}CoO₃-catalyzed bifunctional oxygen electrodes were used on the cathodic side of the cells. The 100 cm² unit cell had an open circuit voltage of 1.4 V (O₂) in moderately alkaline electrolyte. The open circuit voltage and the peak power measured for a stack containing seven cells were ca. 10 V and 90 W, respectively. The current-potential behaviour was determined as a function of the number of bipolar cells, and the maximum discharge capacity was determined at different discharge rates.

1 INTRODUCTION

A rechargeable battery providing both high specific energy and high specific power would be an attractive power source candidate for many applications. The Zn/air battery system stands out on its high energy density, good environmental compatibility, low cost of active materials, and wide operating temperature range. Recently, we developed electrically rechargeable monopolar zinc/oxygen cells showing a service life of ca. 450 cycles. For these cells pasted Zn-electrodes and La_{0.6}Ca_{0.4}CoO₃-catalyzed bifunctional oxygen electrodes were developed [1].

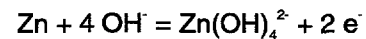
Here we will present the concept and power output of our rechargeable bipolar battery. A compact bipolar cell arrangement is interesting in order to diminish the ohmic resistance of the module and to obtain high specific power. In the bipolar system all cells are internally connected in series and the output is high-voltage/low-current, which is desirable for electric-vehicle (EV) applications.

Instead of using pasted Zn-electrodes, a highly porous and conductive copper foam material (Sorapec, France) was used as the matrix for the zinc deposit. While for the first formation of metallic Zn on the foam highly alkaline electrolyte was pumped through the porous zinc electrode, a stationary, moderately alkaline electrolyte (chemically saturated with ZnO) was used for the electrically rechargeable operating mode.

2 EXPERIMENTAL

The components of a single cell and of the bipolar stack are depicted in Figure 1. The main components of the bipolar cell were the zinc-plated reticulated copper foam anode (1 and 5), the La_{0.6}Ca_{0.4}CoO₃-catalyzed bifunctional oxygen diffusion electrode (4), the PVC frames (2) for sealing the cells, and the cathode supports needed to constitute the zinc/oxygen cells in the bipolar arrangement (1 and 5). After the first charge (8 Ah for the 100 cm² zinc electrode), the electrolyte was replaced by a 20 wt% KOH solution presaturated with ZnO. Cycle life tests as well as current-potential measurements were carried out with stationary moderately alkaline electrolyte in which the fol-

lowing two consecutive reactions take place at the zinc electrode:



Cycling was performed at 10 mA/cm² charging and 20 mA/cm² discharging currents, respectively. The cycled capacity was 5 Ah for the 100 cm² zinc electrode.

The current-potential curves were measured galvanostatically. For each chosen current the potential of the battery was measured after a cell operating time of 30 s. The power of the stack was calculated from measured current-voltage curves.

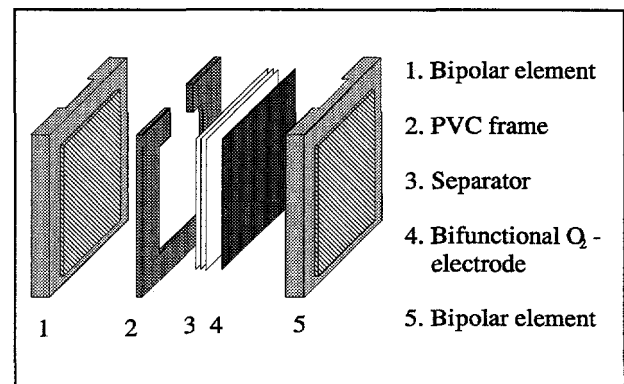


Fig. 1: Exploded view of the stack components. Geometric surface area: 100 cm².

3 RESULTS AND DISCUSSIONS

The power curves for bipolar stacks containing one to seven cells are plotted in Figure 2. These measurements were performed after the first charge and for 100%-charged cells.

The peak power of a single cell is 13 W (1300 Wm⁻²) and was obtained at a current density of 2000 Am⁻². The excellent conductivity provided by homogeneously distributed zinc in the foam electrode and its highly porous structure (porosity of ca. 0.8) are responsible for the high current density and the high peak power of the battery.

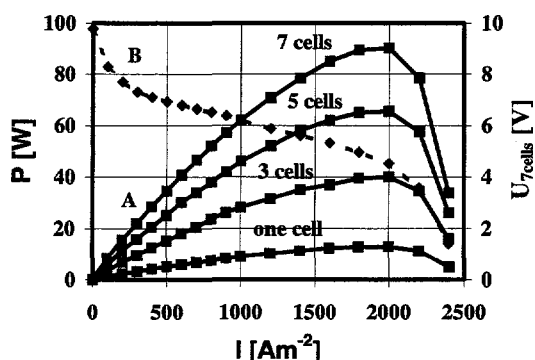


Fig. 2: Power curves (A) for bipolar stacks containing 1 to 7 cells and a plot of voltage vs. current density for the bipolar stack containing 7 cells (B).

Due to the absence of shunt currents and the use of bifunctional electrodes with identical electrochemical behaviour, the experimentally measured power of the batteries was very close to the expected value ($P_{\text{bipolar stack}} = N \times P_{\text{one cell}}$). For the bipolar stack with seven cells a peak power of 90 W could be demonstrated. Based on the mass of the cell components a maximum specific power of ca. 90 W/kg was calculated. The polarization curve measured for the bipolar stack containing 7 cells shows a battery-voltage decay at current densities higher than 200 mA/cm². This voltage decay can be attributed to oxygen diffusion hindrance in the gas-diffusion electrode.

Figure 3 demonstrates the availability of high discharge rates from the bipolar stack. The discharge experiment was performed with one cell and with the stack of seven cells at a current density of 1000 Am⁻². The power output was constant at ca. 9 W for one cell and 63 W for the stack until 60 % of the nominal capacity (8 Ah) of the battery was discharged. The electrolyte temperature increased from 25 °C to 42.5 °C during the discharge experiment.

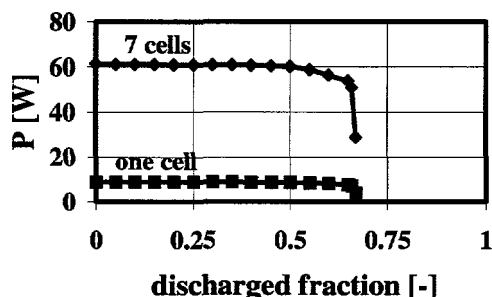


Fig. 3: Zinc/oxygen power and available capacity measured for a single cell and for the bipolar stack at a discharge current density of 1000 Am⁻².

The cycle life performance was studied for a single cell. Figure 4 presents the charge and discharge potential vs. time plots obtained during the first cycle, the 14th cycle and during the first cycle after regeneration of the zinc-foam electrode.

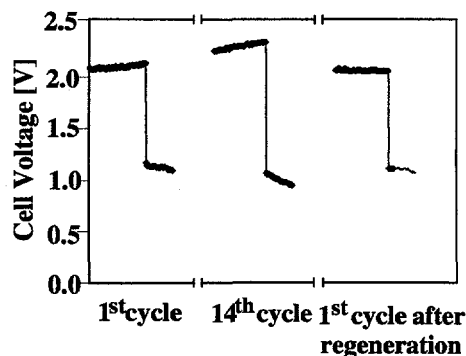


Fig. 4: Charge and discharge voltages during the first cycle, the 14th cycle and after regeneration of the foam electrode. Charge and discharge current densities are 100 and 200 Am⁻², respectively.

For the first cycle, the voltages during charge and discharge were 2.1 and 1.1 V, respectively. After 14 cycles the overvoltages increased for both reactions by about 100 mV. The higher polarization of the cell developing with increasing cycle numbers is due to an increase in polarization of the zinc-foam electrode. Visual observation showed a dense, compact zinc area at the bottom of the zinc-foam electrode. After regeneration of the three-dimensional electrode, the voltages were identical with the initial values.

4 CONCLUSIONS

The combination of metallic foam as the support material for the zinc deposit in the Zn electrode with La_{0.6}Ca_{0.4}CoO₃-catalyzed bifunctional oxygen electrodes results in a rechargeable zinc/oxygen battery showing peak power densities for a single cell of 130 mWcm⁻². With a battery stack containing seven cells (100 cm²) a peak power of 90 W could be demonstrated. A specific power of ca. 90 W/kg was calculated for peak power conditions. Approximately 60 % of the nominal capacity (8 Ah) could be discharged at a constant stack power of ca. 60 W.

Redistribution and dissolution of the zinc induced by natural convection resulted in a limited cycle life. However, at periodic service intervals the zinc electrode can be regenerated to obtain the original performance of the battery.

5 ACKNOWLEDGMENTS

The authors acknowledge the financial support of this work provided by the Swiss Federal Office of Energy. We also thank Mrs. G. Masanz (PSI) for preparing the bifunctional O₂-diffusion-electrodes.

6 REFERENCES

- [1] S. Müller, F. Holzer, O. Haas, C. Schlatter, Ch. Cominellis, *The Electrochem. Soc. Proc.* Vol. 95-14, Pennington, NJ (1996).

PROGRESS TOWARDS A 20 AH/12 V ZINC/AIR - BATTERY

F. Holzer, S. Müller, O. Haas

Electrode areas, for the bifunctional O_2 -electrodes and the pasted Zn-electrodes, have been successfully scaled up from 25 cm² up to 250 cm². A filter press type cell was used to measure the cycle life of larger electrodes (100 cm²). Up to now, more than 100 charge-discharge cycles (900 hours) with these scaled up Zn/ O_2 -cells could be demonstrated.

Electrically rechargeable Zn/air-batteries are being considered for both electric vehicle and portable electronic device applications. The high theoretical (1150 Wh/kg) as well as practical specific energy (60-150 Wh/kg) are major advantages of the secondary zinc/oxygen battery. The low cost and low toxicity of the materials involved are also important factors.

The preparation of the 25 cm² pasted Zn-electrodes (filter-table) and the $La_{0.6}Ca_{0.4}CoO_3$ -activated bifunctional oxygen electrodes (rolling-technic) has been described elsewhere [1, 2].

Increasing the cellulose amount and optimizing the fiber length of the cellulose (Cellulose Attisholz AG, Attisholz, CH), in the 25 cm² pasted Zn-electrode, has improved considerably the cycle life and peak power behaviour of the Zn/ O_2 -cells. The preparation of larger Zn-electrodes on a pasting-device (used to manufacture the electrodes for the lead-acid-battery; Electrona S.A., Boudry, CH), required significant changes in the preparation process. The rheological properties of the ZnO-paste were optimized to the industrial pasting-machine. This optimized paste functioned well in preparing Zn-electrodes by hand or by machine.

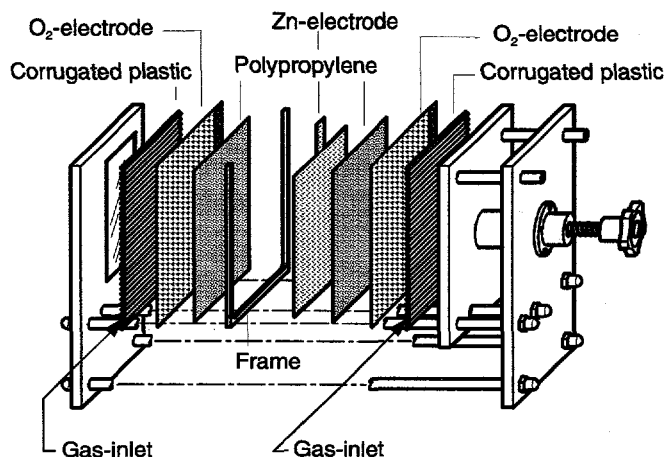


Fig. 1: Exploded view of a single Zn/air-cell. The pasted Zn-electrode is held between two bifunctional O_2 -electrodes.

A filter press type cell (constructed in collaboration with Larag AG, Wil, CH) as depicted in Figure 1 was used for testing the larger electrodes. The pasted Zn-electrode, which is wrapped in three layers of Celgard-separator, is sandwiched between two bifunctional oxygen electrodes (catalyst: $La_{0.6}Ca_{0.4}CoO_3$). The corrugated plastic is used as gas distributor. An advan-

tage of the filter press design is the easy modular build up of the cells.

In a next step, the life time of a single cell arrangement with electrode-areas of 100 cm² was tested. The electrolyte consisted of 15 % KOH + 1.5 M KF and was presaturated with ZnO. The zinc electrode had a nominal capacity of 10 Ah. 2/3 of the nominal capacity could be cycled at low charge-discharge rates, and 1/3 of the nominal capacity was cycled at ~6 h charge- and ~3 h discharge times. Figure 2 shows the cell voltage of the first 100 cycles.

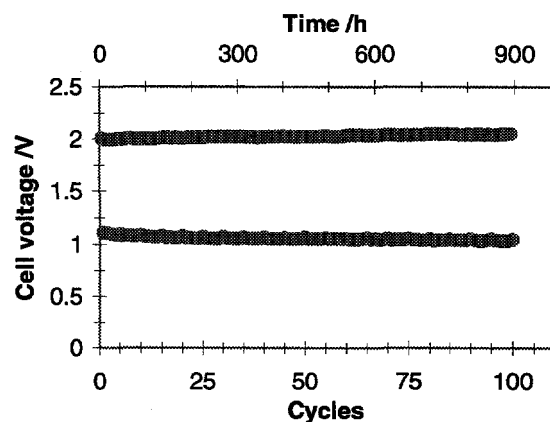


Fig. 2: Charge- and discharge voltage of the first 100 cycles (900 hours) of a Zn/ O_2 -cell with 100 cm² electrode area.

The next step in this project will be the demonstration of a 12 V / 20 Ah Zn/air-battery. By connecting 10 cells in series (200 cm² electrodes, 20 Ah nominal capacity), a battery voltage of 12 V can be achieved.

ACKNOWLEDGMENTS

The financial support of the Swiss Federal Office of Energy and PSEL (Projekt- und Studienfonds der Elektrizitätswirtschaft) is gratefully acknowledged. The authors thank Mrs. G. Masanz and Mr. J.-C. Sauter for excellent technical support.

REFERENCES

- [1] S. Müller, K. Striebel, O. Haas, *Electrochim. Acta* **39**, 1661 (1994).
- [2] S. Müller, F. Holzer, C. Schlatter, C. Cominellis, O. Haas, *Electrochem. Soc. Proceedings 95-14*, 135 (1996).

POROUS GRAPHITE ELECTRODES FOR RECHARGEABLE ION-TRANSFER BATTERIES

P. Novák, W. Scheifele, O. Haas

The influence of preparation pressure and pore-forming additives on the properties of graphite-based, Li^+ -intercalating electrodes for ion-transfer batteries have been investigated. The electrochemical performance of graphite electrodes could be improved by adjusting the porosity. Specific charge of $>300 \text{ Ah/kg}$ (with respect to the graphite mass) could be achieved.

1 INTRODUCTION

Rechargeable lithium ion-transfer batteries are among the most promising new battery systems. Graphite-based negative electrodes (LiC_6) combine high specific charge with favorable cell safety and cycling behavior. Their moderate rate capability, however, as well as their strong tendency to co-intercalate solvent molecules which leads to exfoliation of the graphene layers still present some challenges [1].

Enlargement of the electrode/electrolyte interfacial area is one way to improve the electrode rate capability. The microscopic interfacial area depends strongly on the porosity and the pore distribution of the electrode. Our principal aim in this work was to elaborate simple but effective methods of tailoring the electrode porosity, allowing the preparation of rather thick electrodes ($\sim 500 \mu\text{m}$) with acceptable current densities. For identical cell hardware, thicker electrodes provide higher specific energies.

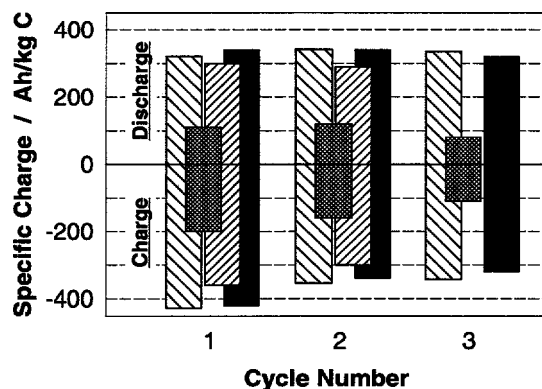


Fig. 1: Specific charge of graphite electrodes: (hatched) without an additive, preparation pressure 0.2 t/cm^2 ; (dotted) without an additive, preparation pressure 3.8 t/cm^2 ; (diagonal lines) porous, with 50 % LiCl added, preparation pressure 3.8 t/cm^2 , H_2O -extracted; (solid black) porous, with 50 % NH_4HCO_3 added, preparation pressure 4 t/cm^2 , thermally decomposed.

2 EXPERIMENTAL

Approximately $500 \mu\text{m}$ thick electrodes were prepared from graphite TIMREX KS 44 and either poly(vinylidene fluoride) (PVDF) or poly(tetrafluoroethylene) (PTFE) binder as described in [2]. In one case, a blend of graphite and binder was mixed with NH_4HCO_3 , pressed, and finally heated in vacuum. Porous electrodes resulted from the complete de-

composition of NH_4HCO_3 . Alternatively, porous electrodes were prepared by mixing the graphite/binder blend with LiCl , pressing the mixture, and extracting the LiCl with water.

Electrochemical data were gained in model coin cells using an electrolyte consisting of $1 \text{ M LiN}(\text{SO}_2\text{CF}_3)_2$ in an ethylene carbonate/dimethyl carbonate mixture.

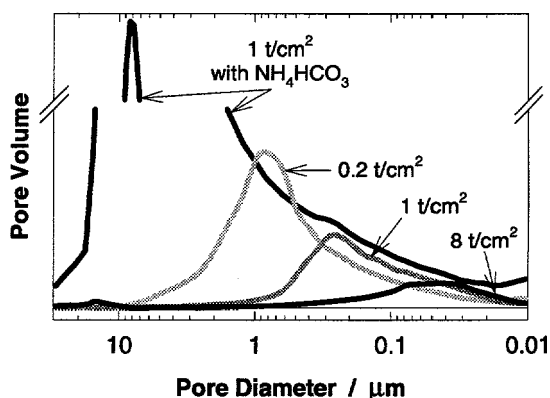


Fig. 2: Pore size distributions of a porous graphite electrode prepared with 50 % NH_4HCO_3 (thermally decomposed) and graphite electrodes prepared at various preparation pressures without pore-forming additives.

3 ELECTRODES WITHOUT ADDITIVES

The electrochemical performance of standard graphite electrodes prepared without additives depends on the pressure used in their preparation. Increased preparation pressure reduces the specific charge significantly (Figure 1) and increases the electrode polarization. The electrochemical behavior correlates well with porosimetry results. The porosity and the median pore diameter are reduced with increasing preparation pressure (Figure 2).

From the perspective of reversible specific charge and electrode rate capability, insufficient porosity and low median pore diameter (due to high preparation pressure) are detrimental to the electrode performance. We attribute this behavior to insufficient wetting of the bulk electrode by the electrolyte. To achieve an optimum porosity the electrode preparation would have to be optimized at very low preparation pressures ($\leq 0.2 \text{ t/cm}^2$). This optimization results in electrodes with acceptable specific charges (Figure 1) but inadequate mechanical stability for practical applications.

4 POROUS ELECTRODES

The porosity of graphite electrodes can be controlled by dispersing pore-forming additives (LiCl or NH_4HCO_3) in the electrode mass during the preparation process. An advantage of this method is that the electrode porosity can be varied almost independent of the preparation pressure.

Electrodes prepared using 50 wt.% LiCl had a porosity of ~60 vol.% with a pore diameter distribution of 2 to 8 μm . As intended, the charge/discharge performance of porous graphite electrodes improved dramatically in comparison to compact ones prepared at high pressures (Figure 1). An alternative pore-forming method using 50 wt.% of NH_4HCO_3 provided similar results, i.e. a porosity of ~60 vol.% and a pore diameter distribution of 1 to 10 μm (Figure 2). The pore-forming method using NH_4HCO_3 was superior, however, because it yielded slightly higher specific charges and was simpler to use.

The effect of varying amounts of NH_4HCO_3 and of different binder materials in the electrode mass has been examined in detail. Porosities ranging typically from ~35 vol.% to ~70 vol.% have been reached. The pore diameter distribution was affected to a small extent by the amount of NH_4HCO_3 , and the type of binder material showed no critical influence also on the porosity.

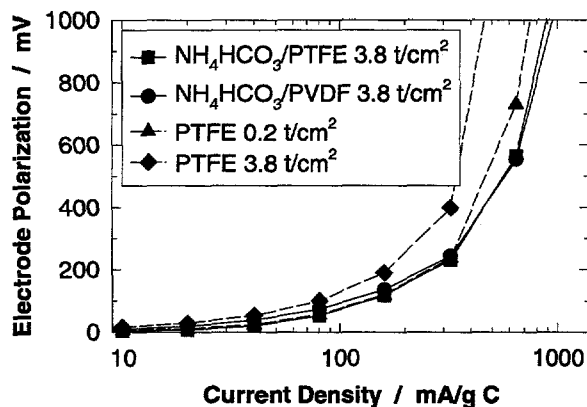


Fig. 3: Polarization curves of graphite electrodes prepared at various preparation pressures with and without NH_4HCO_3 (binders PTFE or PVDF).

Mechanically stable 500 μm thick electrodes have been developed through optimization of the electrode composition and the conditions of electrode preparation. Their porosity and, therefore, their electrochemical properties are almost insensitive to the applied preparation pressure. The two polarization curves for electrodes prepared without pore-forming additives shown in Figure 3 confirm the beneficial effect of the pore-forming additives. Slightly better specific charges were measured when PTFE was used as a binder instead of PVDF (Figure 4). We suspect that in the case of PVDF, which was applied from a solution, a part of the graphite surface is covered and therefore blocked by a thin PVDF film. In contrast

PTFE has a fibrous morphology in the electrode and therefore cannot block the surface.

During the first seven charge/discharge cycles on our optimized porous graphite electrodes shown in Figure 4, a reproducible (around $\pm 5\%$) and stable specific charge of ~340 Ah/kg (with respect to the graphite mass) was observed even at current densities of up to 1.5 mA/cm^2 (ca. 50 $\text{mA}/\text{g C}$). Moreover, the irreversible charge loss in the first cycle was moderate, typically ~20% of the reversible charge. Up to 30 cycles at 1.5 mA/cm^2 have been carried out on a number of electrodes to confirm that the specific charge of >300 Ah/kg is stable.

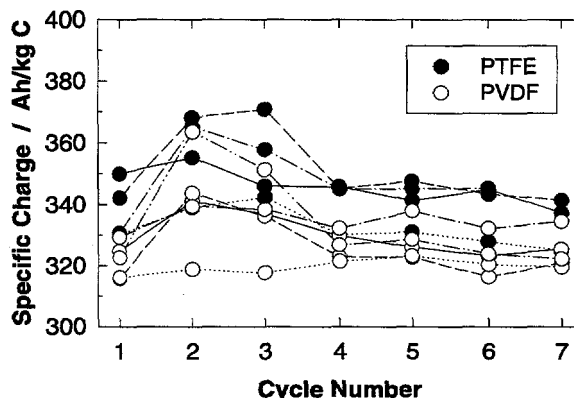


Fig. 4: Reproducibility of specific charge for Li^+ deintercalation (discharge, in Ah/kg with respect to the graphite mass) of porous graphite electrodes prepared by using the binders PTFE or PVDF; cycling with ca. 1.5 mA/cm^2 (ca. C/7) between +0.005 and +1.8 V vs. Li/Li^+ .

5 CONCLUSION

LiCl and NH_4HCO_3 pore-forming additives facilitated custom tailoring of the porosity of graphite electrodes. The preparation of mechanically stable electrodes through high preparation pressures was possible, and the electrochemical performance of graphite electrodes was improved.

6 ACKNOWLEDGMENTS

Support from TIMCAL AG, Sins, and the Swiss Federal Office of Energy, Bern, as well as the collaboration of Dr. M. Winter are gratefully acknowledged.

7 REFERENCES

- [1] M. Winter, J.O. Besenhard, P. Novák, "Deckschichten auf LiC_6 -Anoden in wiederaufladbaren Li-Zellen", GDCh-Monographie 3, pp. 438-446, (1996).
- [2] P. Novák, W. Scheifele, M. Winter, O. Haas, "Graphite Electrodes with Tailored Porosity for Rechargeable Ion-Transfer Batteries", J. Power Sources, in press (1997).

USE OF AB INITIO QUANTUM CHEMICAL METHODS IN BATTERY TECHNOLOGY

E. Deiss

Ab initio quantum chemistry can nowadays predict physical and chemical properties of molecules and solids. An attempt should be made to use this tool more widely for predicting technologically favorable materials. To demonstrate the use of ab initio quantum chemistry in battery technology, the theoretical energy density (energy per volume of active electrode material) and specific energy (energy per mass of active electrode material) of a rechargeable lithium-ion battery consisting of a graphite electrode and a nickel oxide electrode has been calculated with this method.

1 INTRODUCTION

With ab initio quantum chemical methods physico-chemical properties of molecules and solids can be calculated. Ab initio means that no further input is needed except the chemical composition. The calculation is based on the solution of the Schroedinger equation. The mainly used numerical method to solve this equation is the Density Functional Theory (DFT) based on the work of Hohenberg and Kohn [1] who proved that the total energy of a system is a unique functional of the electron density. As a consequence of this fact, Kohn and Sham [2] could divide the Schroedinger equation into a set of self consistent one-electron equations which can be solved iteratively. An attempt should be made to use this tool for predicting technologically favorable new materials. To demonstrate the use of ab initio quantum chemistry in battery technology, the theoretical energy density and specific energy based on the active electrode material of a rechargeable lithium-ion battery will be calculated and compared with measured data.

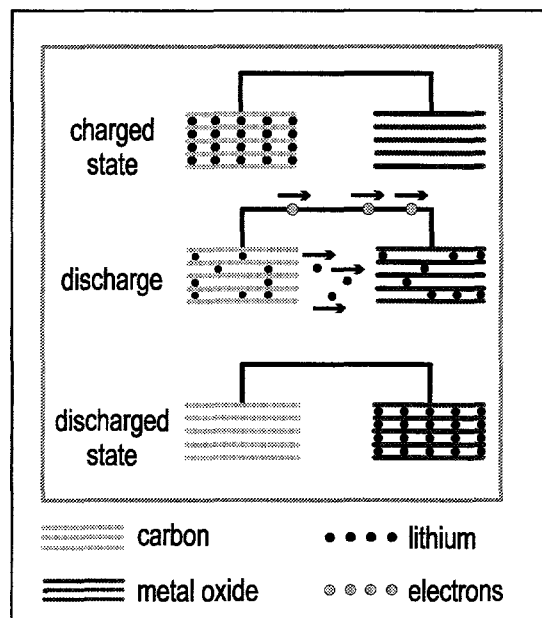


Fig. 1: Schematic representation of a lithium-ion battery.

The discharge of such a battery (Figure 1) is achieved by a lithium transfer from a negative anodic electrode (e.g. coke or graphite) to a positive cathodic electrode (e.g. nickel-, cobalt or manganese oxide). Further improvements of these commercially available batteries are now focused on the environmental compatibility, the energy and power density, the specific energy and power, the cycling behavior and the cost.

2 CALCULATION AND RESULTS

The graphite/ NiO_2 battery to be calculated consists in the charged state of a LiC_6 and a NiO_2 electrode and the following reaction takes place during discharge:



The energy density $E^{d,T}$ and specific energy $E^{s,T}$ of the battery reaction depend on the Gibbs energy change ΔG^T between product and educt of the reaction above as follows:

$$\Delta E^{d,T} = -\Delta G^T / V \quad (2)$$

$$\Delta E^{s,T} = -\Delta G^T / m \quad (3)$$

V denotes the volume and m the mass of the active material. To obtain the energy density and specific energy we have to search for ΔG^T and V , whereas m is obtained from tabulated data. If we neglect any temperature effects then ΔG^T is equal to the zero temperature change of Gibbs energy and can be expressed in terms of the total energies E_n^{tot} of the species n involved in the reaction as follows:

$$\Delta G^{T=0} = E_{\text{LiNiO}_2}^{\text{tot}} + 6E_{\text{C}}^{\text{tot}} - E_{\text{LiC}_6}^{\text{tot}} - E_{\text{NiO}_2}^{\text{tot}} \quad (4)$$

E_n^{tot} result from the formation of the electrode material from the separated electrons and atomic nuclei. To calculate these energies with their associated structures the WIEN95 [3] code was used. The structures have been calculated by volume optimization of the crystallographic data, as a global energy minimization by a variation over all possible structures would be

prohibitive. $E^{d,T=0}$ and $E^{s,T=0}$ are then calculated according to eq. (2) and (3) and are listed in Table 1.

To estimate the temperature dependence of the energy density and the specific energy, the room temperature change in vibrational energy $\Delta E^{vib,T=300}$ and in entropy $\Delta S^{T=300}$ must be included as follows:

$$\Delta G^{T=300} = \Delta G^{T=0} + \Delta E^{vib,T=300} - T \cdot \Delta S^{T=300} \quad (5)$$

Since the structures remain almost unchanged during intercalation, we assumed that the entropy term $\Delta S^{T=300}$ can be neglected, which could also be verified experimentally [4]. The vibrational energy represents the energy absorbed by vibration. This term was calculated by a harmonic approximation using the Amsterdam Density Functional (ADF) code [5,6]. Table 1 show the predicted room temperature values of $E^{d,T}$ and $E^{s,T}$.

3 DISCUSSION

From inspection of Table 1 we ascertain a deviation of calculated from measured values of 14.3 % for the energy density and 14.7 % for the specific energy, if temperature effects are not considered. If temperature effects are included in the calculation, the corresponding deviations are 13.5 % and 13.8 % resp. Accurate measured data are difficult to obtain. We think that an error of at least 10 % of the measured values derived from discharge curves [7] is reasonable. Within this band of uncertainty limits we consider our method as valid for predicting these energies.

Temperature effects play a minor role in our calculations as can be seen in Table 1. Inclusion of the temperature effect enhances the energy density and the specific energy by only 1 %.

Our results demonstrate that it is possible to predict technologically interesting materials with ab initio methods, which unlike to semiempirical methods are free of adjustable parameters. This will encourage us to calculate other essential parameters as electric conductivities or diffusion coefficients of intercalation electrodes with ab initio methods. The rather large amount of computing time needed for non empirical ab initio calculations compared to semiempirical methods is less and less a problem with the rapidly growing of computer power today.

| | | calc. | exp. |
|---------------|---------|-------|------|
| $E^{d,T=0}$ | [Wh/L] | 1538 | |
| $E^{d,T=300}$ | [Wh/L] | 1553 | 1795 |
| $E^{s,T=0}$ | [Wh/kg] | 481 | |
| $E^{s,T=300}$ | [Wh/kg] | 486 | 564 |

Table 1: Calculated and measured energy densities $E^{d,T}$ and specific energies $E^{s,T}$ for a discharge of 1 mol of Li as described by eq. (1)

4 CONCLUSIONS

We have shown that it is possible to calculate the theoretical energy density and specific energy based on the active electrode material of a $\text{LiC}_6/\text{NiO}_2$ battery using ab initio quantum chemical methods. This should encourage researchers to use this tool more widely for technological material design.

5 ACKNOWLEDGMENTS

The author wish to thank the BEW (Swiss Federal Office of Energy) for financial support, and Dr. O. Haas and Prof. C. Daul for fruitful discussions.

6 REFERENCES

- [1] P. Hohenberg and W. Kohn, Phys. Rev., **136**, B864, (1964).
- [2] W. Kohn and L.J. Sham, Phys. Rev., **140**, A1133, (1965).
- [3] P. Blaha, K. Schwarz, P. Dufek and R. Augustyn, WIEN95, Technical University of Vienna, improved and updated Unix version of the original copyrighted WIEN-code which was published by K. Schwarz, P. Sorantin and S.B. Trickey in Comput. Phys. Commun., **59**, 399, (1990).
- [4] P.C. Dickens and C.J. Reynolds, Solid State Ionics, **5**, 331, (1981).
- [5] ADF 2.0.1, Department of Theoretical Chemistry, Vrije Universiteit, Amsterdam.
- [6] E.J. Baerends, J. Comp. Phys., **99**, 84, (1992).
- [7] K. Sawai, Y. Iwakoshi and T. Ohzuku, Solid State Ionics, **69**, 273, (1994).

GLASSY CARBON BASED SUPERCAPACITOR STACKS

M. Bärtsch, A. Braun, R. Kötz, O. Haas

Considerable effort is being made to develop electrochemical double layer capacitors (EDLC) that store relatively large quantities of electrical energy and possess at the same time a high power density. Our previous work has shown that glassy carbon is suitable as a material for capacitor electrodes concerning low resistance and high capacity requirements. We present the development of bipolar electrochemical glassy carbon capacitor stacks of up to 3 V. Bipolar stacks are an efficient way to meet the high voltage and high power density requirements for traction applications. Impedance and cyclic voltammogram measurements are reported here and show the frequency response of a 1, 2, and 3 V stack.

1 INTRODUCTION

Conventional electrolytic capacitors exhibit a very high specific power (W/kg) but quite low specific energy (Wh/kg). On the contrary, batteries feature high energy density, but they suffer from relatively low power density. For a wide spectrum of applications energy storage devices are needed which offer at the same time good energy and power density, i.e. energy systems which deliver within seconds several watt-hours of energy. These devices could be applied, for example, to provide peak power to load-level electric car batteries, as energy source for electrically heated catalysts or, in general, where intermittent high power is required.

Electrochemical double layer capacitors (EDLC), also known as supercapacitors or ultracapacitors (if pseudo-capacitance is included), seem to be very promising to meet the above mentioned energy and power requirements. The double layer arises primarily from the electrostatic interaction between electronic charge in the electrode phase and the ions and dipoles in the electrolyte phase. The larger the electrode/electrolyte interface the bigger the capacity to store electrical energy. Metal-oxides, doped conducting polymers, carbon or graphitic powder and, in our case, glassy carbon (GC) can be used as electrode materials.

A smooth glassy carbon surface has a double layer capacitance of about $20 \mu\text{F}/\text{cm}^2$ (aqueous electrolyte). High capacitance is obtained when the surface is modified by electrochemical or chemical treatment in solution or air in a way that the effective surface increases by several orders of magnitude. Glassy carbon possesses the great advantage that the active layer, which makes up the very large double layer capacitance, forms a part of the current collecting electrode. Thus, contact resistance may be efficiently reduced.

2 BIPOLAR CONCEPT

The voltage of a unit cell capacitor comprised of two electrodes, which are activated on one side, is 1 or 3V depending on the electrolyte (aqueous or organic, respectively). In order to have several hundred volts,

which are needed in some traction applications, the cells have to be connected in series either in a monopolar or bipolar way. The total resistance should be kept small so that the power density is optimized. For this reason, it is preferable to use the bipolar configuration in which bipolar electrodes, activated on both sides, are placed between two end plates activated only on one side (Figure 1). An ion conducting separator is used in order to avoid short current between the electrodes. It should be as thin and porous as possible so as to obtain a low separator resistance. Further, it must not be electronically conducting.

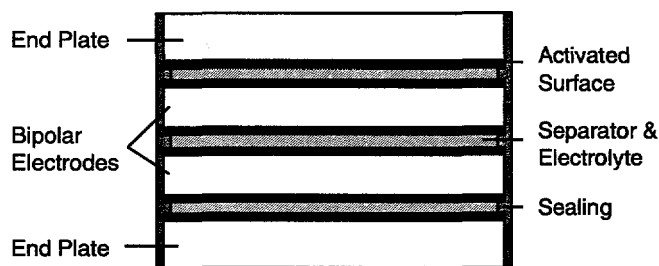


Fig. 1: View of a 3 cell capacitor stack with glassy carbon electrodes.

To avoid leakage currents on the periphery of the stack, it has to be sealed with an insulating seal to inhibit ionic and electronic contact from one cell to the other.

3 EXPERIMENTAL

The GC electrodes (19.64 cm^2 , $5 \text{ cm } \varnothing$, 1 mm thick) were activated in air at 490°C for one hour. Afterwards they were treated in $3 \text{ M H}_2\text{SO}_4$ and distilled water. Celgard[®] 3401 ($25 \mu\text{m}$ thick) was used as separator and was soaked with $3 \text{ M H}_2\text{SO}_4$ before mounting. The impedance spectra as well as the cyclic voltammograms were measured with a EG&G potentiostat 273A in conjunction with a Solartron SI 1255 HF frequency response analyzer. The capacitance, $C(v)$, was calculated from the imaginary part of the impedance, $Z(v)''$:

$$C(v) = -1/(2\pi v Z(v)'') \quad (1)$$

4 RESULTS AND DISCUSSION

One unit cell capacitor plus a two and a three volt capacitor stack were built. Figure 2 shows the cyclic voltammograms (CV) a), b) and c) of the three capacitors consisting of air activated GC electrodes. All CVs were measured with a scan rate of 10 mV/s. Curve a) shows the charging from 0 to 1 V with an average current of about 50 mA. The average charging currents for the 2 and 3 V stacks are 29 and 20 mA, respectively. Because of the series nature of the stack, the total capacitance is given by

$$1/C = \sum(1/C_i). \quad (2)$$

The capacitance of a capacitor is $C = Q/V$ (Q : charge, V : voltage). If Q is replaced by $I \cdot t$, then

$$C \cdot V = I \cdot t \quad (3)$$

(I : current, t : time). Based on eqs. (2) and (3) the current ratio is expected to be a):b):c) = 6:3:2 which is in good agreement with the measured values of b) and c). The product $C \cdot V$ corresponds to the integral under the CV curve and is, according to (3), the same in all three cases. The CV of an ideal capacitor would be a rectangle. Capacities which do not arise from a pure double layer and small leakage currents lead to a slight deviation of the CV curve from a rectangle.

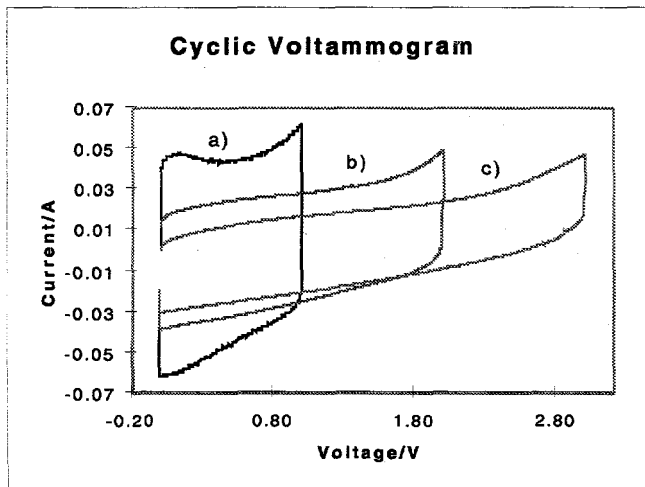


Fig. 2: Cyclic voltammograms of GC unit cell a), a 2 V, b), and a 3 V, c), capacitor stack. Scan rate 10 mV/s. Electrolyte is 3 M H_2SO_4 .

The capacitance vs. frequency curves of the 1, 2, and 3 V 20 cm^2 capacitors are shown in Figure 3 and calculated as defined by eq. (1). The impedances were measured in each case with a fully charged capacitor. The capacities at 0.1 Hz are 2.9 F (1 V), 1.6 F (2 V), and 1.0 F (3 V). The value of 1.6 F is a bit smaller than the expected value of 2 F according to eq. 2. The capacitance decreases steadily with increasing frequency and is one order of magnitude smaller at

1000 Hz compared to 0.1 Hz. For an ideal capacitor, C is constant with frequency. However, for real capacitors, dispersion processes generally cause the value of C to decrease as the frequency increases. It is assumed that the formation of the electrochemical double layer is not complete at higher frequencies because of the limited mobility of the ions.

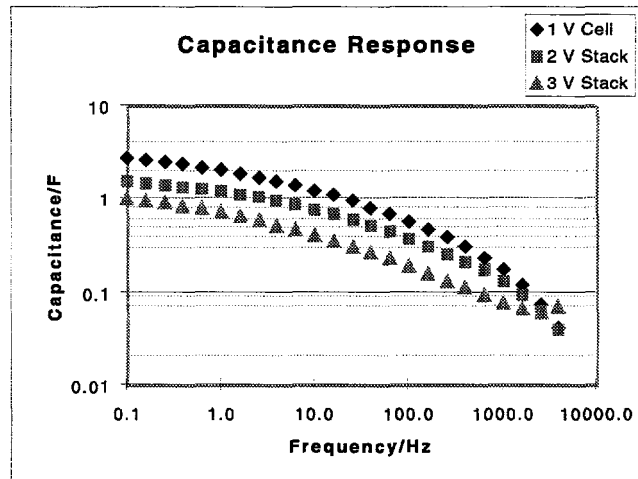


Fig. 3: Frequency dependence of the AC capacitance for the 1, 2 and 3 V capacitors.

5 CONCLUSIONS

Supercapacitors have the potential to deliver the energy and power that is needed in a variety of applications. After having succeeded in building a unit cell capacitor with GC electrodes [1], we wanted to scale-up our device to a low voltage capacitor stack. The capacitance response of the 2 and 3 V stack corresponds to what would be expected based on the unit cell measurement. We could demonstrate a 3 V GC capacitor stack with air activated electrodes and 1 F capacitance. The fast activation in air seems to be a good alternative to electrochemical activation.

These initial results are quite promising, however, building even larger stacks with much higher voltages and lower total resistance still remains a big challenge.

6 ACKNOWLEDGMENTS

Financial support by the Board of the Swiss Federal Institutes of Technology FIT Board [Swiss Priority Program on Materials Research] is gratefully acknowledged.

7 REFERENCES

- [1] M.G. Sullivan, M. Bärtzsch, R. Kötz, O. Haas, ECS Meeting San Antonio, Texas, Meeting Abstracts, Vol. 96 (2), p. 845 (1996).

FUEL CELL MEMBRANE PREPARATION : EFFECTS OF BASE POLYMER

H.P. Brack, G.G. Scherer

Radiation grafted films and membranes prepared from the partially fluorinated base copolymer poly(ethylene-alt-tetrafluoroethylene) or ETFE have better mechanical properties than those prepared from poly(tetrafluoroethylene-co-hexafluoropropylene) or FEP. The influence of the base copolymer film type on the grafting rate and yield is reported in the present investigation. An understanding of the effects of these parameters is important so that the grafting process can be carried out reproducibly in as short a time as possible. The grafting rate and yield as a function of the irradiation dose has been found to be much higher for the partially fluorinated base copolymer ETFE.

1 INTRODUCTION

The pre-irradiation grafting method is being used in our laboratory to develop polymer electrolyte membranes [1] for fuel cell applications. In our membrane preparation method, fluoropolymer films, such as poly(tetrafluoroethylene-co-hexafluoropropylene), FEP, or poly(ethylene-alt-tetrafluoroethylene), ETFE, are pre-irradiated using a gamma irradiation or electron beam source and then grafted by reaction with styrene to yield FEP-g-PS or ETFE-g-PS. Grafted films are transformed into proton-conducting membranes, FEP-g-SPS or ETFE-g-SPS, by sulfonating the grafted aromatic chains using chlorosulfonic acid.

We had earlier worked exclusively with FEP [1] (325 kg/mol) films, but we are now evaluating ETFE (906 kg/mol) films as starting materials. Desirable mechanical properties such as strength and flexibility improve with increasing molecular weight and are better for ETFE compared to FEP. Improved mechanical properties such as greater tensile strength and percent elongation at the break point can be quite important in the fuel cell application because of the presence of mechanical and swelling stresses [2]. Indeed ETFE-based membranes and grafted films have been found to have superior mechanical properties (Table 1).

| Material | Young's Modulus (N/mm ²) | Percent Elongation at Break Point (%) | Tensile Strength (N/mm ²) |
|---------------------|--------------------------------------|---------------------------------------|---------------------------------------|
| grafted FEP film | 1x10 ³ | < 1 | 6 |
| grafted ETFE film | 9.7 x10 ² | 40 | 37 |
| FEP-based membrane | 79 | 21 | 6 |
| ETFE-based membrane | 187 | 19 | 42 |

Table 1: Film and Membrane Mechanical Properties.

The present study investigates the effects of polymer type, partially fluorinated ETFE versus perfluorinated FEP on the rate and extent of grafting. Conducting this kinetic investigation in a manner similar to the previous one on FEP[3] makes it possible then to readily compare the data for the two polymer types. Understanding these effects is important for optimizing and controlling the grafting process. For example, it is important to prepare membranes reproducibly and quickly.

The grafting yield can be defined on a molar basis from the number of moles of base polymer "mer" units in the ungrafted film, N_{bp} , and the number of moles of mer units in the grafted side chains, N_g , as shown in Equation (1):

$$\text{mole \%} = N_g / (N_g + N_{bp}) \times 100\% \quad (1)$$

2 ETFE FILMS COMPARED TO FEP FILMS

The grafting rate and maximum graft yield for gamma/air irradiated ETFE films were found to increase when either the (1) styrene concentration or (2) pre-irradiation dose, D , increased. The maximum grafting yields for ETFE are compared with those determined previously for FEP [3] in Figure 1. Shown also for comparison is the maximum grafting yield of an electron irradiated ETFE film. It is much higher than for the gamma irradiated film due to a lesser loss of reactive radical sites during the much shorter electron irradiation time.

The determination of the reaction order with respect to irradiation dose, D , and a comparison to the previously determined reaction order [3] for FEP are shown in Figure 2. The grafting rate, R_g , for ETFE was found to be described by the following rate expression (2):

$$R_g \propto [D]^{0.47} [\text{styrene}]^{1.6} \quad (2)$$

Gupta [3] found the following rate expression for the grafting on FEP:

$$R_g \propto [D]^{0.60} [\text{styrene}]^{1.9} \quad (3)$$

The following four factors are likely to be important in determining the higher maximum grafting levels and rates (on a molar basis) achieved with pre-irradiated ETFE than with pre-irradiated FEP films:

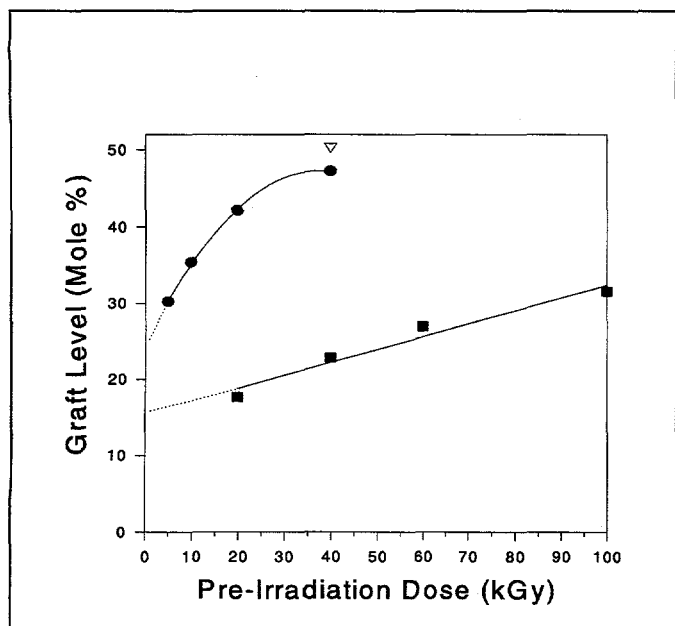


Fig. 1: Maximum grafting level for ∇ e-/air and \bullet gamma/air irradiated 100 μm ETFE and \blacksquare 50 μm FEP films.

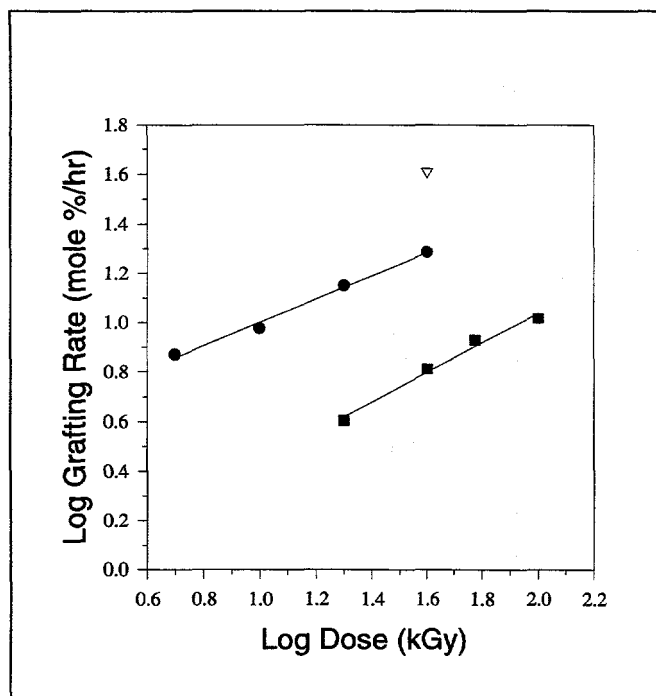


Fig. 2: Log-log plot of grafting rate vs. pre-irradiation-dose for the reaction of ∇ e-/air and \bullet gamma/air irradiated 100 μm ETFE and \blacksquare 50 μm FEP films with styrene.

(1) C-H bond strengths are less than those of C-F bonds [4]. A greater number of radicals would be expected to form per quantum of energy absorbed for ETFE films compared to FEP films.

(2) Infrared measurements indicate that hydroperoxides are formed in ETFE films upon irradiation in air [5]. This means that autoxidation reactions [4] are creating many hydroperoxides groups from each initial radical. No evidence has been found for similar

autoxidation processes in FEP, perhaps because the bond strength [4] of C-F is higher than that of C-H and O-F bonds.

(3) ETFE swells slightly in benzene, whereas FEP does not measurably swell. This may enhance the diffusion of monomer into the ETFE film during grafting.

(4) The higher maximum grafting levels achieved with ETFE films in comparison to FEP films indicates that the PS graft component may be more compatible with partially fluorinated ETFE than with perfluorinated FEP.

3 CONCLUSION

The nature of the base polymer has been found to exert a great influence on the grafting kinetics and maximum grafting yield.

4 ACKNOWLEDGMENTS

Stress-strain measurements by Dr. C. Löwe and C. Walder of EMPA-Dübendorf and sample irradiation by M. Steinemann of the PSI Hot Laboratory and C. Günthard of Studer AG, CH-4658 Däniken are gratefully acknowledged. Dr. N.D. McKee of DuPont Fluoroproducts, Wilmington, DE, USA and R. Hodann of Nowofol GmbH, D-83310 Siegsdorf are thanked for technical product information and the gifts of some FEP and ETFE materials. The financial support of the Swiss Federal Office of Energy (BEW) is gratefully acknowledged.

5 REFERENCES

- [1] B. Gupta, G.G. Scherer "Proton Exchange Membranes by Radiation-Induced Graft Copolymerization of Monomer into Teflon-FEP Films" in *Chimia*, **48**, pp. 127-137 (1994).
- [2] G.G. Scherer, H.P. Brack, F.N. Büchi, B. Gupta, O. Haas, M. Rota, "Materials Research Aspects of Membrane Development for Polymer Electrolyte Fuel Cells" in *Hydrogen Energy Progress XI*, **2**, pp. 1727-1736 (1996).
- [3] B. Gupta, F.N. Büchi, G.G. Scherer "Cation Exchange Membranes by Pre-Irradiation Grafting of Styrene into FEP Films I. Influence of Synthesis Conditions" in *J. Polymer Sci.: Part A: Polymer Chem*, **32**, pp. 1931-1938 (1994).
- [4] T.H. Lowry K.S. Richardson, "Mechanism and Theory in Organic Chemistry" Harper and Row, New York (1981).
- [5] H.P. Brack, G.G. Scherer, "Investigation of Radical Formation and Degradation in Gamma- and Electron-Irradiated Fluoropolymers" *Polymers for Advanced Technologies 1995 3rd Annual Symposium*, Pisa, June (1995).

CYCLIC VOLTAMMETRIC INVESTIGATIONS OF MICROSTRUCTURED AND PLATINUM-COVERED GLASSY CARBON ELECTRODES IN CONTACT WITH A POLYMER ELECTROLYTE MEMBRANE

G.G. Scherer, Z. Veziridis, M. Staub, H. Freimuth (Institut für Mikrotechnik Mainz IMM, Mainz, Germany)

Model gas diffusion electrodes were prepared by microstructuring glassy carbon surfaces with high aspect ratios and subsequent deposition of platinum. These electrodes were characterized by hydrogen under-potential deposition (H-upd) in contact with a polymer electrolyte membrane employing cyclic voltammetry. H-upd was found on platinum areas not in direct contact to the solid electrolyte, as long as a continuous platinum-path existed. A carbon surface between platinum acts as barrier for H-upd.

1 INTRODUCTION

Studies of the interface between a platinum screen and a proton-conducting polymer electrolyte membrane by cyclic voltammetry in the H-upd region [1] demonstrated that all of the platinum surface was electrochemically active, although a major part of it was not in direct contact to the membrane. The electrochemically active area could be further increased by stapling two platinum screens behind each other. When carbon felt was sandwiched between the membrane and the platinum screens an increased double layer charging was observed due to the increased surface area. However, the characteristic features of H-upd on platinum nearly disappeared due to a "barrier effect" caused by the intermediate carbon surface.

These observations are of utmost importance for the formation of an ideal interface in Polymer Electrolyte Fuel Cells. Here the active layer of a gas diffusion electrode (gde), which consists mainly of randomly oriented carbon particles onto which platinum (Pt/C) is dispersed, is in contact with the proton-conducting membrane [2]. The solid electrolyte does not penetrate into the pores of the gde, hence, only the topmost platinum nano-particles are in direct contact with the electrolyte and are, therefore, electrochemically active. The "barrier" effect of the carbon surface must be overcome to achieve a higher platinum utilization. One possibility is the impregnation of the active layer with solubilized membrane material, similar to the wetting of pores by an aqueous electrolyte [2]. This "barrier" effect is clearly not observed when Pt-black is utilized in the active layer of a gde [3].

The true geometric area of the interface has to be known to study this "barrier" effect. Therefore, glassy carbon model electrodes with a well known geometric surface area were prepared [3] in this investigation. They consisted of *comb-like* microstructured surfaces with *high aspect ratios* onto which platinum was deposited in different ways, yielding platinum surfaces of different total area. These electrodes were used to determine quantitatively the electrochemically active interface with a solid polymer electrolyte, e.g., a Nafion 117 membrane.

2 EXPERIMENTAL

The surface of glassy carbon slabs (1X1 cm², HTW, D-86672 Thierhaupten) was microstructured into a comb-like structure by use of a rotating blade micro-saw (Disco Corp.) (Figure 1 to Figure 3). Typical dimensions of these structures were 140 μm in depth and 15 to 20 μm in width for the channels and ridges, respectively, thus yielding aspect ratios of 8.

Platinum was deposited by sputtering either (I) onto the flat, nonstructured surface, which then was structured subsequently (Figure 1) or (II) onto the already structured surface (Figure 2 and 3). The platinum distribution was probed by Auger spectroscopy.

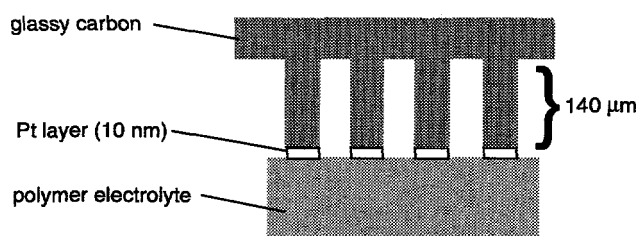


Fig. 1: Microstructured glassy carbon surface with platinum coverage of the plateaus (not to scale); electrode no. I.

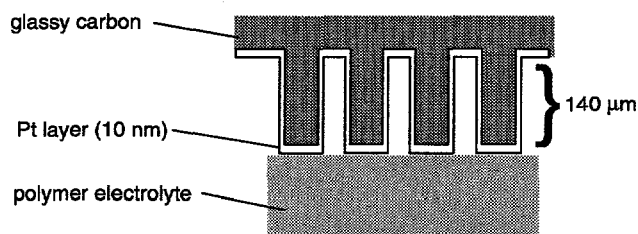


Fig. 2: Microstructured glassy carbon surface with full platinum coverage of the comb-like structure; electrode no. II.

Cyclic voltammetry was carried out in a solid state electrochemical cell in the potential range between +50 and 700 mV with respect to a dynamic H₂-electrode. The microstructured glassy carbon slab was pressed under defined load from the top against the membrane surface. The electrochemically active area of platinum can be determined with an experimental error of a few percent from the charge consumed during H-upd in this potential range [4].

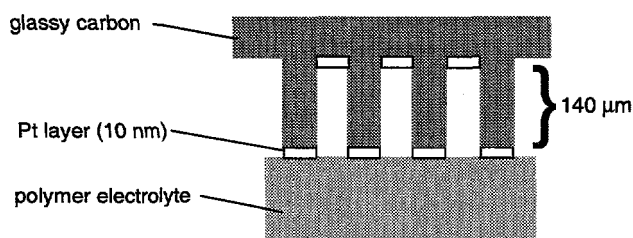


Fig. 3: Microstructured glassy carbon surface with platinum coverage of the plateaus and of the bottom of the channels; electrode no. III.

3 RESULTS AND DISCUSSION

Carbon is widely utilized in electrochemistry as support material for precious metal electrocatalysts, e.g., in fuel cells for the hydrogen oxidation and oxygen reduction reactions. Carbon shows good chemical stability, is electron-conducting, and has a low specific weight and a high surface area. Discrete electrocatalyst particles in the nm range are deposited onto bigger carbon particles, yielding a high dispersion and therefore high surface area of the precious metal. For many applications, e.g., in low temperature fuel cells low precious metal loadings are of particular importance for cost reasons. Hence, the behaviour of the carbon surface as a "barrier" for electrochemical activity has to be understood.

Cyclic voltammograms of the two electrodes represented in Figure 1 and 2 in contact with a Nafion 117 membrane, respectively, are shown in Figure 4. It is evident, that electrode No. II has a much higher electrochemical active area than electrode No. I, although in both cases only the platinum covered plateaus are in direct contact to the membrane surface.

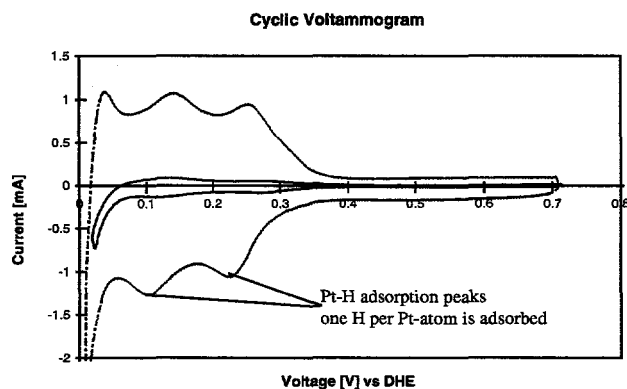


Fig. 4: Cyclic voltammograms in the H-upd range of platinum-covered glassy carbon electrode, represented by Figure 1 and Figure 2, in contact to a Nafion 117 membrane.

A quantitative evaluation of the charge consumed in the H-upd range yields the respective geometric platinum covered areas, 0.91 and 10.92 cm², respectively. This result is plausible for the electrode No. I, the result for the electrode No. II is surprising. Platinum at a distance of 140 μm away from the membrane surface is still detectable by H-upd. Principally, this confirms

the earlier observation [1] where H-upd on the entire surface of screens with a wire diameter of 76 μm were found. However, our results allow a quantitative determination due to the defined geometry of the interface.

The cyclic voltammogram with electrode No. III yields the same active area as with electrode No. I. For the same electrode (Figure 3), however in contact with 1 N sulfuric acid (also present in the channels), a twice as high active area due to the platinum deposited at the bottom of the channel is measured.

These results can be rationalized as follows: Platinum located up to a 140 μm away from the direct contact to the membrane surface is active for H-upd when a continuous "platinum path" is provided. In contrast, when the "platinum path" is interrupted by a glassy carbon surface (Figure 3) only the platinum in direct contact to the proton-conducting membrane is active.

It is known that the mechanism for H-upd in an aqueous electrolyte involves "instantaneous" surface equilibration between different platinum adsorption states [5]. However, it is still unclear how upd occurs in the absence of direct electrolyte contact. It is further known that water spreads effectively on a platinum surface. Whether an adsorbed water film alone or the presence of "conducting impurities" in the latter can be made responsible to explain our results is still a matter of speculation. As a relevant conclusion, we can simulate the behaviour of porous gas diffusion electrodes, either composed of Pt/C or Pt-black active layers, with our model interfaces to further investigate the important role of carbon as support material in gdes with low precious metal loading.

4 ACKNOWLEDGEMENT

Financial support from the Swiss Federal Office of Energy (BEW, Bern) and from Elektrowatt AG, Zürich, is gratefully acknowledged. The authors thank Dr. B. Schnyder for carrying out Auger measurements.

5 REFERENCES

- [1] J. McBreen "Voltammetric Studies of Electrodes in Contact with Ionomeric Membranes", *J. Electrochem. Soc.* 132, pp. 1112-1116 (1986).
- [2] G.G. Scherer "Interfacial Aspects in the Development of Polymer Electrolyte Fuel Cells" *Solid State Ionics*, Band 94, p. 249 (1997).
- [3] M. Staub, Diss. No. 11285, ETH Zürich (1996).
- [4] T. Biegler, D.A.J. Rand, R. Woods "Limiting Oxygen Coverage on Platinized Platinum; Relevance to Determination of Real Platinum Area by Hydrogen Adsorption" *J. Electroanal. Chem.* 29, pp. 269-277 (1971).
- [5] F.E. Woodward, C.N. Reilley "The Mechanism for Hydrogen Adsorption on Platinum Electrodes from Acidic Aqueous Media" *J. Electroanal. Chem.* 167, pp. 65-77 (1984).

POLYMER ELECTROLYTE FUEL CELLS : FLOW FIELD FOR EFFICIENT AIR OPERATION

F.N. Büchi, A. Tsukada, O. Haas, G.G. Scherer

A new flow field was designed for a Polymer Electrolyte Fuel Cell stack with an active area of 200 cm² for operation at low air stoichiometry and low air over pressure. Optimum of gas flow channel dimensions were calculated based on the required pressure drop in the flow field. Single cells and a bi-cell stack with the new flow field show an improved current/voltage characteristic when operated at low air stoichiometries as compared to that of the previous non optimized design.

1 INTRODUCTION

The overall efficiency of the H₂/air polymer electrolyte fuel cell system (PEFC) depends not only on the efficacy of the electrochemical conversion, but also on the extent of the parasitic power that the system needs for reactant supply, gas humidification, cooling, and system control. Air compression is by far the biggest parasitic load for the system, reducing the net power output by up to 30 % [1] (i.e. FC-Bus, Ballard Power Systems; Daimler NeCar II [2]).

In order to reducing the parasitic load for air compression it is necessary to operate the fuel cell stack at low air stoichiometry (λ_{air}) and low air over pressure. Optimized gas flow fields are needed to achieve satisfactory electrochemical performance under these conditions.

2 FLOW FIELD CONSIDERATIONS

The flow field determines the distribution of hydrogen and air (or oxygen) over the active area on the respective sides of the fuel cell. The requirements of the gas flow fields for optimum electrochemical performance of the fuel cell are :

- homogeneous distribution of reactant gases over the entire active area of each cell
- high utilization of reactant gases
- ready removal of water from the cathode. Gas flow channels should not be blocked by accumulating water droplets
- homogeneous distribution of reactant gases to all individual cells in the multi-cell stack.

In order to fulfill the above requirements, the flow fields need to have the following properties :

- for equal distribution of the gases in the cell, all channels need to have the same pressure drop
- to readily remove water droplets from the cathode flow field, a pressure drop in each gas flow channel of ten to thirty millibars is needed
- in order to fuel all cell in the multi-cell stack equally, the pressure drop in the manifold has to be at least an order of magnitude lower than the pressure drop in the individual cells.

These considerations are more stringent on the air side because of the high sensitivity of the electrochemical performance on the relatively low oxygen partial pressure in air. Therefore we put emphasis for optimization on the cathode side flow field.

Based on the above requirements we choose a radiator type flow field based on many parallel, low cross section channels, connected at in- and outlet with a high cross section distributor channel as shown in Figure 1. Because all flow field channels have the

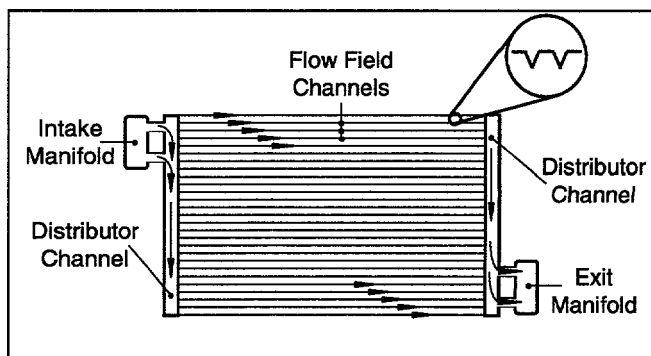


Fig. 1: Schematic of radiator type flow field.

same length and cross section, they have an equal pressure drop and therefore equal gas flow rate. The low cross section of the flow field channels also promotes mixing of the air stream and therefore allows for a high utilization of oxygen in air, i.e. allows for operation at low air stoichiometries. The pressure drop in the channels at the desired point of operation (and respective air flow), needs to be controlled by proper channel dimensioning. Distributor channels and manifolds need to be dimensioned, so that their pressure drop is at least an order of magnitude lower than the one in the flow field channels.

3 PRESSURE DROP CALCULATIONS

The pressure drop for the triangular shaped flow field channels was calculated and is shown in Figure 2 for a channel length of 15 cm (so a square flow field yields approx. 200 cm²) and the indicated channel width. To allow for a contact area of 50 %, the necessary air flow for an air stoichiometry of $\lambda_{air} = 2$ was

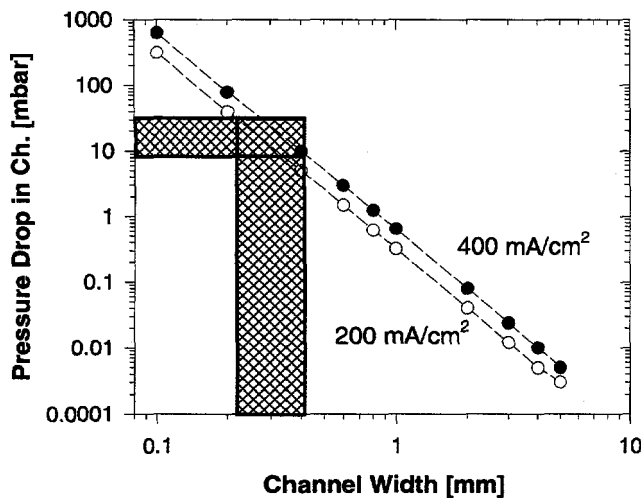


Fig. 2: Pressure drop of air flowing at 60 °C in triangular shaped channel of given width and 150 mm length, for two current densities at $\lambda_{\text{air}} = 2$. The shaded area denotes range of optimum channel dimensions and pressure drops.

calculated over twice the channels surface for two current densities. It can be seen from this figure, that the channel dimensions with the desired pressure drop have width in the order of 0.2 - 0.5 mm.

Based on the above calculation the channel width was set to 0.5 mm. For an active area of 200 cm², this choice results in a flow field with 145 parallel channels (with a length of 145 mm). Figure 3 shows a section of this a flow field.

The anode flow field was based on the same channel structure and similar channel dimensions were used.

4 FUEL CELL PERFORMANCE

Flow fields with an active area of 200 cm² were machined in stainless steel plates (1.4301). Cells with the new flow fields were tested in single cell and bi-cell (bipolar) stack configurations. The cells were operated in the H₂/air mode at 60 °C at 1.2 bar_a gas pressures. Air was humidified at the cell temperature and hydrogen was supplied dry. The membrane/electrode assemblies were made from Nafion 115 membranes (Nafion 105 in the bi-cell stack) and commercial elec-

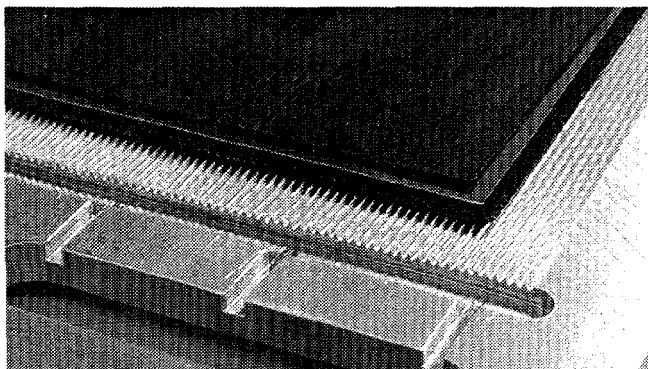


Fig. 3: Section of cathode flow field, including intake air manifold and distribution channel.

trodes. Current Voltage characteristics were measured under constant gas flow conditions. The results for an air flow of 13 ml/(min cm²) (corresponding to an air stoichiometry $\lambda_{\text{air}} = 1.9$ @ 400 mA/cm²) are presented in Figure 4. The single cell with the new flow field exhibits a linear behavior in the current density region 100 to 450 mA/cm², proving that the new flow field structure allows for operation at low air stoichiometry at pressures close to 1 bar_a. In the bi-cell stack both cells show a close performance, indicating that in a multi cell stack, individual cells will perform similar. Therefore the improved flow field should make it possible to manufacture stacks operating at low air over pressure and low air stoichiometries, i.e. requiring only moderate parasitic power for the air supply. This result also shows a considerable improvement, as compared to the cell with the previous flow field [3], where performance dropped off sharply at $\lambda_{\text{air}} < 5$ under low pressure conditions.

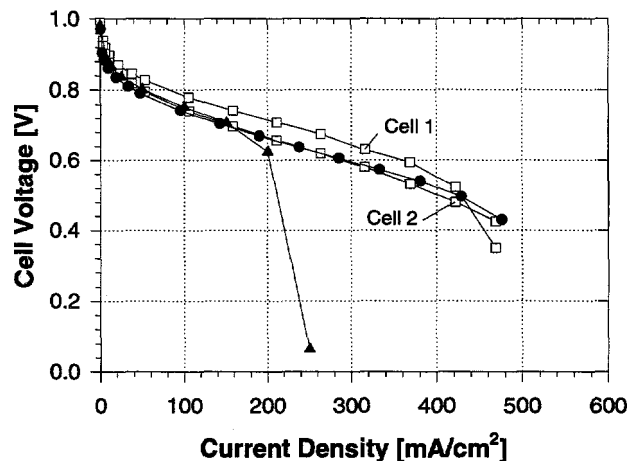


Fig. 4: Current-voltage curves of H₂/air PE fuel cells. ● new flow field single cell, □ new flow field bi-cell stack, ▲ old flow field single cell. Gas pressures 1.2 bar_a, $\lambda_{\text{air}} = 1.9$ @ 400 mA/cm², other conditions see text.

5 ACKNOWLEDGMENT

Continuous support of this work by the Swiss Federal Office of Energy (BEW) is gratefully acknowledged.

6 REFERENCES

- [1] D. Staschewski, "Performance and Efficiency of Electric Road Vehicles Powered by Hydrogen Fuel Cells", p. 516 - 522, Proc. of the 6th International Energy Conf., Beijing, China, June (1996).
- [2] "NeCar II - Fahren ohne Emissionen" Daimler Benz AG, Kommunikation, Stuttgart (1996).
- [3] M. Rota, F.N. Büchi, G.G. Scherer, "Scale-up of Polymer Electrolyte Fuel Cell" PSI Annual Report 1994/Annex V, 23 (1994).

Combustion Research

CATALYTICALLY STABILIZED COMBUSTION OF LEAN METHANE-AIR-MIXTURES: A NUMERICAL MODEL

U. Dogwiler, P. Benz, I. Mantzaras

The catalytically stabilized combustion of lean methane/air mixtures has been studied numerically under conditions closely resembling the ones prevailing in technical devices. A detailed numerical model has been developed for a laminar, stationary, 2-D channel flow with full heterogeneous and homogeneous reaction mechanisms. The computations provide direct information on the coupling between heterogeneous-homogeneous combustion and in particular on the means of homogeneous ignition and stabilization.

1 INTRODUCTION

In catalytically stabilized thermal combustion (CST) fuel is burnt by heterogeneous catalytic surface reactions and by homogeneous gas phase reactions at high power density. Compared to (non-catalytic) lean premixed combustion, CST shows an improvement in combustion stability and emissions of nitrogen oxides and products of incomplete combustion. Therefore CST has the potential for application in gas turbines.

A catalytic combustor is usually made of a catalytically active monolith-bed consisting of a multitude of tubular channels. The processes in each individual channel are identical and include homogeneous and heterogeneous reactions, diffusive heat and mass transport, convection, heat conduction in the catalytic plates and surface radiation.

A numerical model has been developed that describes CST in a two-dimensional, laminar channel flow with premixed fuel and air. The model is used in conjunction with experiments performed within the PSI project 'catalytic combustion'. The goal is to gain a better understanding of the ignition and stabilization of homogeneous combustion by the hot catalytic surfaces. In particular, the study examines the effect of the fluxes of various species (e.g. radicals) to and away from the surface on the above processes. In addition, despite existing uncertainties in the heterogeneous chemistry, the model can be used for predictions in technical devices.

2 NUMERICAL MODEL

The fluid dynamics model contains all conservation equations for a laminar, stationary, two-dimensional reactive flow. Thermodiffusion and enthalpy transport due to diffusion are included. Surface radiation and one-dimensional heat conduction in the solid plates are also taken into account. For the combustion of methane (main constituent of natural gas) in air, the homogeneous reaction mechanism contains 15 species and 98 reactions [1]. The heterogeneous reaction mechanism for the platinum surface contains 14 species and 26 reactions [2].

The system of elliptic differential equations for the reacting flow field is solved using an ADI (alternating direction implicit) method.

The first order, nonlinear, coupled differential equations for the surface species concentrations (coverages of the Pt-sites) are integrated in time until a quasi-steady state is reached. From the surface concentrations the fluxes of the adsorbing and desorbing gas-phase species are calculated and subsequently used as boundary conditions for the flow field. Further information about the model is given in [3].

3 RESULTS AND DISCUSSION

Computations are performed for a two-dimensional flow field between two extended parallel, catalytically active (Pt) plates. The outer surfaces of the plates are assumed to represent adiabatic walls. The dimensions in mm and the inlet conditions for the methane/air-mixture are given in Figure 1. This configuration (distance between plates: 2mm) approximates a square channel with a 4x4mm cross section (same hydraulic diameter and same volume/surface ratio) similar to the ones used in practical monolith-beds.

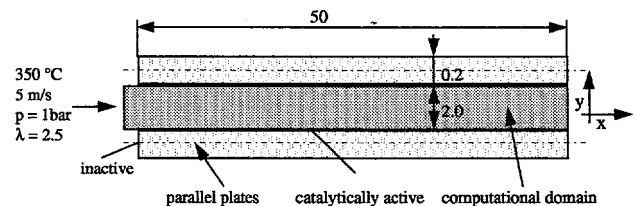


Fig. 1: Schematic of catalytic combustion chamber.

Figure 2 shows the axial profiles of the mean gas temperature T_g , surface temperature T_s , mean gas phase methane concentration $[CH_4]_g$ and the gas phase methane concentration at the surface $[CH_4]_s$. "Light-off" (transition from kinetically controlled heterogeneous surface reactions to diffusion controlled reactions) takes place a few millimeters after the channel inlet ($x=0$ mm), causing a steep increase of T_s and drop of $[CH_4]_s$. In this region homogeneous reactions are inhibited by fuel depletion close to the surface. Heat transport from the hot surface to the gas leads to an increase of T_g with increasing streamwise distance. At $x=35$ mm, homogeneous reactions become dominant; T_g rapidly approaches the adiabatic flame temperature and $[CH_4]_g$ goes to zero.

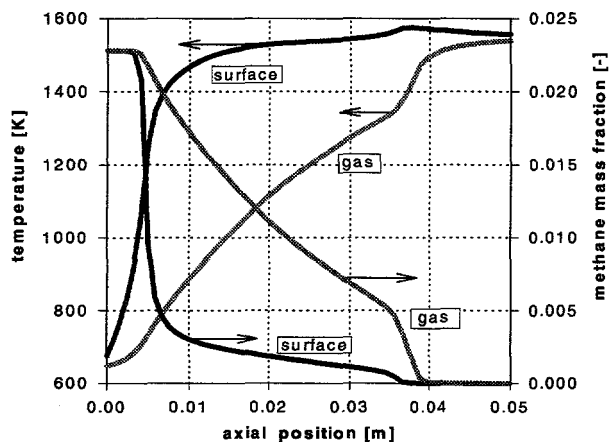


Fig. 2: Temperature and methane concentration as a function of axial position.

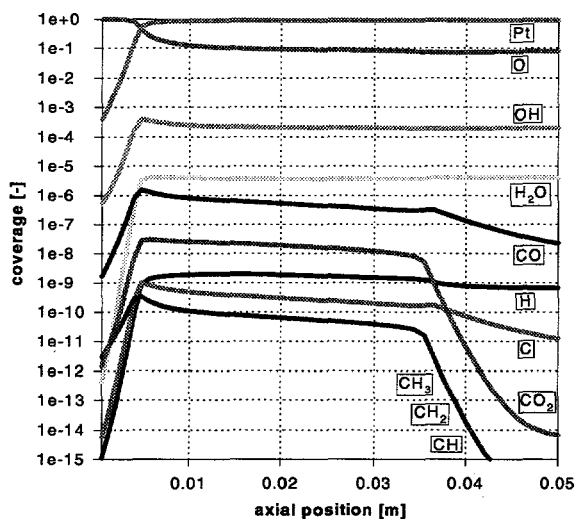


Fig. 3: Surface coverages as a function of axial position.

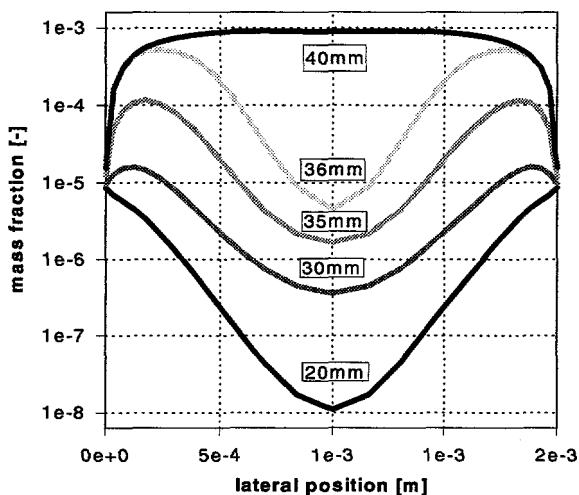


Fig. 4: Lateral OH-profiles at different axial positions.

The axial profiles of the coverages (i.e. the fraction of surface sites covered by a certain species) are shown in Figure 3. At the inlet the surface temperature T_s is low, and the platinum surface is essentially covered with O. This can be explained by a higher sticking probability of O_2 in comparison to CH_4 . An increase of the surface temperature in flow direction by thermal feedback (surface radiation and heat conduction in the solid plates) leads to a point where the adsorption/desorption equilibrium of oxygen shifts to desorption, resulting in bare surface sites onto which CH_4 can collide and react. In the hot region most of the active Pt-sites are vacant. Towards the end of the channel the consumption of fuel and intermediates by homogeneous reactions causes a drop in the coverages of all C-containing species.

Figure 4 shows the lateral concentration profiles of the radical OH at different axial locations x . Prior to the homogeneous ignition ($x \leq 20$ mm) the surface acts as a source for OH-radicals, as seen from the concentration gradient at the surface ($y=0$ mm). Further downstream, due to homogeneous reactions the OH-concentration increases drastically. In the region of homogeneous combustion ($x > 30$ mm) the surface acts as a sink for the radicals.

Further analysis show an enhancement of homogeneous ignition by OH-desorption from the surface.

4 ACKNOWLEDGEMENT

We thank the Swiss federal Office of Energy (BEW) for the financial support.

5 REFERENCES

- [1] J. Warnatz, "The Mechanism of High Temperature Combustion of Propane and Butane", Comb. Sci. Technology, 34, p. 177, (1983).
- [2] O. Deutschmann et al., "Numerical Modeling of Catalytic Ignition", 26th (Int.) Symposium on Combustion, Naples, July 28 - August 2, (1996).
- [3] S. Buser, "Experimentelle und numerische Untersuchungen zur katalytisch stabilisierten Verbrennung von mageren Wasserstoff-Luft-Gemischen in einer Kanalströmung", Diss. ETH Nr. 10488, (1994).

NUMERICAL AND EXPERIMENTAL INVESTIGATION OF NO_x FORMATION IN LEAN PREMIXED COMBUSTION OF METHANE

K. Bengtsson, P. Benz, T. Marti, R. Schären, A. Schlegel

A high pressure jet-stirred reactor has been built and employed to investigate NO_x formation in lean premixed combustion of methane/air. Experimental results are compared with numerical predictions using the model of a perfectly stirred reactor and elementary reaction mechanisms. Four reaction mechanisms are considered with respect to NO_x formation.

1 INTRODUCTION

Lean premixed combustion is the best available technique to reduce NO_x (NO_x=NO+NO₂) formation in gas turbine combustion of clean fuels (e.g. natural gas). To achieve further reductions at expected higher combustion temperatures and pressures in future gas turbines, an improved knowledge of NO_x kinetics is demanded. For gas turbine conditions few experimental kinetic data are available and in particular the pressure dependence of NO_x formation is uncertain. The goal of this project is a better quantitative understanding of NO_x formation at pressures up to 30 bars and flame temperatures in the range of 1400 to 1600°C.

2 NUMERICAL ANALYSIS OF NO_x FORMATION

Turbulent premixed combustion can be modelled using a perfectly stirred reactor (PSR) followed by a plug flow reactor (PFR). The PSR represents the thick turbulent flame brush and the PFR simulates the burn-out zone. In this simple model the chemistry is decoupled from the flow field, thus numerical studies with detailed chemistry are easy to perform.

Predictions of NO-concentrations for combustion of methane/air in a PSR using the chemical kinetics package CHEMKIN-II [1] are shown in Figure 1. The NO₂-concentrations are not considered as they are negligible compared to the NO-concentrations. Four different "elementary" reaction mechanisms of the C/H/O/N-system are used: Miller-Bowman [2], GRI [3], Bockhorn [4], Leeds+NO (mechanism of Ref. [5] supplemented by NO reactions from [4]). All mechanisms contain about 500 reactions and 50 species. The differences in the calculated concentrations are substantial and emphasize the existing uncertainties. In addition, reaction path analysis and sensitivity analysis have been performed. At 1 bar, in all mechanisms NO is mainly formed through the N₂O- and Zeldovich- (O super-equilibrium) submechanisms, the Fenimore submechanism being of less importance. At 10 bars the N₂O-submechanism is dominant in all reaction mechanisms. Figure 2 shows the calculated reaction path diagram for 10 bars (Miller-Bowman mechanism) illustrating the major steps in NO formation. The most important route is: N₂ → N₂O → NO (important reactions: N₂ + O + M → N₂O + M, N₂O + O → 2 NO). In all reaction mechanisms the NO concentration is most

sensitive to the reactions forming or consuming O, H, OH, HO₂. The differences between the reaction mechanisms in the C/H/O-system have a major influence on the predicted NO concentrations.

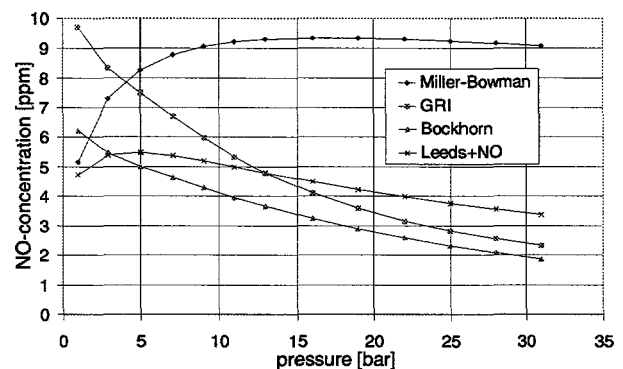


Fig. 1: Model predictions for the pressure dependence of NO-concentrations in a PSR from four reaction mechanisms. Reactor temperature = 1500°C, residence time = 1.0 ms, equivalence ratio = 0.5, methane.

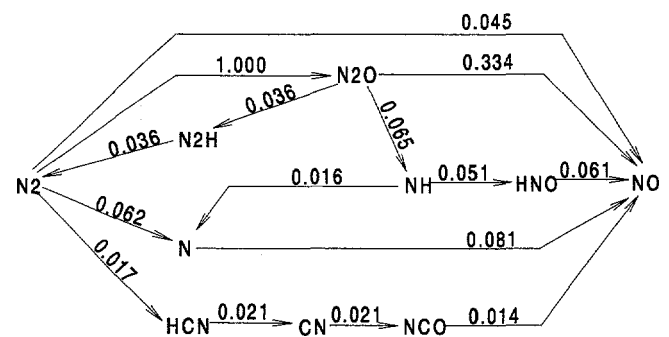


Fig. 2: Reaction path diagram of the NO formation with the Miller-Bowman mechanism. Diagram shows relative N-atom fluxes ≥ 0.01 . PSR, methane, temperature = 1500°C, equivalence ratio = 0.5, pressure = 10 bars, residence time = 1.0 ms.

3 EXPERIMENT

A test rig was built which can be operated at pressures up to 30 bars and at a maximum thermal power of 100 kW. Gaseous fuel and air are premixed and

preheated up to 550°C. The test rig can be used for various combustion projects.

For the investigation of NO_x formation a jet-stirred reactor coupled with a tubular reactor that fit into the pressurized container of the rig was constructed. Efforts were made in the design of the jet-stirred reactor to attain as good as possible PSR-conditions. The characteristic mixing time of the reacting gas by turbulence must be much smaller than the characteristic time for chemical reaction, i.e. the Damköhler number Da must be $\ll 1$. This is a major requirement for the success of the kinetic experiment. In the ideal case of uniformity throughout the reactor the application of diagnostics is easy compared to thin flames.

The jet-stirred reactor has a volume of 30 ml and is made of castable ceramics embedded in insulating material. Premixed and preheated methane and air are fed through 32 small tubes into the reactor. At a residence time of 1 ms in the jet-stirred reactor, the velocity of the jets at the inlet is sonic and high turbulence intensity and therefore fast mixing in the reactor is achieved.

Temperatures are measured with thermocouples, the gas composition is determined by a cooled gas sampling probe and conventional gas analysers.

4 EXPERIMENTAL RESULTS

Figure 3 shows the measured NO_x concentrations in the stirred reactor as function of temperature for different pressures. The concentrations increase with increasing temperature as expected. At 1.3 bars the measurements correspond well to the predictions of a PSR using the Miller-Bowman, Bockhorn and Leeds+NO mechanisms. With increasing pressure the measured NO_x concentrations decrease. This could be attributed partly to the kinetics, since all reactions mechanisms, except Miller Bowman's, show the same trend. However at high pressures the measured concentrations are remarkably lower than the PSR predictions with all mechanisms. We assume that deviations from PSR-behaviour at high pressures become relevant. At high pressures the chemical reaction times are shorter, i.e. the Damköhler number is bigger which lowers the NO concentration [6]. In addition, for the chosen residence time of 1.8 ms in the stirred reactor the velocity of the incoming jets is about half the speed of sound and therefore mixing is not optimally fast. Further improvements of the experiment and refinements of the numerical model are needed to assess the NO_x-kinetics at high pressure.

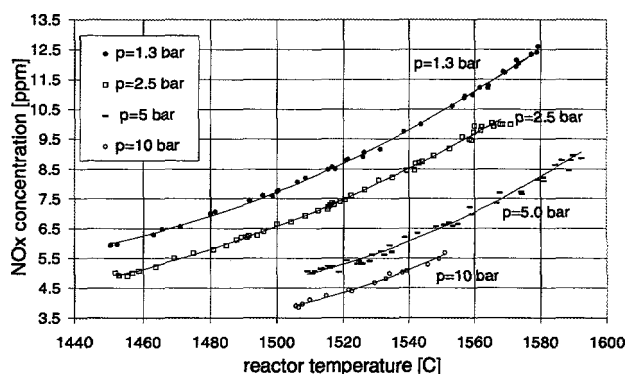


Fig. 3: Measured NO_x concentrations at different reactor temperatures and pressures: 1.3, 2.5, 5.0, 10.0 bars. Equivalence ratio = 0.55, residence time at 1550°C = 1.8 ms, methane.

5 ACKNOWLEDGEMENTS

This work is supported by Swiss National Energy Research Foundation (NEFF) and ABB.

6 REFERENCES

- [1] R.J. Kee, F.M. Rupley, J.A. Miller, "Chemkin-II: A Fortran Chemical Kinetics Package for the Analysis of Gas-Phase Chemical Kinetics", Sandia Report SAND89-8009B · UC-706, (Re-printed 1996).
- [2] J.A. Miller, C.T. Bowman, "Mechanism and Modeling of Nitrogen Chemistry in Combustion", Prog. Energy Combust. Sci. Vol. 15, pp. 287-338 (1989).
- [3] G.P. Smith, D.R. Crosley, D.M. Golden, M. Frenklach, W.C. Gardiner, R.K. Hanson, C.T. Bowman, "GRI-Mech 2.11", Annual Report SRI International (1996), in press. Mechanism available from the World Wide Web.
- [4] A. Schlegel, "Experimentelle und numerische Untersuchung der NO_x-Bildung bei der katalytisch stabilisierten und der nicht-katalysierten, mageren Vormischverbrennung", Diss. ETH Nr. 10887 (1994).
- [5] M.J. Pilling, T. Turanyi, K.J. Hughes, A.R. Clague, "The Leeds Methane Oxidation Mechanism", Version 2.1 26th Feb. 1996, School of Chemistry at Leeds University, UK. Mechanism available from the World Wide Web.
- [6] S.M. Correa, M.E. Braaten, "Parallel Simulations of Partially Stirred Methane Combustion", Combustion and Flame 94:469-486 (1993).

FORMATION OF NITRIC OXIDE IN AN INDUSTRIAL BURNER MEASURED BY 2-D LASER INDUCED FLUORESCENCE

A. Arnold, R. Bombach, B. Käppeli

We have performed two-dimensional Laser Induced Fluorescence (2-D LIF) measurements of nitric oxide and hydroxyl radical distributions in an industrial burner at atmospheric pressure. The relative 2-D LIF data of NO were set to an absolute scale by calibration with probe sampling combined with gas analysis.

1 INTRODUCTION

Detailed investigations of combustion processes are necessary in order to lower pollutant formation. Numerical simulation models can help to find the optimal combinations of various combustion parameters. Non intrusive experimental studies are required to supply quantitative data for the validation of numerical results and to provide input parameters for these models. For this purpose several laser-based spectroscopic methods have been developed and successfully applied in recent years [1,2].

IN the two-dimensional laser induced fluorescence technique (2-D LIF) a laser beam is formed into a light sheet which intersects the flow field under study and excites the molecules or atoms in a two-dimensional plane. The occurring fluorescence is collected with a two-dimensional detector such as an intensified CCD camera.

The easiest way to quantify 2-D LIF data is an external calibration. In the case of many stable species this can be done using probe sampling combined with conventional gas analysis.

In the flame under study the major part of the total NO amount is formed via the so called "Zeldovich" reaction path [3], i.e. via the reaction of atomic oxygen with molecular nitrogen. This reaction is extremely sensitive on the temperature. So the NO is mainly formed in the hottest zones of the flame and the total amount remains constant in the colder exhaust gases.

2 TYPE OF BURNER

The flame under study was a premixed methane / air flame at atmospheric pressure stabilized on a perforated steel sheet of 100x100 mm². Above each hole in the steel sheet a small flame was located leading to an array of about 170 stationary flames. The burner was operated at three different thermal loads (1,5 MW/m², 2 MW/m², 3 MW/m²) whereby the fuel to air ratio (Φ) was controlled by probe sampling in the exhaust gases. To provide optical access, parts of the burner housing were replaced by quartz windows.

3 DETECTION SCHEME

For the measurements of NO we used a frequency doubled YAG pumped dye laser system. The resulting UV output (286 nm) was mixed with the fundamental infrared beam (1064 nm) of the YAG laser to generate

radiation at a wavelength of about 226 nm. Here, NO can be excited to its A state [4]. In the same spectral range oxygen has strong absorption lines as well. So, for a sensitive and specific detection of NO the laser system has to be tuned to a line where oxygen does not absorb. Else an additional spectral filtering of the LIF signal would be necessary. Furthermore the thermal population of the rotational level chosen for excitation should be almost constant within the temperature range of the flame. These requirements were realized by exciting the R₁(21) rotational line in the (0-0) band of the A-X system of NO and using an interference filter ($\lambda_{\text{max}}=254$ nm, FWHM=7 nm, T_{max}=15 %) to transmit the fluorescence in the (0-2) and (0-3) band [5].

Since the LIF signal is proportional to the laser intensity one has to correct the LIF raw images for the intensity distribution of the light sheet. To obviate this procedure we have developed a new method for illuminating the plane where NO should be detected. Figure 1 shows the experimental set-up.

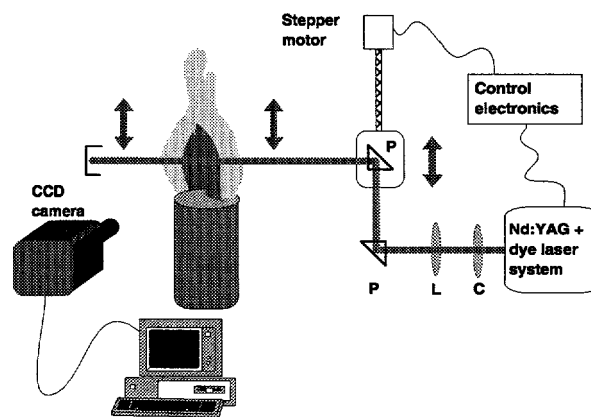


Fig. 1: Experimental arrangement for 2-D LIF measurements (P: prism, L: spherical lens, C: cylindrical lens).

While integrating the LIF signal on the CCD chip of the intensified camera we moved the position of the light sheet up and down orthogonally to the burner surface, i.e. in the plane of the light sheet. This procedure causes a perfectly homogeneous intensity distribution of the laser light. Furthermore a region of about 150 mm in height could be illuminated, thus avoiding a series of measurements for different light sheet positions which have to be put together to get the whole image. A typical result can be seen in Figure 2.

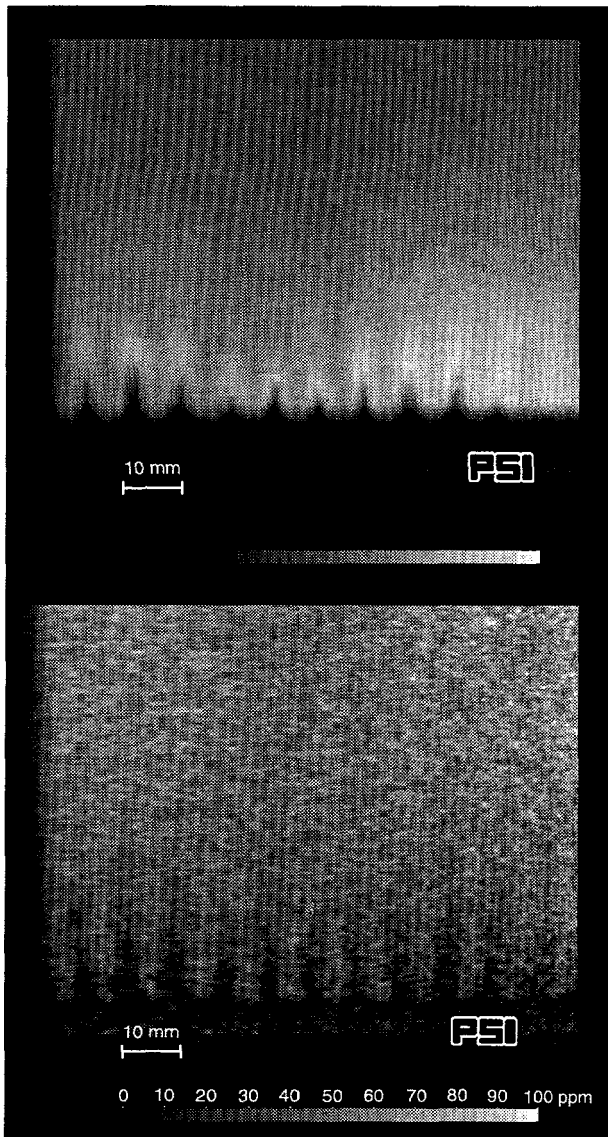


Fig. 2: Top: Relative OH concentration field at $\Phi = 0.87$, and a thermal load of 3 MW/m^2 , Bottom: Calibrated NO concentration field

The fluorescence quantum yield, i.e. the fraction of excited molecules which actually fluoresce, is affected by collisions (electronic quenching). As the quenching rate varies within the flame it has to be taken into account to analyze the LIF images. It was shown in [6] that the variation of the quenching rate in the flame front of a methane / air flame is on the order of 20 %, whereas downstream the flame front the quenching rate can be considered as constant. Since the major part of the total NO amount is generated behind the flame front these variations are negligible.

A comparison of these data with numerical results is in progress. The numerical simulation model which is used needs relative OH concentration profiles as an input parameter. Therefore, we performed OH radical measurements using the same procedure. Detailed

information about the OH detection scheme used can be taken from [7]. The corresponding relative OH concentration field can be seen in Figure 2.

Figure 3 shows the measured NO concentration as a function of height above the burner surface. It can be clearly seen that with increasing height the NO concentration approaches a constant value.

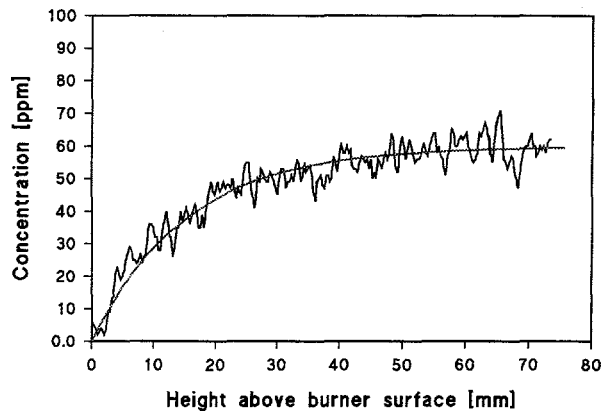


Fig. 3: Calibrated NO concentration as a function of height above the burner surface at $\Phi = 0.87$, and a thermal load of 3 MW/m^2 . The dashed curve is a guide to the eye.

In conclusion, we have measured absolute NO concentration fields in an industrial burner at atmospheric pressure using a combination of 2-D LIF and gas analysis. A comparison with numerical simulations is in work.

4 ACKNOWLEDGMENT

The authors are grateful to Urs Dogwiler for performing the gas analysis.

The financial support of the Swiss Federal Office of Energy (BEW) is gratefully acknowledged.

5 REFERENCES

- [1] A. Eckbreth: *Laser Diagnostics for Combustion Temperature and Species* (Abacus Press, Tunbridge Wells, UK, 1988).
- [2] A. Arnold et al.: *Ber. Buns. Ges. Phys. Chem.* **97**, 1650-1661 (1993).
- [3] J. Zeldovich: *Acta physicochimica U.R.S.S.* **21**, 4 (1946).
- [4] D.R. Grieser: *Appl. Opt.* **19**, 741 (1980).
- [5] I. Deezi: *Acta Phys.* **9**, 125 (1958).
- [6] A. Bräumer: *Dissertation, Universität Heidelberg* (1995).
- [7] A. Arnold, R. Bombach, B. Käppeli, A. Schlegel: *Appl. Phys. B*, accepted for publication, (1997).

BEAM STEERING EFFECTS IN TURBULENT HIGH PRESSURE FLAMES

B. Hemmerling, B. Käppeli

The propagation of a laser beam through a flame is influenced by variations of the optical density. Especially in turbulent high pressure flames this may seriously limit the use of laser diagnostic methods.

The nonintrusive investigation of combustion processes has proven highly productive during recent years. Among the most established methods are coherent anti-Stokes Raman scattering (CARS) and laser-induced fluorescence (LIF). They are routinely employed for measurements of temperature and species concentrations in technical combustion devices. However, in large scale, turbulent high pressure flames LIF and CARS experience limitations with respect to accuracy and applicability by beam steering effects.

In a nonhomogeneous medium the local propagation velocity of light is changed by variations of the index of refraction. If a light wave propagates through such a medium its wavefront will be distorted. Different parts of the wavefront travel at different velocities resulting in deflection, focusing and defocusing of the light beam, and in the appearance of a granular pattern of the intensity, the so called speckles.

The index of refraction depends on the composition of the medium, on temperature, and density. In a gas the thermo-optic coefficient ($\partial n / \partial T$) is usually small and can be neglected in comparison to the change of the refractive index caused by the variation in density and gas composition.

We carried out preliminary investigations of beam steering effects in a test rig which was built as a joint test facility for high pressure combustion by Asea Brown Boveri (ABB), Switzerland, the Federal Institute of Technology, Zurich, and the Paul Scherrer Institute. The test rig was equipped with a double cone burner developed by ABB. At the outlet the double cone burner had a diameter of 100 mm. It was mounted in a liner with a diameter of 155 mm. Holes with a diameter of 35 mm in the wall of the liner allowed for the optical access. Within the liner, the burner could be translated in axial direction with respect to the axis of optical access.

At 18 bar, the maximum operating pressure of the test rig, a thermal power of 8 MW is achieved with a fuel throughput of 200 g per second, and an air mass flow of 4.5 kg per second. The burner air can be preheated up to 500 °C. Typically, the air/fuel ratio was about $\lambda=2$. The turbulent Reynolds number exceeds 10^6 , and the Karlovitz and Damköhler numbers are larger than unity. Little is known about flames under these conditions. However, thick turbulent flames are expected.

To investigate beam steering effects we sent a laser sheet through the combustion chamber and recorded the emerging beam with a CCD camera. We used a combination of a cylindrical lens ($f=-65$ mm) and a spherical lens ($f=1000$ mm) to form the laser sheet. As light source we employed a frequency doubled Nd:YAG laser. The width of the laser sheet was limited by the diameter of the optical access holes in the liner. We estimate its thickness in the middle of the combustion chamber to about 300 μm . At the CCD camera, which was located about 700 mm away from the centre of the combustion chamber, the diverging laser sheet had again a thickness of about 1 mm. Due to the size of the CCD chip (8.5x12.7 mm²) only a part of the transmitted laser sheet could be recorded.

Figure 1 depicts a series of single shot recordings of head-on views of the laser sheet passing the combustion chamber. We binarized the pictures to get a good black and white representation. Arbitrarily, the threshold between black and white was set to 30% of the maximum intensity for each image. From top to bottom: The first picture shows the laser sheet without flame. We obtained the second image with the natural gas/air flame at 4 bar. The laser sheet is strongly fragmented and its envelope indicates distortion and an increased width. The process of fragmentation proceeds with increasing pressure. In the third picture, obtained at a pressure of 7 bar, the laser sheet can hardly be recognized. As shown with the fourth image at 14 bar the whole viewing area of the CCD camera is homogeneously filled with a speckle pattern.

For all laser-diagnostic methods the fragmentation of the laser sheet results in a deterioration of spatial resolution. Caused by the nonlinear dependence of the signal on the laser intensity and the necessity to obey phase matching conditions the CARS signal is more strongly affected by beam steering effects than for example the LIF signal. To define regions of applications for these measuring techniques it is necessary to investigate the influence of beam steering effects on the process of signal generation in more detail. On the other hand one can deduce information about the turbulence spectrum in the combustion chamber from an analysis of the speckle pattern. In the following we present some attempts to characterize the observed images. A more complete treatment is subject of forthcoming work.

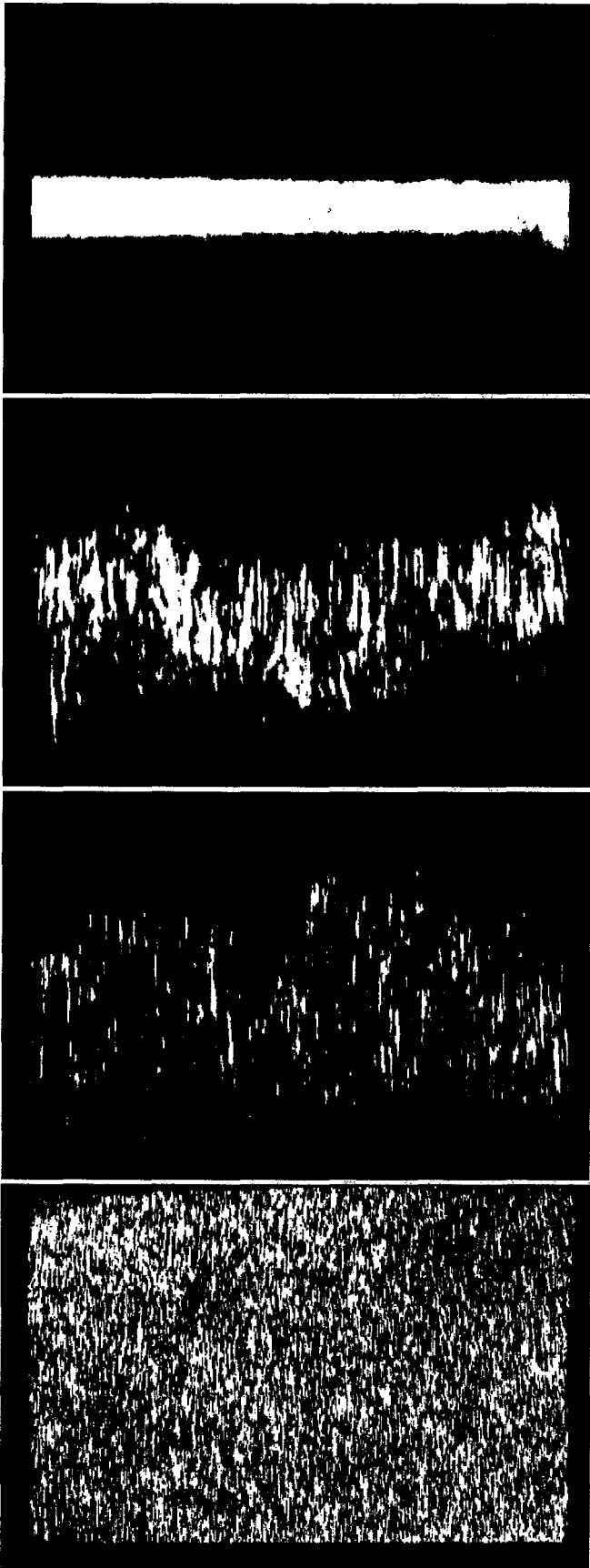


Fig. 1: Series of single-shot images showing the head-on view of the laser sheet passing the combustion chamber. From top to bottom: without flame, 4 bar, 7 bar, and 14 bar.

With increasing pressure the size of the fragments decreases. We define as ensemble averaged size of a fragment the area which is enclosed by the $1/e$ contour of the autocorrelation function computed over the image area. For well developed speckles, i.e. the phases of individual contributions are approximately uniform distributed over $(-\pi, \pi)$, the autocorrelation function of the image is proportional to the far-field diffraction pattern which would be produced by an illuminated object having the shape of the front face of the laser sheet [1]. This is well documented by the elongated shape of the speckles in Figure 1. A logarithmic plot of speckle size versus pressure shows an exponential behavior.

In case of coherent illumination the probability distribution of speckle intensity obeys negative exponential statistics [1]. However, the analysis of the images of Figure 1 reveals that with increasing pressure the maximum of the probability distributions is shifted towards higher intensity. This could be attributed to an increasing loss of spatial coherence of the incident laser light. Unfortunately flame radiation adds, especially at high pressure, an intensity background to the images that complicates an unambiguous analysis of the observed intensity distributions.

To characterize the degree of fragmentation we also determined the fractal dimension D_f of the observed images [2]. For a speckle contour one has $1 < D_f < 2$; the rougher the contour the higher the fractal dimension. We found that the fractal dimension depends on the threshold which we used to binarize the images. To compare the obtained images in terms of fractal dimension one has to introduce, somehow artificially, a class of images which were binarized using the same threshold. For a threshold set to 30% of the maximum intensity we obtained $D_f = 1.1$ for the image of the laser sheet without flame (see Figure 1). The fractal dimension increases from 1.32 ± 0.16 at 4 bar to 1.43 ± 0.13 at 14 bar (given are mean and standard deviation of five single-shot measurements, respectively). However, the dependence on the threshold and the strong single shot fluctuation does not favour a characterization of the obtained images by fractal dimension.

ACKNOWLEDGMENT

We thank the Swiss Federal Office of Energy (BEW) for financial support.

REFERENCES

- [1] J.W. Goodman, *"Statistical Optics"*, Wiley & Sons, New York, (1984).
- [2] B.B. Mandelbrot, *"The Fractal Geometry of Nature"*, W.F. Freeman & Co, New York, (1977).

A STUDY OF RELAXATION MECHANISMS IN THE $A^2\Sigma^+$ STATE OF NITRIC OXIDE BY TIME RESOLVED DOUBLE RESONANT POLARIZATION SPECTROSCOPY

A. Stampanoni-Panariello, R. Bombach, B. Hemmerling, W. Hubschmid

Double resonant polarization labeling spectroscopy is applied to detect nitric oxide in flames and to characterize rotational energy transfer and orientation changing collisions in its first excited electronic state.

1 INTRODUCTION

Nitric oxide (NO) is an important pollutant produced in combustion processes and plays a significant role in atmospheric chemistry. Therefore, optical methods which allow monitoring its concentration in a non-intrusive, temporally and spatially resolved ways have been widely pursued [1]. For accurate quantitative detection of NO by laser induced fluorescence (LIF) a detailed knowledge of the collisional re-distribution by vibrational and rotational energy transfer (VET, RET) and electronic quenching of electronically excited NO radicals is required.

Absorption or degenerate four wave mixing (DFWM) spectra of the A-X system of NO are obscured by the presence of strong predissociative lines from molecular oxygen which accidentally absorbs in the same wavelength range around 226 nm. Furthermore, in hydrocarbon flames a nonresonant background hinders the sensitive detection of NO by DFWM. All these problems may be overcome by employing double resonance techniques.

Double resonance polarization labeling spectroscopy (DRPLS) [2] is based on the alignment or orientation of molecules by optical pumping with a narrow band polarized laser. The sample of molecules is placed between two crossed polarizers. The induced anisotropy alters the probe beam polarization at those frequencies which interact with the oriented or aligned molecules. Light at these frequencies can then pass through the crossed polarizers. Therefore, using a broad band probe laser and a spectrometer permits the multiplex detection of all allowed transitions.

2 EXPERIMENTAL SETUP

The experimental arrangement used in this work is shown in Figure 1. The radiation from a pulsed tunable dye laser having a pulse duration of about 10 ns and a spectral bandwidth of 0.15 cm^{-1} at 226 nm is used to induce individual transitions in the $A^2\Sigma^+ v' = 0 \leftarrow X^2\Pi_{3/2,1/2} v'' = 0$ system of NO. The output of this laser will be referred to as the pump beam. A second dye laser (probe beam) is used to generate spectrally broad light at about 600 nm with pulse duration of about 7 ns and bandwidth of approx. 100 cm^{-1} . The probe beam excites the P and R rotational branches of the $E^2\Sigma^+ v'' = 0 \leftarrow A^2\Sigma^+ v' = 0$ system. The probe beam passes polarizer PL1, the sample cell, and finally polarizer PL2 which is crossed

to PL1. The extinction ratio of both polarizers is 10^5 . Before it enters the cell the pump beam is circular polarized by a $\lambda/4$ plate. To eliminate the contribution to the linewidth by Doppler-broadening, pump and probe beam are counterpropagating and overlap in the cell at an angle of about 1° . Both lasers are synchronized to each other by a digital delay generator. The signal is focused onto a slit of a monochromator with 1 m focal length, operated in first order. A back illuminated CCD camera is attached at its output. Perpendicularly to the pump beam direction spectral dispersed fluorescence from the $A^2\Sigma^+ v' = 0 \rightarrow X^2\Pi_{3/2,1/2} v'' = 0$ system and total fluorescence from the $E^2\Sigma^+ \rightarrow A^2\Sigma^+$ system are recorded. The synchronization of the lasers and the data acquisition is performed with a personal computer.

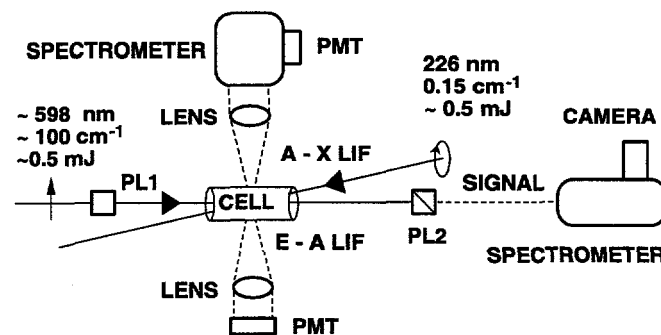


Fig. 1: Experimental arrangement for the detection of NO by double resonant polarization spectroscopy and LIF. (PL1, PL2: polarizer. PMT: photomultiplier tube).

3 RESULTS

DRPLS is first applied for measurements in a NO-seeded methane-air flat flame (Figure 2). The narrow band pump laser is scanned over a range of 0.3 nm to excite individual rovibrational lines in the $A(v' = 0) \leftarrow X(v'' = 0)$ system and the probe laser is set to the center wavelength 597 nm. The upper and the lower spectrum in Figure 2 are the fluorescence signals of the $E(v' = 0) \rightarrow A(v'' = 0)$ and of the $A(v' = 0) \leftarrow X(v'' = 0)$ system, respectively. Since both electronic states, A and E, belong to the same Rydberg series, transitions between them are highly diagonal. Consequently suppression of stray light from the probe beam is difficult to achieve and affects the signal to noise ratio of the $E(v' = 0) \rightarrow A(v'' = 0)$ fluorescence spectrum.

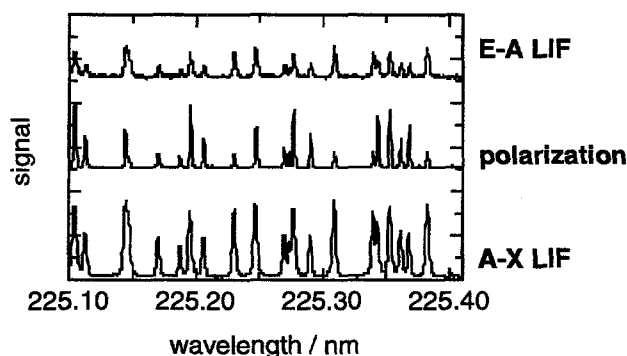


Fig. 2: LIF and polarization spectra in a NO seeded methane-air flat flame. The center wavelength of the probe beam is set to 597 nm corresponding to the $E(v'=0) \rightarrow A(v''=0)$ R(21) transition. The lines of the $A(v'=0) \leftarrow X(v''=0)$ LIF spectrum can be unequivocally assigned.

The polarization spectrum (middle spectrum) exhibits a high signal to noise ratio. Due to the quadratic dependence of the signal on the population the polarization spectrum shows line intensities which are different from those obtained by LIF.

Rotational energy transfer (RET) can be investigated by delaying the probe pulse with respect to the pump pulse. For this aim cell experiments at room temperature and NO pressure of about 1 mbar are carried out. Figure 3 shows polarization spectra for different time delays between pump and probe pulses. By pumping the ${}^S R_{21}(4)$ transition of the $A(v'=0) \leftarrow X(v''=0)$ system the level $N=6$ has been populated. The strong line at 600.97 nm, clearly visible at zero time delay, is the probed P(6) transition of the $E(v'=0) \rightarrow A(v''=0)$ system (mother line). With increasing time delay collision induced satellites arise around the mother line according the selection rule $\Delta N = \pm n$, with n being an integer.

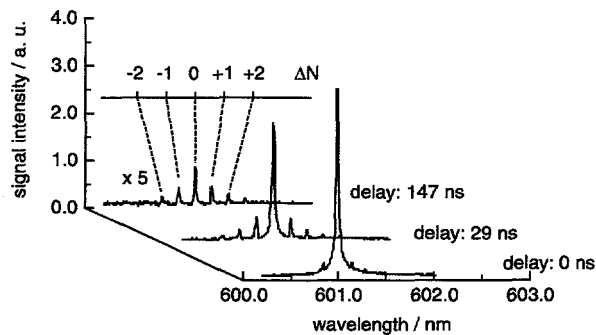


Fig. 3: Rotational energy transfer starting from level $N=6$. The spectra for delay 0 ns and 29 ns are averaged over 10 shots while the spectrum for delay 147 ns is averaged over 20 shots.

The time delay between pump and probe pulse is varied from -19 ns up to 267 ns in steps of 2 ns to 10 ns. Figure 4 shows the integrated intensity of mother line and of two satellites ($\Delta N = -1, -2$) versus time delay. The decay of the integrated intensity of the mother line is fitted with an exponential and yields a decay constant $\tau = 42.2 \pm 0.8$ ns. From the measurement of the pressure dependence of the decay time of the polarisation signal a total quenching cross section $\sigma_{\text{pol}} = 104.5 \pm 1.8 \text{ \AA}^2$ is determined. The cross section by DRPLS includes contributions from LIF, RET, and from the loss of alignment (or orientation). LIF measurements yield a quenching cross section $\sigma_{\text{LIF}} = 45 \pm 2 \text{ \AA}^2$, which agrees with measurements by Zhang et al. [3]. The difference of σ_{pol} and σ_{LIF} is therefore attributed to orientation changing collisions and to RET. A more complete analysis of the temporal evolution of mother line and satellites will be the subject of future work.

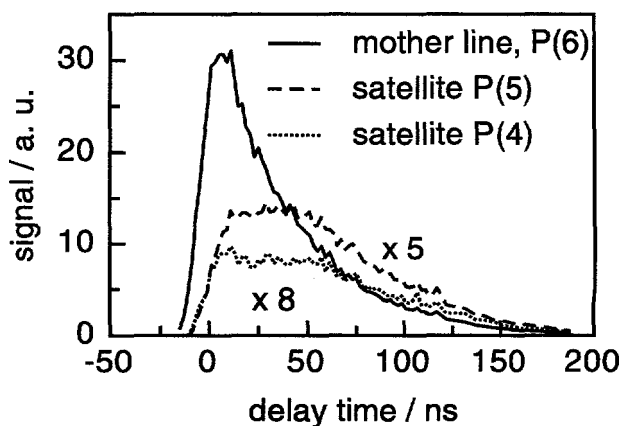


Fig. 4: Temporal development of the integrated intensity of mother line and collisional populated rotational satellites. $T=295$ K, $P_{\text{NO}}=1$ mbar.

LIF and DRPLS measurements have been carried out at room temperature and different NO pressures. The results of this work suggest that DRPLS has a potential for characterizing dynamic effects occurring on the ns scale of combustion relevant species.

4 ACKNOWLEDGMENT

The financial support of the Swiss Federal Office of Energy (BEW) is gratefully acknowledged.

5 REFERENCES

- [1] S.S. Penner, C.P. Wang, M.Y. Bahadori, 20th Symposium (International) on Combustion, 1149 (1984).
- [2] R. Teets, R. Feinberg, T.W. Hänsch, A.L. Schawlow, Phys. Rev. Lett. **37**, 683 (1976).
- [3] R. Zhang, D.R. Crosley, J. Chem. Phys. **102** 7418, (1995).

LASER-INDUCED GRATINGS IN THE GAS PHASE EXCITED VIA RAMAN-ACTIVE TRANSITIONS

*D.N. Kozlov (General Physics Institute, Russian Academy of Sciences, Moscow, Russia),
R. Bombach, B. Hemmerling, W. Hubschmid*

We report on a new time resolved coherent Raman technique that is based on the generation of thermal gratings following a population change among molecular levels induced by stimulated Raman pumping. This is achieved by spatially and temporally overlapping intensity interference patterns generated independently by two lasers. When this technique is used in carbon dioxide, employing transitions which belong to the Q-branches of the $\nu_1/2\nu_2$ Fermi dyad, it is possible to investigate molecular energy transfer processes.

Laser-induced gratings (LIGs) are spatial modulations of the complex index of refraction produced by the interference of laser beams usually originating from one laser [1]. Resonant excitation of gratings is accompanied by a change of the population distribution among atomic/molecular energy levels. Eventually, subsequent collisional relaxation leads to the formation of thermal gratings. Electrostrictive gratings are generated at any frequency of the laser and have been observed in solids and liquids [2], and in gases [3-5].

Results on resonantly excited gratings in gases and their use for spectroscopy and diagnostics have been presented in a number of articles. There, dipole-allowed molecular transitions have been used for the creation of the gratings. However, it is not always possible to find a dipole-allowed transition in the spectral range conveniently accessible by lasers. Therefore, there is an interest to employ two-photon excited Raman transitions for the generation of gratings.

In the present contribution we report, to our knowledge for the first time, about light scattering on gratings formed by stimulated Raman pumping in the gas phase (RLIGs) [6]. One can generate such gratings of vibrational state populations by spatially and temporally overlapping the interference pattern produced by one pulsed laser with the beam of a second pulsed laser that differs in frequency from the first by a Raman frequency of the medium. On the expense of a slightly increased complexity of the experimental setup, the contrast of the grating can be enhanced by overlapping the two interference patterns formed independently by the two lasers. The grating is read out by a continuous laser.

In a gas the dependence of the refractive index on temperature is usually small and can be neglected in comparison to the change of the refractive index caused by the variation of density. The density change effected by electrostriction and by release of resonant

absorbed laser energy in the form of heat can be quantitatively described using the linearized hydrodynamic equations [7]. As a solution of these equations one finds a superposition of a standing acoustic wave (due to adiabatic compression) and a stationary (nonoscillating) density modulation (due to isobaric heating). For small attenuation the oscillation period of the standing acoustic wave is $T_g = \Lambda/v$, where v is the adiabatic sound velocity, $\Lambda = \lambda/[2\sin(\theta/2)]$ is the fringe spacing of the interference pattern generated by two beams of one of the lasers intersecting each other at an angle θ , and λ is the wavelength of the laser generating the grating.

The properties of LIGs formed by thermalization of absorbed laser energy depend on the time constant τ_r of the energy release. Fast energy release ($T_g \gg 2\pi\tau_r$) generates a standing acoustic wave and a stationary density modulation with equal amplitude. Slow energy release ($T_g \ll 2\pi\tau_r$) favours the generation of the stationary density modulation whereas the development

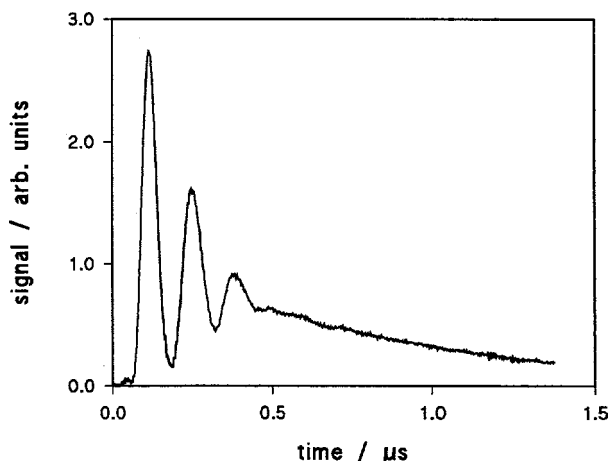


Fig. 1: Temporal behaviour of a single-pulse RLIG signal obtained at 0.2 bar of CO₂. The excitation is resonant to the ν_1 Q-branch.

of the acoustic waves is subject to destructive superposition of acoustic waves generated at different times.

Figure 1 shows the temporal evolution of the single-pulse RLIG signal obtained at room temperature and 0.2 bar of CO₂. The grating was generated by a Nd:YAG laser working at 532 nm and a narrow band dye laser tuned to 574.4 nm. Therefore, their frequency difference corresponds to an excitation of the ν_1 Q branch (1388.2 cm⁻¹). The signal oscillates with a period $T \approx 120$ ns and is damped with a time constant of about 300 ns. As a small peak at the beginning of the temporal development of the RLIG signal (at $t \approx 45$ ns in Figure 1) the electrostrictive contribution to the scattering efficiency is recognizable. The stationary density modulation persists longer in the excitation area than the acoustic waves and leads to the extended unstructured tail of the RLIG signal.

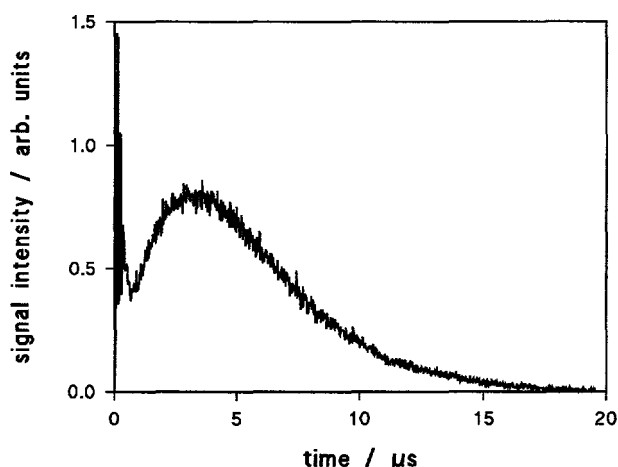


Fig. 2: Temporal behaviour of a single-pulse RLIG signal obtained for a mixture of 0.1 bar CO₂ and 1.9 bar Ar. The excitation is resonant to the ν_1 Q-branch.

Figure 2 demonstrates the effect of slow release of absorbed laser energy. The depicted temporal behaviour of the scattering efficiency is obtained at resonance for a mixture of 0.1 bar CO₂ and 1.9 bar argon. The slow release of absorbed laser energy causes the development of a stationary density modulation which leads to a maximum in the temporal evolution of the scattering efficiency about 3.5 μ s after occurrence of the laser pulses setting up the grating.

Electrostriction and fast energy exchange between the laser excited 1000 or 0200 level of CO₂ and the thermal bath characterize the early phase in the temporal evolution of the grating scattering efficiency ($0 \leq t \leq 400$ ns). The energy exchange takes place in course of population redistribution within the multiplet of vibrational states $\{10^0, 02^0, 02^0\}$ due to collisions with CO₂ in the ground state or with Ar atoms. At room temperature and a pressure of 0.2 bar, transitions from the vibrational states 10^0 or 02^0 to 02^0

occur in 9-15 ns [8]. Likewise fast is the vibration-vibration relaxation of CO₂ (02^0) by collisions with CO₂ in the ground state yielding CO₂ in the vibrational state 01^0 [8]. If buffer gas is added these processes may go on significantly faster. Subsequent vibration-translation (v-T) relaxation is very slow. For CO₂ and Ar as collision partners the time constants of relaxation are 38 μ s (0.2 bar CO₂) and 22 μ s (0.1 bar CO₂ and 1.9 bar Ar), respectively [9,10]. Therefore, v-T relaxation of CO₂ (01^0) primarily sustains the formation of a stationary density modulation late in the temporal evolution of the scattering efficiency (see Figure 2). For the excitation of distinct molecular levels the pathway of energy release is different and may lead to differences in the temporal behaviour of the scattering efficiency.

Molecular diffusion washes out the spatial density modulation of molecules in the excited state and controls the amount to which the relatively slow v-T relaxation contributes to the formation of a stationary density modulation. Moreover, the already established temperature variation is destroyed by heat conduction. Adding buffer gas slows down the diffusion of excited CO₂ molecules enabling a larger part of them to release the excited state energy spatially in phase.

ACKNOWLEDGMENT

We thank the Swiss Federal Office of Energy (BEW) for financial support.

REFERENCES

- [1] H.J. Eichler, P. Günter, D.W. Pohl, "Laser Induced Dynamic Gratings" (Springer, Berlin, 1986).
- [2] K.A. Nelson, D.R. Lutz, M.D. Fayer, L. Madison, Phys. Rev. B 24, 3261 (1981).
- [3] B. Hemmerling, A. Stampanoni-Panariello, Appl. Phys. B 57, 281 (1993).
- [4] E.B. Cummings, Opt. Lett. 19, 1361 (1994).
- [5] A. Stampanoni-Panariello, B. Hemmerling, W. Hubschmid, Phys. Rev. A 51, 655 (1995).
- [6] D.N. Kozlov, R. Bombach, B. Hemmerling, W. Hubschmid, accepted by Opt. Lett.
- [7] W. Hubschmid, B. Hemmerling, A. Stampanoni-Panariello, J. Opt. Soc. Am. B 12, 1850 (1995).
- [8] A.M. Brodnikovskii, S.M. Gladkov, M.G. Karimov, N.I. Koroteev, Sov. ZhETPh 84, 1664 (1983).
- [9] F. Lepoutre, G. Louis, H. Manceau, Chem. Phys. Lett. 48, 509 (1977).
- [10] C. Allen, T.J. Price, C.J.S. Simpson, Chem. Phys. Lett. 45, 183 (1977).

STIMULATED EMISSION PUMPING OF NH IN FLAMES BY USING TWO-COLOR RESONANT FOUR-WAVE MIXING

P.P. Radi, H.-M. Frey, B. Mischler, A.P. Tzannis, P. Beaud, T. Gerber

In this work we examine the analytical potential of two-color resonant four-wave mixing for the determination and characterization of trace elements in a combustion environment. Experimental results for NH in flames at atmospheric pressure are presented. The selectivity of the technique is used to simplify the Q-branch region of the (0-0) $A^3\Pi-X^3\Sigma$ vibronic transition of NH. In addition, we demonstrate that the technique is sensitive to state changing collisions.

1 INTRODUCTION

Two-color resonant four-wave mixing (RFWM) has been used for double resonance spectroscopy of stable molecules in sample cells [1], [2], [3] and in free-jet expansions [4]. The aim of this work is to apply the method to a relevant species in a flame and characterize the analytical potential of the technique for the detection of trace elements in combustion processes.

2 EXPERIMENTAL SETUP

The arrangement of the optical system is shown on Figure 1. To establish a forward box RFWM configuration, the output of the PUMP laser system is split by a beamsplitter (BS) into two beams of equal intensity.

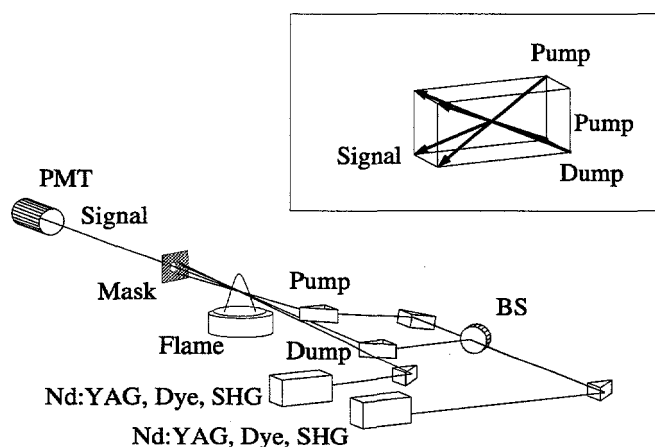


Fig. 1: Experimental setup.

Three prisms are used to offset the pump beams vertically and to direct them to the interaction zone. The PUMP beams are tipped out of the horizontal plane by an angle of $\sim 1^\circ$. As sketched on the inset of Figure 1, the DUMP beam is aligned to meet the phase matching conditions. NH measurements are performed in a NH_3/O_2 flame stabilized on a welding torch. Fuel and air flows are determined by using mass flow controllers.

3 RESULTS AND DISCUSSION

Figure 2 demonstrates the advantage of spectral simplification of the RFWM technique. The rotational Degenerate Four-Wave Mixing (DFWM) spectrum of the NH radical in the Q-branch region in the (0-0) band of

the $A^3\Pi-X^3\Sigma$ electronic transition is shown in Figure 2a. A congested spectrum displaying a series of overlapping transitions is observed. In contrast, Figure 2b depicts the two-color RFWM spectrum on the same frequency scale. The PUMP laser is tuned to overlap with the $Q_1(5)$ transition in the (1-0) band at 32770 cm^{-1} exciting molecules in the $J=5$ and $v=1$ level of the $^3\Pi$ state. Scanning the frequency of the DUMP laser in the vicinity of 337 nm reveals two strong transitions only, originating from the $Q_1(5)$ rotational transi-

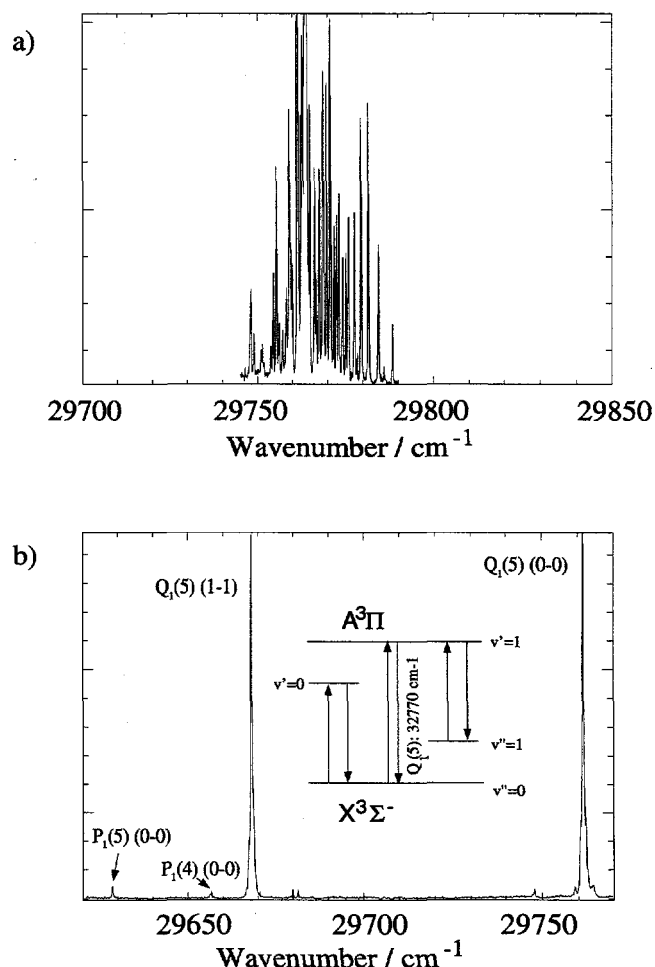


Fig. 2: Spectral simplification of the NH spectrum by intermediate level labelling.

tions in the (1-1) and (0-0) vibrational bands. The two processes involved are (1) stimulated emission pumping (SEP) involving the first vibrational state of

the $A^3\Pi$ state and (2) upward transition due to diffraction from the transient grating produced from the depletion of the ground state by the PUMP laser [1]. The signal-to-noise ratio of $\sim 100:1$ is typical for the two-color RFWM experiments performed on NH by using the excitation scheme shown on the inset of Figure 2b.

In Figure 3 the DUMP laser is tuned to the $Q_3(9)$ transition in the (0-0) band while scanning the PUMP laser in the vicinity of the $Q_3(9)$ upward transition in the (1-0) band. An intense upward transition appears in the scanned region at the frequency of the (1-0) $Q_3(9)$ transition since the PUMP laser is in resonance with the ground state selected by the DUMP laser ($F_3(9)$ of $X^3\Sigma^-(v''=0)$). In addition, signals are observed when the PUMP laser is tuned to states ($Q_3(J=12-6)$) that are inducing rotational energy transfer (RET) to $F_3(9)$. Note, that a strong tendency of symmetry conservation ($F_3 \rightarrow F_3$) is observed in the case of NH, in contrary to the findings for the OH radical [5]. The sensitivity of

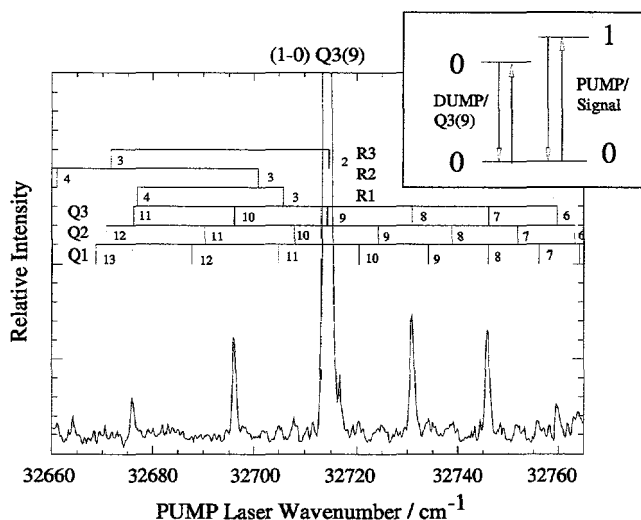


Fig. 2: Spectral simplification of the NH spectrum by intermediate level labelling.

the method for collisionally induced energy transfer processes is interesting since information on relaxation processes of the excited level as a function of chemical composition and temperature throughout the reaction zone is of importance for the quantitative analysis of LIF measurements in combustion systems. The initial results shown in Figure 3 suggest that two-color RFWM might be an alternative and complementary method for the investigation of collisional effects in flames exhibiting high spectral and spatial resolution. However, a more careful set of the two-color RFWM

experiments needs to be performed and is under way in this laboratory. In particular weak fields have to be employed in order to avoid saturation of the signals.

4 SUMMARY

Initial experiments that demonstrate the detection of NH in atmospheric flames by using two-color RFWM are presented as a promising spectroscopic technique for combustion diagnostics. The method has the potential to monitor trace species that do not fluoresce or have poor fluorescent quantum yields (for example radicals like CH_3 , C_2H , C_2H_3 and C_6H_5). In particular, we believe that the technique is advantageous for the detection of polyatomic molecules displaying a congested one-photon spectra due to thermal population of many ro-vibrational levels in the ground state. The resulting one-color broad-band spectra prevent selective detection of specific levels and are, therefore, not useful for diagnostic purposes. Intermediate level labelling by using two input frequencies that interact with two distinct molecular transitions can simplify such spectra significantly, enabling the selective detection of such molecules. Additionally, the observed sensitivity for dynamic processes is of particular interest. An investigation of the collisional state changes in the upper and ground level could yield information on rotational energy transfer and other energy-transfer mechanisms occurring in a flame environment.

5 ACKNOWLEDGEMENTS

The authors thank Eric A. Rohlffing, Sandia, for the helpful discussions. This work is supported by the Swiss Department of Energy (BEW).

6 REFERENCES

- [1] M.A. Buntine, D.W. Chandler and C.C. Hayden, *J. Chem. Phys.* 97(1), 707, (1992).
- [2] E.F. Cormack, S.T. Pratt, P.M. Dehmer and J.L. Dehmer, *Chem. Phys. Lett.* 211(1), 147, (1993).
- [3] M.N.R. Ashfold, D.W. Chandler, C.C. Hayden, R.I. McKay and A.J.R. Heck, *Chem. Phys.* 201, 237, (1995).
- [4] S. Williams, J.D. Tobiasson, J.R. Dunlop and E. Rohlffing, *J. Chem. Phys.* 102(21), 8342 and references therein, (1995).
- [5] P.P. Radi, H.-M. Frey, B. Mischler, A.P. Tzannis, P. Beaud, T. Gerber, *Chem. Phys. Lett.*, in print.

ROTATIONAL ENERGY TRANSFER OF THE $A^2\Sigma^+(v'=1)$ STATE OF OH

P. Beaud, P. Radi, H.-M. Frey, B. Mischler, A.P. Tzannis, T. Gerber

Spectrally and temporally resolved laser excited fluorescence of OH is investigated in the picosecond time domain. The total rotational energy transfer (RET) rate from the excited state is determined from the experimental data. Simulated spectra obtained by modelling RET with the energy corrected sudden approximation agree well with the measured spectra.

Laser-induced fluorescence of OH is a commonly used tool in combustion diagnostics. The knowledge of the collisional deactivation of the excited state is, however, essential to obtain quantitative results from LIF measurements. Due to the fast time scales involved in atmospheric pressure flames ultrafast excitation and detection on a picosecond time scale is required. Moreover, to distinguish between quenching, vibrational (VET) and rotational energy transfer (RET), simultaneous spectrally and temporally resolved detection of the LIF signal is required.

Recently we presented measurements of temporally and spectrally resolved fluorescence decays of OH $A^2\Sigma^+(v'=1,0)$ using picosecond excitation and detection [1]. We developed an empirical model to describe the time dependence due to rotational state relaxation, quenching, and VET. By applying this model to the measured 1-0 and 0-0 emission bands, rotational state specific quenching and VET rates can be determined. In this work the 1-1 emission band is used to study RET and molecule reorientation within the $v'=1$ rotational level. The time dependence of the population of rotational state, i , within the excited state $A^2\Sigma^+(v'=1)$ is described by:

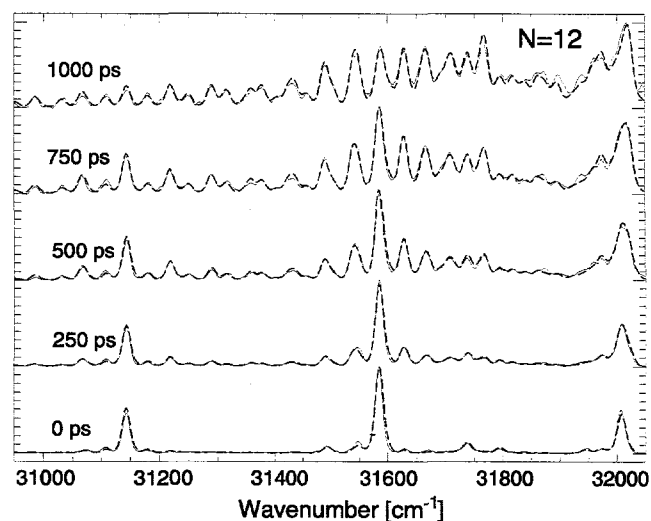
$$\frac{dn_i}{dt} = - \left(Q_i + V_i^{10} + \sum_{i \neq j} k_{ij} \right) n_i + \sum_{i \neq j} k_{ji} n_j \quad (1)$$

where Q_i is the electronic quenching and V_i^{10} the VET rate. The matrix k describes the energy transfer within the rotational states. The total RET rate ($k_L = \sum_{i \neq j} k_{ij}$) out of the initially excited rotational state is determined from the experimental data. The results are summarised in the following table.

| | $N=4$ | $N=12$ |
|--|----------------|----------------|
| Q [10^8 s^{-1}] | 10.0 ± 1.3 | 5.41 ± 0.6 |
| V^{10} [10^8 s^{-1}] | 5.23 ± 0.2 | 1.93 ± 0.1 |
| k_L (experiment) [10^8 s^{-1}] | 56.5 ± 3 | 26.1 ± 3 |
| k_L (simulation) [10^8 s^{-1}] | 55.0 | 28.9 |

At typical flame temperature of ~ 2000 K approximately 20 rotational states are occupied which requires the knowledge of 40×40 coefficients (since each rotational state is split into two spin components). However, the OH emission spectrum is rather dense and the spectral resolution of the experiment is insufficient to determine these rates individually. Therefore the RET matrix is obtained by comparing the experi-

mental spectra with simulated ones. The derived quenching and VET rates are used as input for the simulation. RET is modelled with the energy corrected sudden (ECS) approximation [2,3] in conjunction with an energy gap power law [4]. Using the parameter values derived from the global fit, the simulated total RET rates out of the initially excited state agree well with the experimental result (see Table). In the Figure the measured (solid) and simulated (dashed line) temporal evolution of the 1-1 emission band following excitation to the $F_1(12)$ rotational state is shown.



Generally, the RET matrix should be determined separately for each collision partner [5]. However, we observed, that the model fits the experiment fairly well even without specifying collisions with different flame species. Incorporating separate RET matrices for each collision partner (in our flame dominantly N_2 , H_2O and CO_2) will predominantly affect the transfer rates which involve a change of electron spin [5].

ACKNOWLEDGEMENT

Financial support from the Swiss Federal Energy Office (BEW) is gratefully acknowledged.

- [1] P. Beaud et al., PSI annual report, Annex V (1985); P. Beaud et al., to be published.
- [2] M. Alexander, J. Chem. Phys. 76, 3637 (1982).
- [3] A. DePristo et al., J. Chem. Phys. 71, 850 (1979).
- [4] T. Brunner et al., Phys. Rev. Lett. 41, 857 (1978).
- [5] R. Kienle et al., submitted to Appl. Phys. B.

PHASE-CONJUGATE RESONANT HOLOGRAPHIC INTERFEROMETRY APPLIED TO NH CONCENTRATION MEASUREMENTS IN A 2D DIFFUSION FLAME

A.P. Tzannis, P. Beaud, H.-M. Frey, T. Gerber, B. Mischler, P.P. Radi

Resonant Holographic Interferometry is a method based on the anomalous dispersion of light having a frequency close to an electronic transition of a molecule. We propose a novel single-laser, two-colour setup for recording resonant holograms and apply it to 2D species concentration measurements. The second color is generated by optical phase-conjugation from Stimulated Brillouin scattering in a cell. Phase-Conjugate Resonant Holographic Interferometry (PCRHI) is demonstrated in a 2D NH₃/O₂ flame yielding interferograms that contain information on the NH radical distribution in the flame. Experimental results are quantified by applying a numerical computation of the Voigt profiles.

Resonant Holographic Interferometry (RHI) has gained attention as a non-intrusive technique in reacting gaseous flows since it combines the species selectivity of spectroscopy with the high sensitivity and the substantial spatial resolution capabilities of interferometry [1]. The interaction of light with a medium can be described by the complex refractive index. In addition to the bulk refractive index a resonant contribution is obtained in the proximity of an electronic transition of a molecule. The frequency (ν) dependence of the complex refractive index [2], $n'(\nu)$ is represented by $n'(\nu)=[n_0+n(\nu)]-i\kappa(\nu)$, where $n(\nu)$ and $\kappa(\nu)$ contain the population density, the line shape (taking into account Doppler and collision broadening) and the line strength for a given temperature.

Near an electronic transition of a molecule, a light wave will experience an attenuation of its intensity due to absorption, originating from the imaginary part of the complex refractive index. The substantial change in the real part of the refractive index generates a relative phase shift between two waves of slightly different frequencies as they pass through the flame. In fact, the phase velocity of the two waves will be altered according to the total real part of the refractive index, $n_0+n(\nu)$. The bulk refractive index n_0 of the flame is eliminated, by interferometric subtraction, yielding the net contribution of the resonance effect to the refractive index $n(\nu)$. Holography is applied to perform the interferometric subtraction. The two waves are recorded on the same holographic plate and subsequently reconstructed simultaneously to interfere. Fringe shifts are observed in areas where the resonant species have introduced a refractive index difference for the two exposure frequencies.

In order to provide the two frequencies required for RHI, we apply optical phase-conjugation by Stimulated Brillouin scattering in order to generate the second frequency [3]. By tightly focusing ~50% of the laser light into a cell containing n-hexane, an acoustical wave is generated that diffracts part of the incoming light in the reverse direction. The resulting beam is phase-conjugate to the incoming light yielding a second 'laser beam' of high temporal and spectral quality. The process introduces a shift towards lower frequency, due to the diffraction of the beam on the

acoustic wave. The frequency shift of ~8.5GHz introduced by the phase-conjugation matches approximately the linewidth of many molecular transitions at typical flame temperatures.

For the experiment, a Wolfhard-Parker slot burner is used to stabilize an NH₃/O₂ flame. The object beam passes parallel to the slot axis and samples a 2D flame and consequently a 2D refractive index field. The two following figures show the resonant effect. In Figure 1 both wavelengths are OFF resonance, and only reference fringes are seen, since the two wavefronts are slightly tilted with respect to each other. The bulk refractive index n_0 of the flame has been eliminated. In Figure 2 the two wavelengths are tuned to the proximity of the Q₃(5) transition in the (0,0) vibrational band of the A³Π-X³Σ⁻ system of NH, such that they match approximately the two opposite-signed maxima of the dispersion curve $n(\nu)$. Fringe shifts appear where the two wavefronts interact with the NH radicals. Applying a computation of the complex refractive index, quantitative information on the NH concentration distribution is obtained.

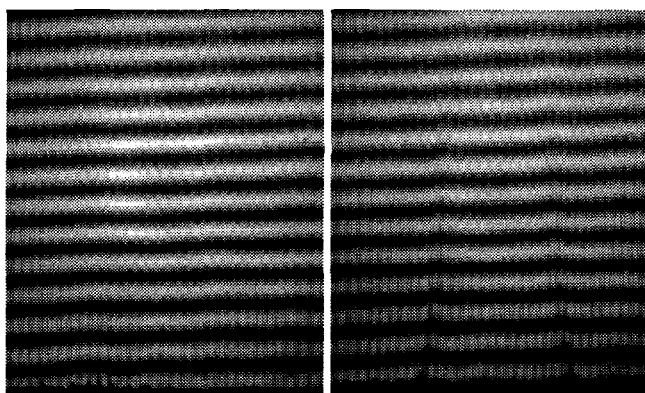


Fig. 1: OFF resonance. Fig. 2: ON resonance.

The financial support of the Swiss Department of Energy (BEW) is gratefully acknowledged.

- [1] J.M. Sirota and W.H. Christiansen, in *21st Fluid Dynamics, Plasma Dynamics and Lasers Conference* (AIAA, Seattle WA, 1990).
- [2] G. Blendstrup, D. Bershader, P.W. Langhoff, *AIAA J.* **16**, 737 (1978). A.P. Tzannis et al, to be published in *Applied Optics*.
- [3] A. Yariv, *Quantum Electronics*, 475-481 (1988).

MASS SPECTROMETRIC CHARACTERIZATION OF A PYROLYTIC RADICAL SOURCE USING FEMTOSECOND IONIZATION

H.M. Frey, P. Beaud, B. Mischler, P.P. Radi, A.P. Tzannis, T. Gerber

Radicals play, as reactive species, an important role in the chemistry of combustion. In contrast to atmospheric flames where spectra are congested due to high vibrational and rotational excitation, experiments in the cold environment of a molecular beam (MB) yield clean spectra that can be easily attributed to one species by Resonantly Enhanced Multi Photon Ionization (REMPI). A pyrolytic radical source has been set up. To characterize the efficiency of the source 'soft' ionization with femto second pulses is applied which results in less fragmentation, simplifying the interpretation of the mass spectrum.

1 INTRODUCTION

Radicals are of special interest in combustion research since they are the short lived species in chemical reactions that finally are responsible for the heat release in a flame. Successful spectroscopic investigations by Laser Induced Fluorescence (LIF), Degenerate Four Wave Mixing (DFWM) and 2-Color Four Wave Mixing (2-CFWM) [1] of radicals such as OH and NH in flames depend on an exact knowledge of the spectroscopy of the species of interest. By monitoring the evolution from the formation and decay of these molecules in combustion processes, we gain insight about reaction pathways. In addition we are able to extract reaction rates when applying a time resolving spectroscopic technique.

2 APPARATUS

The design of the radical source follows the original set-up of Chen [2]. A Neon gas pulse with the precursor to be pyrolyzed is expanded through a silicon carbide tube that is resistively heated to 2100 K. The residence time in the hot zone is on the order of a few μ s which permits one or several unimolecular decomposition events during the flow time through the hot nozzle. Immediately after the reaction zone the molecules are expanded into high vacuum to form a supersonic MB. No recombination or further decomposition is possible in the collision free environment of the MB. After ionization with a femtosecond laser (Clark MXR) detection takes place in a reflectron type time of flight mass spectrometer. Data are collected with a digitizer and stored for further data treatment on a PC.

3 RESULTS

Pyrolysis of CS_2 : To probe the cooling of the beam CS_2 is introduced into the nozzle at a source temperature of 1200°C. In the mass spectrum in Figure 1 dissociation is evident in the MS, but also dimer formation (S_2) due to collisions and subsequent cooling in the MB during the expansion can be observed.

Pyrolysis of CH_3CN : In Figure 2 mass spectra are shown with different nozzle temperatures, showing the onset of CH_3^+ formation in the source.

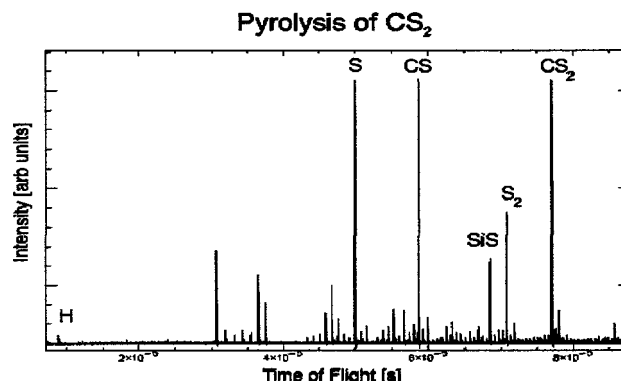


Fig. 1: Mass spectrum of CS_2/Ne expansion at 1200°C.

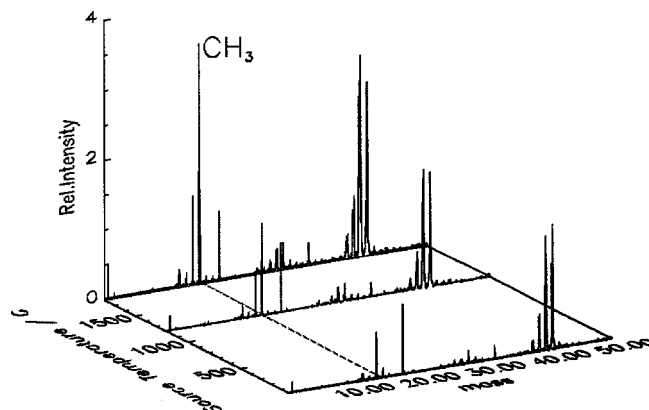


Fig. 2: Mass spectra for increasing nozzle temperature. At 1800°C, CH_3^+ becomes the most abundant signal in the beam.

4 CONCLUSION

A radical source has been set up and tested successfully to produce radicals in the defined environment of a molecular beam, in satisfying concentration to perform spectroscopy.

5 REFERENCES

- [1] P.P. Radi, H.M. Frey, B. Mischler, P. Beaud, A. Tzannis, T. Gerber, Chem. Phys. Lett. Accepted for publication.
- [2] D.W. Kohn, H. Clauberg, P. Chen, Rev. Sci. Instrum. **63**, 4003, (1992).

Consequences of Energy Use for Atmosphere and Climate

VERTICAL OZONE TRANSPORT IN THE ALPS (VOTALP): THE VALLEY EXPERIMENT 1996

*M. Furger, J. Dommen, W.K. Graber, A. Prévôt, L. Poggio, S. Andreani, J. Keller,
W. Portmann, D. Bürki, R. Erne, R. Richter, M. Tinguely*

The EU project VOTALP started its valley campaign in the summer of 1996 in the Mesolcina valley. The influence of thermal circulations on ozone concentrations and on the exchange of ozone and its photochemical precursors between the valley atmosphere and the free troposphere above was the main focus of the study. PSI has participated with various measurement systems (conventional meteorological surface stations, radiosondes, scidar/DOAS systems, chemical analysers). An overview of PSI's activities in the field campaign is given, and some preliminary results are presented.

1 INTRODUCTION

VOTALP is an EU research project to study the production and transport of ozone in the Alps [1]. The two-year project is coordinated by the Institute of Meteorology and Physics (IMP) of the University of Agricultural Sciences in Vienna, Austria. Universities and research institutions of Austria, Germany, Italy, Slovenia and Switzerland are collaborating. PSI contributes with various measurement systems and performs model calculations.

One of the goals of the project is to investigate the effects of exchange processes between the valley atmosphere and the free troposphere on the ozone concentrations in the valleys and aloft. For that purpose, a valley campaign was organised in the summer of 1996 in southern Switzerland. Data preparation and analysis is in progress, but some preliminary results can be presented here.

2 THE VALLEY CAMPAIGN

2.1 Campaign location and setup

The Mesolcina valley in southern Grisons, Switzerland, was selected as the campaign site for the valley experiment. This valley is approximately north-south oriented. It has relatively simple sidewalls without major tributary valleys (except the Calanca valley at the southern end), and a well-defined termination at the northern end. The San Bernardino highway provides an important source of ozone precursors.

Measurements were obtained in a monitoring mode over a time period of six weeks, and in the form of two intensive observing periods (IOPs). During the IOPs (Table 1) the full set of instruments and platforms was operated simultaneously, while monitoring was performed with a reduced set. The IOP activities were coordinated by PSI. Daily weather advice was received from the Swiss Meteorological Institute in Locarno-Monti and in Zurich.

Fair weather situations with weak pressure gradients, no large-scale precipitation and sufficient sunshine, favouring intensive valley circulations and high ozone concentrations, were desired.

| Name | Date | Weather characteristics |
|------------|---------------------|---|
| Monitoring | July 15 - Aug 23 | variable, atypical summer weather |
| IOP-1 | July 19 - 23 | high pressure, weak northerly winds aloft |
| IOP-2 | Aug 16 - 18 | high pressure, sunny and warm |

Table 1: Field campaign dates and weather characteristics.

2.2 Instrumentation

To obtain a database useful for subsequent modeling of the relevant processes, numerous measuring systems were deployed by the participating institutes (Table 2). Nine automated meteorological towers and one 30m tower, equipped in part with ozone and other chemical sensors and eddy correlation sensors, complemented the few existing ozone monitoring stations. Two acoustic wind profilers (sodars) were operated at both ends of the valley, and even radar wind profiler data were available from an independent experiment in Magadino. Temperature profiles were measured with hourly rawinsonde ascents. Two instrumented motorgliders were financed and partially equipped by PSI to measure trace gas concentrations within and above the valley and over the surrounding crests. Profiles of aerosol concentrations had been measured during IOP-1 with a LIDAR. Besides meteorological parameters, CO₂, O₃, H₂O, NO, NO₂, NO_x, VOC, H₂O₂ and dust particles were measured at specific sites.

A novelty in instrumentation for such an experiment was the deployment of scidar/DOAS systems. These systems consist of a scintillometer (scidar) to optically measure the path-averaged crosswind [2], and a DOAS (differential optical absorption spectrometer) to measure the path-averaged concentration of chemical species in the atmosphere. The combination of these instruments allows for the determination of fluxes across the light beams. With a suitable setup of a couple of such light paths, a trace gas budget for the enclosed volume of air can be calculated.

| Instrument/ Platform | Number | Institute |
|--------------------------------|--------|------------------|
| meteorological/chemical towers | 9 | PSI (4), IMP (5) |
| 30m tower | 1 | PSI |
| SODAR | 2 | IMP |
| aerosol LIDAR | 1 | IfU |
| motorgliders | 2 | PSI/Metair |
| rawinsonde | 1 | PSI |
| ozone sonde | 1 | CNR |
| scidar/DOAS | 5 | PSI |
| VOC sampling | 3 | ECOSENSE |
| chemical measurements | 1 | LAPETH/PSI |

IMP: Institut für Meteorologie und Physik, Vienna. IfU: Institut für atmosphärische Umweltforschung, Garmisch. CNR: National Research Council, Italy.

Table 2: Instrumentation.

PSI installed five scidar/DOAS systems; two across the southern end of the valley, two across the northern end, and one parallel to the valley sidewall. Beam lengths ranged from 0.6 to 2.7 km. The installation and operation of the systems proved to be hard physical work, and outages during IOP-1 were numerous, mainly caused by electric power failures. System reliability has been substantially improved for IOP-2.

3 PRELIMINARY RESULTS

The dataset obtained during the field campaign 1996 is in the process of assembly and quality checking. A preliminary analysis of the data gives first insights into the complex processes occurring in the Mesolcina valley.

An example illustrating the interaction between ozone-rich valley air and 'clean' free tropospheric air is shown in Figure 1. The measurements were obtained in Pian San Giacomo at the valley sidewall during IOP-1. Three features can be identified: 1) an approximately linear increase of ozone concentration during up-valley wind phases, 2) a rapid drop of ozone concentration at the time of transition from up-valley to down-valley winds, and 3) a stepwise increase from night to night of nighttime ozone levels. The increase during the day can be explained by local ozone production, mainly caused by emissions of vehicles.

The concentration drop in the evening cannot be explained by photochemical processes, but rather by a substitution of the respective airmass. Relatively clean air is transported downward along the slopes, replacing the local, contaminated valley air. The concentration drop around 16.00 h of the second day has not yet been explained. The stepwise increase of the nighttime ozone concentrations is indicating a gradual

increase of ozone in the residual layer above the valley. The origin of the 'clean' air may be in the free troposphere above the valley or even north of the San Bernardino pass. Aircraft and scidar/DOAS data will help to understand this observation.

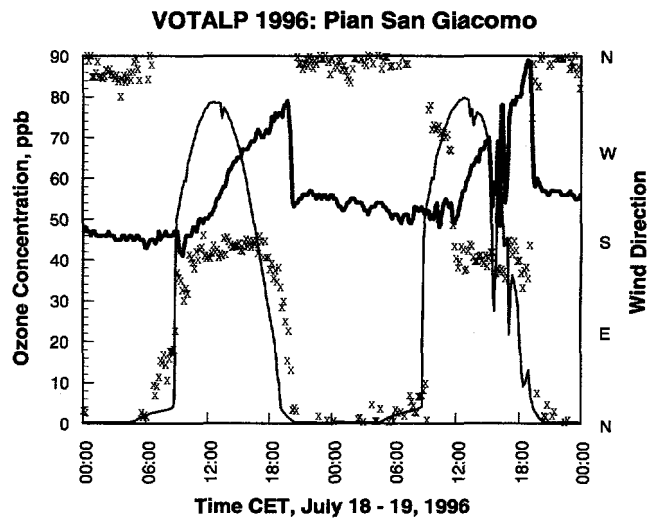


Fig. 1: Time series of ozone (thick line), global radiation (thin line), and wind direction (crosses) for July 18-19, 1996, measured at Pian San Giacomo. Global radiation has been divided by 12 to fit the ozone scale.

Another surprise was the strong influence of the Calanca valley on the thermal wind system in the Mesolcina valley. A preliminary analysis of wind data shows two distinct wind regimes at the place where this tributary valley enters the main valley. How much these effects disturb the processes in the Mesolcina valley is a matter of further investigation.

More detailed analyses are under way. They will increase our understanding of some of the relevant mechanisms of ozone formation and transport in the lower troposphere over the Alps.

4 ACKNOWLEDGEMENTS

The competent weather advice of the Swiss Meteorological Institute in Locarno is gratefully acknowledged. This study was supported by the Swiss Federal Office for Education and Science grant 95.0386-2.

5 REFERENCES

- [1] G. Wotawa, H. Kromp-Kolb, H. Scheifinger, P. Seibert, A. Stohl, E. Mursch-Radlgruber, G. Rengarajan, M. Furger, W. Graber, B. Neiningner, B. Gomiscek, "The EU research project VOTALP - objectives and first results", 24th Intl. Conf. on Alpine Meteorology - ICAM'96, Bled, Slovenia, pp. 297-303, Sept 9-13, (1996).
- [2] L. Poggio, M. Furger, W.K. Graber, "A comparison of scintillation crosswind methods", Proceedings IGARSS'96, Lincoln, Nebraska, pp. 399-401, May 27-31, (1996).

PSI CONTRIBUTION TO THE EU PROJECT ECOMONT

W. Portmann, R.T. Siegwolf, M. Saurer, Y. Scheidegger, P. Geissbühler,
M. Furger, L. Poggio, R. Erne, R. Richter, D. Bürki, W.K. Graber

Land-use changes (intensification, extensification and abandonment) in agriculture and forestry are considered to be the major driving forces for changes in ecosystem function and dynamics, and in landscape patterns in Europe. The aim of the EU project ECOMONT is to investigate the potential risks due to land-use change in the mountainous ecosystem. Fluxes of sensible and latent heat, water vapour, CO₂ and pollutants between the vegetation and the atmosphere are sensitive and critical factors characterising landscape function. The Atmospheric Pollution Section of the PSI contributes to this project with the measurements of these fluxes. The measuring techniques, the experimental setup and first results are presented.

1 INTRODUCTION

„ECOMONT aims at investigating land-use changes in European Terrestrial Mountain Ecosystems in the context of the EU Framework IV (Environment and Climate: Theme 1, Area 1.2.2.1. *The functioning of ecosystems*)“ [1].

Alpine ecosystems are known to be particularly sensitive to perturbations, due to short vegetation periods or natural stressors, such as wind fall, sudden temperature decrease, drought and frost. Consequently, the threshold value for harmful impacts is much lower compared to the ecosystems in less elevated areas of Europe. In mountainous areas the changes in ecosystem processes can also cause a considerable potential of risks (danger of torrents, snow gliding and avalanches, increased development of patches of bare soil and unstable slopes).

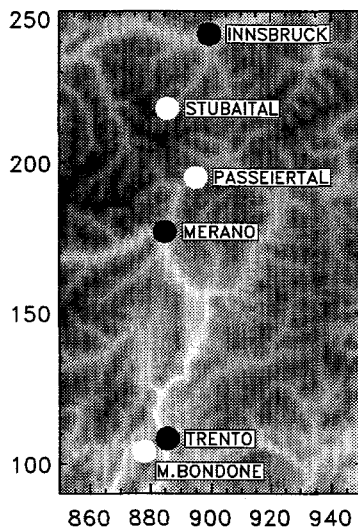


Fig. 1: Map of the three experimental sites in the eastern Alps. Black dots: cities; white dots: experimental sites. Coordinates are in the Swiss km grid.

The three pilot experimental sites Monte Bondone, Passeier Valley and Stubai Valley (Figure 1) give the possibility of investigating the connections between land-use changes and the transport of sensible heat, latent heat, water vapour, CO₂ and pollutants

(combining effects of different canopy structures) across the Alps.

2 EXPERIMENTAL SETUP

Figure 2 shows a schematic of the setup for the flux measurements.

H₂O/CO₂ Exchange Between the Atmosphere and the Vegetation, Measurements of the Essential Transport Processes

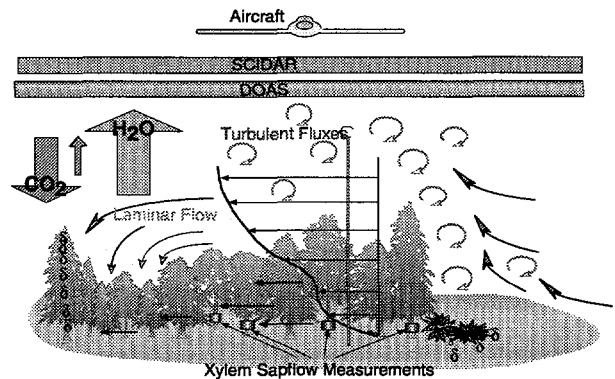


Fig. 2: Schematic of the experimental setup. δ : Stable Isotope Analyses for $\delta^{13}\text{C}$, $\delta^{18}\text{O}$ and $\delta^{15}\text{N}$. SCIDAR: Scintillation Detection and Ranging. DOAS: Differential Optical Absorption Spectroscopy.

2.1 Meteorological Data

The meteorological data are recorded with a 12 m tower on each of the three sites. Parameters and averaging times are chosen according to the WMO (World Meteorological Organisation) standards.

Micrometeorology provides additional information inside a plant stand. Leaf temperatures and photosynthetic active radiation (400-700 nm) in different crown layers, air humidity and air temperature, global radiation and albedo (200-2500 nm) were measured during the summer of 1996 at Monte Bondone.

2.2 Scidar/DOAS

The fluxes through vertical planes surrounding a specific experimental site are determined by combining concentration and total air flux measurements. Concentrations are measured with a DOAS-spectrometer over an open path through the atmosphere. The total air flux is measured with a scintillometer [2] in a paral-

lel light beam. The combination of Scidar and DOAS allows for the measurement of the advective flux perpendicular to the beams.

2.3 Aircraft measurements

A motorglider instrumented with fast responding CO_2 and H_2O devices is able to resolve changes of these gases due to large eddies. It is therefore suitable for determining the corresponding vertical fluxes. The flight paths were chosen to cover the whole experimental site of Monte Bondone. Data of the field campaign of 17 September 96 are being quality controlled and will soon be available for analysis.

2.4 Eddy correlation

The standard technique to determine turbulent fluxes in the atmosphere is the eddy-correlation. Fast-response sensors allow for the instantaneous and simultaneous measurement of the quantities to be correlated, e.g. the vertical wind velocity component, w , and the concentration, c , of CO_2 . The fluxes are computed after calculating the perturbation values of the data points, w' and c' , by simply multiplying and averaging, e.g. $\overline{w'c'}$.

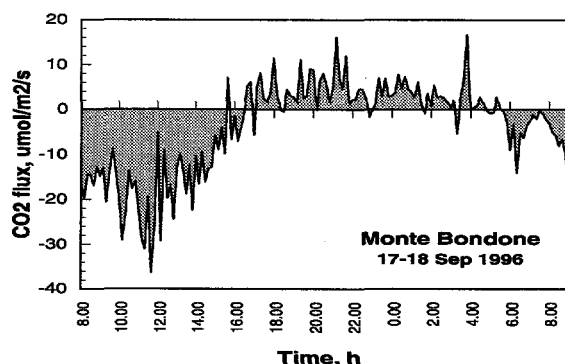


Fig. 3: CO_2 flux above a forest canopy on 17-18 September 1996.

Figure 3 shows a time series of the CO_2 flux on Monte Bondone. The downward flux during the day and the upward flux during the night is clearly visible.

2.5 Xylem sap flow

The flux of water from the vegetation into the atmosphere is one of the dominant fluxes in an ecosystem. It is caused by transpiration in the leaves that goes along with the CO_2 uptake for photosynthesis. To replace this water, plants have to transport water in the xylem from the roots to the leaves. In trees the active xylem is just under the bark in the stem. The temperature difference between a constantly heated tree segment and the non heated segment 15 cm below is inverse proportional to the xylem sap flow [3]. With this heat balance method the sap flow can be measured continuously.

We measured the xylem sap flow at six trees with different exposures (free standing and inside the forest) at each of the three experimental sites.

2.6 Analysis of stable isotopes

The water use efficiency is correlated with the CO_2 gas exchange. Thus, the $^{13}\text{C}/^{12}\text{C}$ ratio gives a long term average estimate of the plant carbon/water relation. A first result of a $^{13}\text{C}/^{12}\text{C}$ analysis is shown in Figure 4. The increase in this ratio with increasing height is obvious.

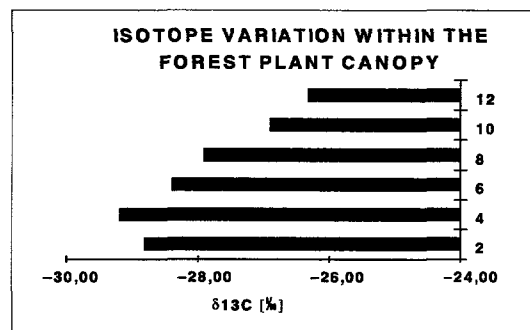


Fig. 4: Variation of $\delta^{13}\text{C}$ of leaf material versus height (in meters) inside the forest.

The use of the stable isotope ^{15}N provides the possibility to distinguish between the nitrogen sources of several plant species (nitrogen fixation, agricultural fertilisation), because plants using atmospheric nitrogen do not discriminate the heavier nitrogen isotope.

3 CONCLUSION

The field measurements started in July 96 with a reduced set of monitoring instruments and the collection of the first samples for the isotope analyses. An intensive observing campaign was performed on Monte Bondone on 17 September 1996, with the complete set of instruments, including the motorglider. Although this was rather late with respect to the vegetation period, interesting results could be found, providing a sound foundation for the measurements of the coming two years.

4 ACKNOWLEDGEMENTS

This study was supported by the Swiss Federal Office for Education and Science grant 95.0383-2.

5 REFERENCES

- [1] A. Cernusca, "Proposal of the EU Project ECO-MONT", (1995).
- [2] L. Poggio, M. Furger, W.K. Graber, "A Comparison of Scintillation Crosswind Methods", IGARSS'96 Digest, Vol. I, pp. 399-401, (1996).
- [3] J. Cermak, J. Jenik, J. Kucera, V. Zidek, "Xylem Sap Flow in a Crack Willow Tree (*Salix fragilis*) in Relation to Diurnal Changes of the Environment", *Oecologia*, 64, pp. 223-229, (1984).

CO₂-RECYCLING BY PLANTS: HOW RELIABLE IS THE CARBON ISOTOPE ESTIMATION ?

R.T.W. Siegwolf, M. Saurer, Ch. Körner (University of Basel, Switzerland)

In the study of plant carbon relations, the amount of the respiratory losses from the soil was estimated, determining the gradient of the stable isotope ¹³C with increasing plant canopy height. According to the literature 8% to 26% of the CO₂ released in the forests by soil and plant respiratory processes are re-assimilated (recycled) by photosynthesis during the day. Our own measurements however, which we conducted in grass land showed diverging results from no indication of carbon recycling, to a considerable $\delta^{13}\text{C}$ gradient suggesting a high carbon recycling rate. The role of other factors, such as air humidity and irradiation which influence the $\delta^{13}\text{C}$ gradient in a canopy as well, are discussed.

1 INTRODUCTION

The estimation of the terrestrial CO₂ balance requires a good knowledge of the carbon sinks and sources. The main sink on terrestrial ecosystems is represented by the autotrophic organisms, mainly vascular plants, whereas the sources are numerous. Besides the heterotrophic organisms, the plants and soil release most of the assimilated carbon from the ecosystem. However it is difficult to distinguish the amount of CO₂ released by the soil and the plants. Since plants discriminate the heavier C-atom during photosynthesis, plant organic material has an amount of ¹³C reduced by about 20 to 25 ‰. As a consequence the CO₂ which originates from decomposed organic material is ¹³C depleted. Therefore $\delta^{13}\text{C}$ gradients of the air (δ_a) and of plant material (δ_p) are used to determine the contribution of respiratory CO₂ from soil and decaying litter as a carbon source for plant growth [2]. The proportion of the re-assimilated CO₂ is estimated to range between 8% and 26% of the total carbon uptake [3].

2 METHODS

Air samples were collected from 5 different levels (200 cm, 60 cm, 30 cm, 10 cm and 2 cm above ground) into evacuated and electro polished 700 ml steel flasks (Figure 1). After purifying, the CO₂ gas was extracted from the air and frozen into glass tubes. At the same levels temperature and the photosynthetic active irradiation were measured. The absolute CO₂-concentration and water vapor pressure values were obtained with an infrared gas analyzer (Li-6262). Plant samples were harvested from 4 different canopy height levels (Figures 2 & 3), dried, and combusted in an elemental analyzer (EA-1108, Carlo Erba). The $\delta^{13}\text{C}$ -ratio of air CO₂ (δ_a) and plant material (δ_p) was determined with a mass spectrometer (Finnigan MAT, Delta S, Bremen).

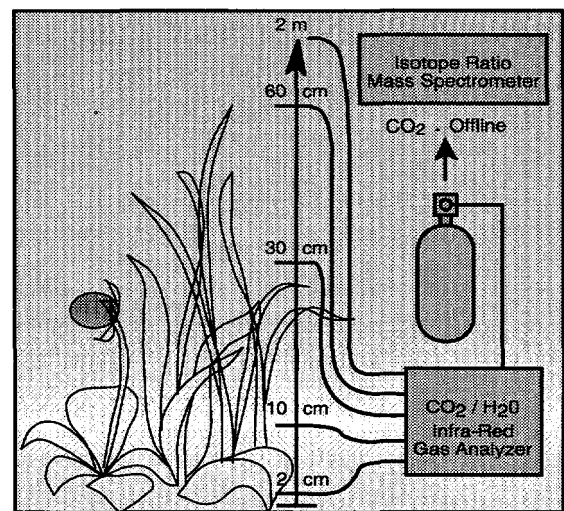


Fig. 1: Experimental setup in the field for measuring the absolute CO₂ concentration, water vapor, air temperature, irradiation and air sampling (see text).

3 RESULTS AND CONCLUSION

In the meadow of Nenzlingen (Switzerland, about 600 m asl) a vertical $\delta^{13}\text{C}$ -gradient was found, which is negatively correlated with the CO₂-concentration within the plant canopy (Figure 2). The maximum δ -values of the air were observed during the day in the canopy layer with the highest photosynthetic activity as a result of the discrimination mechanisms of the CO₂-gas exchange processes. The most negative $\delta^{13}\text{C}$ values are found 2cm above ground, where the air is CO₂-supplied from the soil. This ¹³C depleted CO₂, released by respiratory soil decomposition and root respiration processes is re-assimilated by the above ground photosynthetic active plant tissue. It can be assumed, that

this isotopic gradient will be transferred onto the plant material. Such an isotopic gradient is actually found (Figure 3) and the values of the plant material range between -27.8‰ (33 cm at the top canopy) and -34‰ (1 cm above ground).

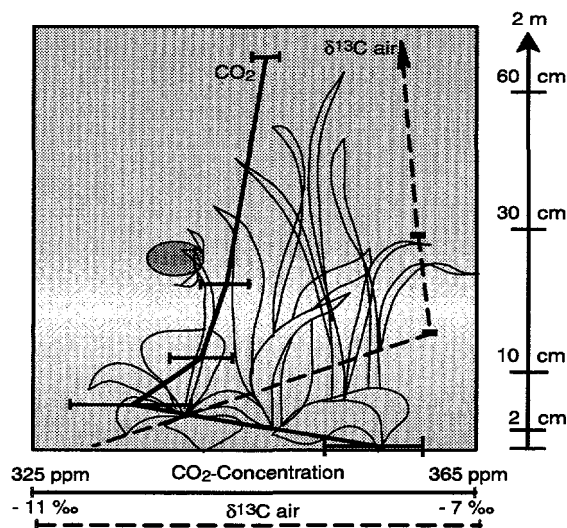


Fig. 2: Gradients of the CO_2 -concentration (solid lines) and the $\delta^{13}\text{C}$ -values of the air through the plant canopy.

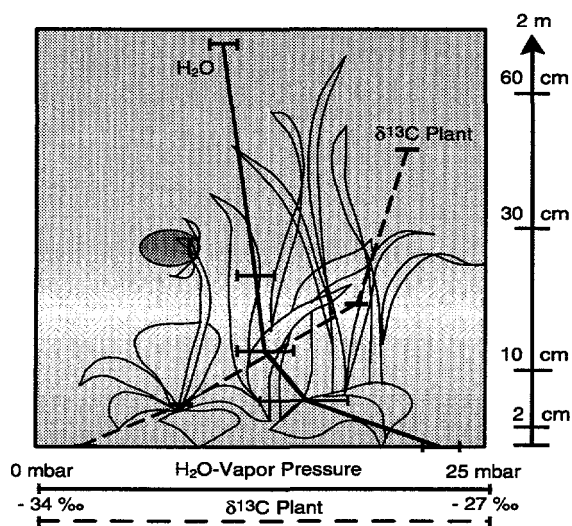


Fig. 3: Gradients of the water vapor pressure (solid lines) and the $\delta^{13}\text{C}$ -values of the plant material through the plant canopy.

The conclusion lies at hand, that the $\delta^{13}\text{C}$ gradient in the plants is a direct result of the $\delta^{13}\text{C}$ gradient of the ambient air in the canopy. The closed canopy structure and biomass distribution in Nenzlingen, preventing a thorough mixture of the canopy air supports this assumption. In contrast to these findings however, no such isotopic gradients were found in a comparative study in the dwarf shrub communities on the Furka

pass, in spite of the fact that some of them formed very dense polsters and thus prevented wind penetration into the canopy.

In both plant stands, a canopy microclimate with higher air humidity and different irradiation conditions, different from that of open plant stands is found. Higher air humidity which correlates with decreasing canopy height leads to a higher stomatal conductance (Figure 3). This leads to a higher intercellular CO_2 concentration, which causes a decreased $\delta^{13}\text{C}$ [1]. On the other hand PEARCY [4] reported a positive correlation of the $\delta^{13}\text{C}$ -values with increasing photon flux density, which can be as much as 2‰ between shaded (-35‰ at avg. PFD $0.2 \text{ mol m}^{-2} \text{ day}^{-1}$) and sunlit leaves (-33‰ at avg. $2 \text{ mol m}^{-2} \text{ day}^{-1}$). Thus the vertical $\delta^{13}\text{C}$ -gradient in plant material is strongly influenced by microclimatical factors as well. Based on these findings further studies are addressing to the following questions:

1. To what degree are the $\delta^{13}\text{C}$ -values influenced by irradiation and air humidity in a canopy, along with the CO_2 , originating from plant/soil decomposition processes and
2. how far are carbon isotope gradients a reliable tool within plant canopies for quantifying the carbon source relationship between atmospheric air and soil.

Taking the micrometeorological factors into account, the use of carbon isotopic gradients in air and plant tissues could be a tool for quantifying the amount of CO_2 originating from the soil.

REFERENCES

- [1] G.D. Fraquhar (1982), M.H. O'Leary and J.A. Berry. On the relationship between carbon isotope discrimination and the intercellular carbon dioxide concentration in leaves. *Aust. J. Plant Physiol.* 9, 121-137, (1982).
- [2] L.S. Sternberg, S.S. Mulkey and S.J. Wright. Ecological interpretation of leaf carbon isotope ratios: Influence of respired carbon dioxide. *Ecology*, 70: 1317-1324, (1989).
- [3] M.S.J. Broadmeadow and H. Griffiths. Carbon Isotope Discrimination and the Coupling of CO_2 Fluxes within Forest Canopies. In: J.R. Ehleringer, A.E. Hall and G.D. Farquhar (eds.) *Stable Isotopes and Plant Carbon-Water Relations*. Academic Press, San Diego, pp. 555, (1993).
- [4] R.W. Pearcy and W.A. Pfitsch. The Consequences of Sunflecks for Photosynthesis and Growth of Forest Understory Plants. In: E.-D. Schulze, M.M. Caldwell (eds.) *Ecophysiology of Photosynthesis*, Ecological Studies 100: 433-460, Springer Verlag, Berlin, New York, pp. 576, (1994).

$^{18}\text{O}/^{16}\text{O}$ DETERMINATION IN ORGANIC MATTER

M. Saurer, R. Siegwolf

The oxygen isotope ratio in plant material can be used to deduce information about the climate and the environment. We present a simple and fast continuous-flow technique for the determination of the $^{18}\text{O}/^{16}\text{O}$ ratio in organic matter. In this method the samples are thermally decomposed in the presence of glassy carbon and the evolving carbon monoxide is used to determine the oxygen isotope ratio. Not only cellulose but also nitrogen-containing materials can be processed when interfering gases (mainly N_2) are separated from CO by gas chromatography.

The oxygen isotope ratio in plant matter provides information

(i) about the climate because, for instance, the $^{18}\text{O}/^{16}\text{O}$ ratio of tree rings is related to the $^{18}\text{O}/^{16}\text{O}$ ratio in the precipitation, which in turn is influenced by air temperature,

(ii) about the environment because of the isotopic enrichment taking place in the leaf water, which is dependent on the transpiration and on the microclimatic conditions in the vegetation layer.

As an example (Figure 1), we present data from a tree ring study which shows that year-to-year variations in $\delta^{18}\text{O}$ of the summer precipitation are recorded in the stem wood [1].

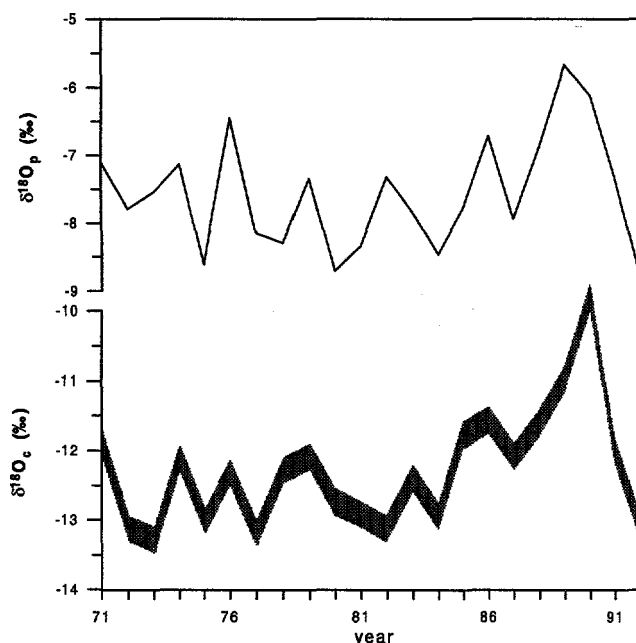


Fig. 1: Upper curve: Mean $\delta^{18}\text{O}_p$ of the precipitation (p) from May to August at Bern. Lower curve: Mean $\delta^{18}\text{O}_c$ -curve of the cellulose (c) of the three beech trees from a site near Bern with measurement precision indicated as width of the band. $\delta^{18}\text{O}$ is the relative deviation of the $^{18}\text{O}/^{16}\text{O}$ of the sample from the $^{18}\text{O}/^{16}\text{O}$ of the commonly used standard (SMOW).

Until recently the progress in this research area was hampered by the tedious nature of sample preparation needed (off-line methods). We adopted an on-line

method [2] and improved it such that the precision is sufficient to resolve natural variations. The principle of the method is as follows (Figure 2): An autosampler is used to drop the sample into the pyrolysis tube of an elemental analyser (without addition of oxygen!) and the glassy carbon at 1100°C has the effect to convert most oxygen of the sample into carbon monoxide (less than 5% are found in form of CO_2). The helium carrier gas sweeps the gases through a CO_2 - and a H_2O -trap and then through a molecular sieve (5A), whereby N_2 and CO are separated. Finally, the $^{18}\text{O}/^{16}\text{O}$ ratio of the carbon monoxide is determined in an isotope ratio mass spectrometer (Finnigan MAT, Bremen).

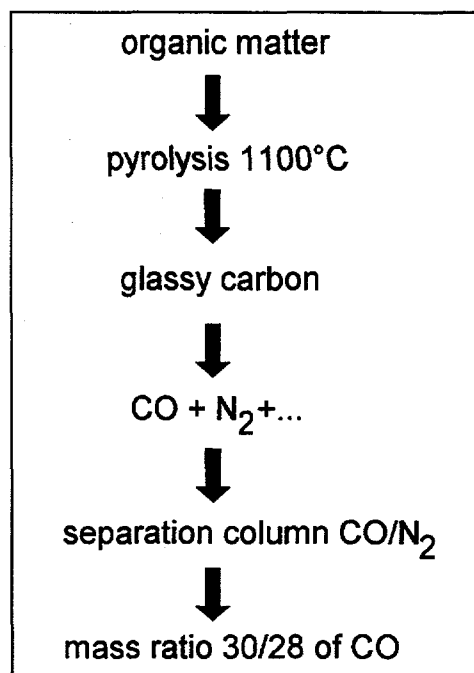


Fig. 2: Schematic diagram of the set-up used to measure the $^{18}\text{O}/^{16}\text{O}$ ratio of organic matter.

REFERENCES

- [1] M. Saurer, S. Borella, M. Leuenberger, " $\delta^{18}\text{O}$ of Tree Rings of Beech (*Fagus sylvatica*) as a Record of $\delta^{18}\text{O}$ of the Growing Season Precipitation", *Tellus*, in press, (1996).
- [2] R.A. Werner, B.E. Komexl, A. Rossmann, H.L. Schmidt, "On-Line Determination of $\delta^{18}\text{O}$ -Values of Organic Substances", *Analytica Chimica Acta* 319, 159-164, (1996).

CLASSIFICATION OF WINDFIELDS: A DIAGNOSTIC TOOL FOR REAL-TIME DETERMINATION OF LOCAL AIR POLLUTION DISPERSION

W.K. Graber, D. Bürki

In the framework of the project "WINDBANK unteres Aaretal" local winds over complex terrain were measured over a 4 month period and a cluster analysis is used to identify 13 different typical wind fields. A subset of representative stations is established to identify the classes for future applications in emergency planning.

1 INTRODUCTION AND DATA ACQUISITION

Atmospheric transportation of air pollutants depends largely on the windfield. In the framework of safety analysis of nuclear power reactors this knowledge of the current wind field marks a focal point for supporting decisions during emergency situations. In this paper, a diagnostic tool is presented, based on a classification scheme of wind measurements from a dense network of 43 stations in a hilly terrain of 50 by 50 km, shown in Figure 1. A detailed description is given in [1]. The measurements cover the time period from July 1 to October 31 of the year 1995. 22 stations (numbers 3 to 23 and 43 in Fig. 1) were placed especially for this project, whereas the other 21 are routine stations. The temporal resolution of the measurements is 10 min. In a database over the 4 month period these values were averaged to hourly means, thus resulting in a set of 2951 hourly values for 43 stations.

2 CLASSIFICATION

A classification according to [2] was realized, starting with a normalization as a first step: For any hourly value the west and south component (u and v) of the wind of each station were divided by the average of the wind speed during that hour. This normalization dampens high wind speeds, which otherwise would form additional classes with similar wind directions, differing only in wind speed. In a next step, the classification according to a complete linkage cluster analysis was performed, based on the distances between any two hourly values of the wind components of all stations: According to the normalisation, the distance between two hourly data sets reaches a maximum of 2, if the winds at all stations are completely antiparallel. After this cluster analysis yielding 13 classes, a redistribution according to [2] was realised. This leads to a smaller scatter of wind directions within the classes. The result for one selected class is shown in Figure 1. It can be shown, that a number of 13 classes covers the meteorological diversity in a well balanced manner (see [1]). Based on the mean values of the wind vectors for all stations a run with the diagnostic models MEDIC and MATHEW was carried out: The first model calculates a 3 dimensional wind field on a regular grid. The second model corrects this "first guess wind field" in accordance with the physical constraint of a divergency free flow field. After the MEDIC and MATHEW run for every class, a run with the dis-

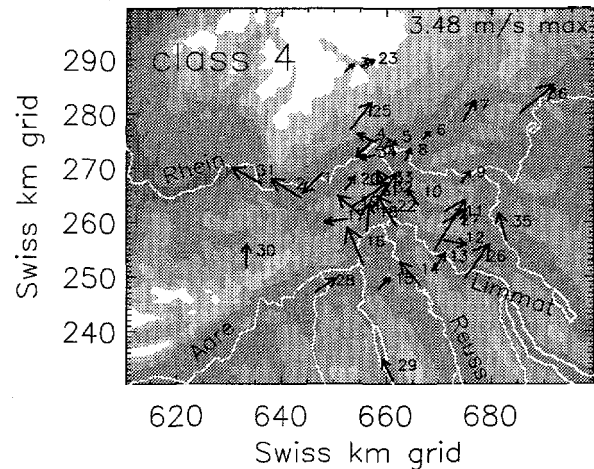


Fig. 1: Map of the area with high resolution wind measurements. Mean wind vectors of class 4 at their respective locations over the topography with station numbers, topography dark shaded for elevations below 300 m and white for elevations higher than 900 m.

persion model ADPIC with a hypothetical point source in the middle of the region was added. All three models are described in detail in [3]. An example of the result of MATHEW for level 700 m above sea level along with the result from ADPIC, both for the class 4, is shown in Figures 2 and 3, respectively. This class shows an interesting bifurcation of the hypothetical plume in the Rheinvalley.

In an application of this classification with respect to emergency planning it is of major concern to establish the currently prevailing wind class as accurately as possible and based on a minimum set of "representative" stations. An examination of the "hitting ratio" for the classes with a reduced set of stations was performed with the data set of the hourly values: For a given hour t out of the 2951 hours, the 13 distances of the mean wind components from the 13 classes are calculated. The minimal distance out of these 13 values points to the class, to which this hour t most likely belongs. Clearly, the hitting ratio is 100% for all classes, if all 43 stations are taken into consideration. By leaving aside the stations one by one, the decrease of the mean hitting rate for 2 different successions is depicted in Figure 4. The upper succession with better performance does not give preference to the routine stations, whereas the lower succession

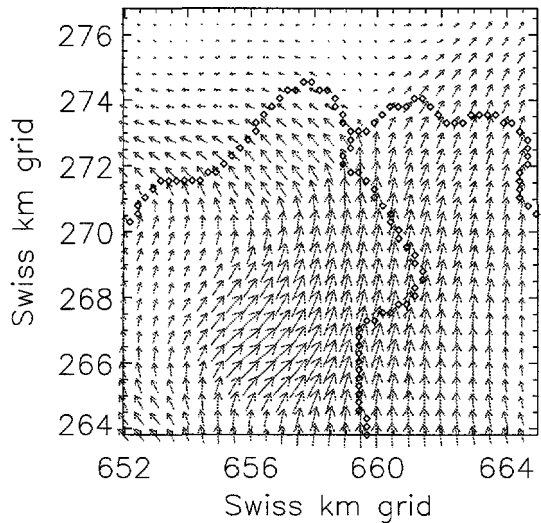


Fig. 2: Interpolated wind field in 700 m above sea level (max. windspeed is 2.4 m/s) over part of the region from Figure 1. The result is shown for class 4 only.

excludes the additional stations (number 3 to 23 and 43) with first priority. If we restrict on 20 routine stations, the mean hitting rate over all classes is 85%, as indicated with a vertical line in Figure 3.

3 CONCLUSION AND FUTURE STEPS

The method presented above is well suited to establish a classification of the wind situations in complex terrain. It was further proved, that a set of 20 representative stations is able to establish the currently preavailable wind field class with a probability of 85%. Based on these 20 routinely installed measuring stations, the determination of the wind class in combination with a dispersion calculation can be used as a tool for decision makers in cases of emergency situations from chemical or radioactive sources. The acquisition time for this wind field is faster and the confidence in the result is better compared to a run of a complex numerical model.

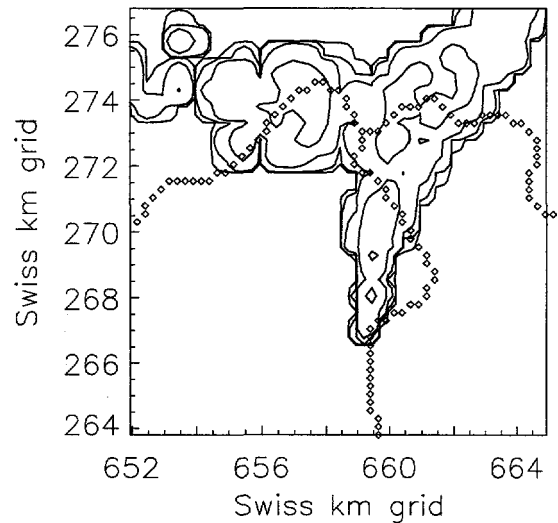


Fig. 3: Dispersion of a hypothetical source of an inert tracer (relative units) over part of the region from Figure 1. The result is shown for class 4 only.

4 ACKNOWLEDGEMENTS

The work is partly financed by the Swiss Federal Energy Agency (BEW), represented by "Hauptabteilung für die Sicherheit der Kernkraftwerke (HSK)".

5 REFERENCES

- [1] Graber W.K. and Buerki D.: Projekt "Windbank unteres Aaretal": Klassifikation von Windfeldern als Grundlage der aktuellen Ausbreitungssituation. PSI-Bericht Nr. 96-11, 83 S, (1996).
- [2] Kaufmann P., Weber R.O.: Classification of mesoscale wind fields in the MISTRAL field experiment. J. Appl. Meteorol., 35,1963-1979, (1996).
- [3] Taylor A., Sugiyama G., Walker H., Forster C.: User's guide to the MATHEW/ADPIC Models. Lawrence Livermore Nat. Lab., Univ. of California, Regional Atmospheric Sciences Div., UCRL-MA-103581 Rev. 2, (1994).

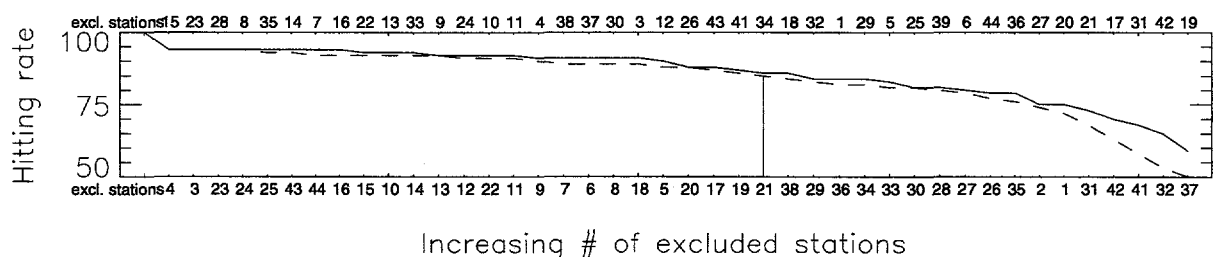


Fig. 4: The hitting rate as a percentage of all hours of the dataset after cumulative excluding of stations indicated according to Fig. 1 above and below the plot (two different successions of excluding stations).

DECADAL CHANGES OF WEATHER TYPES IN THE ALPINE REGION

G. Stefanicki, P. Talkner, R.O. Weber

The annual occurrence of different weather types of Schüepp's synoptic classification in the Alpine region has changed since the beginning of its recording 1945. The annual frequency (number of days) of convective types has increased and that of advective types has decreased. In parallel the number of long-lasting convective episodes rose and the number of long-lasting advective episodes lessened. Most of the change took place in winter. The frequencies of different weather types and the annual mean of certain meteorological parameters are significantly correlated. Moreover, there is a strong interdependence between the subclass of high pressure types and the North Atlantic Oscillation (NAO) index.

1 INTRODUCTION

It is widely accepted that the global climate has changed, accompanied by an increase of the mean temperature of earth's surface. A large number of publications have recently studied climate changes in Europe. We just mention two papers: In [1] an asymmetric diurnal temperature change in the Alpine region was discovered and in [2] Hurrell found that the North Atlantic Oscillation index increased and with it the dry conditions over southern Europe and wetter than normal conditions over northern Europe. On a regional scale, we investigated possible changes of atmospheric circulation patterns in the Alpine region and their possible links to local meteorological parameters and to the large-scale North Atlantic Oscillation index. In particular, we analysed the occurrence of daily synoptic weather types as defined by Schüepp [3]. Based on specific criteria he defined three main classes: the convective types with subclasses of high, flat and low pressure distribution, the advective types with subclasses of westerly, northerly, easterly and southerly winds and a small class of mixed types. The classification was made as a tool for weather prediction in Switzerland. As records from the 500 hPa level are required for the classification the data are available only since 1945.

2 ANNUAL FREQUENCY OF WEATHER TYPES

As a main result we found that the annual occurrence of different weather types over Switzerland has changed since 1945, as Figure 1 demonstrates.

The annual occurrence of convective weather types increased (13 days per 10 years) whereas that of advective weather types decreased correspondingly (11 days per 10 years). Both linear trends are significant at the 0.1% level. The occurrence of the mixed class is roughly an order of magnitude smaller than that of the convective and advective classes. It shows a slight decrease. The increase of the frequency of the convective class is mainly due to the increase of the number of high pressure types (9 days per 10 years) and the decrease of the frequency of the advective class is mainly due to the decrease of the frequency of the weather types with northerly winds (5 days per 10 years). A seasonal analysis indicates that both changes prevalently took place in winter (December,

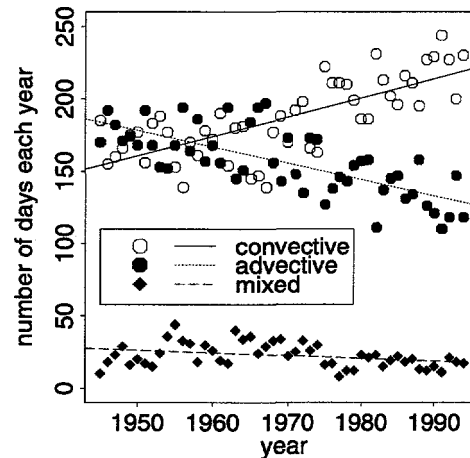


Fig. 1: Annual occurrence of the convective, advective and mixed weather types and their linear trends (data since 1945).

January and February). Moreover, we found that the number of long-lasting episodes within the convective weather types increased and the number of long-lasting episodes of the advective weather types decreased while short periods of one and two days being the most frequent episodes do not show any systematic trend (see Figure 2). The largest portion of increase of the occurrence of the convective types is related to episodes in the range of 3 days to 15 days and roughly within the same range the occurrence of the advective types decreases. The total number of episodes per year has remained practically unchanged, again showing a complementary behaviour of convective and of advective weather types.

3 RELATION TO LOCAL METEOROLOGY

To investigate a possible link between the occurrence of the different weather types and different meteorological quantities we calculated the cross-correlation between the annual occurrence of the different weather types and several meteorological parameters (daily mean temperature, daily minimum and maximum temperature, daily mean pressure and daily cloudiness). Basel-Binningen, Zürich SMA, Neuenburg

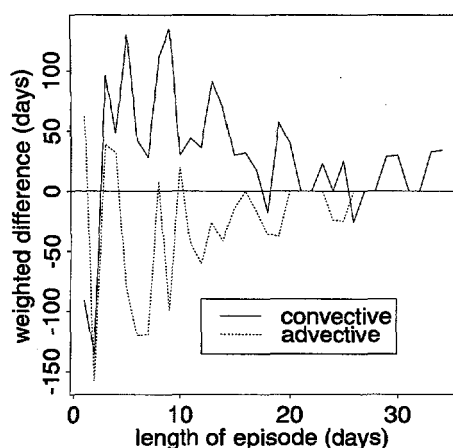


Fig. 2: Weighted distribution of the length of episodes - convective and advective - during the two periods 1945-1969 and 1970-1994. The difference is taken between the second and the first period. The counts are weighted with the length of episodes.

and Lugano as low-lying stations and Säntis, Zugspitze and Sonnblick as stations on a mountain top were chosen. The selected sites are quite representative for the area for which Schüepp's classification was defined. The data have been checked and homogenized - if necessary - by the method described in [1]. At the mountain stations the strongest interdependence was found between the high pressure types and the pressure data with correlation values between 0.74 and 0.64. The high pressure types also correlate well with the different temperature data. The low pressure and westerly wind types have a significant negative correlation with temperature and pressure (values between -0.55 and -0.47) and a significant positive correlation with the cloudiness (values between 0.55 and 0.40). These two weather types are known as types which bring us 'bad' weather and the correlation values support their 'bad' reputation. The results for low-lying stations are similar but in general less pronounced though the differences to the mountain stations are not significant. This might still indicate a more direct influence of the synoptic weather types on the meteorological parameters at mountain stations whereas at low-lying stations a possible direct influence might be masked by boundary layer effects.

4 RELATION TO THE NAO INDEX

A comparison with the North Atlantic Oscillation (NAO) index according to Hurrell [2] has been performed in order to identify possible influences of large-scale atmospheric circulation patterns on the occurrence of regional weather types. The NAO index is a normalized pressure difference between Lisboa (Portugal) and Iceland. The NAO index correlates highly with the 4-months-winter high pressure types (see Figure 3).

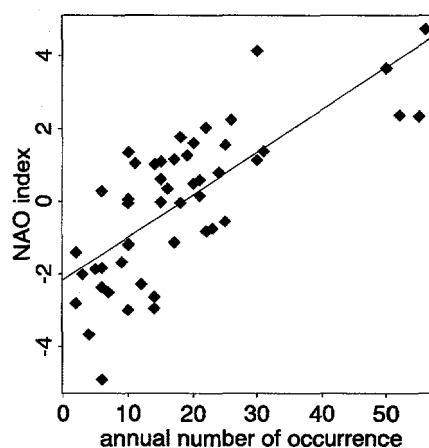


Fig. 3: The NAO index versus the occurrence of high pressure types of the 4-months-winter (December-March). The correlation coefficient is 0.74 and significant at the 0.1% level.

A positive NAO index indicates more high pressure situations occurring in the Alpine region.

5 CONCLUSIONS

We have analysed the occurrence of the different weather types and have found remarkable changes. So the annual number of convective types increased and in parallel the annual number of advective types decreased. We have further found an interdependence between certain weather types and some local meteorological parameters but also with the large-scale NAO index. That gives evidence that the regional-scale weather types are connected to a larger-scale weather system and are also related to local meteorological parameters.

6 ACKNOWLEDGMENTS

We thank the Schweizerische Meteorologische Anstalt (SMA), the Zentralanstalt für Meteorologie und Geodynamik and the Deutsche Wetterdienst for providing the data. The data of the NAO index were kindly given to us by J.W. Hurrell from NCAR in Boulder.

7 REFERENCES

- [1] R.O. Weber, P. Talkner, G. Stefanicki, "Asymmetric Diurnal Temperature Change in the Alpine Region", *Geophys. Res. Lett.*, **21**, 673-676, (1994).
- [2] J.W. Hurrell, "Decadal Trends in the North Atlantic Oscillation: Regional Temperatures and Precipitation", *Science*, **269**, 676-679, (1995).
- [3] M. Schüepp, "Klimatologie der Schweiz, Band III: Witterungsklimatologie", Schweizerische Meteorologische Anstalt, Zürich (1979).

SHORT-RANGE DYNAMICS AND PREDICTION OF MESOSCALE FLOW PATTERNS IN THE MISTRAL FIELD EXPERIMENT

R.O. Weber, P. Kaufmann, P. Talkner

In a limited area of about 50 km by 50 km with complex topography, wind measurements on a dense network were performed during the MISTRAL field experiment in 1991-1992. From these data the characteristic wind fields were identified by an automated classification method. The dynamics of the resulting twelve typical regional flow patterns is studied. It is discussed how transitions between the flow patterns take place and how well the transition probabilities can be described in the framework of a Markov model. Guided by this discussion, a variety of prediction models were tested which allow a short-term forecast of the flow pattern type. It is found that a prediction model which uses forecast information from the synoptic scale has the best forecast skill.

1 INTRODUCTION

For questions of emergency response planning and of air pollution control on a regional scale it is of great importance to know the local wind fields and their climatology in detail. In [1] a method was developed to automatically classify local wind fields and to obtain classes of typical regional flow patterns. In [2, 3] this classification method was used to determine the characteristic flow patterns in an area around Basel. Only twelve classes of substantially different wind fields were found in that region with very complex topography. The dynamics of these twelve flow patterns is investigated [4] following the ideas used in the analysis of synoptic weather types [5, 6]. Most of this discussion concentrates on the question whether the dynamics of synoptic weather types can adequately be described by a Markov model. In a Markov model tomorrow's weather type only depends on today's weather type but on the past ones. An adequate description implies that the Markov model has good forecast skill.

2 MISTRAL FLOW PATTERNS

In 1991-1992, the MISTRAL field experiment ("Modell für Immissions-Schutz bei Transport und Ausbreitung von Luftfremdstoffen", model for impact prevention during transport and diffusion of air pollutants) took place in the region of Basel, Switzerland. This experiment is a part of REKLIP ("Regio-Klima-Projekt", Regio climate project) an international climatological project which takes place through the period 1989-1997. MISTRAL was aimed at measuring in detail the wind fields over a region of complex terrain. For this purpose 50 measurement sites with meteorological masts were operated during about 18 months.

In [2, 3] a one year period from 1 September 1991 to 31 August 1992 was selected and 1-h means of the horizontal wind vectors were formed. The total of these 8784 observed wind fields was classified into 12 classes of typical regional flow patterns by means of an automated two-stage classification scheme [2, 3]. To obtain the relevant features of the regional flow patterns more clearly, outliers (wind fields not well fitting into any of the groups) were excluded in the

classification scheme. For the investigation of the dynamics of the classes it is, however, more convenient to have a contiguous time series of classes. Therefore, the 1531 outlier wind fields are assigned to classes by allocating them to the closest flow pattern [3].

3 DYNAMICS OF FLOW PATTERNS

Based on the classification of the 8784 1-h wind fields of the MISTRAL experiment into 12 classes of typical regional flow patterns, we can analyse the dynamics of these patterns. As these flow patterns are characterised by a finite number, they can be described by a discrete state Markov model (a Markov chain). In meteorology, such Markov chains were first used to model the sequence of dry and wet days [7].

The 12x12 transition probability matrix

$$P(k) = (p_{ij}(k))$$

is estimated from the time series of flow patterns. Each matrix element gives the probability to get from the j -th flow pattern to the i -th flow patterns in k hours. The diagonal elements give the persistence to remain in the same class. For a one-hour time lag this persistence ranges from 0.63 to 0.80. That means that there is a high chance of having the same flow patterns in the next hour.

To analyse the transitions from one flow pattern to the others, a conditional transition probability is calculated which gives the probability to get in k hours from class j to class i under the condition that a transition to another class takes place. In Figure 1 all conditional transition probabilities which are greater than 0.2 are drawn as arrows between the classes. The flow patterns with westerly winds (1, 3, 6 and 7) form a group with mutual transitions between them. Similarly, the classes with easterly winds (4, 8, 9, 10 and 11) build a group. The transition between the westerly and the easterly flow types passes through the southerly (2) or the two northerly (5 and 12) flow patterns.

To see how well the Markov assumption holds for the sequence of flow patterns, the distribution of the length of the flow pattern episodes (=residence times in the classes) is considered. This probability can directly be

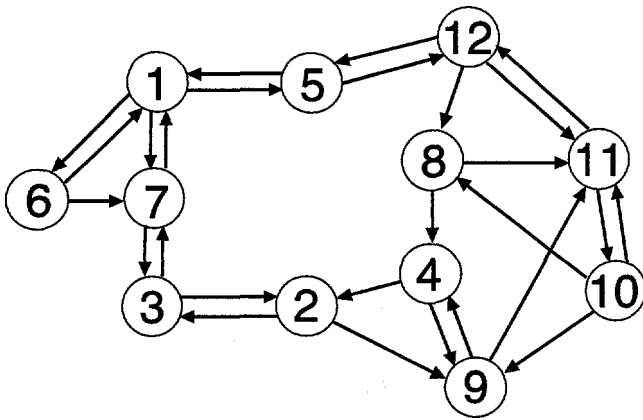


Fig. 1: Transition diagram for the twelve regional flow patterns of the MISTRAL area. The arrows indicate one-hour transitions with a conditional transition probability greater than 0.2.

estimated from the sequence of class numbers by simply counting the episodes of all lengths. Figure 2 shows the distribution of the residence times of classes 5 and 2 as obtained from the data and from a Markov model which makes only use of the estimated diagonal elements of the 1-h transition matrix. For class 5, the agreement between data and model is very good and we conclude that a Markov chain can well describe the residence times of class 5. Among all classes, class 5 is the one which is best approximated by a Markov chain model. The poorest coincidence between observed and modelled distribution of residence time is seen for class 2. For short times, less than 20 hours, large scatter is already present between the observed residence times and the modelled ones. Very long episodes (up to 56 hours) of this class occur, causing strong deviations from the Markov chain model and indicating an intermittent behaviour of the occurrence of class 2.

4 PREDICTION OF FLOW PATTERNS

Several models were developed [4] to predict the flow pattern class some hours ahead from the knowledge of the present class or classes in the past. A simple persistence model assumes that the class remains the same during the predicting interval. A climatology model always predicts the most probable class (here class 1). A Markov chain model uses the information of the transition matrices to make most probable forecasts. After a few hours the prediction of these models becomes unreliable. An improvement over these models can be gained if additional information about changes on the synoptic scale are included in the model [4]. Besides the hour of the day, larger scale

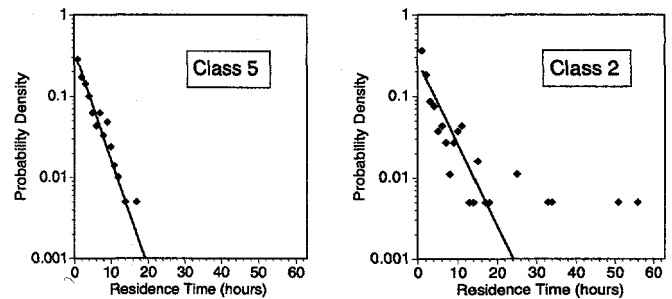


Fig. 2: Distribution of residence times for flow patterns 5 and 2. The solid line represents the distribution of a Markov chain model.

forecasts about possible changes of synoptic wind direction and of the solar radiation are used.

5 ACKNOWLEDGEMENTS

The project REKLIP/MISTRAL is partly funded by the two cantons of Basel. Additional data were kindly provided by the Swiss Meteorological Institute, Zürich and the Geographical Institute of the University of Basel.

6 REFERENCES

- [1] R.O. Weber, P. Kaufmann, "Automated Classification Scheme for Wind Fields", *J. Appl. Meteor.*, **34**, 1133-1141, (1995).
- [2] P. Kaufmann, R.O. Weber, "Classification of Mesoscale Wind Fields in the MISTRAL Field Experiment", *J. Appl. Meteor.*, **35**, 1963-1979, (1996).
- [3] P. Kaufmann, "Regionale Windfelder über Komplexer Topographie", Ph.D. thesis No. 11565, Swiss Federal Institute of Technology (ETH), Zürich, (1996).
- [4] R.O. Weber, P. Kaufmann, P. Talkner, "Short-Range Dynamics and Prediction of Mesoscale Flow Patterns in the MISTRAL Field Experiment", submitted to *Tellus*, (1996).
- [5] A. Hannachi, B. Legras, "Simulated annealing and weather regimes classification", *Tellus*, **47A**, 955-973, (1995).
- [6] R. Vautard, K.C. Mo, M. Ghil, "Statistical Significance Test for Transition Matrices of Atmospheric Markov Chains", *J. Atmos. Sci.*, **47**, 1926-1931, (1990).
- [7] K.R. Gabriel, J. Neumann, "A Markov Chain Model for Daily Rainfall Occurrence at Tel Aviv", *Quart. J. Roy. Meteor. Soc.*, **88**, 90-95, (1962).

CLIMATOLOGY OF LOCAL FLOW PATTERNS AROUND BASEL

R.O. Weber

Recently a method has been developed to classify local-scale flow patterns from the wind measurements at a dense network of stations. It was found that in the MISTRAL area around Basel a dozen characteristic flow patterns occur. However, as the dense network of stations ran only during one year, no reliable climatology can be inferred from these data, especially the annual cycle of the flow patterns is not well determined from a single year of observations. As there exist several routinely operated stations in and near the MISTRAL area, a method was searched to identify the local flow patterns from the observations at the few routine stations. A linear discriminant analysis turned out to be the best method. Based on data from 11 stations which were simultaneously operated during 1990-1995 a six-year climatology of the flow patterns could be obtained.

1 INTRODUCTION

In [1] a method was introduced to classify flow patterns from data of a dense network of anemometers. The method uses a suitably chosen cluster analysis to automatically group the observed flow patterns. The classification scheme was improved by addition of an iterative refinement of the obtained classes [2, 3]. The flow patterns from an area of about 50 km by 50 km around Basel were classified in [2, 3]. During the MISTRAL/REKLIP field experiment in 1991-1992, 50 meteorological stations were operated in that area. The one-hour mean wind observations from these stations allowed to identify 12 main flow patterns. This is a surprisingly small number of substantially different flow patterns considering the very complex topography in the area around Basel. For applications like air pollution control studies it would be of great interest to have a climatology of these flow patterns, giving the frequency and seasonal and diurnal occurrence of these wind fields.

2 IDENTIFICATION OF FLOW PATTERNS

As only one full annual cycle of data was available for the dense network of MISTRAL stations, the diurnal and even more the annual cycle of the flow patterns are not well determined by these data. To obtain more reliable annual and diurnal cycles of the wind regimes data from several years are necessary. Luckily, there are several routinely operated stations in and around the MISTRAL area, whose data records of one-hour means cover several years. The question remains whether the characteristic flow patterns of the MISTRAL area can be determined from the observations at these few routine stations. Two approaches were considered: 1) The distance between wind fields as defined in [1] was used to assign each set of wind observations to the closest flow pattern. 2) A linear discriminant analysis [4] was used to assign the wind observations from the few routine stations to one of the flow patterns.

The two methods were tested with data from the MISTRAL year when both the full dataset and the wind observations from the routine stations were available. The second method, the linear discriminant analysis,

turned out to give a better identification (or hit) rate and proved to be more robust in case some stations did not report valid data.

The more stations are used in the discriminant analysis the better the identification rate becomes, but the shorter the available data record is. A compromise between length of data record and high hit rate, i.e. large number of stations, was searched. A set of 11 stations was chosen with a common data record of 6 years (1990-1995).

3 CLIMATOLOGY

From the 11 routinely operated stations, the best flow pattern was assigned by the linear discriminant analysis for all one-hour means of the full 1990-1995 period.

| Class | Speed | Frequency | 1991/92 |
|-------|---------|-----------|---------|
| 1 | 4.1 m/s | 13.0 % | 14.0 % |
| 2 | 2.7 | 11.1 | 10.3 |
| 3 | 3.0 | 10.4 | 10.3 |
| 4 | 2.1 | 6.1 | 7.8 |
| 5 | 2.6 | 8.2 | 9.1 |
| 6 | 5.7 | 8.6 | 6.7 |
| 7 | 2.6 | 10.3 | 7.9 |
| 8 | 2.6 | 8.0 | 8.1 |
| 9 | 2.2 | 5.8 | 6.8 |
| 10 | 3.6 | 5.5 | 6.1 |
| 11 | 3.1 | 6.8 | 6.6 |
| 12 | 2.6 | 6.2 | 6.2 |

Table 1: Mean wind speed and frequency of the 12 flow patterns as obtained from the 11 routine stations over the period 1990-1995. The last column gives the frequencies of the classes as obtained from the 50 MISTRAL stations for the one-year period in 1991/92, after allocation of the outliers.

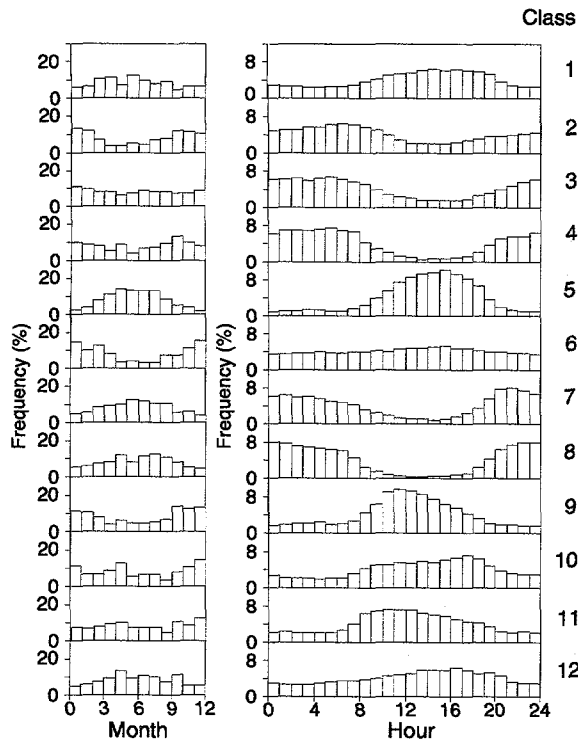


Fig. 1: Annual and diurnal cycle of the 12 characteristic flow patterns of the MISTRAL area around Basel based on data from 11 routine stations from 1990 through 1995.

Table 1 shows the frequency and the mean wind speeds of the 12 flow patterns over the six years. In the last column the frequency of the classes obtained from the 50 stations of the MISTRAL year is given (after allocation of the outliers [3]). The agreement between the frequencies of the 6-year period and the MISTRAL year is good. The mean wind speed identifies classes 1 and 6, both with westerly winds, as high speed flow patterns as in [2, 3] for the one-year period.

In Figure 1 the annual cycle (left column) and the diurnal cycle (right column) of the flow patterns is shown. The diurnal cycles agree very well with those of the one-year MISTRAL period [2, 3] when all 50 stations were in operation. The diurnal cycle of class 1 is more pronounced compared to the results of the MISTRAL

year. The annual cycles of the classes are much more pronounced and smoother than for the shorter data-set. For example, flow patterns 5 (northerly winds) and 7 (westerly winds) occur mostly in late spring and summer, whereas flow patterns 2 (southerly winds), 6 (westerly winds) and 9 (easterly winds) mainly occur in autumn and winter.

4 CONCLUSIONS

It was shown that the flow patterns determined from a dense network of 50 stations can be identified from the data of a few, 11, routinely operated stations. As these few stations are in operations since several years, a climatology of the flow patterns could be obtained. This climatology allows to perform calculations of transport and dispersion of air pollutants in a systematic and efficient way. Evidently, the same method of class identification can also be used in an emergency response system, where the actual flow pattern would be determined from a few meteorological stations.

5 ACKNOWLEDGEMENTS

The project REKLIP/MISTRAL is partly funded by the two cantons of Basel. Additional data were kindly provided by the Swiss Meteorological Institute, Zürich, the Lufthygienamt beider Basel, Liestal, and the Geographical Institute of the University of Basel.

6 REFERENCES

- [1] R.O. Weber, P. Kaufmann, "Automated Classification Scheme for Wind Fields", *J. Appl. Meteor.*, **34**, 1133-1141, (1995).
- [2] P. Kaufmann, R.O. Weber, "Classification of Mesoscale Wind Fields in the MISTRAL Field Experiment", *J. Appl. Meteor.*, **35**, 1963-1979, (1996).
- [3] P. Kaufmann, "Regionale Windfelder über Komplexer Topographie", Ph.D. thesis No.11565, Swiss Federal Institute of Technology (ETH), Zürich, (1996).
- [4] P.A. Lachenbruch, "Discriminant Analysis", Hafner Press, London, (1975).

TOPOLOGICAL ENTROPY OF AUTONOMOUS FLOWS

R. Badii

When studying fluid dynamics, especially in a turbulent regime, it is crucial to estimate the number of active degrees of freedom or of localized structures in the system. The topological entropy quantifies the exponential growth of the number of "distinct" orbits in a dynamical system as a function of their length, in the infinite spatial resolution limit. Here, I illustrate a novel method for its evaluation, which extends beyond maps and is applicable to any system, including autonomous flows: these are characterized by a lack of a definite absolute time scale for the orbit lengths.

1 INTRODUCTION

Recent advances in the mathematical theory of the Navier-Stokes equations (NSE), the primary model for real fluid dynamics, have produced the first connection between two approaches to turbulence that seemed far apart: namely, the conventional, stochastic approach by Kolmogorov, and the dynamical systems approach. Several approximation techniques for the NSE, among which Galerkin's truncation and the inertial manifold, rely on the estimate of the number of "active" degrees of freedom in the turbulent fluid (of the order of 10^9 in the atmosphere) and of the unpredictability of the motion [1]. When these are not too large, turbulence is called weak and can be studied with methods developed in nonlinear dynamics. The present study reports on the generalization of one of these from discrete-time maps to generic flows.

One of the primary indicators of chaos in a dynamical system is the topological entropy K_0 [2] which measures the exponential increase of the number of orbits belonging to sets with suitable separation properties, as a function of the orbit length. Therefore, K_0 quantifies the "richness" of solutions of the system. Its evaluation, however, is mostly restricted to maps (i.e., discrete-time systems) or to periodically forced flows (also characterized by a fixed unit of time: the period T). For these cases, one may define $N_\varepsilon(n)$ as the number of order- n orbits (i.e., the temporal extension of which is n time units) which lie apart by at least a distance ε , so that

$$K_0 = \lim_{\varepsilon \rightarrow 0} \lim_{n \rightarrow \infty} \ln N_\varepsilon(n)/(nT), \quad (1)$$

where $T = 1$ for a map. Such a simple relation, however, is not applicable to generic flows, in some of which (called autonomous) the orbits may intersect any (Poincaré) surface at irregularly spaced times t_n . Therefore, the definition of K_0 must be extended to include a suitable average over these return times.

2 THE METHOD

In Ref. [3], a method has been proposed for the evaluation of K_0 (and the related generalized entropy K_q [4]) both in models and in experiments. The first step requires the construction of a so-called "generating partition" [5] in the chosen Poincaré section which enables one to associate each orbit with a sequence $S = w_1 w_2 \dots$ of symbols from a finite alphabet $A = \{0, 1, \dots, b-1\}$, where w_i is the label of the partition element visited at time t_i . Since, in general, the orbit

does not fill the euclidean space densely, some concatenations of symbols may never occur: i.e., points from some element are not mapped to points of every other element. The probability $P(S)$ is also evaluated for each S (stationary systems are considered). Then, the symbols of the orbit along the time lattice play the role of spin variables and the quantity $E = -\ln P(S)$ is interpreted as the energy of the configuration S . In order to construct a thermodynamic formalism which accounts for the variable lengths of the orbits associated with n -symbol sequences, one introduces the grand-partition function [3]

$$\Omega_n(z; q) \equiv \sum_S P^q(S) z^{t(S)}, \quad (2)$$

where z is the fugacity, S is a level- n sequence, $t(S)$ the corresponding orbit's length, and q a parameter. The term $z^{t(S)}$ provides a detailed compensation for the generally exponential decrease of the probability $P(S) \sim \exp[-\kappa t(S)]$ with $t(S)$, where $\kappa \geq 0$ is called the "local entropy". The series obtained for $n \rightarrow \infty$ converges if $z < z(q)$, where $z(q)$ is the convergence radius. Hence, one may set $z(q) = \exp[(q-1)K_q]$, where K_q is a function having the properties of an average entropy. It is, indeed, immediately verified that Eq. (2) reduces to the original definition of the generalized entropy K_q [4] in case $t(S) = nT$ for all S and a fixed T . Rather than determining $z(q)$ by imposing the arbitrary constraint $\Omega_n(z; q) = 1$ (or any other constant), one compares the partition functions at two consecutive levels:

$$\sum_S P^q(S) z^{t(S)} = [\lambda(z; q)]^{-1} \sum_{S'} P^q(S') z^{t(S')}, \quad (3)$$

where $S = w_1 \dots w_n$ is a generic level- n word and $S' = Sw_{n+1}$ any of its extensions. In the limit $n \rightarrow \infty$, $z(q)$ is determined from the relation $\lambda[z(q); q] = 1$. A standard procedure further permits one to reformulate Eq. (3) as an eigenvalue problem for a generalized transfer matrix $T_n(z, q)$, the entries of which read, at level $n+1$,

$$T_{w_0 w_1' \dots w_n'; w_1 \dots w_{n+1}} \equiv \sigma^q(Sw_{n+1}) z^{t(Sw_{n+1})-t(S)} \cdot \delta_{w_1' w_1} \dots \delta_{w_n' w_n}, \quad (4)$$

where $\sigma(Sw_{n+1}) \equiv P(Sw_{n+1})/P(S)$ is the conditional probability of w_{n+1} given S . As it is well-known (e.g., from Onsager's solution of the Ising model), this procedure is tantamount to performing an order- n word-to-word Markov approximation of the system's scaling dynamics. Here, in particular, the word lengths $t(S)$ may

vary within any fixed level n . The generalized entropy finally reads

$$K_q = \frac{\ln z(q)}{q-1}, \quad (5)$$

where $z(q)$ is the value of z for which the largest eigenvalue $\lambda_1(z; q)$ of \mathbf{T} equals 1, in the limit $n \rightarrow \infty$: i.e., it is the solution of

$$\det(\mathbf{T}_n(z, q) - \lambda \mathbf{I}_n) = 0 \text{ for } n \rightarrow \infty. \quad (6)$$

3 RESULTS

The method has been applied in the cases $q = 0, 1$, and 2 (topological, metric, and correlation entropies, respectively) to the Lorenz system [6] (deduced by a severe Galerkin truncation of the NSE)

$$\begin{aligned} \dot{x} &= -10(x - y) \\ \dot{y} &= -y + 28x - xz \\ \dot{z} &= -\beta z + xy \end{aligned} \quad (7)$$

at $\beta = 8/3$ and $\beta = 1$ and to the Rössler system [7] (which originates from electronics)

$$\begin{aligned} \dot{x} &= -y - z \\ \dot{y} &= x + 0.2y \\ \dot{z} &= 0.2 - 5.7z + xz. \end{aligned} \quad (8)$$

In the former, the Poincaré section has been chosen as $\Sigma = \{(x, z) : x = y, \dot{x} \cdot \text{sgn}(x) < 0\}$; in the second, as the plane $x = 0$ with $\dot{x} > 0$. A binary (ternary) partition has been chosen for the Lorenz system at $\beta = 8/3$ ($\beta = 1$), defined by $x = 0$ ($x = \pm 0.2$) in the (x, z) plane, and a binary partition for the Rössler system, defined by $y = -6.74$ in the (y, z) plane. The value of $t(S)$ has been computed as the average return time of the flow trajectory to Σ within the domain B_S corresponding to each sequence S .

The finite- n estimates $K_q(n)$ generally approach the limit K_q exponentially from above, for the chosen values of q . Quicker convergence is obtained from the difference $\tilde{K}_q(n) = (n+1)K_q(n+1) - nK_q(n)$. In the Lorenz system at $\beta = 8/3$, $K_0 = 0.912 \pm 0.05$, $K_1 = 0.906 \pm 0.002$, and $K_2 = 0.901 \pm 0.005$: these values are reached already for $n = 5$. At $\beta = 1$, slower convergence is observed because of a less uniform distribution of the orbits and of slight intermittent effects: the values $K_0 = 0.640 \pm 0.005$, $K_1 = 0.5 \pm 0.005$, and $K_2 = 0.36 \pm 0.006$ are obtained for $n \geq 6$. Finally, for the Rössler system, the method yields $K_0 = 0.0890 \pm 0.0005$, $K_1 = 0.0710 \pm 0.0005$ and $K_2 = 0.584 \pm 0.001$: the attractor is hence also quite nonuniform and slow convergence is observed for $q > 1$.

The results are confirmed by independent estimates based on average local expansion rates of the flow (which are not applicable to time series, at variance with the present method) [3]. In particular, K_1 coincides with the sum of the positive average Lyapunov exponents in

hyperbolic systems [8]: this is generally a good approximation also in nonhyperbolic cases as the ones considered here. Moreover, the theory reproduces a formula for the metric entropy K_1 known as Abramov's theorem [3,8].

These results show that the new method not only yields a unified approach to the definition and estimation of generalized entropies (and similar quantities, such as dimensions) for maps and flows, but also proves applicable in practice, at variance with, e.g., formulas for the topological entropy of flows. Applications to delay-differential equations which display high-dimensional attractors are in progress. Knowledge of the function K_q is equivalent to that of the free energy in a conventional statistical system and carries all necessary information about possible phase transitions.

4 ACKNOWLEDGEMENTS

The author is indebted to M. Finardi for an early collaboration and to P. Talkner for useful discussions.

5 REFERENCES

- [1] R. Badii and A. Politi, *Complexity: hierarchical structures and scaling in physics*, Cambridge University Press, Cambridge (1997).
- [2] R.L. Adler, A.G. Konheim, and M.H. McAndrew, *Trans. Am. Math. Soc.* 114, 309 (1965).
- [3] R. Badii, *Phys. Rev. E* 54, 4496 (1996).
- [4] A. Renyi, *Probability theory*, North-Holland, Amsterdam (1970).
- [5] E. Ott, *Chaos in dynamical systems*, Cambridge University Press, Cambridge (1993).
- [6] E.N. Lorenz, *J. Atmos. Sci.* 20, 130 (1963).
- [7] O.E. Rössler, *Phys. Lett. A* 57, 397 (1976).
- [8] I.P. Cornfeld, S.V. Fomin, and Ya.G. Sinai, *Ergodic theory*, Springer, New York (1982).

SADDLE POINT AVOIDANCE IN BARRIER CROSSING PROBLEMS

P. Talkner and A.N. Drozdov (present address: Universidad de Sevilla, Spain)

The long-time behavior of the stochastic dynamics of a two-dimensional system having two metastable states is investigated by means of the low-lying part of the corresponding two-dimensional Smoluchowski operator. In particular, its dependence on three parameters describing the strength of the noise, the coupling of the two degrees of freedom and a ratio of relaxation-times is considered. Further information characterizing the transition process between the metastable states is gained from the corresponding eigenfunctions.

1 INTRODUCTION

The coexistence of various locally stable states is a common feature of many different models describing diverse phenomena such as chemical reactions, biological evolution, first order phase transitions, switching between the insulating and conducting states of a tunnel diode, and jumps of the magnetic flux in a SQUID to name but a few [1]. Multistability is only possible in systems with nonlinear equations of motion. In the simplest case there are two locally stable steady states and an unstable one. The presence of Gaussian, or other unbounded noise in such a system in principle destabilizes all states and allows the system to visit its whole state space. The residence times, however, of the different parts of the state space may vary by many orders of magnitude. In particular when the noise is weak one finds the system mostly in a close vicinity of one of the formerly stable states. Attempts to escape from there happen on microscopic, in general rather short time-scales but most of them are not successful. Since after each unsuccessful escape event the system falls back into about the same initial state the life-time is exponentially distributed and can be characterized by a rate. This means that weak noise renders the formerly stable states metastable with exponential decay at a rate Γ .

For the sake of concreteness we consider a charge transfer reaction that takes place in a polar solid or liquid [2]. The reaction itself is characterized by a spatial coordinate of the charge defining a reaction coordinate x with, say, $x = -1$ at reactants and $x = 1$ at products. At both states $x = \pm 1$ the energy of mean force $U(x)$ is assumed to have the same value and larger values elsewhere. A simple function with these properties is

$$U(x) = \frac{1}{4}x^4 - \frac{1}{2}x^2. \quad (1)$$

The influence of the polarization of the surrounding medium can properly be described by a single solvation coordinate y that in general increases the energy of the mean force according to

$$V(x, y) = U(x) + \frac{\gamma}{2}(x - y)^2 \quad (2)$$

where γ is a coupling constant. Units are chosen such that in the constrained equilibrium at a fixed position x of the charge the solvation coordinate takes the value $y_{eq}(x) = x$. The remaining degrees of freedom of the reacting molecules and the surrounding medium make up the heat bath that causes both noise and dissipation in the system. As a further simplifying assumption the friction force giving rise to dissipation is supposed

to be large enough such that any inertial effects can be neglected. The coupled equations of motion of the reaction and solvation coordinates then read

$$\begin{aligned} \dot{x} &= -\partial_x V(x, y) + \sqrt{2D}\xi_x(t) \\ \dot{y} &= -\epsilon\partial_y V(x, y) + \sqrt{2\epsilon D}\xi_y(t) \end{aligned} \quad (3)$$

where ∂_x and ∂_y denote the partial derivatives with respect to x and y , respectively, and $\xi_x(t)$ and $\xi_y(t)$ are independent Gaussian white noises describing the small but frequent impacts of the heatbath on the system, i.e.

$$\begin{aligned} \langle \xi_x(t) \rangle &= \langle \xi_y(t) \rangle = 0, \\ \langle \xi_x(t)\xi_y(s) \rangle &= 0, \\ \langle \xi_x(t)\xi_x(s) \rangle &= \langle \xi_y(t)\xi_y(s) \rangle = \delta(t-s), \end{aligned} \quad (4)$$

where $\delta(t)$ denotes the Dirac δ -function. Further, D gives the strength of the noise in convenient units, and $\epsilon = \tau_y/\tau_x$ denotes the ratio of relaxation times τ_x and τ_y of the reaction and solvation coordinate, respectively. Note that due to detailed balance of the considered process [3] the parameter ϵ also enters the strength of the noise in the y direction and consequently renders the diffusion in the x - y plane anisotropic.

2 KRAMERS-LANGER THEORY

According to the classical theory by Kramers and Langer [4] a typical escape path leads over the saddle point of the potential $V(x, y)$. The resulting rate has the form of an Arrhenius law

$$\Gamma = \frac{\sqrt{2}}{2\pi} \kappa \exp\{-E\}, \quad (5)$$

where $E = (4D)^{-1}$ is the activation energy in thermal units and κ the transmission factor

$$\kappa = \frac{1}{2} \left\{ 1 - \gamma - \gamma\epsilon + [(1 - \gamma - \gamma\epsilon)^2]^{1/2} \right\}. \quad (6)$$

The Kramers-Langer theory is known to give the correct rate in the so-called weak noise limit, i.e. when D goes to zero [5]. Berezhkovskii and Zitserman have argued that the typical trajectories do not go over the saddle of the potential $V(x, y)$ when the anisotropy parameter ϵ is an additional small parameter [6]. Accordingly, the rates are expected to grossly deviate from the Kramers-Langer result in this parameter region. In two recent publications [7] we presented a thorough numerical analysis of this problem covering the relevant part of the parameter space spanned by D , ϵ and γ . Further, we compared the numerical results with different approximate analytic theories that are valid in particular

regions of parameter space.

3 THE SMOLUCHOWSKI EQUATION

An equivalent description of the process defined in (3) is given by the Smoluchowski equation that governs the time evolution of the probability $p(x, y, t)$ of finding the system at the state (x, y) at time t . It reads

$$\partial_t p(x, y, t) = Lp(x, y, t), \quad (7)$$

where L is the Smoluchowski operator

$$L = D \left(\partial_x e^{-V(x,y)/D} \partial_x e^{V(x,y)/D} + \epsilon \partial_y e^{-V(x,y)/D} \partial_y e^{V(x,y)/D} \right). \quad (8)$$

The time evolution of the probability $p(x, y, t)$ can be represented in terms of the eigenvalues λ_n and the right- and left-eigenfunctions $P_n(x, y)$ and $Q_n(x, y)$, respectively, of the Smoluchowski operator being defined as

$$\begin{aligned} LP_n(x, y) &= -\lambda_n P_n(x, y), \\ L^\dagger Q_n(x, y) &= -\lambda_n Q_n(x, y), \end{aligned} \quad (9)$$

where L^\dagger denotes the adjoint, or backward Smoluchowski operator [3]. The small eigenvalues govern the time evolution at large times and, hence, are of particular interest. If the transitions between two metastable states determine the slow motion of the system, the smallest non-vanishing eigenvalue yields the transition rates. It is separated by a large gap from the remaining eigenvalues that characterize fast relaxation processes. We found this type of spectrum of eigenvalues for all parameter values but those with very small coupling constants γ . The solvation coordinate then becomes extremely sluggish. It dominates the long-time behavior and the low-lying part of the spectrum consists of almost equidistant eigenvalues.

The rate regime covering the rest of the parameter space with not too small values of the coupling constant γ can still be subdivided into the Kramers-Langer regime in which the rate formula (5) applies with an accuracy of better than 25% and the anisotropic regime. The former regime is characterized by the fact that the noise strength is the only relevant small quantity. In the latter regime the anisotropy parameter ϵ is also small while the coupling constant has some intermediate value. Then the reaction coordinate almost instantaneously follows the motion of the solvation coordinate that moves in an effective bistable one-dimensional potential [7]. This effective potential has a different barrier height than the bare one. Consequently, in the anisotropic regime the rate deviates already in the activation energy from the prediction of the Kramers-Langer theory.

In the rate regime the eigenfunctions belonging to the smallest non-zero eigenvalue λ_1 contain further relevant information about the long-time dynamics. The corresponding left-eigenfunction $Q_1(x, y)$ is either 1 or

-1 in most of the state space and changes within a narrow region between these two values. It can therefore be used as a site-localizing function [9]. Its node-line coincides with the stochastic separatrix [1] from which the system proceeds to either reactants or products with equal probability. Whereas in the Kramers-Langer regime the stochastic and the deterministic separatrices coincide, the two considerably deviate in the anisotropic regime. The right-eigenfunction $P_1(x, y)$ is given by the product of the left-eigenfunction and the equilibrium probability density being proportional to $\exp\{-V(x, y)/D\}$. The function $\rho(x, y)$ that equals $P_1(x, y)$ where the latter is positive and zero elsewhere is a stationary current-carrying probability density. It describes a probability flux from sources distributed according to the equilibrium density to the stochastic separatrix which is absorbing. The probability flux through the stochastic separatrix as it varies along this curve indicates where most of the trajectories leave the initial metastable state. In the Kramers-Langer regime this predominantly happens near the saddle point. Preliminary results show that in the anisotropic regime the probability flux has two maxima away from, and a minimum at the saddle point. This indicates that indeed the exit from a metastable state need not lead over a saddle-point.

4 ACKNOWLEDGMENTS

It is a pleasure to thank Prof. A. M. Berezhkovskii and Prof. V. Yu. Zitserman for valuable discussions.

5 REFERENCES

- [1] P. Hänggi, P. Talkner, M. Borkovec, *Rev. Mod. Phys.* 62, 251 (1990); G. R. Fleming, P. Hänggi, *Activated Barrier Crossing*, World Scientific, Singapore, 1993; P. Talkner, P. Hänggi, *New Trends in Kramers' Reaction Rate Theory*, Kluwer, Dordrecht, 1995.
- [2] A. N. Berezhkovskii, *Chem. Phys.* 164, 331 (1992).
- [3] H. Risken, *The Fokker Planck Equation*, Springer Verlag, Berlin, 1989.
- [4] H. A. Kramers, *Physica* 7, 284 (1940); J.S. Langer, *Ann. Phys. (N.Y.)* 54, 258 (1969).
- [5] M. M. Klosek-Dygas, B. M. Hoffman, B. J. Matkowsky, A. Nitzan, M. A. Ratner, and Z. Schuss, *J. Chem. Phys.* 90, 1411 (1989).
- [6] A. M. Berezhkovskii, V. Yu. Zitserman, *Chem. Phys. Lett.* 158, 369 (1989).
- [7] A. N. Drozdov, P. Talkner, *J. Phys. Chem.* 105, 4117 (1996); *Phys. Rev. E* 54, 6160 (1996).
- [8] G. J. Moro, *J. Chem. Phys.* 103, 7514 (1995).
- [9] D. Ryter, *Physica A* 142, 103 (1987); P. Talkner, *Chem. Phys.* 180, 199 (1994).

THE NOVEL PHENOMENON OF NOISE-CATALYZED CHAOS-ORDER TRANSITIONS

F. Gassmann

Numerical simulations of the Lorenzian water wheel have been used to investigate the influence of stochastic noise on the lifetimes of chaotic transients. Whereas in one region of parameter space no noise dependency could be detected, a shortening of the lifetimes by more than four decades was found in another region. This large effect was produced by a significant modification of the attraction basin of a quasistable stationary state rather than by affecting the chaotic orbits before the chaos-order transitions occurred. This novel phenomenon of noise-induced chaos-order transitions is not related to stochastic resonance or other noise-induced effects.

1 INTRODUCTION

Complex systems often show ordered stationary or periodic states after a shorter or longer chaotic transient when initialized at random. As stochastic environmental or internal noise is always present in natural systems, the combined effect of chaos and stochastic noise determining the time needed for the system to "find" an ordered state is of interest. Up to now much work has been devoted to investigations of noise-induced transitions from a given stationary state over a barrier to another stationary state. More recently, theoretical and experimental studies dealt with noise-induced escape from basins of different types of attractors of dissipative, non-linear dynamical systems far from equilibrium. In contrast to these investigations, we are interested here in noise dependency of transitions from chaos to a steady state. Franaszek [1] showed for the logistic map and the Hénon map that chaotic evolution may be elongated by a maximum of about 20% when small amplitude noise is added and shortened with noise of larger amplitude. However, Blackburn, Grønbech-Jensen, and Smith [2] found no noise dependency for a mathematical pendulum with its point of suspension subjected to a harmonic vertical displacement, neither in simulations nor experimentally with an electronic analog. Also, recent investigations by Lai [3] with a diffusively coupled logistic map lattice revealed only a negligible effect for this 20-dimensional spatio-temporal system. Based on these results he concludes that "the presence of noise is not advantageous in attempts to reduce the transient lifetime".

2 THE SYSTEM

We describe here results based on numerical simulations of a Lorenzian water wheel with 12 buckets and thus 14 phase space dimensions that was inspired by the techno-scientific masterpiece exhibited at the Technorama in Winterthur. This water wheel was used for testing the numerical model based on the following equations approximately describing the real system:

$$\begin{aligned} \dot{\varphi} &= \omega, \quad \varphi_i \equiv \left(\varphi + \frac{2\pi i}{n} \right) \bmod 2\pi \\ \dot{\omega} &= \frac{1}{\tau^2} \sum_{i=0}^{n-1} v_i \sin \varphi_i - \frac{1}{\tau_2} \omega + \sigma \xi \\ \dot{v}_i &= \frac{\delta_i}{\tau_0} - \frac{1}{\tau_1} v_i, \quad 0 \leq v_i \leq 1 \\ \delta_i &= \begin{cases} 1 & \text{for } |\varphi_i - \pi| > \pi - \frac{\pi}{n} \\ 0 & \text{elsewhere} \end{cases} \end{aligned} \quad (1)$$

The system consists of n (here $n = 12$) buckets spaced equally around the rim of a wheel rotating around a horizontal axis. The top bucket fills when passing under the faucet ($\delta_i = 1$) that delivers water at a steady rate. The buckets leak steadily, and a friction, proportional to angular velocity ω dissipates energy. One arbitrarily chosen bucket defines the angular position φ and v_i is the normalized water content in bucket i . Key parameters of the system are the time constants τ_0 , τ_1 and τ_2 signifying the time for an empty bucket to be filled, the time for a full one to get empty and the friction time constant (set to 1.8 s) respectively. A last parameter τ^{-2} is the maximum angular acceleration exerted from a single full bucket and disappears when time is normalized to τ . Noise is coupled to the system as additive torque noise. σ stands for its amplitude and ξ are numbers from a pseudo random generator with homogeneous distribution on the interval $[-1, 1]$. A new random number is used for every time step Δt set to 0.2 s.

3 RESULTS

Figure 1 shows an overview on the types of behavior found with computer simulations approximately integrating Eq. (1) without noise. The results of 60×200 randomly initialized transients of at most 200'000 time steps each are shown. Detected ordered states were the stationary states, all symmetrically oscillating pendulum states with different amplitudes, periodic rolling

states with variable angular velocity but without changes of sign and other periodic states with periods shorter than 80 s. The latter were defined by maxima of the autocorrelation of ω exceeding 0.97. If none of these states were detected after 200'000 time steps, the asymptotic state at the respective parameter values is either chaotic or has a period longer than 80 s or the chaotic transient exceeds 40'000 s. For parameter combinations indicated by points A and B, transition times to ordered states (mainly stationary rotations) for randomly initialized transients quickly approaching the chaotic attractor were statistically analyzed and found to be exponentially distributed analogous to radioactive decay statistics [1,2,4]. In point A, no noise effect could be observed as described in [2].

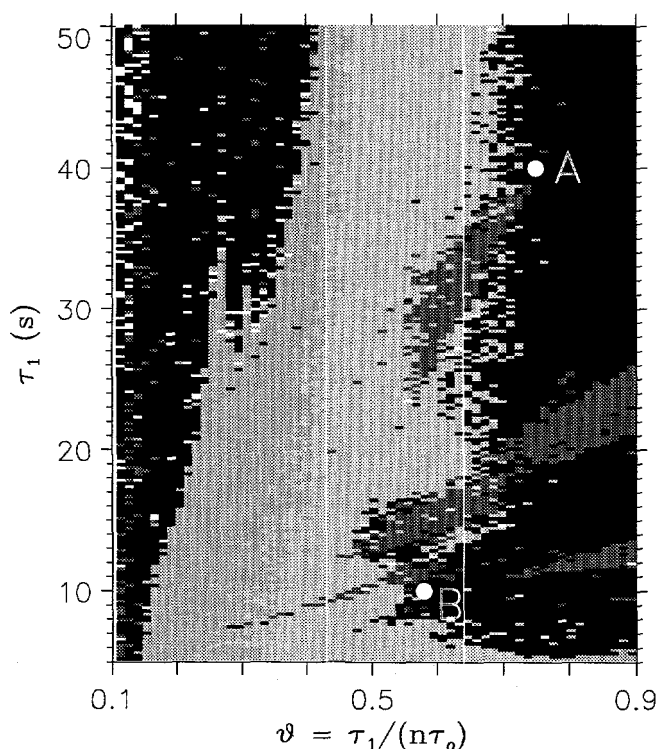


Fig. 1: Solution types on the $v - \tau_1$ plane for $\tau_2 = 1.8$ s and $n = 12$ without noise. Detected states are stationary (light grey), rolling (grey), pendulum (dark grey) and other states with short period (white). The area with no detected short-periodic states (black) contains chaos, states with long period and very long chaotic transients. The vertical lines are theoretical stability limits for the stationary rotation [4]. A and B are the two points to be investigated here: at A no and at B very large noise dependency of the lifetimes of chaotic transients was found.

In contrast to previously known results, 28 series of 10'000 chaotic transients with parameters according to point B revealed a very large noise dependency of their mean lifetimes as shown in Figure 2. To our knowledge, such important noise-induced shortening of mean transition times to an ordered state by more than 3 decades is reported here for the first time. At

noise amplitudes exceeding 0.5 s^{-2} a sharp increase of mean transition times arises from noise-induced escape from the steady state back to the chaotic attractor, a well known process that can be described by an Arrhenius relation. Inspection of many transitions by a method described in detail in [4] shows that the novel noise effect cannot be understood as a noise-induced escape from the chaotic attractor but rather as a noise-induced *trapping* of the chaotic trajectories by a probabilistic basin of the attractor for the stationary states. In addition, we show in [4] that the shortening of chaos lifetime increases to over 4 decades with decreasing time step so proving the physical reality of the novel phenomenon.

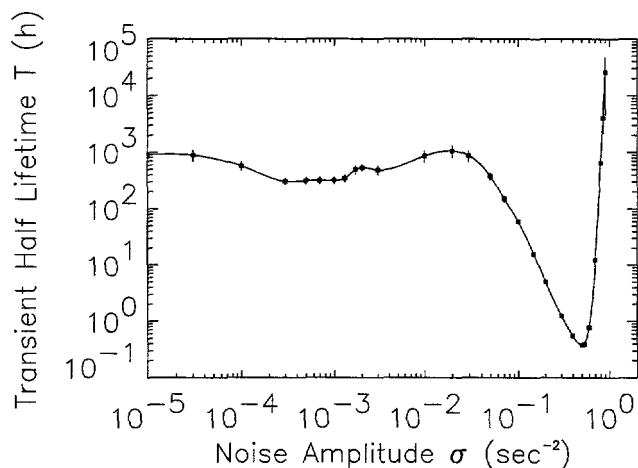


Fig. 2: Noise dependency of mean transition times from chaos to a stationary state at point B. Error bars indicate \pm twice the standard deviation.

4 CONCLUSIONS

The here reported noise-catalyzed spontaneous emergence of order out of chaos is clearly different from the well known stochastic resonance [5]. The general characterization of systems and locations in parameter space showing this novel large noise effect is at the moment an open question. Potential fields of interest might be biological evolution theory, cognition physiology, economy, ecology, climate dynamics or other research areas dealing with complex multistable systems subjected to high noise levels. Further, as interesting technical applications of stochastic resonance emerge now, 15 years after discovery of the phenomenon, such applications of our novel effect are to be expected for the future.

5 REFERENCES

- [1] M. Franaszek, Phys. Rev. A **44**, 4065, (1991).
- [2] J.A. Blackburn, N. Grønbech-Jensen and H.J.T. Smith, Phys. Rev. Lett. **74**, 908, (1995).
- [3] Y.C. Lai, Phys. Letters A **200**, 418, (1995).
- [4] F. Gassmann, submitted to Phys. Rev. E., 12.9.1996.
- [5] M.I. Dykman et al., Nuovo Cimento D **17**, 661, (1995).

SWISS TAXATION POLICIES TO CURB CO₂ EMISSIONS

O. Bahn, E. Fragnière (HEC-Lausanne, Switzerland), S. Kypreos

This study offers insights about the design of economically efficient policies to curb carbon dioxide (CO₂) emissions in Switzerland. The method uses MARKAL, a bottom-up engineering model of the energy system. Based on a stochastic programming approach, this study proposes as a first option the introduction of a hedging carbon tax. Using then a multinational MARKAL model, this study considers as a second alternative an international co-operation to curb jointly CO₂ emissions by means of a uniform carbon tax.

1 INTRODUCTION

Sustainable development requires avoiding drastic climate change. To this end, the United Nations Framework Convention on Climate Change called in 1992 for the "stabilisation of greenhouse gas concentrations in the atmosphere". Stabilising concentration at a "safe" level may require significant CO₂ emission reduction. This in turn might require major changes in energy markets and systems. It is therefore important to design economically efficient policies to curb CO₂ emissions. This paper gives some insights for Switzerland, using MARKAL models. It studies specifically Swiss taxation options to reduce CO₂ emissions. A detailed report of this study can be found in [2].

2 NATIONAL TAXATION OPTIONS

To study the curbing of Swiss CO₂ emissions by means of a carbon tax, we first follow a scenario-by-scenario analysis with a MARKAL model for Switzerland [5]. We analyse three scenarios for CO₂ emission control: baseline (no reduction), cumulative stabilisation (relative to 1990, between 2000 and 2030), and cumulative 10% reduction (relative to 1990, between 2000 and 2030) to reach by 2030 a 20% reduction (from the 1990 level). The associated CO₂ emission levels are given in Figure 1. Swiss MARKAL computes also the marginal costs of CO₂ reduction. They correspond to the carbon taxes needed to reach the specified CO₂ emission control targets. These taxes are high, especially in the reduction scenario. Indeed, it requires a tax that increases from 23 Swiss cents per litre of gasoline in 2000 to 1 SFr in 2030.

We believe that such costs may go beyond the limits of the Swiss willingness to pay for avoiding climate change, which is still perceived as an uncertain threat. Alternative taxation policies should therefore be found. This paper proposes as a first option a hedging taxation strategy. It is designed with a two-stage stochastic version of Swiss MARKAL [4]. We consider again three alternative CO₂ emission control policies (no reduction, cumulative stabilisation and 10% reduction) that define three states of the world (SW1, SW2 and SW3, respectively) to which an assumed probability (25%, 50% and 25%, respectively) is associated. We have chosen this probability distribution following a Bayesian approach, that reflects our level of conf-

dence in the different outcomes. We suppose furthermore that all uncertainties related to climate change will be resolved by the year 2010. The decisions to be taken before 2010 are common to the three states of the world. They constitute the hedging strategy. The corresponding CO₂ emission levels are also given in Figure 1.

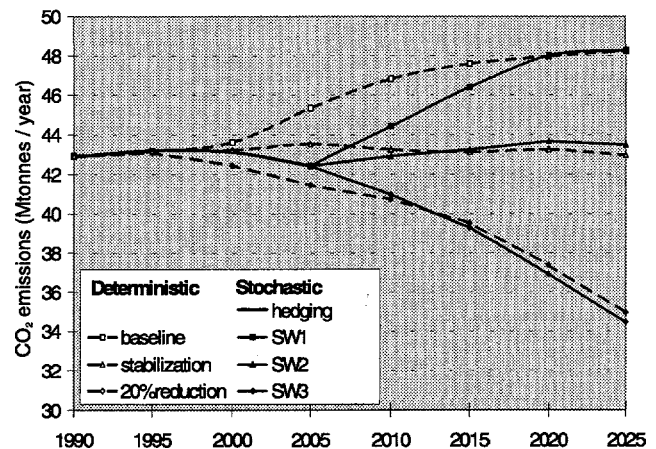


Fig. 1: CO₂ emission paths for deterministic (dashed lines) and stochastic (solid lines) cases.

For the years 2000 and 2005, the stochastic Swiss MARKAL model provides only one set of marginal costs. This defines a hedging taxation strategy, namely a tax to be imposed on CO₂ emissions to hedge for climate change. This tax is low (around 9 to 11 Swiss cents per litre of gasoline) and thus more easily acceptable by taxpayers. Its introduction corresponds to a "least regret" strategy, which balances present regret of imposing premature and costly emission reduction with future regret of neglected reduction in the past. After 2010, when uncertainties about climate change are resolved, taxes are either removed (when SW1 occurs), or adjusted to meet the CO₂ reduction targets (SW2 and SW3). In particular, carbon taxes to achieve a cumulative 10% reduction are again high (from 42 Swiss cents per litre of gasoline in 2010 to 1.11 SFr in 2030). We believe thus that the hedging taxation strategy is a good short term strategy. But in the longer term, if the necessity to reduce significantly CO₂ emissions is confirmed, another taxation policy should be found.

3 INTERNATIONAL UNIFORM TAX

An efficient alternative taxation policy for Switzerland can be designed at the international level. For (industrialised) countries committed to reduce their emissions by a given level, a suitable strategy is to introduce a uniform carbon tax. It enables one to reach the committed overall reduction target at least cost, taking into account differences in national emission reduction costs. The idea is to share reduction efforts among the participating countries, such as to equalise their marginal abatement costs. This level gives the value of the uniform tax to be imposed in each country.

To illustrate the benefits to be gained from harmonisation of marginal reduction costs, we have simulated a co-operation among three European countries (Belgium, the Netherlands and Switzerland), using a multinational MARKAL model [3]. Two scenarios related to CO₂ emissions are considered: baseline (no reduction), and cumulative 10% reduction (relative to 1990, between 2010 and 2030). Along with this reduction scenario, two situations are simulated. When each country reduces separately its CO₂ emissions, and when the same overall reduction is obtained at the international level. This second situation is simulated by the multinational MARKAL model.

The uniform carbon tax computed by the multinational MARKAL model is rather low: from 9 Swiss cents per litre of gasoline in 2010 to 24 in 2030. Moreover, when harmonising their emission reduction efforts, Belgium, the Netherlands and Switzerland can expect savings of about 2.6 billion SFr (1990) over 20 years. The model indicates also that Belgium and Switzerland have a direct profit from the co-operation, whereas the Netherlands has to bear an increase in its total abatement costs. Indeed, when co-operating, Belgium and Switzerland are "allowed" to emit more CO₂, whereas the Netherlands, given its lower marginal cost of reduction, has to compensate by reducing further its emissions. To secure the co-operation of the Netherlands, it must be compensated for its total abatement cost rise. Belgium and Switzerland can offer the Netherlands (through compensation payments) a "fair" sharing of their co-operation dividends, to ensure that every country receives a net benefit from the co-operation [1].

4 CONCLUSIONS

Curbing CO₂ emissions in Switzerland turns out to be costly, compared with other industrialised countries. We believe that the high carbon tax necessary to achieve a cumulative 10% reduction between 2000 and 2030, as estimated by the Swiss MARKAL model, may not be easily accepted by the Swiss taxpayers. As a first alternative taxation policy, we propose to introduce a low level carbon tax, as computed by the

Swiss stochastic MARKAL model, to hedge for climate change. This would gain time to resolve scientific and policy uncertainties surrounding the climate change issue, and to proceed with future more efficient (both in term of emission and energy) technologies [6]. In the longer term, if the necessity to significantly reduce CO₂ emissions is confirmed, an efficient taxation policy could be designed at the international level (uniform carbon tax, as estimated by the multinational MARKAL model), by harmonising emission reduction efforts among willing (industrialised) countries.

The international taxation policy approach enables one to take into account differences in national emission reduction costs. Moreover, transfer payments can be set up to fairly divide the co-operation dividends among the participants, to ensure that each receives a net benefit. In a modified form, this approach could be extended to include developing countries [2]. From this perspective, a "Joint Implementation" strategy allows to integrate issues of economic efficiency, ecological integrity and international equity. We believe thus that international co-operation to control CO₂ emissions is a valuable policy to achieve a sustainable future without drastic global climate change.

5 REFERENCES

- [1] O. Bahn, "Techniques de décomposition dans l'analyse des choix énergétiques et environnementaux", Ph. D. Thesis, University of Geneva, Switzerland, (1994).
- [2] O. Bahn, E. Fragnière, S. Kypreos, "Swiss energy taxation options to curb CO₂ emissions", The 1996 European Environment Conference, Conference Proceedings, ERP Environment, Shipley, West Yorkshire, UK, pp. 1-6, September, (1996).
- [3] O. Bahn, A. Haurie, S. Kypreos, J.-P. Vial, "A decomposition approach to multiregional environmental planning: a numerical study", Operations Research and Environmental Management, Kluwer Academic Publishers, pp. 119-132, (1996).
- [4] E. Fragnière, A. Haurie, "A stochastic programming model for energy/environment choices under uncertainty", Int. J. Environment and Pollution 6 (4-6), pp. 587-603, (1996).
- [5] S. Kypreos, "CO₂ emission control in Switzerland using mathematical programming", INFOR 30(3), pp. 194-206, August, (1992).
- [6] A. Manne, R. Richels, "Buying greenhouse insurance: the economic costs of carbon dioxide emission limits", MIT Press, Cambridge, (1992).

MODELLING REGIONAL TRADE OF CO₂ CERTIFICATES

B. Büeler (IFOR-ETHZ & PSI), O. Bahn, S. Kyreos, H.-J. Lüthi (IFOR-ETHZ)

Many countries have developed energy models (such as MARKAL-MACRO---MM) to assess their energy policies, in particular concerning the curbing of their carbon dioxide (CO₂) emissions. To integrate national MM models, we propose a multi-regional MARKAL-MACRO (3M) model. It enables one to study an international co-operation to curb jointly CO₂ emissions through a market of emission permits. Furthermore, from a decision support perspective, the 3M model can be used to integrate aspects of ecological sustainability (in relation to the global climate change issue), economic welfare, efficient resource use and technological innovation. To solve 3M, we follow two alternative mathematical methods.

1 INTRODUCTION

To assess energy policies designed to curb CO₂ emissions, many countries have developed energy models, such as MARKAL and MARKAL-MACRO (MM). To evaluate the dividends to be gained from co-operating on CO₂ abatement using these tools, one can integrate these models. The coupling of national MARKAL models, by introducing global environmental constraints and minimising the overall energy costs, has been reported in [1]. This paper is concerned with the integration of national MM models into a competitive economic equilibrium framework to study an international market of emission permits [2]. It is the first effort towards the development of a regionalised global trade model that considers explicitly, through rich technological details, the reference energy system of each region. The integration of national MM models consists first in extending them by coherent trade and budget relationships. As a second step, two mathematical approaches are followed to obtain alternative formulations. Numerical applications shall be reported in forthcoming publications.

2 MARKAL-MACRO

MM [3] is a link of two sub-models: MARKAL, a bottom-up engineering model of the energy system, and MACRO, a top-down macro-economic growth model. It enables one to study equilibrium on national energy markets. Its specificity is the following. First, it contains through rich technological details a sophisticated description of the energy sector (MARKAL), from primary sources to energy services. Second, it uses an aggregate production function for the rest of the economy (MACRO).

The mathematical formulation of MM is cast as a convex non-linear optimisation problem, where equilibrium on energy markets is determined by a single optimisation. The model maximises a utility function U , defined as the integral over a time horizon T of the discounted logarithm of consumption C_t . The production function, which performs the linkage between the MARKAL and MACRO sub-models, is a nested constant elasticity of substitution function. It relates economic output Y_t to the primary inputs capital K_t , labour L_t and energy services $D_{k,t}$ (k are the categories of energy services). It allows substitution between the pair capital-labour

and energy services, when the relative prices change. Accumulation of capital K_t depends on new investments I_t and on depreciation of existing capital. Demands for energy services $D_{k,t}$ are primarily determined by economic output (MACRO), prices of energy services (MARKAL) and exogenous parameters (elasticity of substitution and energy efficiency improvement independent of price changes). Economic output is distributed between consumption, investment and the payment of energy costs EC_t (computed by MARKAL, include the cost of curbing pollutant emissions).

3 MULTI-REGIONAL MARKAL-MACRO

Let us suppose that a group of R regions (e.g. countries) decides to co-operate to curb their CO₂ emissions. This co-operation is implemented through a market of emission permits, to reach overall reduction targets. In addition to these permits, the regions may exchange other tradable goods. To study these markets, we propose a multi-regional MM (3M) model.

Before describing 3M, let us introduce some additional notations. We denote by $x_{g,r,t}$ the net export of good g by region $r \in R$ in period $t \in T$, and by p_g the market price of g . By dropping indices for x , we mean the corresponding vector, like $x_{g,r} = (x_{g,r,t})_T$ which contains all time-related components. Furthermore, v^T denotes thereafter the transpose of vector v , and $u^T v$ the scalar product of vectors u and v . Currently, our model considers only two goods: good 0, an aggregate good in monetary unit (numéraire good) whose price p_0 is a price index; and good 1, the CO₂ emission permits. For the latter, we denote by $w_{0,r}$ the initial allocation (endowment) of permits for region r . To take inter-regional trade into account, regional MM models are modified as follows. First, the economic output of each region r can also be used for export:

$$Y_{r,t} = C_{r,t} + I_{r,t} + EC_{r,t} + x_{0,r,t}.$$

And second, each region r cannot emit more CO₂ ($EM_{r,t}$) than the amount of permits it possesses (initial endowment minus net export of permits):

$$EM_{r,t} \leq w_{1,r,t} - x_{1,r,t}.$$

The 3M model can then be formulated following two equivalent alternatives.

3.1 Market equilibrium conditions

In this approach, a budget constraint is first added to each regional MM model:

$$p_0^T x_{0,r} + p_1^T x_{1,r} \geq 0,$$

to ensure that, for each region r , trade accounts are balanced over the model time horizon. Let now $p^* = (p_0^*, p_1^*)$ denote market equilibrium prices. 3M can then be formulated as the following four conditions (E1)–(E4), which define the markets' equilibrium:

(E1) Each region r maximises its utility U_r .

(E2) At the markets' equilibrium, there is an excess of supply over demand:

$$e(p^*)^T = \left(\sum_{r=1}^R x_{0,r}(p^*), \sum_{r=1}^R x_{1,r}(p^*) \right) \geq 0.$$

(E3) Equilibrium prices are feasible: $p^* \geq 0$.

(E4) Prices for goods in strict excess at the markets' equilibrium are zero: $p^{*T} e(p^*) = 0$.

Based on the excess function $e(p)$, the equilibrium conditions (E1)–(E4) can be cast as the following variational inequality problem (VIP):

$$\left\{ \text{Find } p^* \in \mathfrak{R}_+^d: e(p^*)^T (p - p^*) \geq 0, \forall p \in \mathfrak{R}_+^d \right\}.$$

Given pseudo-monotonicity of $e(p)$, a cutting plane algorithm can be applied to solve this VIP formulation. Finally, let us notice that the computation of $e(p)$ requires only the solving at each iteration of R independent optimisation problems, which we do in parallel on a network of independent workstations.

3.2 Aggregated utility function

An alternative approach consists in aggregating, with appropriate weights η_r ($r \in R$) called Negishi weights [4], the regional utility functions into a global welfare function. 3M is then formulated as follows:

$$\left\{ \begin{array}{l} \max \sum_{r=1}^R \eta_r U_r \\ \text{s.t.} \\ \left(\sum_{r=1}^R x_{0,r}, \sum_{r=1}^R x_{1,r} \right) \geq 0, \\ \text{regional MM equations, } \forall r \in R. \end{array} \right.$$

The first constraint of this problem corresponds to a global excess constraint. Let $p = (p_0, p_1)$ denote the dual variables associated with it for a given Negishi weights vector η . Then η^* corresponds to an equilibrium if and only if the budget constraint holds for each region $r \in R$, namely if:

$$p_0^{*T} x_{0,r} + p_1^{*T} x_{1,r} = 0, \forall r \in R.$$

To solve this problem, one has to determine appropriate Negishi weights. This is done through an iterative approach that increases η_r when region r does not use all the wealth it could have ($p^T e_r > 0$), and decreases it otherwise.

The much larger optimisation problem induced by the Negishi-formulation can imply computational intractability, when the number R of regions to be solved increases. However, by dualising the global excess constraint, the problem can be decomposed, so as to solve again at each iteration R independent optimisation problems, which we do in parallel on a network of independent workstations.

4 CONCLUSIONS

Multi-regional energy models can contribute to evaluate the economic implications of international policy co-ordination for CO₂ emission abatement. The 3M model we propose enables one to study an international market of CO₂ emission permits. From a decision support perspective, 3M can be used to integrate aspects of ecological sustainability (in relation to the global climate change issue), economic welfare, efficient resource use and technological innovation. Furthermore, the specificity of our approach is to use regional models that are developed by local expert teams, but are structurally consistent.

The mathematical methods we use for integrating regional MM models, namely the VIP and Negishi approaches, are general. They can in principle be used to couple other kinds of models into an economic equilibrium framework. The implementation of these methods has been done in parallel on a network of independent workstations. This is a clear advantage for solving large multi-regional models, when the number of regions is large.

5 REFERENCES

- [1] O. Bahn, A. Haurie, S. Kypreos, J.-P. Vial, "A decomposition approach to multiregional environmental planning: a numerical study", Operations Research and Environmental Management, Kluwer Academic Publishers, pp. 119-132, (1996).
- [2] B. Büeler, "Entscheidungsunterstützendes Modellsystem zur Energieplanung", Projektbericht 3, ETHZ and PSI, March - August (1995).
- [3] A.S. Manne, C. Wene, "MARKAL-MACRO: a linked model for energy-economy analysis", Brookhaven National Laboratory, Upton, NY, BNL-47161, (1992).
- [4] T. Negishi, "General equilibrium theory and international trade", North-Holland Publishing Company, Amsterdam, (1972).

APPENDIX

TEACHING ACTIVITIES

University Level Teaching

PD DR. TH. H. SCHUCAN
"Sonnenenergie und Energiespeicherung"
Universität Basel, SS 1996.

PD DR. TH. H. SCHUCAN
"Energie und Umwelt"
Universität Basel, WS 1996/97.

PD DR. P. TALKNER
"Hydrodynamik II"
Universität Basel, WS 1995/96.

PD DR. P. TALKNER
"Stochastische Prozesse in der Physik I"
Universität Basel, SS 1996.

PD DR. P. TALKNER
"Stochastische Prozesse in der Physik II"
Universität Basel, WS 1996/97.

PROF. DR. A. WOKAUN
"Katalyse"
ETH Zürich, SS 1996.

PROF. DR. A. WOKAUN
"Physikalisch-chemische Grundlagen der Energienutzung"
ETH Zürich, WS 1996/97.

Lecture Courses at other Schools

DR. J. DOMMEN
"Chemie und Werkstoffe"
Technikum Winterthur Ingenieurschule, GS 95/96.

DR. W. DURISCH
"Strom aus Solarzellen"
Juventus Ingenieurschule Zürich (JSZ), 3. Quartal 1996.

DR. O. HAAS
"Brennstoffzellen und chemische Speicherung"
Kurs: Ingenieurschule Burgdorf, Nachdiplomstudium/
Energietechnik, 2. Quartal 1996.

F. HOLZER, DR. O. HAAS
"Brennstoffzellen und Batterien"
Praktikum: Ingenieurschule Burgdorf, Nachdiplom-
studium/Energietechnik, 2. Quartal 1996.

PUBLICATIONS

Books

F. GASSMANN
"Effet de serre - Modèles et Réalités"
Georg Editeur, Genève, 141 p., 1996.

J.G. HIGHFIELD
"The Central Role of Catalysis in a Future Energy
Cycle based on Renewable Hydrogen and Carbon
Dioxide as Liquefier"
Trends in Physical Chemistry, 5, pp.91-159, (Re-
search Trends, Trivandrum, India) 1995.

Papers

S. ANDREANI-AKSOYOGLU
"Impacts of Air Pollutants on Ecosystems"
A review, PSI-Bericht Nr. 96-05, 1996.

S. ANDREANI-AKSOYOGLU, J. KELLER
"Influence of Meteorology and Other Input Parameters
on Levels and Loads of Pollutants Relevant to Energy
Systems"
A Sensitivity Study. In: Caussade B., Power H.,
Brebba C.A. (editors): Air Pollution IV: Monitoring,
Simulation and Control. Computational Mechanics
Publ., pp. 767-778, 1996.

A. ARNOLD, R. BOMBACH, B. KÄPPELI,
A. SCHLEGEL*
"Quantitative Measurements of OH Concentration
Fields by Two-Dimensional Laser-Induced Fluores-
cence (2-D LIF)"
First European Conference on Small Burner Techno-
logy and Heating Equipment (ECSBT1) 1 (1996)
pp. 255-260, ETH Zurich, 1996.
* University of California, Berkeley

K.J. ARROW*, J. PARIKH**, G. PILLET
"Decision-Making Frameworks for Addressing Climate
Change"
Chapter 2, "Climate Change 1995: Economic and
Social Dimensions of Climate Change"
Edited by J.B. Bruce, H. Lee, E.F. Haites, Contribution
of Working Group III to the Second Assessment
Report of the Intergovernmental Panel on Climate
Change, Cambridge University Press, pp. 53-77, 1996.
* Stanford University, USA
** Indira Gandhi Institute of Development Research,
India

R. BADI

"Topological Entropy of Autonomous Flows"
Phys. Ref. E **54**, R4496, 1996.

O. BAHN, E. FRAGNIÈRE*, S. KYPREOS

"Swiss Energy Options to Hedge for Climate Change"
Econometrics of Environment and Transdisciplinarity,
in A. Baranzini and F. Carlevaro (Eds), Proceedings
List International Conference of Applied Econometrics
Association, Vol. II, Lisbon, Portugal, pp. 481-492,
April 1996.

* HEC, Lausanne

O. BAHN, E. FRAGNIÈRE*, S. KYPREOS

"Swiss Energy Taxation Options to Curb CO₂ Emissions"

The 1996 European Environment Conference, Conference Proceedings, ERP Environment, Shipley, West Yorkshire, UK, pp. 1-6, September 1996.

* HEC, Lausanne

O. BAHN, A. HAURIE, S. KYPREOS, J.-P. VIAL*

"A Decomposition Approach to Multiregional Environmental Planning: A Numerical Study"

C. Carraro and A. Haurie (Eds), Operations Research and Environmental Management, Kluwer Academic Publishers, pp. 119-132, 1996.

* Université Genève

A.M. BEREZHKOVSII*, P. TALKNER,
J. EMMERICH**, V.YU. ZITSERMAN***

"Thermally Activated Traversal of an Energy Barrier of Arbitrary Shape"

J. Chem. Phys. **105**, 10890, 1996.

* Karpov Institute, Moscow

** Universität Leipzig

*** Institute of High Temperatures, Moscow

D. BERLOWITZ

"Implicit Coupling of Turbulent Diffusion with Chemical Reaction Mechanisms for Prognostic Atmospheric Dispersion Models"

ETH Dissertation Nr. 11657, Zürich 1996.

D. BERLOWITZ, J. DOMMEN

"Photochemical Characterization of an Urban Air Mass: Measurements and Model Calculations"

Proceedings of EUROTRAC Symposium 96, Vol. I, Eds.: P.M. Borrell, P. Borrell, K. Kelly, T. Cvitas and W. Seiler. Computational Mechanics Publications, Southampton, 1996.

CH. BERNHOFER*, L.W. GAY**, A. GRANIER***,
U. JOSS, B. KÖSTNER****, R. SIEGWOLF,
J.D. TENHUNEN****, R. VOGT*****

"The HarteX-Synthesis: An Experimental Approach to Water and Carbon Exchange of a Scots Pine Plantation"

In Theor. Appl. Climatol. **53**, 173-183, 1996.

* Universität Dresden

** Universität Arizona, Tucson, USA

*** INRA Champenoux, France

**** Universität Bayreuth

***** Geographisches Institut, Universität Basel

A. BILL, B. ELIASSON*, E. KILLER*

"Hydrogenation of Carbon Dioxide in a Packed-Bed Reactor"

Hydrogen Energy Progress XI, Proceedings of the 11th World Hydrogen Energy Conference, Stuttgart, Germany, 2, pp. 1989-1995, 1996.

* ABB Corporate Research Centre, Baden

A. BILL, B. ELIASSON*, F. GEIGER, J. HIGHFIELD,
E. UENALA

"The Role of Simple Alcohols in Renewable Hydrogen Energy Cycles"

Proc. 11th International Symposium of Alcohol Fuels (ISAF XI), Sun City, South Africa, April 1996.

* ABB Corporate Research Centre, Baden

R. BOMBACH, B. HEMMERLING, W. HUBSCHMID,
D.N. KOZLOV*

"Laser-Induced Gratings in Carbon Dioxide Excited via Raman-Active Resonances"

Proc. SPIE - Int. Soc. Opt. Eng. **2778**, pp. 680-681, 1996.

* General Physics Institute, Moscow

S. BRAUN*, W. FLUECKIGER*, S. LEONARDI**,
W.K. GRABER, U. JOSS, W. NATER,
R.T.W. SIEGWOLF

"Belastung des Gebirgswaldes. Ansätze einer Risiko-bewertung"

BUWAL, 1996: Umwelt-Materialien 59, Bern, 1996.

* Institut für angewandte Pflanzenbiologie, CH-4124 Schönenbuch, Switzerland

** Labor for Ecotoxicology, CH-4208 Nunningen BL, Switzerland.

R. BRAZDIL*, M. BUDÍKOVÁ*, I. AUER**,
R. BÖHM**, T. CEGNAR***, P. FAŠKO****,
M. LAPIN****, M. GAJIĆ-CAPKA*****,
K. ZANINOVIĆ*****, E. KOLEVA*****,
T. NIEDŹWIEDŹ*****, Z. USTRNUL*****,
S. SZALAI*****, R.O. WEBER

"Trends of Maximum and Minimum Daily Temperatures in Central and Southeastern Europe"

Int. J. Climatology, **16**, 765-782, 1996.

* Masaryk University, Brno

** Central Inst. for Meteorol. and Geodynam., Vienna

*** Hydrometeorological Inst., Ljubljana

**** Slovak Hydrometeorological Inst., Bratislava

***** Meteorolog. and Hydrolog. Service, Zagreb

***** National Inst. of Meteorol. and Hydrol., Sofia

***** Inst. of Meteorol. and Water Managem., Cracow

***** Hungarian Meteorol. Service, Budapest

F.N. BÜCHI, M. WAKIZOE*, S. SRINIVASAN*

"Microelectrode Investigations of Oxygen Permeation in Perfluorinated Proton Exchange Membranes with Different Equivalent Weight"

J. Electrochem. Soc. **143**, p. 927, 1996.

* Center for Electrochemical Systems and Hydrogen Research, Texas A&M Univ., College Station, TX, USA

F.N. BÜCHI, G.G. SCHERER

"In situ Resistance Measurements of Nafion 117 Membranes in Polymer Electrolyte Fuel Cells"
J. Electroanal. Chem. **404**, 37, 1996.

A. CUELLAR

"Heat Transfer and Dehydrogenation in Catalytic Fixed Bed Reactors with ex situ Membranes"
Ph. D. Thesis, ETH Zürich, Nr. 11658, 1996.

A.N. DROZDOV*, P. TALKNER

"Thermally Activated Escape Processes in a Double Well Coupled to a Slow Harmonic Mode"
J. Chem. Phys. **105**, p. 4117, 1996.

* Universidad de Sevilla

A.N. DROZDOV*, P. TALKNER

"Activated Rate Processes in a Double Well Coupled to a Slow Harmonic Mode":
Test of Finite-Barrier Corrections for the Rate, Phys. Rev. E **54**, 6160, 1996.

* Universidad de Sevilla

W. DURISCH, B. HOFER

"Klimatologische Untersuchungen für Solarkraftwerke in den Alpen am Beispiel Laj Alv, Disentis, Graubünden"
PSI Bericht Nr. 96-01, ISSN 1019-0643, Jan. 1996.

W. DURISCH, J. URBAN*, G. SMESTAD**

"Characterisation of Solar Cells and Modules under Actual Operating Conditions"
Proc. of the World Renewable Energy Congress, Denver, Colorado, USA, Vol. 1, pp. 359-366, Edited by A.A.M. Sayigh, PERGAMON, 15-21 June 1996.

* Technical College Ulm, FHU, D-89075 Ulm, Germany

** Earth Systems Science and Policy, California State University at Monterey Bay, CSUMB, 100 Campus Center, Seaside California 93955, California, USA

W. DURISCH, S. LEUTENEGGER*, TH. URHEIM

"Kleinwechselrichter für Photovoltaik-Insulanlagen im Vergleichstest"
Bulletin SEV/VSE **10/96**, p. 38, 1996.

* LEC, 8700 Küsnacht

W. DURISCH, B. HOFER, D. WUILLEMIN

"Klimatologische Untersuchungen für Solarkraftwerke in den Alpen"
Bulletin SEV/VSE **10/96**, p. 16, 1996.

W. DURISCH

"Solarstrahlung für konzentrierende Systeme"
Workshop Industrielle Solarkalzinierung, PSI, Tagungsbericht, 3. Okt. 1996.

K. EHRENSBERGER, E. STEINER, P. KUHN

"Experimental Studies on the Hydrogen Yield of a Solar Thermochemical 2-Step Cycle with Mixed Iron Oxide Systems"
Proc. 11th World Hydrogen Energy Conference, Stuttgart, Germany, 23-28 June, pp. 843-848, 1996.

B. ELIASSON*, U. KOGELSCHATZ*, E. KILLER*, A. BILL

"Hydrogenation of Carbon Dioxide and Oxidation of Methane in an Electrical Discharge"
Hydrogen Energy Progress XI, Proceedings of the 11th World Hydrogen Energy Conference, Stuttgart, Germany, **3**, pp. 2449-2459, 1996.

* ABB Corporate Research Centre, Baden

E. FALGE*, W. GRABER, R.T.W. SIEGWOLF, J.D. TENHUNEN*

"A Model of the Gas Exchange Response of *Picea Abies* to Habitat Conditions"
Trees, **10**, pp. 227-287, 1996.

* Universität Bayreuth

R.P. FRIEDMAN*, J.M. GORDON*, H. RIES

"Compact High-Flux Two-Stage Solar Collectors Based on Tailored Edge-Ray Concentrators"
Solar Energy, **56**, pp. 607-615, 1996.

* Ben-Gurion University of the Negev, Beer-Sheva, Israel

M. FURGER, M. JENNI*, W. SCHMID**

"The Severe Storm of 22 July 1995 in northern Switzerland - a Tornado Case Study?"
Proc. 24th Int. Conf. on Alpine Meteorology, ICAM 96, Bled, Slovenia, Sept 9-13, pp. 153-159, 1996.

* Geographisches Institut Uni Bern

** Atmosphärenphysik ETH, Zürich

J. GANZ, A. MEIER, D. MISCHLER, H.R. TSCHUDI

"Properties of Volumetric Gas-Particle Solar Reactors"
Proc. 8th Int. Symp. on Solar Thermal Concentrating Technologies, Köln, Germany, 6-11 Oct. 1996.

F. GASSMANN, W. FELLER, O. SCHAUB*, K. KAMBER*, N. MOUSSIOPOULOS**, V. MEGARITI**

"Results of Wind Field Project MISTRAL and Application for Planning and Emergency Response"
Proc. of the Air Pollution '96 Conf., Toulouse, France, Comp. Mech. Publ., Southampton, 1996.

* Suisselectra AG, Basel

** Aristotle University, Thessaloniki, Greece

F. GASSMANN

"Klimaänderungen: Stehen uns Überraschungen bevor?"
VGL Information, Schweiz. Vereinigung für Gewässerschutz und Lufthygiene, Zürich, No.3, pp. 4-7, 1996.

F. GASSMANN

Contributor for "Decision-Making Frameworks for Addressing Climate Change"
IPCC Second Assessment 1995, Working Group III, Economic and Social Dimensions of Climate Change, Cambridge Univ. Press, 1996.

S. GHASHGHAIE*, W. BREYMAN***, J. PEINKE***, P. TALKNER, Y. DODGE****

"Turbulent Cascades in Foreign Exchange Markets"
Nature **381**, 767, 1996.

* Universität Bern

** Universität Basel

*** Universität Bayreuth

**** Université de Neuchâtel

S. GHASHGHAIE*, W. BREYMAN**, J. PEINKE***, P. TALKNER

"Turbulence and Financial Markets, in *Advances in Turbulence VI*"

Ed. by S. Gavrilakis et al., Kluwer Academic Publishers, Dordrecht, p. 167, 1996.

* Universität Bern

** Universität Basel

*** Universität Bayreuth

W.K. GRABER, R.T.W. SIEGWOLF, W. NATER, S. LEONARDI*

"Mapping the Impact of Anthropogenic Depositions on High Elevated Alpine Forests"
Environmental Software, Vol. 11, Nos. 1-2, pp. 59-64, 1996.

* Laboratory for Ecotoxicology, CH-4204
Himmelried, Switzerland

W.K. GRABER, D. BUERKI

"Projekt 'Windbank unteres Aaretal': Klassifikation von Windfeldern als Grundlage der aktuellen Ausbreitungssituation"
PSI-Bericht Nr. 96-11, 1996.

W.K. GRABER

"Herkunft des Ozons an einem Sommertag: Mögliche Reduktionsszenarien im Alpenraum"
In: Luftreinhaltung in der Schweiz - eine Bilanz, SSM-Tagungsband zur Tagung in Luzern, 12. Nov. 1996.

W. GRASSE*, C. TYNER**, A. STEINFELD, M. BECKER*

"The SolarPACES Annual Report 1995"

* DLR, Germany

** Sandia Laboratories, USA

C.E. GREGOIRE PADRO*, J.S. BADIN**, TH.H. SCHUCAN, J.S. RIBBERINK***

"Methodology Development for Analysis of Integrated Systems"

Hydrogen Energy Progress XI, Proceedings of the 11th World Hydrogen Energy Conference, Stuttgart, Germany, 1, pp. 391-396, 1996.

* National Renewable Energy Laboratory, USA

** Energetics Inc., USA

*** Netherlands Energy Research Foundation, NL

B. GUPTA*, F.N. BÜCHI, M. STAUB, D. GRMAN**, G.G. SCHERER

"Cation Exchange Membranes by Pre-irradiation Grafting of Styrene into FEP Films. II. Properties of Copolymer Membranes"

J. Polym. Sci.: Part A: Polym. Chem. **34**, p. 1873, 1996.

* Indian Institute of Technology, New Dehli, India

** EMPA, CH 8600 Dübendorf

B. GUPTA*, F.N. BÜCHI, G.G. SCHERER, A. CHAPIRO**

"Crosslinked Ion Exchange Membranes by Radiation Grafting of Styrene/Divinylbenzene into FEP Films"
J. Membrane Sci **118**, p. 231, 1996.

* Indian Institute of Technology, New Dehli, India

** CNRS, F-94320 Thiais

O. HAAS, R. KÖTZ

"Energiespeicherung im Supercap"

Schweizerische Technische Zeitschrift **5**, p. 26, 1996.

O. HAAS, S. MÜLLER, K. WIESENER*

"Übersichtsartikel: Wiederaufladbare Zink-Luftsauerstoff-Batterie"

Chemie Ingenieur Technik **68**, p. 524, 1996.

* Thomas-Mann-Strasse 44, D-01219 Dresden

CH. HAHN, S. KAISER*, A. WOKAUN

"Interaction of a Congo Red Dye Probe with Lecithine Vesicles Probed by Forced Rayleigh Scattering"
Tenside Surf. Det. **33**, pp. 209 - 213, 1996.

* Physikalische Chemie, Universität Bayreuth

P. HÄNGGI*, R. BARTUSSEK*, P. TALKNER, J. LUCZKA**

"Noise-Induced Transport in Symmetric Periodic Potentials: White Shot Noise Versus Deterministic Noise"
Europhys. Lett. **35**, p. 315, 1996.

* Universität Augsburg

** Silesian University, Katowice

W. HEDIGER

Contributor, "Decision-Making Framework for Addressing Climate Change"

J.B. Bruce, H. Lee and E. Haites (Eds), Climate Change 1995: Economic and Social Dimensions of Climate Change, Contribution of Working Group III to the Second Assessment Report of the Intergovernmental Panel on Climate Change, Cambridge University Press, pp. 53-77, 1996.

B. HEMMERLING, R. BOMBACH, W. HUBSCHMID

"Laser-Induced Gratings in Oxygen Excited via the $b^1\Sigma_g^+(v'=0)$ State"

Chem. Phys. Letters **256**, pp. 71-76, 1996.

V. HERRNBERGER,* W.K. GRABER, M. HUTTER
 "Needs of Users Versus Capabilities of Decision Support System, a Realizable Challenge or an Incompatibility per se?"

Proc. 4th DSS-Workshop, Aronsborg, Sweden, p. 6, October 1996.

* Abteilung für Strahlenhygiene, PSI

J.G. HIGHFIELD, A. BILL, E. UENALA, F. GEIGER, B. ELIASSON*

"The Role of Simple Alcohols in Renewable Hydrogen Energy Cycles"

Eleventh International Symposium on Alcohol Fuels, Sun City, South Africa, 2, pp. 528-539, 1996.

* ABB Corporate Research Centre, Baden

W. HUBSCHMID, R. BOMBACH, B. HEMMERLING, A. STAMPANONI-PANARIELLO

"Sound Velocity Measurements in Gases by Laser-Induced Electrostrictive Gratings"

Appl. Phys. B 62, pp. 103-107, 1996.

W. HUBSCHMID, B. HEMMERLING, A. STAMPANONI-PANARIELLO

"Dissipative processes in laser-induced electrostrictive gratings"

in *ICONO '95: Nonlinear Spectroscopy and Ultrafast Phenomena*, Vladimir V. Shuvalov und Alexei M. Zheltikov (Eds.), Proc. SPIE 2797, pp. 189-195, 1996.

A. JAKOB, S. STUCKI, R.P.W.J. STRUIS

"Complete Heavy Metal Removal from Fly Ash by Heat Treatment: Influence of Chlorides on Evaporation Rates"

Environ. Sci. Technol., 30, pp. 3275-3283, 1996.

F. JOHO

"Synthesen, elektrochemische, strukturelle und spektroskopische Untersuchungen zu Elektrodenmaterialien für Ionentransferbatterien"

Dissertation, ETH Zürich Nr. 11745, 1996.

U. JOSS, W.K. GRABER

"Profiles and Simulated Exchange of H₂O, O₃, NO₂ Between the Atmosphere and the HartX Scots Pine Plantation"

Theor. Appl. Climatol., 53, pp. 157-172, 1996.

P. KAUFMANN, R.O. WEBER

"Classification of Mesoscale Wind Fields in the MISTRAL Field Experiment"

J. Appl. Meteor., 35, 1963-1979, 1996.

P. KAUFMANN

"Bodennahe regionale Windfelder über komplexer Topographie"

Dissertation ETH Nr. 11565, Zürich, 1996.

M. KILO*, M. HUND*, G. SAUER*, A. BAIKER**, A. WOKAUN

"Reaction Induced Surface Segregation in Amorphous CuZr, NiZr and PdZr Alloys – an XPS and SIMS Depth Profiling Study"

J. of Alloys and Compounds 236, 137-150, 1996.

* Physikalische Chemie II, Universität Bayreuth

** Lab. für Technische Chemie, ETH Zürich

B. KÖSTNER*, P. BRION**, R. SIEGWOLF, A. GRANIER***

"Estimates of Water Vapor Flux and Canopy Conductance of Scots Pine at the Tree Level Utilizing Different Xylem Sap Flow Methods"

Theor. Appl. Climatol. 53, 105-113, 1996.

* Universität Bayreuth

** CEREG Strassburg, France

*** INRA Champenoux, France

A. KRIBUS, H. RIES, W. SPIRKL

"Inherent Limitations of Volumetric Solar Receivers" ASME J. Solar Energy Eng., 118, pp. 151-155, 1996.

J. KRÜGER*, W. KAUTEK*, M. STAUB, G.G. SCHERER

"Femtosecond-Pulse Laser Micromachining of Metal Layer Composites"

in "Laser in Research and Engineering", (Eds.). W. Waidelich, H. Hügel, H. Opower, H. Tiziani, R. Wallenstein, W. Zinth, Springer Verlag, Berlin, Heidelberg, New York, p. 966, 1996.

* Bundesanstalt für Materialprüfung, D-12200 Berlin

S. KYPREOS

"Allocation of Carbon Taxes Revenues"

C. Carraro and A. Haurie (Eds), Operations Research and Environmental Management, Kluwer Academic Publishers, pp. 133-152, 1996.

S. KYPREOS

"The MARKAL-MACRO Model and the Climate Change"

PSI Bericht Nr. 96-14, 1996.

R. LAMPRECHT, W.K. GRABER

"Modeling Dry Deposition of Dust Along the Dalton Highway"

In: Reynolds J.F. and Tenhunen J.D. ed.: Ecological Studies. Vol. 120, Springer, Berlin, 437, pp. 325-345, 1996.

T. LIPPERT*, J. DAUTH**, B. DEUBZER**, J. WEIS**, A. WOKAUN

"Photolysis of an Arylalkyl - Triazenido - Platinum(IV) Complex"

J. Rad. Chem. 47, 889-897, 1996.

* Physikalische Chemie II, Universität Bayreuth

** Wacker-Chemie GmbH, Burghausen, D

A. LUZZI*, K. LOVEGROVE*, M. SCHUBNELL,
H.R. TSCHUDI

"Further Investigation of Solar Ammonia Dissociation Reactors"

Proc. 8th Int. Symp. on Solar Thermal Concentrating Technologies, Köln, 1996.

* Australian National University, Canberra, Australia

G. MARIA, A. MARIN, C. WYSS, S. MUELLER,
E. NEWSON

"Modelling and Scaleup of the Kinetics with Deactivation of Methylcyclohexane Dehydrogenation for Hydrogen Energy Storage"

Chem. Eng. Sci., **51**, pp. 2891-2896, 1996.

G. MARIA, D.W.T. RIPPIN*

"Recursive Robust Kinetics Estimation by using a Mechanistic Shortcut Technique and a Pattern Recognition Procedure"

Comp. and Chem. Eng., **20**, pp. 587-592, 1996.

* ETH Zürich

G. MARIA, P. TERWIESCH*, D.W.T. RIPPIN*

"Reliable Online Kinetics Identification for a Semi-batch Process by Parallel Use of Shortcut Transfer of Information Rule and Regressive Estimators"

Chem. Eng. Comm., **143**, pp. 133-147, 1996.

* ETH Zürich

A. MEIER, J. GANZ, A. STEINFELD

"Modeling of a Novel High-Temperature Solar Chemical Reactor"

Chemical Engineering Science, Vol. **51**, pp. 3181-3186, 1996.

B. MISCHLER, P. BEAUD, T. GERBER,
A.-P. TZANNIS, P.P. RADI

"Degenerate Four-Wave Mixing of S₂ and OH in Fuel-Rich Propane/Air/SO₂ Flames"

Combust. Sci. and Tech., **119**, pp. 375-393, 1996.

S. MÜLLER, F. HOLZER, C. SCHLATTER,
C. COMNINELLIS*, O. HAAS

"New Generation of Rechargeable Zinc/Air Batteries" in Rechargeable Zinc Batteries, Commemorating the 100th Birthday of A. N. Frumkin/1995. The Electrochem. Soc. Proc., Pennington, NJ, Vol. **95-14**, p. 135, 1996.

* Swiss Federal Institute of Technology, CH-1015 Lausanne, Switzerland

S. MÜLLER, E. NEWSON, D. IMHOF*,
L.M. VENANZI, R. KOEPEL*, A. BAIKER*

"Heterogenised Platinum Clusters as Dehydrogenation Catalysts"

11th Int. Congress on Catalysis, Baltimore, USA, June 30 - July 5, 1996.

* ETH Zürich

S. MÜLLER, C. SCHLATTER, C. COMNINELLIS*,
O. HAAS

"Development of a 100 W Rechargeable Bipolar Zinc/Oxygen Battery, Contemporary Trends in Electrochemical Engineering"

Proceedings of the 4th European Symposium on Electrochemical Engineering, Prag, August 28-30, 1996.

* Swiss Federal Institute of Technology, CH-1015 Lausanne, Switzerland

S. MÜLLER, F. HOLZER, J. DESILVESTRO*,
O. HAAS

"Aluminum Alloys in Sulfuric Acid, Part II: Aluminum-Oxygen Cells"

J. Appl. Electrochem. **26**, pp. 1217-1223, 1996.

* Leclanché, 48 Avenue de Granson, CH-1400 Yverdon les Bains, Switzerland

S. MÜLLER, F. HOLZER, C. SCHLATTER,
C. COMNINELLIS*, O. HAAS

"Alkalische wiederaufladbare Zink/Luft-Batterie" PSI-Bericht 96-19, November 1996.

* Swiss Federal Institute of Technology, CH-1015 Lausanne, Switzerland

H.J. MUHR*, R. NESPER*, B. SCHNYDER,
R. KÖTZ

"The Boron-Heterofullerenes C₅₉B and C₆₉B. Generation, Extraction Mass Spectrometric and XPS Characterization"

Chemical Physics Letters **249**, p. 399, 1996.

* Laboratorium für Anorganische Chemie, ETH Zürich

B. NEININGER*, J. DOMMEN

"Polimet: Luftverschmutzung und Meteorologie in der Schweiz"

Buwal: Umwelt-Materialien 63. Bern, 1996.

* MetAir AG, CH-8308 Illnau

E. NEWSON, TH. HAUETER, P. HOTTINGER,
F. VON ROTH, G. SCHERER, TH.H. SCHUCAN

"Seasonal Storage of Hydrogen in Stationary Systems" Hydrogen Energy Progress XI, Proceedings of the 11th World Hydrogen Energy Conference, Stuttgart, Germany, **2**, pp. 1017-1026, 1996.

J.-C. PANITZ, A. WOKAUN

"Self-Diffusion of Water in Quaternary Surfactant Systems"

Tenside Surf. Det. **33**, pp. 205-208, 1996.

J.-C. PANITZ, A. WOKAUN

"Effects of Excitation Wavelength on the Raman Spectra of Vanadium(V) Oxo Compounds"

J. Phys. Chem. **100**, pp. 18357-18362, 1996.

P.P. RADT, B. MISCHLER, T. GERBER,
H. DREHER*, B. LEHMANN*, M. OCHS*
"Imaging of the Reaction Zone in a 100 KW Oil-Burn-
ing Furnace by use of a Broad-Band Excimer Laser"
Appl.-Phys. B V. 62: pp. 65-69, 1996.

* Lab. for Energysystems, ETH, Zürich

M. RAUCH*, H. KEPPLER*, B. POE*, W. HÄFNER**,
A WOKAUN

"A Pressure-Induced Phase Transition in MgSiO₃-rich
Garnet Revealed by Raman Spectroscopy"
American Mineralogist 81, pp. 1289-1292, 1996.

* Bayerisches Geoinstitut, Universität Bayreuth

** Physikalische Chemie, Universität Bayreuth

H. RIES, W. SPIRKL*

"Nonimaging Secondary Concentrators for Large Rim
Angle Parabolic Troughs with Tubular Absorbers"
Appl. Opt., **35**, pp. 2242-2245, 1996.

* Ludwig Maximilians-Universität, München

F. SALADIN, A. MEIER, I. KAMBER

"A Miniaturized Reactor for Photocatalysis and for
Simultaneous *in situ* Spectroscopy"

Rev. Sci. Instrum. **67**, pp. 2406-2409, 1996.

M. SAURER, S. BORELLA*, M. LEUENBERGER*
„ $\delta^{18}\text{O}$ of Tree Rings of Beech (*Fagus Silvatica*) as a
Record of $\delta^{18}\text{O}$ of the Growing Season Precipitation"
Tellus, 1996.

* Physikalisches Institut, Universität Bern

G.G. SCHERER, H.P. BRACK, F.N. BÜCHI,
B. GUPTA*, O. HAAS, M. ROTA

"Materials Research Aspects of Membrane Develop-
ment for Polymer Electrolyte Fuel Cells"

Hydrogen Energy Progress XI, Proc.11th World Hy-
drogen Energy Conference, Stuttgart, 1996.

* Indian Institute of Technology, New Dehli, India

G.G. SCHERER

"Fuel Processing for Polymer Electrolyte Fuel Cells"
Proceedings of the First IEA-Workshop, Paul Scherrer
Institut, CH-5232 Villigen, September 25-27, 1995,
published 1996.

C. SCHLATTER

"Etude d'une Batterie Zn/O₂ Rechargeable Selon une
Configuration Bipolaire"

Thèse No. 1486, EPFL, 1996.

A. SCHLEGEL, P. BENZ, T. GRIFIN*,
W. WEISENSTEIN*, H. BOCKHORN**

"Catalytic Stabilization of Lean Premixed Combustion:
Method for Improving NO_x Emissions"

Combustion and Flame 105, pp. 332-340, 1996.

* ABB Corporate Research, Department of Aero-
dynamics, CH-5405 Baden-Dättwil

** Lehrstuhl für Technische Chemie, Fachbereich
Chemie, University of Kaiserslautern, BRD

M. SCHUBNELL, H.R. TSCHUDI, CH. MÜLLER

"Temperature Measurement under Concentrated Ra-
diation"

Solar Energy 58, pp. 69-75, 1996.

M. SCHUBNELL, I. KAMBER, P. BEAUD

"Photochemistry at High Temperatures - Potential of
ZnO as a High Temperature Photocatalyst"

Appl. Phys. A 64, pp. 109-113, 1996.

V. SHKLOVER*, T. HAIBACH*, F. RIED**,
R. NESPER***, P. NOVÁK

"Crystal Structure of the Product of Mg²⁺ Insertion into
V₂O₅ Single Crystals"

J. Solid State Chem. **123**, p. 317, 1996.

* Laboratorium für Kristallographie, ETH Zürich

** Inst. für Mineralogie und Petrographie, ETH Zürich

*** Laboratorium für Anorg. Chemie, ETH Zürich

B.L. SMITH, T.V. DURY, A. MEIER, J.L. XIA*

"Some Aspects of CFD Modelling at PSI, Switzerland"

Proc. 3rd CFX Int. Users Conference, London, UK,
30 Oct. - 1 Nov. 1996.

* ETH Zürich

A. STEINFELD, P. KUHN, Y. TAMAURA*

"CH₄-Utilization and CO₂-Mitigation in the Metallurgi-
cal Industry via Solar Thermochemistry"

Energy Conversion and Management, Vol. **37**, pp.
1327-1332, 1996.

* Tokyo Institute of Technology, Japan

A. STEINFELD, C. LARSON*, R. PALUMBO*,
M. FOLEY*

"Thermodynamic Analysis of the Co-Production of
Zinc and Synthesis Gas Using Solar Process Heat"

Energy - The International Journal, Vol. **21**, No. 3,
pp. 205-222, 1996.

* Valparaiso University, USA

A. STEINFELD, P. KUHN, A. RELLER*,
R. PALUMBO**, J. MURRAY***, Y. TAMAURA****

"Solar-Processed Metals as Clean Energy Carriers
and Water-Splitters"

Hydrogen Energy Progress XI, pp. 601-609, *Proc.
11th World Hydrogen Energy Conference*, Stuttgart,
Germany, 23-28 June 1996.

* University of Hamburg, Germany

** Valparaiso University, USA

*** Portland State University, USA

**** Tokyo Institute of Technology, Japan

A. STEINFELD, R. PALUMBO*, J. LEDE**,
Y. TAMAURA***, A. RELLER****

"The Solar Thermal Reduction of Metal Oxides"

*Proc. 8th Int. Symp. on Solar Thermal Concentrating
Technologies*, Cologne, Oct. 6-11, 1996.

* Valparaiso University, USA

** CNRS-Nancy, France

*** Tokyo Institute of Technology, Japan

**** University of Hamburg, Germany

A. STEINFELD

"Solar-Processed Metals: Energy Vectors of the 21st Century"

Proc. 3rd. Sabin Conference on Energy and The Environment, Weizmann Institute, Israel, Nov. 26, 1996.

R. STRUIS, S. STUCKI, M. WIEDORN

"A Membrane Reactor for Methanol Synthesis"

J. Membrane Sci. **113**, pp. 93-100, 1996.

M. SULLIVAN, R. KÖTZ, O. HAAS

"Electrochemical Modified Glassy Carbon as an Electrochemical Capacitor Material"

Proceedings of the Symposium on Supercapacitors, The Electrochemical Society Proceedings Series, F.M. Delnick and M. Tomkiewicz Editors, Pennington, NJ, PV **95-29**, p. 198, 1996.

Y. TAMAURA*, M. TSUJI*, K. EHRENSBERGER, A. STEINFELD

"The Solar-Driven Coal/Fe₃O₄ Redox System"

Proc. 7th International Conference on Ferrites, Bordeaux, France, Sept. 3-6, 1996.

* Tokyo Institute of Technology, Japan

Y. TAMAURA*, M. KOJIMA*, N. HASEGAWA*, M. TSUJI*, K. EHRENSBERGER, A. STEINFELD

"Solar Energy Conversion into H₂ Energy Using Ferrites"

Proc. 7th International Conference on Ferrites, Bordeaux, France, Sept. 3-6, 1996.

* Tokyo Institute of Technology, Japan

A. TIMINGER*, H. RIES, W. SPIRKL*

"An Asymmetric CPC-Type Secondary Concentrator for Radiation from a North Field of Heliostats"

Proc. 8th Int. Symp. Solar Thermal Concentrating Technologies, Köln, Germany, 1996.

* Ludwig Maximilians-Universität, München

H.R. TSCHUDI, M. SCHUBNELL

"Temperature Measurements in Hot Volumetric Absorbers by Multiwavelength Probing"

Proc. 8th Int. Symp. on Solar Thermal Concentrating Technologies, Köln, 1996.

H.R. TSCHUDI

"Mapping of two Families of Rays by a Reflecting Contour"

J. Opt. Soc. Am. A **13** pp. 1117-1120, 1996.

M. TSUJI*, Y. WADA*, Y. TAMAURA*, A. STEINFELD, P. KUHN, R. PALUMBO**

"Coal Gasification Using the ZnO/Zn Redox System"

Energy and Fuels, Vol. **10**, pp. 225-228, 1996.

* Tokyo Institute of Technology, Japan

** Valparaiso University, USA

J. WEIGEL, R.A. KÖPPEL*, A. BAIKER*, A. WOKAUN
"Surface Species in CO and CO₂ Hydrogenation over Copper / Zirconia: On the Methanol Synthesis Mechanism"

Langmuir **12**, pp. 5319-5329, 1996.

* Lab. für Technische Chemie, ETH Zürich

J. WEIGEL, CH. FRÖHLICH*, A. BAIKER*, A. WOKAUN

"Vibrational Spectroscopic Study of IB Metal / Zirconia Catalysts for the Synthesis of Methanol"

Appl. Catal. A: General **140**, pp. 29-45, 1996.

* Lab. für Technische Chemie, ETH Zürich

J. WEIGEL

"Surface Species in Carbon Monoxide and Carbon Dioxide Hydrogenation Reactions over Zirconia Supported Catalysts for the Synthesis of Methanol a Drift Spectroscopical Study"

ETH Dissertation Nr. 11912, 1996.

R. WILLI*, B. RODUIT*, R. KÖPPEL*, A. WOKAUN, A. BAIKER*

"Selective Reduction of NO by NH₃ over Vanadia-Based Commercial Catalyst: Parametric Sensitivity and Kinetic Modelling"

Chem. Eng. Sci. **51**, pp. 2897-2902, 1996.

* Lab. für Technische Chemie, ETH Zürich

M. WINTER, J.O. BESENHARD*, P. NOVÁK

"Deckschichten auf LiCn-Anoden in wiederaufladbaren Li-Zellen"

GDCh-Monographie **3**, p. 438, 1996.

* Technische Universität Graz

A. WOKAUN

"Catalysis in General Energy Research"

Chimia **50**, pp. 94-98, 1996.

TALKS

S. ANDREANI

"Three Dimensional Modeling of Photochemical Air Pollution with the UAM"

Seminar Klimamodelle, ETH, Zürich, 13.6.1996.

P. BEAUD, D. FRANZKE, P. RADI, T. GERBER

"Time Resolved Study of Energy Transfer and Quenching of Excited OH in an Atmospheric Pressure Methane Air Flame"

IEA Conference, 18th Task Leader Meeting, Cranfield, England, Aug. 7-9, 1996.

P. BEAUD

"Time Resolved Study of Energy Transfer and Quenching of the A₂+(v=1) State of OH in Atmospheric Pressure Methane-Air Flame"

ERCOFTAC, Villigen, 27.6.1996.

K. BENGTTSSON

"Numerical and Experimental Investigation of NO_x Formation in Lean Premixed Combustion of Methane"
ERCOFTAC Meeting, PSI, 27 June 1996

**A. BILL, B. ELIASSON*, E. KILLER*,
U. KOGELSCHATZ***

"Greenhouse Gas Chemistry"
3rd International Conference on Carbon Dioxide Removal, Cambridge, USA, September 1996.

* ABB Corporate Research Centre, Baden

**A. BILL, B. ELIASSON*, E. KILLER*,
U. KOGELSCHATZ***

- "Direct Oxidation of Methane to Methanol in a Silent Discharge"
- "Methanol Synthesis from Pure CO₂"

Swiss Physical Society (Spring Meeting), Fribourg, Switzerland, March 1996.

* ABB Corporate Research Centre, Baden

R. BOMBACH

"Quantitative zweidimensionale laserinduzierte Fluoreszenz von OH-Radikalen im PSI Hochdruckbrenner"
ERCOFTAC Joint Annual Meeting of the Competence Centers on Measuring Techniques and Combustion and Pollution Formation, PSI Villigen, 27. Juni 1996.

H.P. BRACK

"Membrane Development for Polymer Electrolyte Fuel Cells: Contact Angle Investigations"
Chemistry Department, Polytechnic University, Brooklyn, NY, USA, January 4, 1996.

H.P. BRACK

"Development of Low Cost Membranes for Polymer Electrolyte Fuel Cells at the Paul Scherrer Institute"
Chemical Sciences Division, Department of Applied Science, Brookhaven National Laboratory, Upton, NY, USA, January 5, 1996.

H.P. BRACK

"Investigation of Radiation Induced Molecular Weight Changes in FEP Films by Melt Flow Index (MFI) Measurements"
Jahrestag. der Fachgruppe Rheologie der Polymer-Gruppe der Schweiz, Ciba-Geigy AG, Basel, 28.3.96.

H.P. BRACK

"Preparation of Fuel Cell Membranes by the Radiation Grafting Method"
Polymer Science and Engineering Department, University of Massachusetts at Amherst, Amherst, MA, USA, October 1, 1996.

H.P. BRACK

"Polymer Effects and Kinetics in the Preparation of Fuel Cell Membranes by the Radiation Grafting Method"
Chemistry Department, Brown University, Providence, RI, USA, October 3, 1996.

H.P. BRACK

"Preparation of Fuel Cell Membranes by the Radiation Grafting Method at PSI"
DuPont Fluoroproducts, Wilmington, DE, USA, October 18, 1996.

H.P. BRACK

"Crosslinking Considerations in the Preparation of Radiation-Grafted Membranes"
Herbsttagung der Polymer-Gruppe der Schweiz, Ciba Geigy AG, Basel, 28. November 1996.

F.N. BÜCHI

"Ex-situ Sorption and Conductivity Properties of Nafion Membranes"
1st Contractors Meeting, Joule III Project Second Generation SPFC Development, Petten, NL, May 8, 1996.

F.N. BÜCHI

"In-situ Conductivity and Water Transport Properties of Nafion Membranes"
2nd Contractors Meeting, Joule III Project Second Generation SPFC Development, PSI, CH, 12. September 1996.

F.N. BÜCHI

"Resistance and Water Transport Properties of Nafion Membranes in Internally Humidified PEM Fuel Cells"
190th Meeting of the Electrochemical Society, San Antonio, TX, USA, October 6-11, 1996.

F.N. BÜCHI

"Water Distribution in Nafion Membranes under Fuel Cell Conditions - Experimental and Modeling Results"
3rd Contractors Meeting, Joule III Project Second Generation SPFC Development, Siemens, Erlangen, D, 11. Dezember 1996.

F.N. BÜCHI

"Polymerelektrolyt Brennstoffzelle - Systemaspekte eines Brennstoffzellen-Stapels"
Schweizerische Tagung über das Anwendungspotential von Niedertemperatur-Brennstoffzellen, Ingenieurschule Grenchen-Solothurn, Grenchen, 4. Dezember 1996.

B. BÜELER, S. KYPREOS

"Multi-Regional MARKAL-MACRO: Introduction of CO₂ Trade Certificates and Solution Concepts"
Second International Conference on Computing in Economics and Finance, Geneva, Switzerland, June 26-28, 1996.

E. DEISS

"Modeling of Lithium Thin-Film Electrochemical Cells"
Herbstversammlung NSCG, Basel, 21. November 1996.

W.K. GRABER

"Herkunft des Ozons an einem Sommertag: Mögliche Reduktionsszenarien im Alpenraum"

Tagung der Schweizerischen Studiengruppe für Motorbetriebsstoffe (SSM) über 'Luftreinhaltung in der Schweiz - eine Bilanz', Tagung im Verkehrshaus Luzern, 12. Nov. 1996.

O. HAAS

"High Specific Power Zinc/Oxygen Batteries"

189th Meeting of the Electrochem. Soc., Los Angeles, May 6-11, 1996.

O. HAAS

"Wissenschaftliche Grundlagen und charakteristische Merkmale der wichtigsten wiederaufladbaren Batterien"

Condensateurs Fribourg SA, Fribourg, 6. Februar 1996.

O. HAAS

"Electrochemical Applications of Electroactive Polymers"

47th Annual Meeting of the International Society of Electrochemistry, Balatonfüred, Hungary, September 1-6, 1996.

O. HAAS

"Bipolare Zellen für die Elektrochemieprojekte am PSI"

12. PSI-Tagessymposium Elektrochemische Energiespeicherung, 11. September 1996.

O. HAAS

"Verfahrenstechnische Aspekte der wiederaufladbaren Li⁺-Ionen-Transfer-Batterien"

Jahrestagung Gesellschaft Deutscher Chemiker, Fachgruppe Angewandte Elektrochemie, Monheim, 9.-12. Oktober 1996.

O. HAAS

"Energy and Chemistry"

University of Fribourg, CH, 18. November 1996.

P. HÄRING

"Monitoring of Electrochemically Induced Dimensional Changes on the Nanometer Scale by In-Situ Atomic Force Microscopy"

Digital Instruments Electrochemistry Workshop, Karlsruhe, Deutschland, März 1996.

P. HÄRING

"Electrochemical Oxidation/Reduction of Thin Electroactive Films. An In-Situ Scanning Probe Microscopy Study"

Euroanalysis IX, Bologna, Italy, September 1996.

W. HEDIGER

"Toward an Ecological Economics of Sustainable Development"

- UT-MIT-ETH Joint Workshop on Alliance for Global Sustainability, The University of Tokyo, Japan, January 17-19, 1996.

- International Sustainable Development Research Conference, Manchester, UK, March 18-19, 1996.

W. HEDIGER

"Ecosystem Management and Sustainability: An Ecological-Economic Model"

Inaugural Conference of the European Branch of the International Society for Ecological Economics, Université de Versailles, Saint Quentin en Yvelines, France, May 23-25, 1996.

W. HEDIGER

"Framing Sustainability: a Socio-Ecological Economic Approach to Sustainable Development"

8th International Conference on Socio-Economics, Geneva, Switzerland, July 12-14, 1996.

W. HEDIGER

"Optimal Pollution Control and Ecological Sustainability"

The Fourth Biennial Meeting of The International Society for Ecological Economics, Boston University, Boston, MA, August 4-7, 1996.

B. HEMMERLING

"CARS Measurements of Temperature Fluctuations in a High Pressure Gas Turbine Combustor"

4th International Symposium on Special Topics on Chemical Propulsion, Stockholm, 27-31 May 1996.

W. HUBSCHMID

"Quantitative Measurements of OH Concentration Fields by 2-D LIF"

Eighteenth Task Leaders Meeting, International Energy Agency Executive Committee on Energy Conservation and Emissions Reduction in Combustion, Cranfield (GB), 6-9 August 1996.

J. HUSLAGE

"Swelling and Conductivity Measurements of Various Proton-Conducting Membranes in Dependence of their Pretreatment"

3rd Contractors Meeting, Joule III Project Second Generation SPFC Development, Siemens AG, Erlangen, 12. Dezember 1996.

A. IMHOF

"Industrielle Solarkalziniierung"

- Fa. Krupp-Polysius, D-Beckum
- Holderbank Management & Beratung, AG
- World Business Council for Sustainable Development, Herden
- Energiewirtschaftsdepartement, Aarau
- ABB - Industrie AG, Baden
- Bomin Solar Research GmbH, D-Lörrach
- MAERZ AG, Zürich
- Gewerbeverband, Basel
- BEW, Bundesamt für Energiewirtschaft, Bern
- BAWI, Bundesamt für Aussenwirtschaft, Bern
- BUWAL, Bundesamt für Umwelt, Wald und Landschaft, Bern
- DEZA, Delegierter für Entwicklungszusammenarbeit, Bern
- Zementfabrik, Rüdersdorf bei Berlin, Deutschland

J. KELLER

"Environmental Impacts of Air Pollutants from Swiss Energy Systems"
REMAPE Workshop, Copenhagen, Denmark, 26-27 September 1996.

P. KESSELRING

"Erneuerbare Energien, Möglichkeiten und Grenzen"
Rotary Club, Uster, 25.4.1996.

P. KESSELRING

"Energie und nachhaltige Entwicklung"
Kader der Flughafenimmobilien Gesellschaft, Kloten, 6.5.1996.

P. KESSELRING

"Solar Energy, some Technical and Techno-Political Considerations"
Universität Klagenfurt, 30.7.1996.

P. KESSELRING

"Fuel from Renewables"
Plenarvortrag, EUROSUN 96, Konferenzzentrum Freiburg im Breisgau, 17.9.1996.

P. KESSELRING

"Survey on Solar Chemistry"
8th International Symposium on Solar Thermal Concentrating Technologies, Köln, 10.10.1996.

P. KESSELRING

"Das integrierte Projekt 'Abfall' des Schwerpunktprogrammes Umwelt"
Baudepartement des Kantons Aargau, Abteilung Umweltschutz, Interkantonales Abfallclub-Treffen, 12.12.1996.

R. KÖTZ

"An Electrochemical Capacitor Based on Modified Glassy Carbon Electrodes"
190th Meeting of the Electrochemical Society, St. Antonio, Texas, October 6-11, 1996.

R. KÖTZ

"Electrochemical Capacitors Based on Modified Glassy Carbon"
The 6th International Seminar on Double Layer Capacitors and Similar Energy Storage Devices, Deepfield Beach, Florida, December 9-11, 1996.

R. KÖTZ

"Supercapacitors"
PPM Module 3, Meeting '96, Materials for Micromechanics and Electronics, EPFL Lausanne, 8. November 1996.

J. KRITZENBERGER, A. WOKAUN

"Zeitaufgelöste FTIR-Untersuchung der katalytischen Oxidation von Kohlenmonoxid unter periodischer Variation der Eduktkonzentrationen"
Bunsentagung Jena, Germany, 1996.

S. KYPREOS

"Markal-Macro/Trade"
IEA/ETSAP Workshop, Leuven, Belgium, May 3-10, 1996.

S. KYPREOS

"Swiss Energy Options to Hedge for Climate Change"
International Seminar on Energy Technology Assessment: Data, Methods and Approaches, Leuven, Belgium, May 6-7, 1996.

S. KYPREOS

"The MARKAL-MACRO Model and the Climate Change"
Europhysics Study Conference on Economy-Energy-Entropy, CERN, Geneva, Switzerland, May 10-13, 1996.

S. KYPREOS, M. JAKOB, O. BAHN

"Energy Economics"
Seminar on Comprehensive Assessment of Energy Systems (GaBE), Paul Scherrer Institute, September 23, 1996.

S. KYPREOS, O. BAHN

"Swiss Taxation Policies and Recent Developments in Energy Economics at PSI"
IIASA-IEA/ETSAP Meeting, November 4-7, 1996.

G. MARIA

"Interactive, Shortcut, Estimation Method for Process Kinetic Identification"
TU Erlangen, Germany, February 22, 1996.

A. MEIER

"CFD Simulation of a Novel High-Temperature Solar Chemical Reactor"
3rd CFD Day of the Leonhard Euler Research Center, ETH Zürich, Switzerland, January 22, 1996.

S. MÜLLER

"PSI Zinc/Air Battery"
- Electricité de France (EDF), Moret, April 16, 1996.
- BEW-Workshop "Accumulateurs", Paul Scherrer Institut, Villigen, 12. Dezember 1996.

S. MÜLLER

"Development of a 100 W Rechargeable Bipolar Zinc/Oxygen Battery, Contemporary Trends in Electrochemical Engineering"
4th European Symposium on Electrochemical Engineering, Prag, August 28-30, 1996.

E.J. NEWSON

"Heterogenised Platinum Clusters as Dehydrogenation Catalysts"
UOP Platforming Goup, Des Plaines, Illinois, USA, July 8, 1996.

E.J. NEWSON

"Kinetics with Deactivation for Methylcyclohexane Dehydrogenation"
UOP Platforming Goup, Des Plaines, Illinois, USA, July 8, 1996.

P. NOVÁK

"Lithium-Systeme: Stand der Technik und zukünftige Entwicklungen"

Condensateurs Fribourg SA, Fribourg, 6. Februar 1996.

P. NOVÁK

"Insertionselektroden für Ionentransferbatterien"

Technische Universität Dresden, 29. Oktober 1996.

P. NOVÁK

"Komponenten für Ionentransferbatterien"

BEW-Workshop „Accumulateurs“, Paul Scherrer Institut, Villigen, 12. Dezember 1996.

P.P. RADI, B. MISCHLER, H.M. FREY, P. BEAUD, A.-P. TZANNIS, T. GERBER

"Stimulated Emission Pumping of OH and NH in Flames by Using Two-Color Resonant Four-Wave Mixing"

IEA Conference, 18th Task Leader Meeting, Cranfield, England, Aug. 7-9, 1996.

M. SAURER

"Stabile Isotope als Indikatoren für C/N- und H₂O-Flüsse"

WSL, Birmensdorf, 21.11.96.

G.G. SCHERER

"State of the Art of SPFC at PSI - A Short Overview"

Kick-off Meeting, Joule III Project Second Generation SPFC Development, Siemens AG, Erlangen, January 30-31, 1996.

G.G. SCHERER

"Low and Medium Temperature Fuel Cells - A Brief Overview"

International Workshop on Electrochemistry „Solid versus Liquid State“, Max Planck Gesellschaft, Schloss Ringberg, Tegernsee, March 4-8, 1996.

G.G. SCHERER

"Polymer Electrolyte Membranes For Fuel Cells"

Army Research Office Workshop „Disposable Fuel Cells“, University of Minnesota, Minneapolis, April 11-12, 1996.

G.G. SCHERER

"Forschungsarbeiten zum Thema Polymerelektrolyt Brennstoffzellen am Paul Scherrer Institut"

Forschungszentrum Jülich GmbH, Institut für Energieverfahrenstechnik, Jülich, May 8, 1996.

G.G. SCHERER

"The Influence of Irradiation Conditions on the Mechanical Properties of Grafted Films"

IEA Spring Meeting of Fuel Cell Annex VIII, Forschungszentrum Jülich GmbH, Jülich, May 9-10, 1996.

G.G. SCHERER

"Materials Research Aspects of Membrane Development for Polymer Electrolyte Fuel Cells"

11th World Hydrogen Energy Conference, Stuttgart, June 23-28, 1996.

G.G. SCHERER

"Brennstoffzellen - Stand der Technik"

Winterthurer Energie- und Umwelt-Apero, Technikum Winterthur, Winterthur, September 11, 1996.

G.G. SCHERER

"Humidification Studies in 1-D Polymer Electrolyte Fuel Cells"

IEA Fall Meeting of Fuel Cell Annex VIII, Kissimmee, Florida, November 21-22, 1996.

G.G. SCHERER

"Wie funktioniert eine Polymerelektrolyt Brennstoffzelle"

1. Schweizerische Tagung über das Anwendungspotential von Niedertemperatur-Brennstoffzellen, Ingenieurschule Grenchen-Solothurn, Grenchen, December 4, 1996.

G.G. SCHERER

"Fortschritte in der Entwicklung von Polymerelektrolyt Brennstoffzellen am PSI"

Statusseminar Bundesamt für Energiewirtschaft, Paul Scherrer Institut, Villigen, December 12, 1996.

B. SCHNYDER

"XPS and Mass Spectrometric Analysis of Boron Doped Fullerenes"

International Conference on Quantitative Surface Analysis QSA 9, University of Surrey, Guildford, GB, July 15-19, 1996.

M. SCHUBNELL

"Solar Energy Research Activities at PSI"

Australian National University, Canberra, 23.1.1996.

R. SIEGWOLF

"The PSI Contribution to the ECOMONT-Project. The Use of Stable Isotopes in the Characterisation of Land Use Change"

Ecomont-Workshop, Innsbruck, Feb. 27 - March 1, 1996.

R. SIEGWOLF, ST. HÄTTENSCHWILER*,

M. SAURER

"Carbon Isotope Allocation. From alpine Grassland to tropical forests: Biological consequences of elevated CO₂"

ProClim - Forum for Climate and Global Change, Basel, March 14 -16, 1996.

* Botanisches Institut, Universität Basel

R. SIEGWOLF

"The Ecological Effects of LAND Use Change in the Alpine Area. An Overview of the ECOMONT-EU-Project"

Euroflux-Workshop, Edinburgh, UK, 23.-25. Mai, 1996.

R. SIEGWOLF

"Der Einsatz stabiler Isotope in der Umweltforschung"
Vortrag im Rahmen der Seminarreihe des LAPETH,
der ETH Zürich, 1. Juni, 1996.

R. SIEGWOLF

"Auswirkungen der NO_x-Emissionen aus Autoabgasen
entlang einer Autobahn auf die Stickstoff-Isotopen-
verhältnisse, den Stickstoffgehalt von Fichtennadeln
und deren δ¹⁵-Verhältnis"
Arbeitsgemeinschaft Stabile Isotope, Tagung in Berlin,
30.9. - 3.10.1996.

R. SIEGWOLF

"First Results of the ECOMONT - Project: The PSI
Contribution"
Ecomont-Workshop, Innsbruck, Nov. 28 - 30, 1996.

R. SIEGWOLF

"Wechselwirkung zwischen der Atmosphäre und der
Vegetation"
Vorlesung im Rahmen der Reihe „Ausgewählte Kapitel
aus den Umweltwissenschaften“, Fachhochschule
Wädenswil, 10. Dezember, 1996.

A. STAMPANONI

"Collisional Deactivation of Nitric Oxide in the A-State
Investigated by Double Resonance Polarisation Label-
ing Spectroscopy"
ERCOFTAC Joint Annual Meeting of the Competence
Centers on Measuring Techniques and Combustion
and Pollution Formation, PSI Villigen, 27 June 1996.

A. STEINFELD

"Solar-Processed Metals as Clean Energy Carriers"
- Ludwig-Maximilians Universität, München, 26.1.96.
- University of Minnesota, Minneapolis, USA,
12.3.1996.

A. STEINFELD

"Solar Hydrogen via 2-Step Thermochemical Proc-
esses with Metal Oxides Redox Systems"
NREL-National Renewable Energy Laboratories,
Golden, USA, 11.3.1996.

A. STEINFELD

"Solar Thermochemistry for CO₂ Mitigation"
MIT-Energy Laboratory, Boston, USA, 13.3.1996.

A. STEINFELD

"Solar Thermochemical Production of Hydrogen"
International Energy Agency's Hydrogen Program,
Amsterdam, 14.11.1996.

S. STUCKI, R. BÜHLER*, P. HASLER**,
B. COVELLI***, M. MÜLLER****, W. VOCK*****

"Biometh - Feasibility of Methanol Production from
Waste Biomass and its Use as a Fuel in Switzerland"
Proc. 11th Int. Symposium on Alcohol Fuels, ISAF,
Sun City, South Africa, pp. 466-476, April 1996.

* Ingenieurbüro Umwelt + Energie, Maschwanden

** Ingenieurbüro Verenum, Zürich

*** Tecova AG, Wohlen

**** TEMUM, Brugg

***** Ingenieurbüro Abfall + Recycling, Liestal

S. STUCKI

"Methanol as a Transportation Fuel"
Convegno Italo-Svizzero "La Città del Futuro", Milano
12/13 Juni 1996

S. STUCKI, A. JAKOB, J. WOCHLE

"Verfahrenskonzept zur vollständigen Abtrennung von
Schwermetallen bei der thermischen Abfallverwertung"
Tagungsband, VGB-Tagung Thermische Abfallbe-
handlung, Wien, Juni 1996.

S. STUCKI

"Produktion von Wasserstoff"
Giornata di studi "Idrogeno", Associazione delle Az-
iende Elettriche della Svizzera Italiana, Lugano
16. October 1996.

M. STURZENEGGER

"Reactivity of Ironwüstite Phases with Steam"
Center for Solar Energy and Hydrogen Research,
Ulm, Germany, 16 December 1996.

P. TALKNER

"Invariant Densities of Maps with Weak Gaussian
White Noise"
5th International Conference on Path Integrals from
meV to MeV, Dubna, May 27-31, 1996.

P. TALKNER

"Invariant Densities and Rates for Noisy Maps"
Institute of Chemical Physics, Moscow, June 3, 1996.

P. TALKNER

"Anharmonic Barrier Corrections for Kramers' Rates"
Karpov Institute of Physical Chemistry, Moscow,
June 6, 1996.

A. TSUKADA

"Polymerelektrolyt Brennstoffzelle - Von der Einzel-
zelle zum Brennstoffzellen-Stapel"
1. Schweizerische Tagung über das Anwendungspo-
tential von Niedertemperatur-Brennstoffzellen, Inge-
nieurschule Grenchen-Solothurn, Grenchen, 4. De-
zember 1996.

A.-P. TZANNIS

"Resonant Quasi-Heterodyne Holographic Interferometry"

ERCOFTAC Leonhard Euler Research Center, March 30th 1995.

A.-P. TZANNIS

"Resonant Holographic Interferometry"

ERCOFTAC, Villigen, 27.6.1996.

A.-P. TZANNIS, P. BEAUD, H.M. FREY,

T. GERBER, B. MISCHLER, P.P. RADI

"Resonant Holographic Interferometry"

ERCOFTAC Leonhard Euler Research Center, June 27th, 1996.

R.O. WEBER, P. KAUFMANN

"Synoptic-Scale Wind and Regional Flow Patterns"

XXI General Assembly of the European Geophysical Society, The Hague, 6-10 May, 1996.

A. WEIDENKAFF

"High Temperature Solar Chemistry"

Workshop, Fifth International Summer School Solar Energy '96, Klagenfurt, Austria, 29. Juli -9. August 1996.

A. WEIDENKAFF

"Wüstite - A Solar Energy Carrier"

13th International Symposium on the Reactivity of Solids (ISRS-13), Hamburg, Germany, 8.-12. September 1996.

A. WOKAUN

"Technologies for Sustainable Individual Mobility"

UT-MIT-ETH Joint Workshop on Alliance for Global Sustainability, University of Tokyo, Japan, 17.-19. Jan. 1996.

A. WOKAUN

"Oberflächenanalytische Charakterisierung von Cu/ZrO₂-Methanolsynthesekatalysatoren"

ETH Zürich, Kompetenzzentrum für Analytische Chemie, 13. Juni 1996.

A. WOKAUN

"Alternative Fuels and Fuel Cells in Hybrid Vehicles"

Alternative Automotive Fuels-Alternative Automotive Drive Lines, Berlin, 21. Oktober 1996.

A. WOKAUN

"Emerging Technologies for Sustainable Individual Mobility"

Erweiterte Konferenz über hybride Automobilantriebe, ETH Zürich, 6. November 1996.

POSTERS

A. ARNOLD, R. BOMBACH, B. KÄPPELI

"Quantitative Measurements of Species Concentration Fields by 2D-LIF"

26th International Symposium on Combustion, Napoli, 28 July - 2 August 1996.

J.L. BARRAS*, C. DAUL*, E. DEISS

"Modeling of the Intercalation Process of Lithium Ions into Manganese Oxide"

Monte Verita Conference on „Structural and Dynamic Modeling of Mechanical Behaviour of Solids“, Ascona, September 2-6, 1996.

* Universität Fribourg

A. BILL, B. ELIASSON*, E. KILLER*,

U. KOGELSCHATZ*

"Hydrogenation of Carbon Dioxide in a Packed-Bed Reactor"

11th World Hydrogen Energy Conference, Stuttgart, Germany, June 1996.

* ABB Corporate Research Centre, Baden

H.P. BRACK, B. KELLER*, D. WEBER*,

G.G. SCHERER

"Wetting Properties of Radiation Grafted ETFE Films and Membranes"

Frühjahrstagung der Polymer Gruppe der Schweiz, ETH-Zürich, Zürich, 14. März 1996.

* EMPA, CH-8600 Dübendorf

H.P. BRACK, G.G. SCHERER

"Preparation of Fuel Cell Membranes by the Pre-Irradiation Grafting Method: Effects of Base Polymer Nature"

2nd IUPAC Symposium on Free Radical Polymerization: Kinetics and Mechanisms, Santa Margherita Ligure, Italy, May 26-31, 1996.

D. CLEMENS, C. TERRIER*, A. VANANTI*, P. BÖNI,

B. SCHNYDER, S. TIXIER, M. HORISBERGER

"Magnetic In-plane Anisotropy in Sputtered FeCo Films and Multilayers"

1st European Conference on Neutron Scattering (ECNS'96), Interlaken, 8.-11. Oktober 1996.

* ETH Zürich

W. DURISCH, A. WÖRZ*

"Charakterisierung von Solarzellen und Solarmodulen unter realen Betriebsbedingungen"

Sommet Mont-Soleil. Photovoltaik heute und morgen - eine schweizerische Standortbestimmung, Testzentrum Mont-Soleil ob Saint-Imier, 23. Oktober 1996.

* Fachhochschule Ulm, Deutschland

D. FRANZKE, C. HAHN, TH. KUNZ,
J. KRITZENBERGER, C. SCHERER*, O. NUYKEN*,
A. WOKAUN
"Azophosphonates - A new class of Materials for
Photoablation"
XVIth IUPAC Symposium on Photochemistry, Uni-
versity of Helsinki, Finland, 21-26.7.1996.
* TU München

H.M. FREY
"Stimulated Emission Pumping of OH and NH Using 2-
CFWM"
Herbstversammlung der neuen Schweizerischen
Chemischen Gesellschaft, Basel, 23.11.1996.

M. FURGER, L. POGGIO, W.K. GRABER
"Measuring Path-Averaged Fluxes of H₂O and O₃ in
an Alpine Valley with Optical Methods"
Poster presented at the MAP Meeting Hall/Tirol,
23-24 May 1996.

S. GHASHGHAIE*, W. BREYMAN***, J. PEINKE***,
P. TALKNER, Y. DODGE****
"Die Dynamik von Wechselkursmärkten als turbulenter
Prozess"
Frühjahrstagung der DPG, Regensburg, March 25-29,
1996.
* Universität Bern
** Universität Basel
*** Universität Bayreuth
**** Université de Neuchâtel

B. GUPTA*, F.N. BÜCHI, G.G. SCHERER,
A. CHAPIRO**
"Radiation Grafting - A Versatile Route to the Mem-
brane Development"
XIV National Symposium on „Membranes in Chemical
and Biochemical Industries“, Indian Institute of Techno-
logy, New Dehli, February 16-17, 1996.
* Indian Institute of Technology, New Dehli, India
** CNRS, F-94320 Thiais

P. HÄRING, R. KÖTZ, O. HAAS,
H. SIEGENTHALER*
"In-Situ Scanning Probe Microscopy of Electroactive
Films during Electrochemical Oxydation/Reduction"
Workshop on Nanoscience, Hasliberg Wasserwendi,
CH, 14.-18. Oktober 1996.
* Universität Bern

B. HEMMERLING, R. BOMBACH, W. HUBSCHMID,
A. STAMPANONI
"Application of Laser-Induced Gratings for Diagnostic
Purposes in Gases"
ECW'96: 15. European CARS Workshop, University of
Sheffield, 27-29 March 1996.

F. HOLZER, S. MÜLLER, O. HAAS
"Improved Zinc Electrodes with High Power Capability"
47th ISE-Meeting, Balatonfüred, Hungary, September
1-6, 1996.

W. HUBSCHMID, R. BOMBACH, B. HEMMERLING
"Laser-Induced Gratings in the Red System of Mo-
lecular Oxygen"
OSA meeting on Laser Applications to Chemical and
Environmental Analysis, Orlando (USA), 18-22 March
1996.

A. IMHOF
"Decomposition of Limestone in a Solar Reactor"
World Renewable Energy Congress IV, Denver, 12-
22 June 1996.

A. IMHOF
"Decarbonization of Limestone with Solar Energy"
Eurosun 1996, Freiburg, Germany, 16-19 Sept. 1996.
Int. Symposium on Solar Thermal Concentrating
Technologies, Köln, Germany, October, 6-11, 1996.

A. IMHOF
"Entsäuerung von Kalkpulver in einem Solarreaktor"
Kongress der Int. Konferenz für Industrielle Energie-
wirtschaft, Leipzig, Deutschland, 23.-25. Sept. 1996.

A. JAKOB, S. STUCKI, B. SCHNYDER, R. KÖTZ
"Examination of ZnO - SiO₂ Diffusion Profiles by XPS"
XIIIth International Symposium on the Reactivity of Solids
(ISRS), Hamburg, Germany, September 8-12, 1996.

F. JOHO, P. NOVÁK, O. HAAS, R. NESPER*
"In-Situ Infrared Investigation of Organic Electrolytes
for Rechargeable Lithium Ion Batteries"
Proceedings 47th ISE Meeting, Veszprém, Hungary,
p. P5b-6, 1996.
* Laboratorium für Anorg. Chemie, ETH Zürich

F. JOHO, R. NESPER*
"Kristallstruktur von Mg₃V₁₀O₂₈(H₂O)₂₈ und Modelle zur
Wasserstoffbrückenordnung"
8. Vortragstagung der Fachgruppe Festkörperchemie
der GDCh, Darmstadt, 20.-22. März 1996.
* Laboratorium für Anorg. Chemie, ETH Zürich

I. KAMBER, M. SCHUBNELL
"Photochemistry at 773 K-Influence of above Bandgap
Irradiation on the Reaction ZnO + CH₄ → Zn + CO + H₂O"
8th Workshop on Quantum Solar Energy Conversion;
Rauris (A), 1996.

I. KAMBER
"Interaction of CO₂ with small TiO₂ Fragments"
- An EHMO study; Eleventh International Conference
on Photochemical Conversion and Storage of Solar
Energy (I.P.S.-11); Bangalore (IN), 1996.

D.N. KOZLOV*, R. BOMBACH, B. HEMMERLING,
W. HUBSCHMID
"Possibilities and Perspectives of Dynamic Information
by Raman Spectroscopic Methods"
ECW'96: 15. European CARS Workshop, University of
Sheffield, 27-29 March 1996.
* General Physics Institute, Moscow

P. NOVÁK, W. SCHEIFELE, M. WINTER, O. HAAS
 "Graphite Electrodes with Tailored Porosity for Rechargeable Ion-Transfer Batteries"
 8th Int. Meeting on Lithium Batteries, Extended Abstracts, Nagoya, (I-A-30), pp. 214-215, 1996.

L. POGGIO, M. FURGER, W.K. GRABER
 "A Comparison of Scintillation Crosswind Methods"
 Proc. Int. Geosci. and Remote Sensing Symp., Lincoln USA, 399-401, 27-31 May 1996.

P.P. RADI, B. MISCHLER, H.M. FREY, P. BEAUD, A.-P. TZANNIS, T. GERBER
 "Stimulated Emission Pumping of OH and NH in Flames by Using Two-Color Resonant Four-Wave Mixing"
 IEA Conference, 18th, Task Leader Meeting, Cranfield, England, Aug. 7-9, 1996.

P.P. RADI, B. MISCHLER, H.M. FREY, P. BEAUD, A.-P. TZANNIS, T. GERBER
 "Stimulated Emission Pumping of OH and NH in Flames by Using Two-Color Resonant Four-Wave Mixing"
 26th Symposium (Intl.) on Combustion, Napoli, Italy, 1996.

P.P. RADI, B. MISCHLER, H.M. FREY, P. BEAUD, A.-P. TZANNIS, T. GERBER
 "Stimulated Emission Pumping of OH and NH in Flames by Using Two-Color Resonant Four-Wave Mixing"
 XV. European CARS Workshop, Sheffield, England, March 27-29, 1996.

F. SALADIN, I. KAMBER
 "Photosynthesis of small Hydrocarbon Molecules from Gaseous CO₂ / H₂O at the Surface of TiO₂"
 - Eleventh International Conference on Photochemical Conversion and Storage of Solar Energy (I.P.S.-11), Bangalore (IN); 1996.
 - Joint Meeting of the French, German and Swiss Sections of the European Photochemistry Association (EPA); Konstanz (D), 1996.

M. SAURER, R.T.W. SIEGWOLF
 "Oxygen Isotope Composition of Cellulose of Trees from Several Sites in Switzerland"
 Stable Isotopes and the Integration of Biological, Ecological and Geochemical Processes, Newcastle, 9-11 July, 1996.

R.T.W. SIEGWOLF, M. SAURER, CH. KÖRNER*
 "CO₂-Recycling by Plants: how Reliable is the Carbon Isotope Estimation?"
 Stable Isotopes and the Integration of Biological, Ecological and Geochemical Processes, Newcastle, 9-11 July, 1996.
 * Universität Basel

M.E. SPAHR, P. NOVÁK, O. HAAS, R. NESPER*
 "Electrochemical Li⁺ Insertion Properties of Lithium-Nickel-Manganese Oxides Correlated to the Manganese Content and Electrode Porosity"
 Herbstversammlung NSChG, Basel, 21. November 1996; Abstract Chimia 50, 1996, 324.

* Laboratorium für Anorganische Chemie, ETH Zürich

M.E. SPAHR, P. NOVÁK, O. HAAS, R. NESPER*
 "Novel Lithium Insertion Electrode Materials Based on the Li-Ni-Mn-O System"
 8th Int. Meeting on Lithium Batteries, Extended Abstracts, Nagoya, (II-B-41), pp. 486-487, 1996.

* Laboratorium für Anorganische Chemie, ETH Zürich

A. STAMPANONI, R. BOMBACH, B. HEMMERLING
 "Double Resonance Polarisation Labeling Spectroscopy of Nitric Oxide"
 26th International Symposium on Combustion, Napoli, 28 July - 2 August 1996.

A. STEINFELD
 "Solar-Processed Chemical Fuels as Clean Energy Carriers"
Greenhouse Issues 27, 1996.

P. TALKNER, R. BADII, R. BARTUSSEK*, P. HÄNGGI*
 "Stroboskopische Beschreibung von periodisch gekippten Ratchets"
 Frühjahrstagung der DPG, Regensburg, March 25-29, 1996.

* Universität Augsburg

A. TARANCÓN*, H.P. BRACK, H. BÜHRER*, G.G. SCHERER
 "A Thermogravimetric Analysis Investigation of Thermal Degradation in ETFE-g-PS Films and ETFE-g-SPS Membranes"
 Frühjahrstagung der Polymer-Gruppe der Schweiz, ETH-Zürich, Zürich, 14. März 1996.

* Technikum Winterthur, Chemieabteilung, CH-8401 Winterthur

Z. VEZIRIDIS, G.G. SCHERER, H. FREIMUTH*
 "Microstructured Electrodes"
 Schweizerischer Nationalfonds „Workshop on Nanoscience“, Hasliberg/Wasserwendi, 14-18. Oktober 1996.
 * Institut für Mikrotechnik Mainz, D-55129 Mainz

C. VON SCALA, R. STRUIS, S. STUCKI
 "The Influence of Heavy Metals on the Gasification of Wood"
 9th European Bioenergy Conference, Copenhagen, Denmark, 24-27 June 1996.

A. WEIDENKAFF, P. NÜESCH, A. WOKAUN,
A. RELLER*

"Mechanistic Studies of the Water-Splitting Reaction
for Producing Solar Hydrogen"

13th International Symposium on the Reactivity of Solids (ISRS-13), Hamburg, Germany, 8. - 12. September 1996.

* Inst. of Inorg. and Appl. Chem., Univ. of Hamburg,
D-20146 Hamburg, Germany

APPLICATION FOR A PATENT

A. BILL, B. ELIASSON*, E. KILLER, U. KOGELSCHATZ
"Verfahren und Vorrichtung zum Umwandeln eines
Treibhausgases"

Nr. 6196 21 653.2, 30. Mai 1996.

* ABB Corporate Research Centre, Baden

J. STEBANI*, A. WOKAUN, TH. LIPPERT**,
TH. KUNZ

"Verfahren zur Mikrostrukturierung von Polymeren"

Nr. 96116472.0-2115, 18. Dez. 1996.

* D-47800 Krefeld, Deutschland

** Los Alamos, New Mexico, 87544, USA

CONFERENCES, WORKSHOPS & EXHIBITIONS

O. HAAS

12. Tagessymposium Elektrochemische Energiespei-
cherung.

Paul Scherrer Institut, 11. September 1996.

A. IMHOF

Workshop am PSI über "Industrielle Solarkalzinie-
rung"

unter Mitwirkung von Holderbank-Management AG;
Krupp-Polysius, D-Beckum; ABB-Industrie AG, Baden;
ABB-Linkman Systems Ltd., London; Bomin Solar
Research GmbH, D-Lörrach; Fricker Consulting,
Rickenbach und dem PSI; 3. und 4. Oktober 1996.

I. POPELIS*, G.G. SCHERER, L. DUBAL**

1. Schweizerische Tagung über das Anwendungspo-
tential von Niedertemperatur-Brennstoffzellen.

HTL Ingenieurschule Grenchen-Solothurn, Decem-
ber 4, 1996.

* HTL Ingenieurschule Grenchen-Solothurn, 2540
Grenchen

** Bundesamt für Energiewirtschaft, 3003 Bern

A. TSUKADA, C. MARMY, A. BRACHER,
F. HILDEBRAND, M. PROBST, S. KROMER,
R. SCHÄREN, F.N. BÜCHI, J. HUSLAGE,
G.G. SCHERER

Hybridkonferenz, ETH Zürich, 6. November, 1996.

MEMBERSHIPS IN EXTERNAL COMMITTEES

W. DURISCH

International Energy Foundation, IEF

Advisory Committee

W. DURISCH

Swiss Society of Engineers and Architects (SIA),
Fachgruppe für Verfahrens- und Chemieingenieur-
Technik (FVC),

Delegate

W. DURISCH

UNESCO, World Renewable Energy Congress,

Steering Committee

F. GASSMANN

CCA, Commission sur le Climat et l'Atmosphère,
SANW-Kommission

Secretary

F. GASSMANN

Arbeitsgruppe Ausbreitung der Schweiz. Alarmzen-
trale SNAZ

Member

F. GASSMANN

Internationaler Lenkungsausschuss des Projektes
REKLIP

Member

T. GERBER

ERCOFTAC 'European Research Community On
Flow Turbulence And Combustion'

Scientific Committee

T. GERBER

European CARS Workshop

Steering Committee

T. GERBER

Towards Clean Diesel Engines

Steering Committee

T. GERBER

IEA Implementing Agreement Energy Conservation
and Emissions Reduction in Combustion

Task Leader

W. GRABER

Member of the Project Coordination Committee (PCC)
of the EC-Project on "Vertical Ozone Transport over
the Alps (VOTALP)"

W. GRABER

Member of the Project Coordination Committee of the
EC-Project on "Ecological Effects of Land Use
Changes in European Terrestrial Mountain, Ecosys-
tems (ECOMONT)"

O. HAAS

International Society of Electrochemistry (ISE), Divi-
sion Officer Electrochemical Energy Technology.

O. HAAS

Working Party on Electrochemistry of the FELS,
Delegate of the New Swiss Chemical Society.

G.G. SCHERER

IEA Implementing Agreement on „Advanced Fuel Cells“
Annex IV, „Collaborative Research and Development
on Polymer Electrolyte Fuel Cells“
Taskleader „New Membranes and Electrolytes“.

TH.H. SCHUCAN

IEA Implementing Agreement on “Hydrogen Produc-
tion and Utilisation”, Annex XI, “Integrated Systems”,
Subtask Leader “Case Studies”.

TH.H. SCHUCAN

Swiss Academy of Engineering Sciences,
Member of Energy Committee.

A. STEINFELD

Associate Editor of *Energy - The International Journal*

A. STEINFELD

International Energy Agency's SolarPACES Operating
Agent Task II

A. STEINFELD

Editor of “*Solar Chemistry News*”

A. WOKAUN

R'97 (Recovery, Recycling, Re-integration)
Scientific Panel